IMPROVED METHODS FOR CHARACTERISING ACOUSTOPLASTICITY

Colin Francis Souza

A thesis for the degree of Doctor of Philosophy (PhD)

Submitted to the College of Science and Engineering,
University of Glasgow

February 2022

Declaration

I declare that this thesis is a record of the original work carried out by myself under the supervision of Professor Margaret Lucas in the School of Engineering at the University of Glasgow, United Kingdom, during the period of October 2016 to February 2022. The copyright of this thesis therefore belongs to the author under the terms of the United Kingdom Copyright acts. Due acknowledgement must always be made of the use of any material contained in, or derived from, this thesis. The thesis has not been presented elsewhere in consideration for a higher degree.

Signature:

Printed name: Mr Colin Souza

Signature:

Printed name: Prof Margaret Lucas

Abstract

The benefits of high-power ultrasonics to industrial metal forming processes have long been demonstrated in uniaxial mechanical tests. The astonishing reductions in flow stress observed have been linked to changes to surface friction and to an interaction of the excitation with the mechanisms of plastic deformation in metals. Many advanced techniques and material models have been brought to bear on the problem of the underlying physics of acoustoplasticity, and yet all rely fundamentally on accurate force and extension data. The effects of inertia and inhomogeneity in the loading distribution on the specimen have been largely ignored, and yet are incompatible with commonly used instrumentation.

This thesis reports investigations which address the error introduced into force measurement in mechanical testing by ultrasonic excitation. After reviewing experimental mechanics techniques, it was found that the piezoelectric force transducer retained its central role in defining true flow stress reduction. An inertia-based barrier to vibration was introduced between the force transducer and test machine crosshead, to impose the rigid boundary condition desired to ensure the force transducer coincided with a displacement node. Lumped-parameter modelling indicated that the dynamic response of the piezoelectric force transducer's structure could significantly distort the amplitude of an oscillatory force measurand. Either amplification or attenuation could result depending on the proximity of excitation frequency to natural frequency of the force transducer's first longitudinal mode. Simple impulse experiments provided the natural frequency of the force transducer in the free-free condition, a parameter used in later finite element (FE) modelling of the ultrasonic tensile test structure.

Experimental Modal Analysis (EMA) was used to investigate the dynamic response of the ultrasonic tensile test structure, and to map the mode shape of the first longitudinal mode, the mode utilised in ultrasonic tensile testing. A finite element model was constructed of the test apparatus, and subsequently solved in an eigenvalue analysis to extract the natural frequency and mode shape of the first longitudinal mode. When the numerically predicted waveform was compared with that found from EMA, a significant difference was discovered

between the horn and specimen. The compliance of the joint was adjusted until the simulated mode shape converged on its experimental counterpart.

Once experimentally calibrated, the FE model was used to predict the force experienced by the force transducer for increasing values of vibration amplitude. Comparison with experimental force measurements found good agreement. Of greatest importance to the investigation of flow stress, the FE model predicted the indicated value from the force transducer to be 1.91 times greater than the measurand at the specimen-force transducer interface.

Strain gauges were attached to the gauge section of the specimen in the ultrasonic tensile test apparatus, and the vibration varied over a range of amplitudes. By converting the oscillatory strain measurement into force on the specimen cross-section, the loading experienced by the specimen at the strain gauge location was compared to force measurements made simultaneously by the piezoelectric force transducer. The ratio of force amplitude from the force transducer over the force amplitude calculated from the specimen strain measurement was found to vary from 3.13 to 3.50, with a mean of 3.32. Repeating the experiment within the FE model calculated an amplitude ratio of 3.33, constant over all vibration amplitudes. This value was used to develop a correction factor to extrapolate force on the specimen from piezoelectric force transducer measurement. The correction was applied to an ultrasonic tensile test on a soft aluminium. Though the mean stress was reduced during the periods of excitation, no real reduction in flow stress was observed, which is consistent with the theory of stress superposition.

The evolution of plastic deformation was studied over the gauge section of an ultrasonically excited specimen, using an optical metrology system adapted for use on the ultrasonic tensile test. To eliminate oscillatory motion from images, a high-speed strobe lit the specimen in bursts of light synchronised with the ultrasonic excitation. Digital Image Correlation was used to process the image sequence to find strain and strain rate across the whole face of the specimen gauge length. It was observed that the application of ultrasonic excitation disrupted the usual distribution of plastic deformation along the specimen length, focussing deformation towards the location of peak stress amplitude. Again, observations were consistent with the theory of stress superposition.

This thesis demonstrates how the dynamic response of the structure of the specimen and force transducer in an ultrasonic tensile test can significantly distort the force measurement, crucial for accurately identifying a real reduction in flow stress. This has implications for studies of acoustoplasticity aiming at determining underlying physical mechanisms. It is found that, when the effect of inertia is accounted for, the theory of stress superposition is sufficient to explain the stress-strain relationship observed.

Acknowledgements

To my supervisor, Professor Margaret Lucas, I wish to convey my deepest gratitude. Thank you for giving me the opportunity to enter the world of cutting-edge research and to contribute to it. Thank you for your skillful supervision, advice and technical insight. Above all, thank you for your immense patience and unwavering encouragement.

Thanks also to Dr Daniel Mulvihill, for stepping in as my second supervisor, and his assistance with identifying and honing the main themes of my research.

I wish to thank Dr Ron Thomson for providing my academic letter of reference which enabled my return to academia, and pay tribute to a great teacher and enthusiastic engineer who is sadly missed.

I would like to thank the Engineering and Physical Science Research Council (EPSRC grant number EP/M506539/1) for funding this research.

This research was completed at the University of Glasgow James Watt School of Engineering, where the help of the technical, computing and administrative staff is gratefully acknowledged. Thanks go to Mr Denis Kearns and all the staff of the Mechanical workshop, for the manufacture of specimens and fixtures, and invaluable technical advice. Thanks are also due to the staff of the Electrical workshop, most especially Mr Neil Owen and Mr Bernard Hoey for their incredible efforts regarding the design and manufacture of electronic instrumentation, without which key parts of this research would not have been possible.

I would like to thank the members of the Centre of Medical and Industrial Ultrasonics, at the University of Glasgow for advice, support, and friendship – and especially the C-MIU office for that all-sustaining camaraderie. To Dr Nicola Fenu, Dr Nathan Giles-Donovan, Jack Stevenson and the rest of the crew – thanks for daft times and the good memories. In particular I would like to say a huge thank you to Jill Savva – a better desk buddy and running mate I could not have asked for.

Thanks also to members of the University of Glasgow Materials and Manufacturing Research Group, especially Dr Daniele Barbera, Ross Williams and Chris Triantafyllou for help with solid mechanics and material sample preparation.

A very special thank you to Dr Xuan Li for his invaluable help with all things ultrasonic – design, experimental and numerical – and for a warm friendship.

I am much obliged to Dr Patrick Harkness, Dr Kevin Worral, Dr Andrew Feeney and Professor Sandy Cochrane for engaging me on their incredible research projects, which allowed me to continue my journey to completion.

I would like to thank my friends and family for their love and support during my studies. Thank you to my father, Dave Souza. Many thanks to my in-laws, Barbara Charles and Colin Campbell for crucial childcare. To Johnny Boxall – thank you for helping me through the more challenging moments, and putting me back together over the phone so many times.

Finally, thank you to my children, Lily and Struan, for their forbearance with their distracted father. To my wife, Clare – editor, councilor and greatest champion – my profound thanks for your encouragement, patience and unfailing belief in me over these years; it is to this that I owe the completion of this thesis.

I would like to dedicate this thesis to my mother, Elizabeth Souza, whose determination to remain curious and creative was an inspiration.

Nomenclature

Symbol	Definition	Base unit
APE	Acousto-plastic effect	-
A_{XS}	Cross-sectional area (Chp 7)	m^2
b	Burgers vector	-
c	Speed of sound	$m.s^{-1}$
C	Damping matrix	$m.s^{-1}$
CAD	Computer-aided design	-
d	Thickness of the specimen	m
D	Diameter of isolating mass spring rod	m
E	Young's modulus or elastic modulus	Pa
EMA	Experimental Modal Analysis	-
f	Frequency	Hz
F	Force	N
F_{axial}	Force acting in the axial, or longitudinal axis of the specimen	N
F_{osc}	Oscillatory component of force measured by force transducer	N
F_{dyn}	Dynamic force on the specimen at the strain gauge location	N
F_{ex}	Excitation force	N
F_f	Reaction force from foundation	N
F_{ind}	Indicated force	N
F_{mea}	Measurand force	N
F_{PFT_osc}	Oscillatory component of F_{ind}	N
F_{PFT_sta}	Quasi-static component of F_{ind}	N
F_{SG}	Force on specimen cross-section, in specimen axial direction, at strain gauge location	N
F_{SG_osc}	Oscillatory component of F_{SG}	N
F_{SG_sta}	Quasi-static component of F_{SG}	N
FE	Finite Element	-
FEA	Finite Element Analysis	-
FEMU	Finite Element Model Updating	-
FFT	Fast Fourier Transform	-

FOV	Field of view	-
FRF	Frequency response function	-
FT	Fourier transform	-
$GAIN$	Gain setting	-
GF	Gauge factor	-
h_{px}	Height of camera sensor in pixels	px
H	Height of Field Of View	m
$H(\omega)$	Mobility frequency response function	-
k	Wave number	$rad.m^{-1}$
k	Spring stiffness in lumped-parameter system model	$N.m^{-1}$
K	Stiffness matrix	
L	Length of prismatic bar or rod	m
L	Extended length (in strain calculation)	m
L	Length of isolating mass spring rod	m
L_0	Original length (in strain calculation)	m
L1	First longitudinal mode	-
LDV	Laser Doppler Vibrometer	-
M	Mass matrix	kg
M_t	Image magnification from lens and camera	-
m	Mass of point mass in lumped-parameter system model	kg
m_1, m_2	Masses of point masses in lumped-parameter system model	kg
m_r	Modal mass of the r^{th} mode	$kg.m^2$
ODS	Operating deflection shape	-
PFT	Piezoelectric force transducer	-
R	Resistance	Ohm
SEM	Scanning electron microscope	-
SR_{cam}	Spatial resolution of camera	$m.px^{-1}$
SR_{DIC}	Spatial resolution of Digital Image Correlation	m
t	Time	s
t_e	Exposure time	s
t_p	Time at which plastic deformation commences	s
T	Period of one cycle	s
$T(\omega)$	Transmissibility frequency response	-

TEM	Transmission Electron Microscope	-
u	Displacement	m
u_{HT}	Displacement of horn tip	m
U_0	Initial or input displacement amplitude	m
US	Ultrasonic	-
USTT	Ultrasonic tensile test	-
v_2	Velocity of mass m_2 in lumped-parameter system model	$m.s^{-1}$
v	Velocity	$m.s^{-1}$
v_{CH}	Crosshead velocity	$m.s^{-1}$
v_{ref}	Reference velocity measurement	$m.s^{-1}$
v_{resp}	Response velocity measurement	$m.s^{-1}$
V_{AB}	Voltage across bridge	V
V_{EX}	Bridge excitation voltage	V
w	Width of specimen	m
W	Width of Field Of View	m
w_{px}	Width of camera sensor in pixels	px
x	Distance along prismatic bar or rod	m
X	Peak displacement amplitude of S-DOF point mass in lumped-parameter system model	m
X	Displacement vector in N-DOF lumped-parameter model	m
X_{ex}	Nominal displacement caused by excitation force	m
Z_f	Foundation impedance in lumped-parameter model	$m.s^{-1}.N^{-1}$
α_R	Rayleigh mass proportional damping	s^{-1}
β_R	Rayleigh stiffness proportional damping	s^{-1}
β	Magnification factor for lumped-parameter model	-
β_t	Force transmissibility for lumped-parameter model	-
γ	Average pixel displacement during one exposure	px
Δ_{CH}	Crosshead advance	m
δ	Amplifier frequency response amplitude ratio	-
ε	Strain, true strain	-
ε_n	Nominal (engineering) strain	-
ε_p	Plastic nominal strain	-
$\dot{\varepsilon}_p$	Plastic nominal strain-rate	s^{-1}

ε_{SG}	Strain measured by strain gauge	-
ϵ	Extension of specimen	m
ζ	Damping ratio in lumped-parameter system model	-
ζ_r	Damping ratio of the r^{th} mode	
κ	Correction factor for force transducer measurement data	N
ω	Angular frequency	$rad.s^{-1}$
ω_{L1}	Angular frequency of resonance of first longitudinal mode	$rad.s^{-1}$
ω_{mr}	Angular mounted resonance frequency	$rad.s^{-1}$
ω_n	Natural angular frequency	$rad.s^{-1}$
ω_r	Angular resonance frequency of the r^{th} mode	$rad.s^{-1}$
ρ	Material density	$kg.m^{-3}$
ρ_L	Density per length of bar or rod	$kg.m^{-1}$
σ	Normal stress	Pa
$\sigma_{acoustic}$	Amplitude of propagating stress wave	Pa
σ_{axial}	Normal stress on cross-sectional plane of specimen	Pa
σ_0	Normal flow stress	Pa
σ_{osc}	Oscillatory stress amplitude	Pa
σ_{mean}	Mean stress	Pa
$\sigma_{n(axial)}$	Nominal (engineering) stress on cross-sectional plane of specimen	Pa
$\Delta\sigma_m$	Reduction in mean stress	Pa
$\Delta\sigma_{pk}$	True reduction in yield strength	Pa
σ_{SG}	Normal stress in specimen axial direction, at strain gauge location	Pa
Φ	Modal participation factor	-
ω	Angular frequency	$rad.s^{-1}$
ω_{L1}	Angular frequency of resonance of first longitudinal mode	$rad.s^{-1}$
ω_{mr}	Angular mounted resonance frequency	$rad.s^{-1}$
ω_n	Natural angular frequency	$rad.s^{-1}$
ω_r	Angular resonance frequency of the r^{th} mode	$rad.s^{-1}$

Table of Contents

Declaration ii
Abstract iii
Acknowledgements vi
Nomenclature viii
Table of Contents xii
List of Tables xv
List of Figures xvi
1 Introduction 1
1.1 The challenge of ultrasonic mechanical testing 1
1.2 Ultrasound and ultrasonic transducers 4
1.2.1 Brief historical overview 4
1.2.2 Generation of ultrasonic excitation 4
1.3 A background in plastic deformation in metals 7
1.4 Research aims 9
1.5 Summary of Contributions 10
2 Literature review 13
2.1 The Blaha effect; beginnings and controversy 13
2.1.1 Influences on APE – frequency, amplitude and material 17
2.1.2 Constitutive modelling and computational approaches 20
2.1.3 Microstructural approaches 22
2.1.4 Resolving the oscillatory stress - introduction of piezoelectric force transducer 24
2.2 Stress amplitude in the specimen by calculation 26
2.3 Summary 35
3 Experimental mechanics techniques and the ultrasonic tensile test 37
3.1 Tensile testing for characterising APE 37
3.2 The Ultrasonic Tensile Test and mechanical testing 40
3.2.1 Uniaxial test machine and ultrasonic excitation 40
3.2.2 Specimen description 44
3.2.3 Dynamics of USTT 45
3.3 Review of experimental mechanics techniques 50
3.4 Summary 54
4 Investigation of effects of oscillatory loading on the piezoelectric force transducer in a USTT 56
4.1 Influence of sensor location within test structure on USTT 56
4.2 Influence of frequency response of piezoelectric force transducer on the USTT 62

4.3 Analysis of inertial effects by lumped-parameter model 64
4.4 Experimental assessment of PFT frequency response 67
4.4.1 Existing frequency response characterisation methods 67
4.4.2 Natural frequency of the piezoelectric force transducer in free-free boundary conditions 69
4.4.3 FE approximation of the piezoelectric force transducer 70
4.5 Analytical estimation of mounted resonant frequency and amplification factor 72
4.5.1 Approximation as a rod in free-free and fixed-free conditions 72
4.6 Implications of PFT frequency response on APE investigations 74
4.7 Summary 75
5 Force investigation with EMA-calibrated FEA 77
5.1 Introduction 77
5.2 Investigation of USTT structure by Experimental Modal Analysis 78
5.2.1 Fundamental modes of vibration and EMA 78
5.2.2 Experimental Modal Analysis 79
5.2.3 Vibration measurement and FRFs 80
5.2.4 Point and transfer FRFs - FRFs on a continuous structure 81
5.2.5 Excitation 82
5.2.6 Boundary conditions – test structure support 83
5.2.7 Measurements, data acquisition and FRFs 84
5.2.8 Data acquisition and processing for FRFs and modal identification 86
5.2.9 Experimental apparatus and procedure 87
5.3 Natural frequency and mode shape of L1 mode 89
5.3.1 Assessment of the isolating mass 91
5.3.2 Velocity profile 91
5.4 Mobility-transmissibility comparison 92
5.4.1 Results 94
5.5 Summary 94
6 Numerical modelling of USTT apparatus 96
6.1.1 Material properties 98
6.1.2 Boundary conditions 98
6.1.3 Interaction at assembly interfaces 99
6.1.4 Discretisation of domains – mesh design 100
6.1.5 Analysis steps 103
6.2 Experimental calibration of FE model 104
6.2.1 Approximation of joint compliance 107
6.3 Simulation of absolute force measurement from piezoelectric force transducer 109
6.3.1 Steady-state dynamic analysis 109

6.3.2 Analysis definition for steady-state analysis 109
6.3.3 Material definition for steady-state analysis 110
6.3.4 Boundary condition definition for steady-state analysis 111
6.3.5 Variables at resonance of simulated L1 mode 111
6.3.6 Extracting axial force from FE model 112
6.3.7 Comparison of real and simulated force measurement 112
6.3.8 Simulated magnification factor for force transducer structure 114
6.3.9 Specimen stress profile 114
6.4 Summary 116
7 Strain gauge verification of forces and mechanical gain factor 118
7.1 Method 122
7.1.1 Frequency response 128
7.1.2 Frequency response of strain gauges 130
7.1.3 Thermal drift check 131
7.1.4 Cross-sectional area of specimen gauge-length 132
7.2 Static benchmarking 133
7.3 Dynamic test 134
7.3.1 FE model of dynamic strain gauge test 134
7.4 Application of amplitude correction factor to ultrasonic tensile test 141
7.5 Summary 144
8 Full-field measurement of plastic strain in ultrasonic tensile test 147
8.1 DIC for vibrating specimens 147
8.2 Apparatus 149
8.3 Image acquisition 153
8.4 Tensile test programming and test event scheduling 158
8.5 Force measurement and acquisition 159
8.6 Results 160
8.7 Summary 180
9 Conclusions and further work 182
9.1 Conclusions 182
9.2 Innovations 185
9.3 Further work 186
10 List of References 189

List of Tables

Table 2.1 - Example parameters in constitutive equation modelling APE 22
Table 2.2 - Parameters for calculation of oscillatory stress amplitude 33
Table 3.1 - USTT key parameters..... 49
Table 4.1 - Summary of isolating mass parameters..... 62
Table 4.2 - Final parameters of force transducer FE model 71
Table 4.3 - Magnification factors estimated by analytical models..... 74
Table 5.1 - Available FRF definitions 80
Table 5.2 - EMA extracted parameters of L1 mode..... 89
Table 6.1 - Rayleigh damping coefficient calculation.....110
Table 6.2 - Magnification factors from calculation and experiment.....114
Table 7.1 - Strain gauge amplifier cut-off frequencies 130
Table 7.2 – Measured dimensions of specimen gauge length.....132
Table 7.3 - Specimen cross-sectional area.....132
Table 8.1 – Estimated camera spatial resolution.....154
Table 8.2 - Camera temporal resolution 155
Table 8.3 - USTT event sequence 159
Table 8.4 - Full-field strain maps of USTT (auto-scaled) 160
Table 8.5 - Full-field strain maps of USTT (fixed scale) 163
Table 8.6 - Ultrasonic excitation burst times evident in strain datasets.....167

List of Figures

Figure 1.1 - APE in stress-strain data: (a) stress superposition; (b) true flow stress reduction 2
Figure 1.2 - Langevin ultrasonic transducer and wave guide 6
Figure 1.3 - 3D array of regularly repeating atoms 7
Figure 1.4 - Atoms slipping on slip-planes 8
Figure 1.5 - Crystal defect – the edge dislocation 9
Figure 2.1 - First evidence of the Blaha effect. From [1] 13
Figure 2.2 - APE in stress-strain data: (a) real flow stress reduction; (b) stress superposition 16
Figure 2.3 - Compression test of aluminium 1050. From Y. Daud [55] 24
Figure 3.1 - Normal stress in tensile test specimen 37
Figure 3.2 - Extensometer on sheet 1050 specimen 39
Figure 3.3 - Ultrasonic Tensile Test set-up 40
Figure 3.4 - Ultrasonic Tensile Test, ultrasonic stack 41
Figure 3.5 - L500 ultrasonic transducer 42
Figure 3.6 - Specimen geometry 44
Figure 3.7 – USTT specimen 45
Figure 3.8 - Diagram of horn tip and crosshead motion and resulting extension 48
Figure 4.1 - Isolating mass in USTT stack 56
Figure 4.2 - Isolating mass within USTT stack 57
Figure 4.3 - Mass-loaded bar model 57
Figure 4.4 - Convergence of bar node on isolating mass 58
Figure 4.5 - S-DOF lumped-parameter model of isolating mass 59
Figure 4.6 - Magnification factor 60
Figure 4.7 - force transducer measurand and indicated value 63
Figure 4.8 – Lumped-parameter model of piezoelectric force transducer 64
Figure 4.9 - Force transmissibility within force transducer structure 66
Figure 4.10 - Impulse test of force transducer in free-free condition 69
Figure 4.11 – FE mesh of proxy piezoelectric force transducer 71
Figure 4.12 - Rod in the free-free and fixed-free boundary conditions 73
Figure 5.1 – Typical mobility FRF 81
Figure 5.2 - FRF measurement points on USTT stack 85
Figure 5.3 - EMA apparatus 88
Figure 5.4 - LDV laser point on ultrasonic tensile test stack 89
Figure 5.5 - L1 mode shapes from EMA 90
Figure 5.6 - Velocity profile without phase information 92
Figure 5.7 - (a) Transmissibility with two LDVs; (b) Mirror redirecting 1D LDV laser beam to horn bottom 93
Figure 5.8 - Normalised ODS from mobility and transmissibility measurements . 94
Figure 6.1 - FEA model geometry 97
Figure 6.2 - Mesh sensitivity of proxy PFT 102
Figure 6.3 - Specimen mesh detail 103
Figure 6.4 - FE mesh model of USTT 103
Figure 6.5 - colour map of axial displacement on deformed mesh, L1 mode ... 105
Figure 6.6 - Mode shapes neighbouring the L1 mode 105
Figure 6.7 - Simulated and experimental L1 mode shape 106
Figure 6.8 - Compliant pad between horn and specimen 108
Figure 6.9 - Resonant peak in simulated frequency sweep 111
Figure 6.10 - Free Body Cut tool 112
Figure 6.11 – Real and simulated force measurement against displacement 113

Figure 6.12 - Map of normal stress in specimen 115
Figure 6.13 - Specimen axial stress profile 116
Figure 7.1 - Strain gauge sensing direction 123
Figure 7.2 - Strain gauge location on specimen 124
Figure 7.3 - Wheatstone bridge circuit schematic 125
Figure 7.4 - Strain gauge recording apparatus 126
Figure 7.5 - Replica specimen and temperature compensation specimen installed on USTT 127
Figure 7.6 - Strain gauge amplifier roll-off curve - frequency response curve .. 129
Figure 7.7 - Warm-up response of strain gauge amplifier 131
Figure 7.8 - Strain gauge static benchmark 133
Figure 7.9 - Extracting simulated force at strain gauge location 135
Figure 7.10 – Experimental and simulated strain measurement 136
Figure 7.11 - Force from strain gauge and PFT, experimental and simulated .. 138
Figure 7.12 – Amplitude ratio - experiment against simulation 140
Figure 7.13 – USTT with stepped displacement amplitude 142
Figure 7.14 – USTT with constant displacement amplitude 143
Figure 7.15 - USTT with constant displacement, PFT against load cell measurements 144
Figure 8.1 – pixel subset tracking in DIC 148
Figure 8.2 - USTT DIC imaging system 149
Figure 8.3 - Speckled specimen 154
Figure 8.4 - High-speed LED flash; mounted COB LED with driving circuit behind 155
Figure 8.5 - Willert driving circuit for high-speed LED flash 156
Figure 8.6 – Strobe triggering signals: 1. current clamp; 2. signal conditioning unit; 3. trigger; 4. LED current 157
Figure 8.7 – Strobe triggering signals (enlarged): 1. current clamp; 2. signal conditioning unit; 3. trigger; 4. LED current 157
Figure 8.8 - Quasi-static axial strain, against position and time 166
Figure 8.9 - Axial strain against axial position 167
Figure 8.10 - Axial strain before, during and after US Burst 1 168
Figure 8.11 - Locations of strain/time data sets 169
Figure 8.12 - Axial strain against time, at selected locations on specimen 170
Figure 8.13 - Strain-rate against axial position, before, during & after US Burst 1 171
Figure 8.14 - Axial strain-rate against time, at selected locations on specimen 172
Figure 8.15 - Axial strain over gauge length, unexcited specimen 173
Figure 8.16 - Strain over time, unexcited specimen 174
Figure 8.17 - Strain rate over time, unexcited specimen 175
Figure 8.18 - Strain rate over gauge length, unexcited specimen 176
Figure 8.19 - True stress-true strain, USTT experiment with DIC 177
Figure 8.20 - True stress-true strain, unexcited test 178
Figure 8.21 - Comparison of force from PFT and load cell, excited specimen .. 180

1 Introduction

1.1 The challenge of ultrasonic mechanical testing

The plastic deformation of metals is important in many industrial forming processes, from forging critical aerospace components to deep-drawing aluminium cans. It has been demonstrated that high-power ultrasonics can reduce the force required to cause and maintain yielding during plastic deformation of metals, offering opportunities for significant increases in process speed and reduction in tooling wear and demand on energy resources. The effect, which was first observed in the 1950s [1], is known as acoustoplasticity.

Even after decades of research, the fundamental nature of acoustoplasticity is still unclear. While many studies link ultrasonic excitation with real changes in intrinsic material behaviour, a similar number explain acoustoplasticity as stress superposition. Postulated and observed changes in material behaviour have included enhanced dislocation activation [2], di-pole annihilation and sub-grain refinement [3], or sub-grain destruction [4].

Most of the experimental methodologies used have relied on superimposing ultrasonic vibrations during a tensile or compressive test of a metal specimen in a universal test machine. Typical stress-strain curves, as may be found in studies of APE, are shown in Figure 1.1. In Figure 1.1(a) the stress rises beyond the elastic limit to reach the metal's yield strength. The stress required to continue plastic deformation is termed the flow stress.

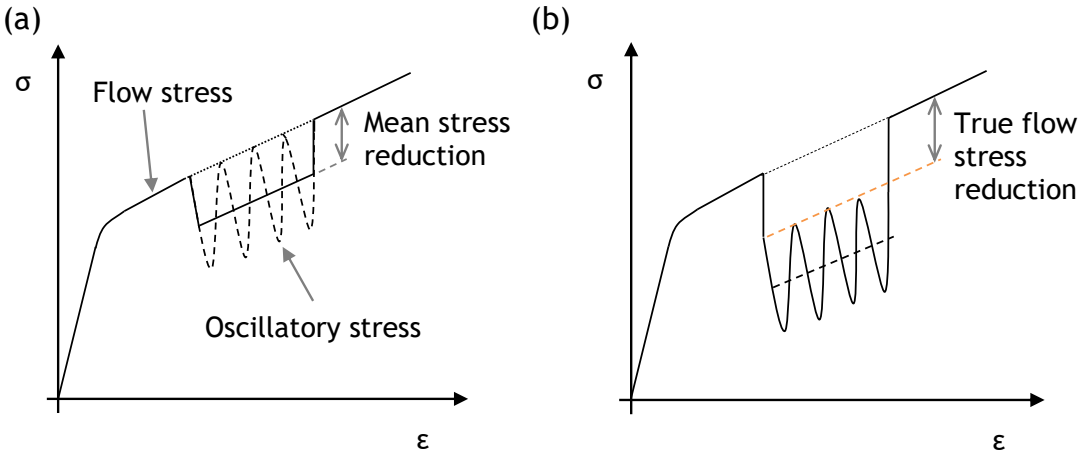

Figure 1.1 - APE in stress-strain data: (a) stress superposition; (b) true flow stress reduction

However, many studies [5]–[8] only derive the stress-strain relationship, under ultrasonic excitation of the specimen, from measurements of force from a load cell that cannot be used to resolve the oscillatory stress. In these measurements, only the mean stress is recorded, resulting in the observation of an apparent reduction in the flow stress.

In the theory of stress superposition, it is proposed that during plastic deformation of a specimen, the peak oscillatory stress under superimposed ultrasonic excitation is consistent with the stress measured under quasi-static conditions for any value of strain [9]. Many researchers attribute their observations to this hypothesis.

Yet others, following very similar methodologies claim to find that the observed reduction in flow stress cannot be fully explained this way. It was claimed that the peak of the oscillatory stress never reaches the normal yield strength of the material, denoted as a true flow stress reduction in Figure 1.1(b). Instead, researchers looked to a fundamental change in material properties. A number of promising theories of acoustoplasticity have been put forward that relate the reduction in flow stress, acoustic intensity and dislocation network evolution, some of which are well supported by evidence from microscopy techniques (e.g. [10]–[12]). Without a direct measurement of the absolute stress in the specimen, including the oscillatory component, it is impossible to confirm or deny that stress superposition can reasonably account for observations of

acoustoplasticity. The foundation of the resulting constitutive models and theories of the acoustoplastic effect is therefore compromised.

Where research studies have measured the dynamic force response [13], [14], it is not clear that the frequency response behaviour of the force transducer has been considered. In a study that measured both the quasi-static and oscillatory stress using a piezoelectric force transducer capable of resolving the high frequency dynamic force response signal [15], the results showed evidence of a reduction in the flow stress which could not be wholly explained by the theory of stress superposition. This has subsequently been cited as evidence of acoustoplasticity being an intrinsic material effect but, again, effects from the dynamics of the force transducer were not completely considered.

Characterisation of acoustoplasticity, from a tensile test with superimposed ultrasonic excitation, relies heavily on the accurate measurement of a true decrease in flow stress. It is therefore necessary to ensure that the force quantity from the force measuring instrument replicates the load experienced by the specimen, or that the latter can be derived from the measurement with confidence. Normal uniaxial testing employs the assumption that the loading on the specimen can be considered quasi-static, and that the force measured by the force transducer is identical to the loading on the test-piece. The oscillatory nature of the loading in an ultrasonic tensile test invalidates this assumption. The specimen exhibits inhomogeneous strain and acceleration fields, and factors such as the impedance of the specimen, the measurement transducers and the joints between them become critical and must be accounted for. For example, it is well known that the location of a force transducer with respect to vibration nodes and anti-nodes affects the force measurement [16], [17] and that mounting a force transducer on a structure affects the dynamic response of the structure and transducer [18].

In addition to the measurement of force on the specimen, characterisation of mechanical properties also requires an accurate measurement of material strain. Again, in normal uniaxial testing, the imposed quasi-static conditions permit strain to be calculated from the displacement of the ends of the specimen gauge length via extensometry techniques. It may even be found from displacement of the test machine crosshead where the plastic deformation is large relative to the

elastic deformation. It is hypothesised that the inhomogeneous loading resulting from ultrasonic excitation may induce a similarly variable distribution in the plastic strain response. This invalidates the assumption that the global strain calculated from displacement of the specimen ends is representative of the local strain response which matches the local loading conditions. The plastic strain distribution over an ultrasonically excited specimen must be investigated and measured to improve mechanical characterisation of acoustoplasticity.

1.2 Ultrasound and ultrasonic transducers

1.2.1 Brief historical overview

Investigations in ultrasound started as early as the 1880s, when Galton first tested the limit of human hearing with an ultrasonic whistle. Ultrasound was defined as the upper 'threshold frequency' detectable by humans, in the region of 10 to 18 kHz [19]. It is now accepted that ultrasound refers to sound waves above 20 kHz in both fluids (pressure waves) and solids (stress waves). The mathematical theory of sound was also becoming established around the same time, with the publication of Lord Rayleigh's Theory of Sound in 1894 [20]. However, the technological enabler of scientific research into ultrasound was the discovery of the piezoelectric effect by the Curie brothers and the invention of the piezoelectric transducer by Langevin, a device which converts an electrical signal into a mechanical movement [21]. The introduction of an oscillator by Wood and Loomis, which could provide high-power ultrasonic signals from 200 to 500 kHz, opened up the possibility of using ultrasound to significantly affect materials [22], [23]. They began research into ultrasonic drilling and machining. Other applications of high-power ultrasound emerged, for example: cleaning, de-gassing, welding and metal-forming. This became the field known as power ultrasonics, covering applications using ultrasound of high intensity and high amplitude to effect permanent change in materials or systems. Power levels commonly range from tens to thousands of watts and frequencies of 20 to 100 kHz [21].

1.2.2 Generation of ultrasonic excitation

In the past, mechanical methods such as Galton's whistle (1900), or the ultrasonic siren (1947), were used to generate oscillations in fluids, and although

the frequency could be controlled somewhat accurately, they were limited in the higher frequencies they could reach [19]. In contrast, the development of the electrical oscillator in the early 20th century provided a means of obtaining a stable, accurate and controllable source of oscillatory excitation. All that was required was a means to convert from the electrical signal to a mechanical sound wave.

A transducer is defined as a device which converts one form of energy to another, although usage of the term is mainly reserved for devices which convert from one form of signal to another, generally taking advantage of a particular physical phenomenon to enact the conversion. An ultrasonic transducer can convert high frequency sound waves in a fluid or a solid into an electrical signal. It may also be constructed to perform the reverse, producing oscillations in a medium upon the supply of an electrical signal. High power transducers, for converting an electrical signal into mechanical ultrasonic vibration suitable for use in industrial applications, have been developed based on two different physical principles, that of magnetostriction, and the piezoelectric effect.

Applying a magnetic field to ferromagnetic materials causes a realignment of the material's internal crystal structure. As different crystallographic directions have different lengths, the reorientation causes a tiny, but useful, mechanical strain within the material. This physical effect, known as magnetostriction, can be exploited to convert an oscillatory electromagnetic field into a mechanical vibration. Though the magnetostrictive type transducer was common in earlier studies of acoustoplasticity, for example [9], it will not be discussed further. The piezoelectric ultrasonic transducer has come to dominate industrial ultrasonic processes and is now almost universal in the field of APE research.

Piezoelectricity is the name given to the electrical charge which is generated within certain materials when they are subjected to an external mechanical stress. Materials which exhibit this physical effect, which is known as the piezoelectric effect, include crystals such as quartz or Rochelle salt, and ceramics such as lead zirconate titanate, commonly known as PZT.

The piezoelectric effect is reversible. Applying an electric field to a piezoelectric material will induce a mechanical strain within it. This is known as

the converse, or indirect piezoelectric effect [19], [21], and is the critical mechanism behind industrial ultrasonic transducers. If the electric field is oscillatory, the mechanical strain will be similarly periodic. In this way an element made from a piezoelectric material can be induced to vibrate. The oscillatory electric potential excites a sound wave within the component which can propagate into other components or a surrounding medium which the element is in contact with.

Although crystals were used to construct early ultrasonic transducers, piezoelectric ceramics dominate modern transducer design, due to their superior mechanical properties and piezoelectric performance, and their manufacturability [21]. Piezoelectric materials often have high compressive strength but do not fare well under tension, suffering brittle fracture when failure does occur. The relatively lower tensile strength restricts the amplitude of a tensile stress wave a piezoceramic element can sustain. To improve the amplitude obtained from piezoceramic elements they are held in compression, preloaded between two clamping parts which also serve as guides for the sound wave generated. Known as a sandwich transducer because of its clamped configuration, this form of transducer was first developed in the early 20th century, and is also called a Langevin transducer, after its designer [21]. It forms the basis for the majority of high-power ultrasonic transducers today. Figure 1.2 illustrates the general layout of a Langevin transducer. In this figure the ultrasonic transducer is connected to a wave guide which permits mounting to a fixture and also amplifies the displacement amplitude. This is further described in Section 3.2.

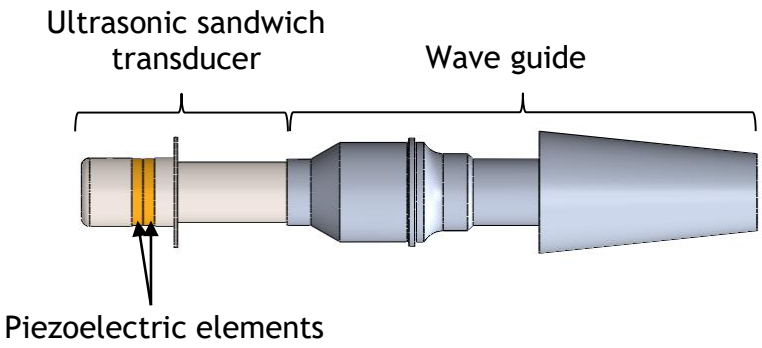

Figure 1.2 - Langevin ultrasonic transducer and wave guide

1.3 A background in plastic deformation in metals

Metal forming, or bulk deformation processes are operations that shape a workpiece by plastic deformation, induced by forces applied by various tools and dies [24]. Some of the theories of acoustoplasticity discussed in this thesis relate the effect of vibrations on the material's yield strength and flow stress, the minimum stress required to maintain plastic flow [25]. A short review of plastic deformation as it relates to metals will prove useful when discussing the state of the literature to date.

In metals the atoms are arranged in regular repeating arrays in three dimensions. They can be viewed as being built up of planes of regularly arranged atoms stacked on top of each other to create a crystal lattice, Figure 1.3. It is the slip, or glide, of these planes over one another which allow permanent deformation to occur [26].

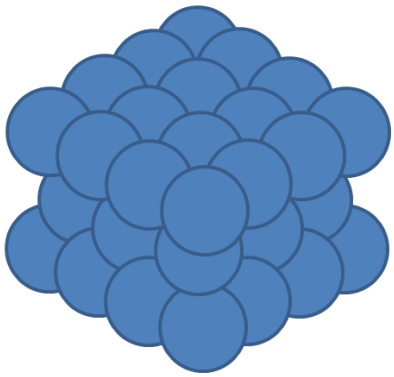

Figure 1.3 - 3D array of regularly repeating atoms

When a shear stress is applied to a metal which is greater than the yield strength the planes slip past each other, allowing plastic flow. From experiment it is known that the mechanism by which the planes move over one-another is not, in fact, simple sliding, but invariably by a process known as dislocation motion [25]. If the crystal lattice were perfect the only available mechanism would indeed be sliding of the lattice planes – each atom breaking and remaking its bonds simultaneously, Figure 1.4. To achieve this would require a stress many times higher than the yield strengths observed in experiment [26]. In 1934 a theory was proposed which used mathematical modelling of loading on defects within the crystal lattice, which seemed to explain the low yield strength of

crystals [27]. In Figure 1.4 the distance b is known as the burgers vector, defined as one unit of slip.

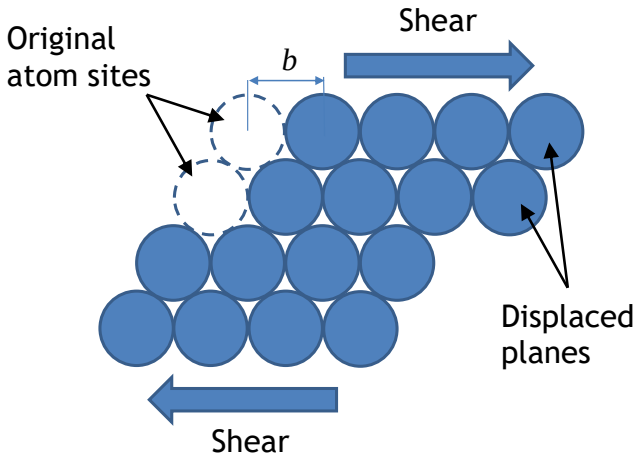

Figure 1.4 - Atoms slipping on slip-planes

This theory, which was to become the Theory of Dislocations, focused on the motion of lattice line defects, the edge dislocation and the screw dislocation. The edge dislocation, illustrated in Figure 1.5, can be described as a defect in which an extra plane of atoms has been inserted into the crystal lattice, terminating part way through it. The end of the plane within the lattice is the edge dislocation, displacing, or dislocating, the regular lattice array by one atom spacing. By distorting the lattice into which the extra plane is forced, the dislocation acts as a stress raiser, enabling a lower shear stress to cause slip. Screw dislocations manifest when the slip from two slipping planes, as in Figure 1.4, has not propagated fully across the whole extent of the crystal. For a full description of edge, screw and other defects, refer to [25], [26]. The ease with which edge and screw dislocations glide along the slip planes determines the yield strength of a metal.

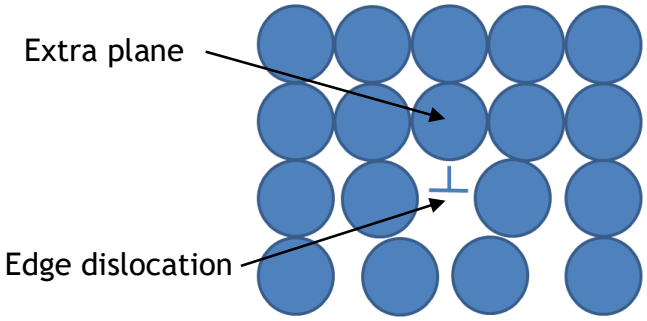

Figure 1.5 - Crystal defect – the edge dislocation

Dislocations require a minimum shear force to overcome the resistance they encounter as they move. They can also be hindered by other defects. The main strengthening mechanisms are:

- Solid-solution of impurities which make the slip planes appear rougher to dislocations;
- Precipitates and dispersions which act like pins in a rubber band, holding back the dislocation at points along its length; and
- Work-hardening, where multiple dislocations, travelling through a metal on different planes, intersect and entangle each other.

These are the mechanisms which occur in a single crystal. It becomes more complex with polycrystalline materials; grain boundaries block dislocation travel, and also allow deformation by permitting slipping between grains. These are the main mechanisms of plastic flow, each of which have, at different times, been put forward as a candidate for the main participant in the reduction in flow stress that characterises the acoustoplastic effect.

1.4 Research aims

The goal of most ultrasonic tensile tests is to incorporate the phenomenon of acoustoplasticity into computational models of a variety of mono- and polycrystalline metals, which are used to identify physical mechanisms playing the most significant role in APE. This thesis addresses the necessary first step of ensuring derivation of stress-strain relationships from accurate observations of stress and strain within a specimen undergoing simultaneous ultrasonic vibration and quasi-static deformation. Additionally, by demonstrating a methodology that

addresses concerns about the fidelity of the measurement of force on the specimen, an assessment of the flow stress reduction is made with the intention of concluding the controversy over the existence of the acoustoplastic effect. Insights are provided into the limitations of the experimental set-ups described in the literature and offer improved approaches with the aim of further closing the gap on the characterisation and understanding of acoustoplasticity.

1.5 Summary of Contributions

This investigation is comprised of three distinct parts. After a review of potential experimental techniques, fidelity of the force measurement is assessed in four stages, using both experimental and analytical methods. The investigation finishes with an experimental measurement of plastic deformation in an excited specimen.

The techniques and instrumentation available for performing mechanical identification are reviewed in the context of the ultrasonic tensile test (USTT). Simple modelling reveals the unique challenge presented by the combination of continuous ultrasonic vibration superimposed on quasi-static deformation, particular to ultrasonic mechanical testing. It is found that the piezoelectric force transducer (PFT) remains a key device for determining the existence of a true reduction in flow stress, the critical feature of acoustoplasticity.

The fidelity of the force measurement made by PFT is assessed in the following four stages. First, the frequency response of the PFT used in this work is investigated. Analytical modelling and experiment are used to characterise the frequency response of the transducer's structure, and estimate the extent to which it distorts the measurement of the amplitude of an oscillatory force at the ultrasonic excitation frequency.

In the second stage, the effect of connecting the PFT to the specimen and test fixtures on force measurement distortion is examined. Experimental Modal Analysis (EMA) is used to characterise the vibration response of the USTT apparatus including the specimen and the PFT. This enables the third stage, in which a finite element (FE) model of the same apparatus is calibrated using the EMA results. The calibrated FE model is used to study the difference between

the amplitude of oscillatory force experienced by the specimen and the PFT. The level of distortion is characterised, permitting the calculation of a correction factor which could be used in future work to ameliorate the effects of apparatus dynamics on APE test data.

In the fourth stage, in order to further support the observations made using the EMA-FEA methodology, the force amplitude distortion is measured directly. Strain gauges are applied to the specimen, and the elastic strain due to ultrasonic excitation is measured simultaneously with force measured from the PFT. Force on the specimen at the location of the strain gauges can be calculated from the strain data and compared to the PFT measurement; both are compared to the FE model. Again, a correction factor is calculated from the difference between force on the specimen and force measured by the PFT.

The correction factors found from the EMA-FEA method and the strain gauge experiment are applied to an USTT of a soft aluminium. The experiment aims to determine if correction will reveal true acoustic softening, or simply stress superposition in a material which it has been previously claimed shows strong evidence of acoustic softening. Tensile testing is selected to avoid the frictional effects present in compression testing, ensuring stress-strain results will reveal exclusively the effect of ultrasonic excitation on material properties.

Finally, the inhomogeneous nature of the plastic deformation response to ultrasonic excitation is assessed using Digital Image Correlation (DIC), a full-field strain measurement technique. DIC is a computational method which can calculate strain from a sequence of images of a specially painted test piece. A high-speed strobe system is developed which, when synchronised with the ultrasonic vibration, eliminates the dynamic motion from images captured by an ordinary computer-operated camera. This enables a standard metrology video system to capture a sequence of images of the USTT free of the error which would otherwise be introduced into the quasi-static plastic strain computation by the elastic dynamic motion of an ultrasonically excited specimen.

Key contributions to knowledge

The key contributions made by this thesis are the exposure of the effect of structural impedance on force measurement within ultrasonic mechanical testing, and the determination of a correction factor to counter the effect in the test data. Future researchers must be alerted to this effect, and can adopt the methods presented here to develop a correction factor for their own apparatus. While the value of the work presented in this thesis is limited to ultrasonic mechanical testing, it will benefit the wider field of ultrasonically assisted metal forming by enabling accurate characterisation of the acoustoplastic effect. This in turn will deliver accurate material models and optimal ultrasonic forming processes, and perhaps even help expose the fundamental nature of acoustoplasticity.

2 Literature review

2.1 The Blaha effect; beginnings and controversy

A seminal work from 1955 by Blaha and Langenecker, reported a tensile test on zinc crystals using a Polanyi apparatus, a load frame with a moving crosshead [1]. Ultrasonic excitation was applied using a liquid carbon tetrachloride coupling, at a frequency of 800kHz and acoustic intensity of approximately 1 $W.cm^{-2}$. The force and specimen extension were recorded, with results presented as the stress-strain relationship, shown in Figure 2.1. In one test, ultrasonic excitation was applied in a sequence of short intervals, starting immediately post-yield. At the instant ultrasonic excitation was introduced, the data showed a drop in stress of 60%.

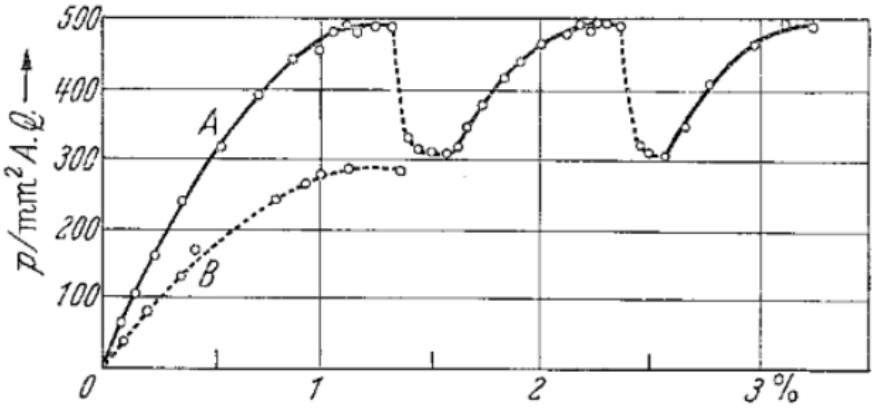

Figure 2.1 - First evidence of the Blaha effect. From [1]

Once ultrasonic excitation was stopped, the stress increased with a gradient consistent with the elastic region, with data finally returning to the stress-strain curve of the quasi-static tensile test it would have followed had it not been interrupted by the interval of ultrasonic excitation. This drop in stress required to continue yielding, known as the flow stress, became known alternately as acoustic softening or the Blaha effect. This established a phenomenon in which a drop in flow stress is observed during mechanical testing with the addition of superimposed ultrasonic excitation of the specimen. Due to its effect on plastic deformation, in later studies acoustic softening has also been called the acousto-plastic effect (APE).

Blaha and Langenecker published their work in what has been described as a brief note [21]. In a single page it described the procedure and observations but did not offer any guesses at possible causes. It was, however, immediately obvious that such an effect could have great implications for the metal forming industries. Many researchers in the fields of high-power ultrasonics took note and began their own investigations into the phenomenon. The influence of a range of excitation frequencies and amplitudes was examined on a wide variety of metals and salt crystals, using ultrasonic test equipment and measurement instrumentation which, although often broadly similar, were inconsistent in detail [21]. A sufficient number of studies confirmed the observation of a reduction in flow stress for the Blaha effect to become accepted. However, the interpretation of the results and attempts to provide a physics-based explanation caused disagreement; the difference between competing theories has even been called a controversy [21]. Although some convergence has been achieved within the field of APE, the matter has still not been fully settled [17], [21], [22].

Nevill and Brotzen followed up in 1957 with a study of an oscillatory tensile test on steel specimens [9]. The experiment is significant for a number of reasons. First, the experimental set-up was similar to Blaha and Langenecker's. A tensile test machine was used to place a thin wire specimen in uniaxial tension. However, in this work the ultrasonic excitation was introduced directly to the specimen via an ultrasonic transducer-horn which also acted as the lower grip of the test machine. The oscillatory strain was therefore superimposed onto the steady strain delivered by the uniaxial test machine. This arrangement set the precedent for virtually all subsequent mechanical-oscillatory tests carried out for the study of acoustoplasticity.

Strain in the specimen was characterised by measuring the crosshead displacement, and calculating the global strain from the initial length of the specimen. A load cell positioned to support the top end of the specimen, opposite the ultrasonic horn, measured the quasi-static load on the specimen. This instrument was limited to measuring the quasi-static, or mean load, as its intrinsic response to a dynamic signal rendered it unable to resolve the high frequency oscillatory component of the load from the ultrasonic excitation. To

combat this, steel was adopted for this study to enable the use of a magnetostrictive stress sensor, placed at the centre of the wire specimen surface to directly measure the oscillatory component of stress on the test piece. The excitation frequency was varied over the range 20 – 80 kHz. By tuning the length of the wire, a steady-state waveform was maintained with a displacement anti-node at the centre of the test piece. It was claimed this set-up allowed observation of the maximum oscillatory stress amplitude on an oscilloscope. It was not, however, an absolute measurement, and could only provide the difference in stress amplitude between tests. It was reported that the application of ultrasonic excitation resulted in a drop in the mean tensile stress, which was found to be proportional to the oscillatory stress amplitude, independent of frequency (in the range tested) and also independent of temperature.

From their observations Nevill and Brotzen concluded that the oscillatory stress amplitude was large enough that the sum of the quasi-static stress and the oscillatory stress exceeded the yield strength of the material. They argued that if this condition exists at the peak in each vibration cycle, a small amount of plastic deformation will occur at the normal yield strength. The accumulation of the plastic strain from the high number of cycles in a period of ultrasonic excitation fulfils the total plastic strain imposed by the movement of the crosshead. The conclusions reached in this work gave rise to the theory of stress superposition; that the effect is purely mechanical and there is no reduction in the material yield strength and no significant effects on the material microstructure. The difference is discussed in greater detail in Figure 2.2.

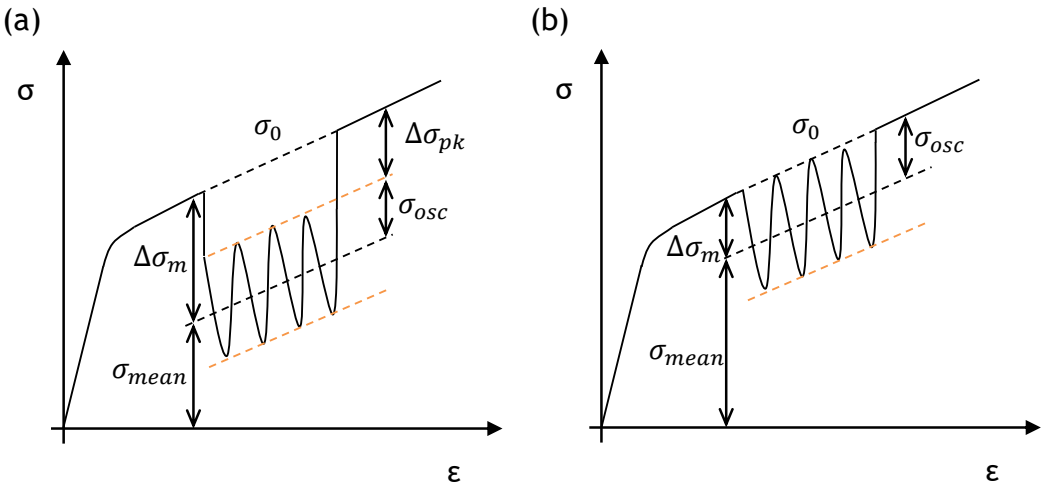

Figure 2.2 - APE in stress-strain data: (a) real flow stress reduction; (b) stress superposition

Figure 2.2 shows graphically the two possible states of APE observation in a stress-strain graph - true flow stress reduction and stress superposition. In Figure 2.2 (a), σ_0 denotes the normal flow stress observed in the stress-strain curve of a material without ultrasonic excitation. During the period of ultrasonic excitation of amplitude σ_{osc}, the total flow stress reduces, now following, on average, a path of σ_{mean} . The flow stress recovers to the usual material yield strength once excitation stops. It is observed that the maximum peaks of the oscillatory stress are lower than the normal flow stress path σ_0, in the absence of ultrasonic excitation. A real reduction in the material yield strength is observed, defined as equation ((2.1):

$$\Delta\sigma_{pk} = \sigma_0 - (\sigma_{mean} + \sigma_{osc}) \tag{2.1}$$

This can be said to be true acoustic softening. By contrast, in Figure 2.2 (b) the peaks of the oscillatory stress do reach the normal flow stress, so that $\sigma_m + \sigma_{osc} = \sigma_0$. In this case, stress superposition is observed. In both cases the reduction in the mean flow stress is defined as equation (2.2):

$$\Delta\sigma_m = \sigma_0 - \sigma_{mean} \tag{2.2}$$

which is the stress found from the quasi-static force measurement from a load cell such as that used in [9], and now ubiquitous in most investigations of APE.

Researchers in the 1930s had already established the theory of dislocation mechanics to explain plastic flow in crystalline materials [27], and how such dislocations interact with applied period stress [28]. Although Nevill and Brotzen were the first to identify the need to link oscillatory loading to mechanisms of dislocation mobility [9], after suggesting theories based on ideas of dislocations absorbing energy by interacting with acoustic waves, they dismissed them in favour of stress superposition. Importantly, the two hypotheses they postulated, that of genuine material property alteration versus a purely mechanical effect, have separately influenced, and often siloed, further research in this field [21].

Subsequently, a large body of studies were published researching acoustoplasticity [21]. Many subscribed to the theory of stress superposition [16], [17], [29], while others persevered with theories centred on dislocation mobility, notably Langenecker [2], [30], [31].

2.1.1 Influences on APE – frequency, amplitude and material

As already mentioned, the primary test parameters investigated by researchers are the frequency and amplitude of ultrasonic excitation, and the test material. Owing to difficulties in changing the frequency of ultrasonic components, which are designed to operate at resonance, studies in which frequency is varied over a range are limited. Of those studies, most find little correlation between frequency and APE, and this has remained the consensus for several decades [21]. The exception is an investigation by Zhou *et al.* [8], [12], in which a commercially pure aluminium and titanium were tested in compression at frequencies of 20.4 kHz, 30.8 kHz and 39.2 kHz at the same displacement amplitude. Individual ultrasonic transducers and horns were constructed for each of these frequencies, ensuring that at each frequency point the ultrasonic excitation apparatus was operating at resonance, and equivalent stress conditions were created within the specimen. It was found that the reduction in flow stress, here called ultrasonic softening, was inversely proportional to the excitation frequency.

In contrast to the investigation of the effect of frequency on APE, controlling the amplitude of vibration displacement or velocity is comparatively easy, being simply achieved by altering the voltage supplied to the ultrasonic transducer.

Many of the hundreds of papers on APE identify some relationship between the vibration amplitude and the magnitude of ultrasonic softening observed. Most observe that the flow stress reduction is proportional to the vibration displacement amplitude, for example [9], [10], [32], [33]. Other relationships have been observed, including the flow stress reduction proportional to square of vibration amplitude [2], and proportional to displacement amplitude to the power of 1.5 [8]. In these investigations, flow stress reduction is reported as the reduction in the mean stress, $\Delta\sigma_m$. This is likely due to the almost universal use of the load cell to measure the force on the specimen, which cannot resolve the oscillatory stress from ultrasonic excitation, as first encountered in [9]. The use of $\Delta\sigma_m$ to characterise APE extends to the few studies where the force measurement instrumentation was capable of resolving the oscillatory force, enabling a direct observation of $\Delta\sigma_{osc}$ [10], [15], [34]. In [15], the oscillatory stress-strain data from experimental ultrasonic tension and compression tests were resolved into the reduction in mean stress $\Delta\sigma_m$ and the oscillatory stress amplitude σ_{osc}. When developing a constitutive model to investigate the softening observed, the same division was employed. First, an FE model of the specimen deformation was developed to replicate exactly the oscillatory stress component. Then, the yield strength of the material was reduced such that the simulated mean stress reduction $\Delta\sigma_m$ matched the experimental value. Though modelled separately, as both mean and oscillatory components were calibrated again experimental data the final outcome is agreement in the true flow stress reduction $\Delta\sigma_{pk}$. Indeed, in [15] good agreement was found between experimental and simulated stress-strain curves. The same is true of [34], where the same approach using $\Delta\sigma_m$ and σ_{osc} was followed. However, in [10] it appears that the oscillatory stress component was discarded and ignored in subsequent constitutive modelling, despite being available from the experimental force measurement. This will not produce a realistic characterisation of the yield strength reduction, unlike the two studies mentioned previously.

As the field of research into APE has progressed a wide variety of metals have been tested, both pure form and alloyed. Early studies focused on single crystals of pure metals such as zinc and aluminium [1], [30], [35], whereas later investigations commonly use polycrystalline alloys or commercially pure metals. Single crystal and polycrystalline salts have also been investigated [36]. For

example, Izumi *et al.* [37], [38] performed ultrasonically assisted compressive tests on copper, brass, mild steel, magnesium and sintered aluminium, finding a significant reduction in the forming force required during ultrasonic excitation for all metals tested. The compressive stress reduction was proportional to the vibration amplitude. In an investigation of ultrasonically assisted forming using a vibrating die, Aziz *et al.* [33] performed ultrasonically excited compressive forming tests on a die cast magnesium (AC50), an austenitic stainless steel (304), an aluminium alloy (A7075) and a commercially pure aluminium (A1050). A piezoelectric force transducer was used to ensure the oscillatory stress was resolved, enabling the proper identification of a true reduction in the flow stress as described in Figure 2.2 (a). Of the four metals tested only the pure aluminium exhibited a real reduction in the flow stress.

In reviewing the literature it is found that commercially pure grades of aluminium, of the 1000 series, are the most consistent in exhibiting acoustoplasticity under a variety of testing conditions, during ultrasonic excitation [8], [15], [16], [33], [39]–[41] (as opposed to ultrasonic 'residual' softening or hardening [10]).

As well as a reduction in the flow stress during ultrasonic excitation, researchers have reported observing a residual softening or hardening of the material after excitation had ceased, and both loss and gains in ductility or extension to failure [2], [5], [8], [10], [42].

For those investigating industrial processes, improvements in surface roughness and wrinkling in deep drawing (an undesirable folding of the work piece) suggested a reduction in friction between work piece and forming dies [21]. This was further confirmed by examination of the effect of barrelling in compressive uniaxial tests, for example [33], [43]. Work on deep drawing [16], wire drawing [44] and uniaxial compressive tests [33] brought out evidence that ultrasonic excitation causes a significant reduction in friction, exhibited as a reduction in the measured forming load. This became known as the Surface Effect, to distinguish it from observations attributable only to apparent changes in material properties, called Volume Effects.

The broad categories of explanation are then as follows: stress superposition; hysteretic heating (temperature); friction reduction (surface effect) and an effect on the flow stress or plastic strain rate of the material (volume effect) [21].

2.1.2 Constitutive modelling and computational approaches

In the 1980s the increased emergence and capability of computational methods resulted in a shift towards predictive modelling and simulation. The developments of finite element analysis (FEA) and the use of constitutive models delivered a new wave of studies incorporating the material response to ultrasonics superimposed on a quasi-steady-state strain. In 1988 Kozlov and Selitser [45], [46] began the move away from simple empirical models by introducing strain-rate dependency. An exponential dependency of plastic strain-rate on stress was adopted, controlled by a model of thermally activated dislocation motion. This has become a popular basis for physics-based model variations that reflect both the current understanding of plasticity and the experimental evidence [47]–[51], including inverse modelling methods where coefficients are calibrated to match experimental data [6].

An emerging approach common in recent works tries to identify the mechanisms of acoustoplasticity by examining the evolving microstructure through modelling pertinent dislocation dynamics within constitutive models [10], [51]. Such computational models are essentially phenomenological in nature, but embody microstructural behaviour by employing functional relationships of the form of fundamental laws governing dislocation mobility. By demonstrating agreement between simulations using the proposed constitutive model and experimental data, researchers claim to identify the fundamental mechanisms which significantly contribute to acoustoplasticity.

In what represents one of the most sophisticated and comprehensive constitutive models yet constructed to represent APE, Sedaghat *et al.* [51] decomposed the flow stress into three components representing the mechanisms which significantly control dislocation motion; athermal stress σ_a, thermal stress σ_{th} and dislocation drag σ_{drag}. The first two stem from the dislocation dynamics theory of thermal activation, which related flow stress σ to global strain ε and

strain rate $\dot{\varepsilon}$, temperature T, and the base resistance to dislocation motion, σ_G. The drag component accounts for the effect that the time rate of strain has on resistance of dislocation movement through a metal lattice, which becomes significant at high strain rates such as those encountered in ultrasonic vibration. The relation included material specific coefficients required to be determined by experiment.

In this work, the theory that ultrasonic excitation must introduce acoustic energy to dislocations with an effect similar to thermal activation was adopted from previous studies. It was proposed that incorporating a form of acoustic stress into the otherwise standard equation for thermally activated flow stress would reproduce the experimental observations of acoustic softening. The acoustic, or oscillatory, stress $\sigma_{acoustic}$ was introduced using a commonly known analytical equation, rearranged into the following equivalent form, equation (2.3):

$$\sigma_{acoustic} = \omega A\sqrt{\rho E} \tag{2.3}$$

Where ω and A are, respectively, the frequency and displacement amplitude of the ultrasonic excitation; ρ is the mass density and E the elastic modulus of the test material. According to Sedaghat the total flow stress is found by summing the components according to equation (2.4):

$$\sigma = \sigma_a + \sigma_{th} + \sigma_{drag} \tag{2.4}$$

Populating each of these components with their respective dislocation dynamics relationships, including the thermal stress modified to account for acoustic stress, the flow stress becomes:

$$\sigma = \sigma_G + \hat{C}\sqrt{1-\exp\left(-k_0\varepsilon\right)}\left\{1-\left[-c_2\left(T\cdot ln\left(\frac{\dot{\varepsilon}}{\dot{\varepsilon}_0}\right)+\frac{\xi V\omega A\sqrt{\rho E}}{k}\right)\right]^{1/q}\right\}^{1/p} + a\dot{\varepsilon}^b \tag{2.5}$$

Where ξ is an ‘effect coefficient’ of ultrasonic excitation which assumes a value particular to each type of forming process, which must be found by experiment.

Typical values for the constitutive model parameters given in [51] for aluminium are presented in Table 2.1.

Parameter	Value
σ_G [MPa]	6×10^7
$\hat{C}$ [MPa]	245×10^3
k_0	0.91
c_2 [K^{-1}]	6.21×10^{-5}
q	1.53
p	1
a [MPa]	2.138×10^{-12}
b	3.369

Table 2.1 - Example parameters in constitutive equation modelling APE

Using such relations produces a constitutive equation which is simple enough to implement in a finite element model, but which still requires experimental data to identify the missing constants unique to a particular material. Being semi-empirical and purposely fitted to the experimental data, they cannot be considered as direct evidence of theories of dislocation dynamics mechanisms proposed as key to acoustic softening, as, perhaps, a constitutive equation developed from first principles could.

2.1.3 Microstructural approaches

In experiments, Scanning Electron Microscopy (SEM) has opened up a wealth of information from post-test examinations of specimen microstructures. A study of low-carbon steel specimens, subjected to a tensile test under superimposed ultrasonic excitation, were subsequently analysed using micro-testing and crystallographic techniques [5] of optical microscopy, SEM, X-ray diffraction (XRD) and electron-beam backscatter diffraction (EBSD) to assess grain rotation and dislocation density. By comparing ultrasonically treated samples with control samples, the crystallographic assessment found evidence of decreased dislocation density and low-angle grain boundary fraction, in addition to preferential grain rotation. The textural weakening and reduction of subgrain formation during deformation was claimed as strong evidence that ultrasonic excitation had a softening effect. The effects were attributed to the excitation

encouraging dislocation annihilation, a conclusion shared by [52]. In this study, EBSD and Transmission Electron Microscopy (TEM) observations were used to make a similar comparison of the microstructure from excited and unexcited specimens of aluminium 1050 and molybdenum. Again, findings included a reduction in dislocation density and subgrain formation, supporting a claim of genuine material softening which only occurred under ultrasonic excitation. It was suggested that these mechanisms of APE are universal across metals of different stacking fault energies and crystal structures.

Examination of microstructural evolution in test specimens is now providing evidence to support understanding of acoustoplasticity and data such as dislocation density for constitutive models. Plastic flow of crystalline metals occurs at the crystal lattice level, through various mechanisms such as lattice slip via dislocation glide, twinning, grain boundary slip, and so on. Various processes affect the rate of flow, for example dislocation motion is impeded by solutes or entanglement with other dislocations, leading to the phenomena of strengthening and work hardening by impeding dislocation motion [53]. As acoustoplasticity exhibits as an apparent reduction in flow stress, it would seem that ultrasonic excitation must affect one or more of these processes of flow. Early studies of acoustoplasticity pointed to ultrasound activating dislocations and enhancing their mobility [2], [54], although the evidence was not direct, the conclusions being inferred from observations.

An obvious step would be to observe the effect of ultrasonic excitation on different flow mechanisms directly, and yet this has never been done. The difficulties of performing an *in-situ* test, introducing ultrasonic vibration into a specimen within an instrument capable of nano-scale observation, are great.

This explains why research into APE has until the present remained based upon mechanical tests, limited as they are to observing a material's behaviour as a response which must be the aggregate of possibly many mechanisms acting unseen within, leaving microscopic assessment of the microstructure to a *post-mortem* examination of the deformed specimen [4], [8], [52]. This technological limitation is a key feature of testing acoustoplasticity. Underlying physics must be inferred from the evidence within the macroscopic response of the material under excitation in combination with post-mortem microscopy.

2.1.4 Resolving the oscillatory stress - introduction of piezoelectric force transducer

An alternative approach to understanding acoustoplasticity was to return to the simple uniaxial tensile test, with the key difference of incorporating a piezoelectric force transducer in the experimental set-up [15], [55]. For the first time resolving the oscillatory part of the absolute stress, this instrumentation enabled direct observation of the real drop in flow stress, crucial in evidencing the existence of the acoustoplastic volume effect. Figure 2.3 shows the stress-strain results from a compression test performed on aluminium 1050, with and without ultrasonic excitation, [55]. In this test, the force applied by the test machine crosshead was measured using a piezoelectric force transducer. In the curve of the excited test piece, dashed lines indicate the amplitude peaks and troughs of the oscillatory component of stress. The peak of the stress amplitude lies below the trajectory of the normal yield curve, and a real reduction in flow stress is observed.

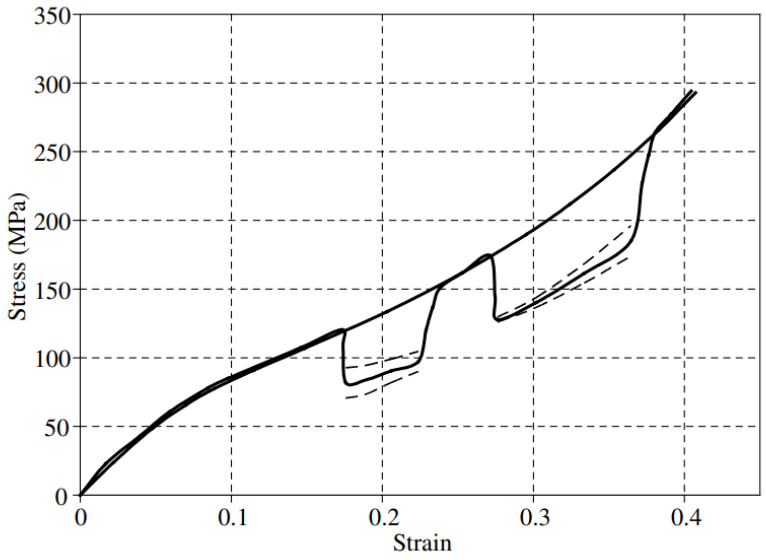

Figure 2.3 - Compression test of aluminium 1050. From Y. Daud [55]

Despite this breakthrough, studies have continued to use load cells, which, as a consequence of their structural characteristics, cannot resolve the ultrasonic oscillatory signal, and instead produce a measurement of the mean flow stress [6]–[8], [56]–[58], while some have not measured any macroscopic drop in forming load directly [3], [52]. A few have continued measurement of the oscillatory force using a piezoelectric force transducer [14], [33], [40], [41]. Of

these, none have explicitly considered and corrected for the effect on the force measurement of frequency response and inertia of the dies, platens or connecting fixtures of the test machine.

In one case concerns have been raised that the compression dies used may have affected the force amplitude observed [59]. Within the results clear signs were identified which indicated that the apparatus had in fact amplified the force amplitude measured. Having studied different frequencies it was found that one particular frequency caused an unusually large force reading. The researchers subsequently investigated the frequency response of their force measurement system by sweeping over the testing frequency range and recording the force amplitude. They observed a resonance peak within their test operating range, leading them to speculate that the unexpectedly large force amplitude was due to the resonance of their vibrating die fixture.

The effect of impedance on stress amplitude generated within the specimen has previously been considered in analytical modelling. In [60], a lumped parameter model of a specimen in a compression test included compliance of the interface between the specimen and the two platens. Estimates of sound wave transmission loss through series modelling of the specimen-platen interfaces have also been used to correct the stress amplitude predicted within the specimen [10], [51].

There are instances where the way in which the ultrasonic excitation was introduced to the specimen leaves the force measurement open to question. Sui *et al*. pursued an unusual approach by using a nano-indentation test machine to create the deformation, with the vibration applied perpendicular to the direction of impingement of the diamond test tip [3], [52]. No attempt was made to measure the oscillatory force directly, presumably because measuring the load applied by the miniature stylus of the nano-indentation test machine presented too great a difficulty. Evidence of the occurrence of acoustoplasticity is instead found in post-mortem microscopy analysis. Signs of textural weakening were reported, in which the microstructural texture and dislocation distribution evolution indicated a reduction in yield strength, compared to the same deformation without ultrasonic excitation. However, without any measurement of the oscillatory stress on the specimen, it is difficult to be certain that the

textural weakening resulted in a real reduction in the flow stress. Dynamic recovery, a process already known to occur under oscillatory loading, could produce similar microstructural changes without altering the flow stress [25].

In some studies ultrasonic excitation was applied to tensile specimens by clamping them between two anvils, one of which was also the ultrasonic horn which excited the specimen perpendicular to the direction of tension [5], [61]. It is unclear how to estimate with any certainty what the oscillatory stress resulting from this system was. Certainly, no attempt was made to measure it. This set-up suffered from the same problems with impact or slapping found in compression tests where the contact between horn and specimen was lost momentarily. This occurs when the specimen's rate of expansion following a compression cycle cannot match the acceleration of the ultrasonically excited platen (or anvil). In [5], this was extreme enough to manifest itself in hardening and even cracking of the metal surface.

2.2 Stress amplitude in the specimen by calculation

In the absence of a direct experimental measurement, several researchers estimate the stress amplitude within the specimen analytically [2], [6], [8], [10], [44], [51], [62]–[64]. The first appears to be Langenecker [2], who expresses the acoustic stress amplitude X as a function of displacement amplitude ξ, 'particle' velocity U, and acoustic intensity I, in equation (2.6):

$$X = \xi\rho\omega c = \rho U c = \sqrt{\frac{2}{\upsilon} IY} \tag{2.6}$$

Where ρ is the material density, ω the angular frequency, c the speed of sound, υ the Poisson's ratio and Y the Young's modulus of the material.

Pohlman and Lehfeld [44] express the same relation in a slightly different form, with different notation in equation (2.7):

$$\hat{\sigma}_s = \omega A \frac{E}{c} \tag{2.7}$$

Where $\hat{\sigma}_s$ is the acoustic stress amplitude, ω the angular frequency, A the particle displacement amplitude, E the material elastic modulus and c the speed of sound. Note that the alternative expression uses the relationship between the speed of sound, elastic modulus and density, equation (2.8) (which is valid for prismatic bars with a lateral dimension much smaller than the length [65]):

$$c = \sqrt{\frac{E}{\rho}} \tag{2.8}$$

The relationship in equations (2.1) and (2.2) is derived from a model of a stress pulse propagating along a semi-infinite bar [65], [66].

In early papers in which this equation appears the approximation was justified as a first order estimate in very simple dynamic/plastic models [44]. However, the equation appears in later works which cite the early studies without consideration of the continued validity of the approximation. It has been incorporated into modern FE models simulating plasticity under vibration where amplitude variation should have been adjusted to account for the boundary conditions and resonance condition (or absence of it) within the specimen geometry modelled in that work [51].

Parameters also in common use are acoustic intensity [2], [8], [62] and acoustic energy density [6], [10], [64] to develop empirical relations between the vibration applied and the effect on flow stress observed. Both are derived from the model of planar sound waves travelling through a medium, and for stress waves travelling along a semi-infinite bar [67], which gives acoustic energy density E_{ac} in a medium as equation (2.9):

$$E_{ac} = \rho v^2 = \frac{1}{\rho c^2} p^2 \tag{2.9}$$

Where ρ is density, v is velocity amplitude and p is the pressure in the case of a fluid, or stress for a solid. Acoustic intensity is then defined as equation (2.10):

$$I_{ac} = \frac{p^2}{\rho c^2} \tag{2.10}$$

Similar to equation (2.2), the relations developed also embody the implicit assumption that the loading on the specimen is a wave of constant amplitude along the length – the amplitude functions are not spatially dependant.

In [65] the equation of a stress wave propagating along a semi-infinite thin rod is derived from the most general form of the solution of displacement u in propagating waves from D'Alembert as follows:

$$u(x,t) = f(x - ct) + g(x + ct) \tag{2.11}$$

Where x is position along the semi-infinite rod, t is time, c is speed of sound in the material, and f and g are arbitrary functions. As only one wave is propagating along the rod it is assumed that equation (2.11) can be simplified to equation (2.12):

$$u(x,t) = f(x - ct) \tag{2.12}$$

The velocity of a 'particle', or single point, within the rod is the differential of the displacement with respect to time, equation (2.13):

$$v(x,t) = \frac{du}{dt} = -c \cdot f'(x - ct) \tag{2.13}$$

The axial stress in the direction of the propagating wave can be introduced using Hooke's law, equation (2.14):

$$\sigma = E\varepsilon \tag{2.14}$$

used in conjunction with the differential form of strain $\varepsilon = \frac{du}{dx}$ to find equation (2.15):

$$\sigma(x,t) = E\frac{\partial u}{\partial x} = E \cdot f'(x - ct) \tag{2.15}$$

Then, combining equations (2.13) and (2.15), stress in a travelling wave can be related to velocity, equation (2.16):

$$v(x,t) = -\frac{c}{E}\sigma(x,t) \tag{2.16}$$

To replicate the equations above the response to steady-state harmonic excitation at the origin $x = 0$ is required. In [65] the equation of motion for a propagating wave in a semi-infinite string is developed. It is adapted here for the semi-infinite bar. For the function $f(x - ct)$ assume a harmonic solution, equation (2.17):

$$u(x,t) = A_1 e^{j(kx+\omega t)} + B_1 e^{-j(kx-\omega t)} \tag{2.17}$$

Where $k = \frac{\omega}{c}$ is a parameter called the wave number. It is noted that equation (2.17) can be viewed as the sum of two propagating waves travelling in the $+x$ and $-x$ directions. The harmonic excitation boundary condition (BC) at $x = 0$ is defined by equation (2.18) with excitation frequency ω and amplitude U_0:

$$u(0,t) = U_0 e^{(j\omega t)} \tag{2.18}$$

It follows that $U_0 = A_1 + B_1$, then

$$u(x,t) = A_1 e^{j(kx+\omega t)} + (U_0 - A_1)e^{-j(kx-\omega t)} \tag{2.19}$$

In [65] is it argued that, because there is no other boundary condition in the semi-infinite bar model, the excited wave will propagate forever in one direction. Without any boundary to reflect this wave and cause a second wave to travel in the opposite direction, one of the two travelling waves in equation (2.17) is redundant, and the coefficient A_1 may simply be set to zero. Equation (2.19) becomes the general solution for a wave propagating in a prismatic, semi-infinite bar, equation (2.20):

$$u(x,t) = U_0 e^{-j(kx-\omega t)} \tag{2.20}$$

Differentiating equation (2.20) with respect to time evaluates the velocity at the BC, equation (2.21):

$$v(x,t) = \frac{du}{dt} = \frac{d}{dt}\left(U_0 e^{-j(kx-\omega t)}\right) = j\omega U_0 e^{-j(kx-\omega t)} \tag{2.21}$$

Substituting equation (2.21) into equation (2.16) results in equation (2.22), rearranged to find oscillatory stress:

$$\sigma(x,t) = -j\frac{E}{c}\omega U_0 e^{-j(kx-\omega t)} = -j\frac{E}{c}\omega U_0 e^{j(\omega t-kx)} \tag{2.22}$$

The amplitude or modulus of equation (2.22) is:

$$|\sigma(x,t)| = \frac{E}{c}\omega U_0 \tag{2.23}$$

Equation (2.23) is identical to equation (2.7) developed in [44] and used subsequently by others (for example, Sedaghat *et al.*), showing these works base the stress amplitude calculation on the assumption of a travelling wave propagating continuously through the specimen. This condition seems improbable given that test pieces are either of the tensile type and terminate in a jaw much larger than the specimen [15], [68]; or of the compressive type, which is generally held against the vibrating horn by a platen much larger and much heavier than the test piece [8], [33], [69]. The superior mass and stiffness of the platens and jaws used in uniaxial testing over that of the specimen will offer an effective boundary to reflect the vibration from the specimen [70].

In studying the waveform developed in test pieces with such boundary conditions, Winsper *et al.* [71] develop the analytical expressions for displacement and dynamic stress in a specimen modelled as a prismatic bar with cross-sectional area A and length L. It was assumed that the test material was homogenous, isotropic and obeys Hooke's law (equation (2.14)). Only longitudinal vibration along the axis of the bar was considered, this axis being defined as the position coordinate x. This limited the stress modelled to the

normal stress perpendicular to the bar cross-section. By balancing the inertial forces and internal stresses over an infinitesimal section of bar, the standard one-dimensional equation of wave motion was arrived at, equation (2.24):

$$\frac{\partial^2 u}{\partial x^2} = \frac{1}{c^2}\frac{\partial^2 u}{\partial t^2} \tag{2.24}$$

Where u is the displacement, t is time and c is the speed of sound as defined by equation (2.8). At one end of the bar a fixed boundary condition was applied by setting the displacement to zero, that is at $x = 0$, $u(0,t) = 0$. At the other the harmonic excitation was represented by imposing a sinusoidal displacement, at $x = L$, $u(L,t) = U_0 \sin \omega t$. A harmonic solution, equation (2.25), was assumed.

$$u(x,t) = X(x) \cdot \sin(\omega t) \tag{2.25}$$

In equation (2.25) the term $X(x)$ is a spatially dependent function which modifies the amplitude of the standing wave over the length of the bar. It was found by introducing the boundary conditions described above and solving for u; for the detailed proof see [71] or a standard text on acoustics, [65], [70].

The resulting expressions for displacement u and the dynamic stress σ_D are equations (2.26) and (2.27) respectively:

$$u(x,t) = U_0 cosec\left(\frac{\omega L}{c}\right) \sin\left(\frac{\omega x}{c}\right) \sin(\omega t) \tag{2.26}$$

$$\sigma_D(x,t) = \frac{\omega E U_0}{c} cosec\left(\frac{\omega L}{c}\right) \cos\left(\frac{\omega x}{c}\right) \sin(\omega t) \tag{2.27}$$

Where x is the axial position coordinate along the bar, t is time, ω is the excitation frequency, and E and c are respectively the elastic modulus and speed of sound of the material.

Equation (2.24) can also be solved assuming a solution of exponential form, equation (2.28):

$$u(x,t) = Ae^{j(\omega t - kx)} + Be^{j(\omega t + kx)} \tag{2.28}$$

Doing so results in a final solution where the time and spatially independent variables are within the one sine (or cosine) term, equation (2.29):

$$u(x,t) = cosec(kL)\sin(\omega t - kx) \tag{2.29}$$

This can be compared to the expression derived for displacement in a propagating wave, equation (2.20), if the latter is decomposed into its harmonic components using Euler's formula, equation (2.30):

$$e^{j(\omega t - kx)} = \cos(\omega t - kx) + j\sin(\omega t - kx) \tag{2.30}$$

Equation (2.20) thus treated becomes equation (2.31):

$$u(x,t) = U_0[\cos(\omega t - kx) + j\sin(\omega t - kx)] \tag{2.31}$$

To find the result to a harmonic input of $u = \cos(\omega t)$ or $u = \sin(\omega t)$ then it is only required to take forward, respectively, the real or imaginary part of equation (2.31) [70]. To compare to the sinusoidal input assumed in [71], the equation for displacement is then equation (2.32):

$$u(x,t) = U_0\sin(\omega t - kx) \tag{2.32}$$

Comparing this equation for displacement in the travelling wave, equation (2.32), to that of the standing wave, equation (2.29), it can be seen that they are identical save for the amplitude modulating $cosec\left(\frac{\omega L}{c}\right)$ term. The impact of this term on the overall amplitude depends on the values of the speed of sound of the material under test, the length of the specimen and the excitation frequency. These parameters are specific to each test set-up and experiment, however, the key point is that the boundary conditions assumed to be in effect on a specimen during an ultrasonically excited uniaxial test have a significant effect on the amplitude predicted by analytical modelling.

As a numerical illustration of the difference between the equations developed based on the assumption of a propagating or standing wave, the oscillatory

stress amplitude shall be calculated here using both equations for the example ultrasonic compression test presented by Sedaghat *et al.* in [51]. They create a FE simulation of an ultrasonically assisted compression test originally performed by Aziz [72], with the goal of demonstrating their constitutive model discussed earlier. They compare the results to experimental data in [72] and find good agreement. As previously discussed, this model included an equation for acoustic stress, equation (2.7), which has been shown to be based on propagating wave theory. According to [51] the specimens were cylindrical with a diameter of Ø8 mm and height 8 mm, and made of commercially pure aluminium 1050. In the ultrasonic compression test, ultrasonic excitation with frequency of 20 kHz was applied by one of two platens to one end of the specimen. The other platen applied the quasi-static compression from the test machine crosshead, which, for the purposes of calculating the oscillatory stress amplitude, can be modelled as a rigid boundary. In the test the amplitude was varied from 5 to 20 μm, however for this comparative study an amplitude of 10 μm was used. These parameters and the material properties are summarised in Table 2.2. The speed of sound was calculated from equation (2.8). Angular frequency ω is related to frequency f by equation (2.33):

$$\omega = 2\pi \cdot f \tag{2.33}$$

Elastic modulus E (GPa)	Mass density ρ (kg.m^{-3})	Excitation frequency f (kHz)	Displacement u (μm)	Length of specimen L (mm)
69.0	2700	20	10	8

Table 2.2 - Parameters for calculation of oscillatory stress amplitude

From the data in Table 2.2, the equation for oscillatory stress based on propagating wave theory, equation (2.23), predicts an amplitude of 17.2 MPa. In contrast, equation (2.27), which was developed using BCs which mirror those of the platens in this example test, predicts an amplitude which varies from 86.8 MPa at the fixed BC to 85.1 MPa at the oscillatory BC. The propagating wave amplitude is a factor of 5 smaller than the standing wave amplitude, greatly

underestimating the oscillatory loading on the specimen. In the case of this test, using the propagating wave-based equation to calculate the real flow stress reduction (equation (2.1)) would produce erroneous results, possibly leading to incorrect conclusions being drawn about the nature, or indeed existence, of acoustoplasticity in the test. Furthermore, applying this equation in modelling of the material behaviour undermines the value of the constitutive equation produced, though it may be difficult to detect if the model was empirically fitted to the experimental data, such as in [51]. Finally, given that the true reduction in flow stress, $\Delta\sigma_{pk}$, is the difference between the peak of the oscillatory stress σ_{osc} and the normal yield strength σ_0 (equation (2.1)), calibrating the empirical constitutive model to replicate the reduction in mean flow stress, $\Delta\sigma_{mean}$ (equation (2.2)), seems less appropriate than using the true flow stress reduction, $\Delta\sigma_{pk}$.

The use of equations for displacement and stress based on a propagating wave has led to discussion of acoustoplasticity framed in terms of applying ultrasonic energy to the test piece in a way which is akin to applying heat. This language disguises the fact that, from the point of view of a material's response, the base key parameter is stress. An ultrasonic vibration results in an oscillatory stress and a resulting oscillatory strain. Characterisation should reduce to relationships between stress and strain parameters. Terms such as 'ultrasonic energy introduced' by the ultrasonic transducer, measured at the ultrasonic generator, are of limited value when the resulting stress or strain within the specimen is not measured. Empirical relationships can be found relating acoustic intensity or energy density to an estimated drop in the flow stress [2], [8], [10], and they have in the past formed the basis for investigation. However, further gains in understanding of underlying processes will only be made by measuring the stress and strain amplitude actually occurring within the test piece.

This thinking has made its way into the multiple constitutive models constructed to identify the underlying physical processes at work in APE. The detailed and complex nature of the phenomenological models, which incorporate established dislocation dynamics relations, obfuscates the unsatisfactory use of strain calculated from travelling wave equations which do not necessarily apply to the test data used in model calibration [10], [51], [64].

2.3 Summary

The approaches to characterising acoustoplasticity may then be summarised as follows:

- Relating macroscopic measurements (such as apparent flow stress reduction) to macroscopic input parameters (such as vibration amplitude);
- Post-mortem microstructural evaluation; and
- Modelling to produce predicted stress-strain curves, to compare to the experimental counterparts.

Despite the macroscopic nature of the base mechanical test, researchers have managed to infer the effect of ultrasonic excitation on plastic flow mechanisms, by using these characterisation methods to make comparisons between a judicious choice of materials, with and without ultrasonic excitation. Often, all three of the above approaches will be carried out to build up a full assessment of the macro- and microscopic effects of ultrasonic excitation on plastic deformation. For example, in their investigation of aluminium and titanium under ultrasonically assisted compression, Zhou *et al*. [8] initially gather evidence from force and vibration measurements to identify the relationship between displacement amplitude and acoustic softening. Following the uniaxial testing, specimens were then examined under an SEM, where EBSD was used to map grain orientation and dislocation density. When compared to unexcited compression specimens it was found that ultrasonic excitation enhanced crystal grain rotation and twinning, which could be viewed as evidence of microstructural softening. These investigative steps have been used by several researchers [3], [7], [11], [41], [52].

Each characterisation route, however, remains dependent on an estimation of force and strain, both quasi-static and oscillatory. In general, questions remain about the veracity of force transducer measurements, when used to record an oscillatory signal at ultrasonic frequencies. In many of the apparatuses used in experiments, the force measuring instrument cannot resolve the oscillatory stress, leaving the true drop in flow stress to be calculated [3], [44], or resulting in the use of the apparent reduction in flow stress [6], [8], [73]. Even when the instrumentation is capable of resolving ultrasonic excitation, the force transducer is remote from the specimen [15], often having a large mass between the specimen and the force transducer, such as the die in the apparatus used by Yao *et al*. [40]. It will be shown in this thesis that lumped masses can impede

oscillatory force signals, even the masses within the structure of the piezoelectric force transducer itself.

Therefore, despite all the advances in constitutive modelling and simulation of ultrasonically excited metal processes, error in the force signal used in the models could undermine their conclusions and the advances towards a proper understanding of acoustoplasticity. Added to this, the continued use of global strain as the measure of plastic deformation leaves constitutive models exposed to inaccuracy introduced by heavily localised plastic deformation during ultrasonic excitation.

Focusing on this fundamental aspect of mechanical testing for acoustoplasticity, this work intends to evaluate the ability of the piezoelectric force transducer to indicate the true stress within the specimen, and explore further methods to enhance knowledge of local stress and strain throughout the specimen.

Creating a methodology for measuring oscillatory stress which addresses the challenges of accurate stress measurement in ultrasonic uniaxial tests will enable trusted assessments of the true flow stress reduction. In the first instance it is hoped this will help settle the debate over the existence of APE. Further, it will provide reliable data and a sound foundation for analysing the key relationships between excitation parameters and APE, and for constitutive modelling.

Exploring the local plastic deformation over the whole specimen as it evolves during ultrasonic excitation will both enhance understanding and provide a measurement of the local strain to match the local stress within the inhomogeneous loading of the specimen. This, again, will provide better data for phenomenological and constitutive modelling.

Ultimately, improving the accuracy of the stress-strain data on which APE constitutive modelling relies will enhance the evidence supporting theories of the mechanisms behind acoustoplasticity.

3 Experimental mechanics techniques and the ultrasonic tensile test

3.1 Tensile testing for characterising APE

Tensile tests of metal specimens are commonly adopted to characterise the stress-strain relationship at a macroscopic level and are also often used to characterise the stress-strain relationship in models of ultrasonically assisted metal deformation processes.

Material constitutive identification (the process of characterising a material's mechanical properties) requires the measurement of two parameters - the extension of the specimen and the force applied to achieve it, from which can be calculated the stress and strain [74], [75]. In normal quasi-static uniaxial testing the force is measured at one end of the specimen, and the extension is found from the displacement of one end of the specimen from the other. This means that the stress and strain calculated from these measurements are global parameters. It is assumed that they are reasonable approximations of the local stress and strain over the gauge length of the specimen. Material constitutive models identified from the stress-strain data thus measured implicitly embody this assumption.

Test pieces with simplified prismatic geometry are loaded uniaxially (in one direction) to reduce the unknown internal loading to one normal stress across the specimen cross-section acting in the direction of the applied force, Figure 3.1.

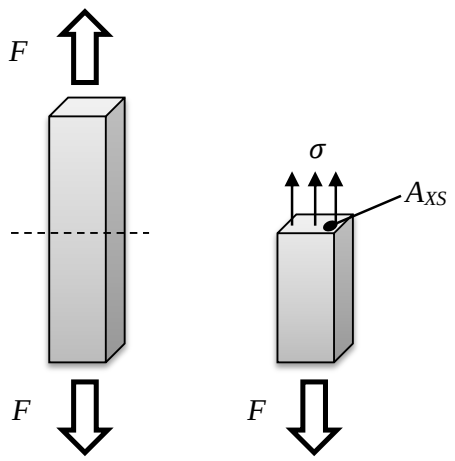

Figure 3.1 - Normal stress in tensile test specimen

By virtue of the long aspect ratio of the specimen geometry, it is assumed that the normal stress acting on the cross-section (herein called the axial stress) corresponds to the principal stress, and that stresses in other directions

are negligible. This simple, one-dimensional stress state is important for correctly identifying the constitutive relationship.

The normal stress calculated from the test force F divided by the undeformed cross-sectional area A_{XS} of the specimen gauge length is known as the nominal, or engineering, stress, equation (3.1):

$$\sigma_{n(axial)} = \frac{F}{A_{XS}} \tag{3.1}$$

Nominal strain ε_n (also known as engineering strain) is calculated from the total extension of the specimen gauge length, measured by an extensometer or video extensometry, equation (3.2):

$$\varepsilon_n = \frac{\epsilon}{L_0} = \frac{L - L_0}{L_0} \tag{3.2}$$

Where L_0 is the original gauge length of the specimen, and L is the extended length, and ϵ is the extension defined as the difference between L and L_0 [75]. True strain is defined by equation (3.3):

$$\varepsilon = \ln(1 + \varepsilon_n) \tag{3.3}$$

As a uniaxial test progresses, the cross-section of the test piece narrows, at first as a consequence of conservation of volume, then, in ductile materials, due to necking (the process in which plastic deformation stops being equally distributed over the gauge length and becomes very localised, reducing the specimen section at that point until failure occurs). These are not accounted for in equation (3.1), which uses the cross-sectional area of the undeformed test piece. Commonly, the change in cross-section from volume conservation is accounted for by calculating the true stress, equation (3.4):

$$\sigma_{axial} = \sigma_{n(axial)} \cdot (1 + \varepsilon_n) \tag{3.4}$$

Historically, strain has been calculated using the displacement of the crosshead on a Universal Testing Machine (UTM). It is assumed that the displacement of the crosshead is identical to the extension of the material specimen ($L - L_0$). In fact, the elastic strain in the assembly between the crosshead and UTM base plate will contribute to the displacement at the crosshead, along with elastic strain and plastic deformation in the specimen, however, test fixtures are designed to be stiff and in the majority of ductile metal testing the elastic strain in the fixtures was commonly assumed to be negligible in comparison to the plastic deformation in the specimen.

This method has been used in many of the studies on acoustoplasticity, from the earliest studies [1], [9] to the present day [64]. In the absence of a better method it is acknowledged as a workable compromise for plastic tests. The elastic deformation can be calibrated out of results by performing purely elastic extension beforehand to create a numerical correction [56].

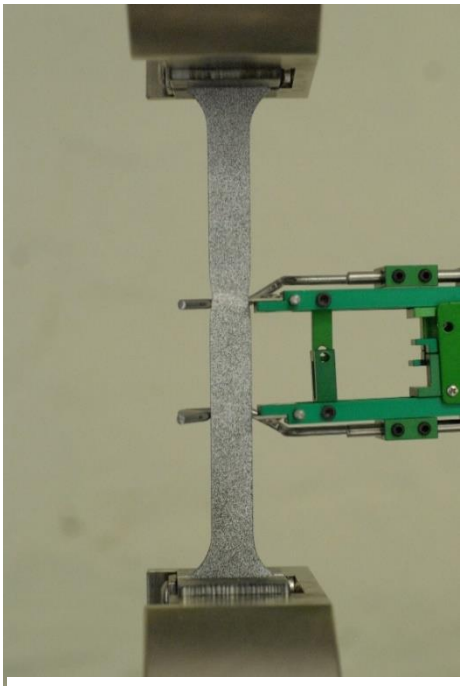

Figure 3.2 - Extensometer on sheet 1050 specimen

There now exist accurate ways to measure strain directly on the specimen. Extensometers clip onto the specimen with two legs and measure the change in distance between them – an example is shown in Figure 3.2. They have been used in research on the acoustoplastic effect, [5]. However, clipping masses onto the specimen in this way must influence the vibration of the specimen. It is also possible that vibration would interfere with the operation of the extensometer, affecting its accuracy.

In a standard quasi-static test force is measured remotely from the specimen and it is assumed that inertial effects are negligible [74], [75]. Furthermore, strain is calculated from total specimen extension. When ultrasonic vibrations are superimposed on a standard quasi-static tensile test, other effects must be accounted for: the test is no longer quasi-static; loading is inhomogeneous and

the stress field is non-uniform; the displacement response is inhomogeneous and both the elastic and plastic strain fields are non-uniform; the test is non-monotonic; and the frequency response and impedance of the test structure and the measurement transducers become influential. All of these factors must be considered, along with the strain and strain-rate dependencies of the specimens, in order to verify the veracity of data from these macroscopic tests.

By considering only the relative motion of the test machine crosshead and the vibrating horn tip, a basic understanding can be developed of the challenges facing instrumentation for stress and strain measurement. This will be considered once the USTT apparatus and specimen used in this thesis have been described, to provide a basis for discussion.

3.2 The Ultrasonic Tensile Test and mechanical testing

3.2.1 Uniaxial test machine and ultrasonic excitation

The ultrasonic tensile test (USTT) apparatus used in this study (Figure 3.3) is configured within a universal test machine load frame (Instron 5966), which

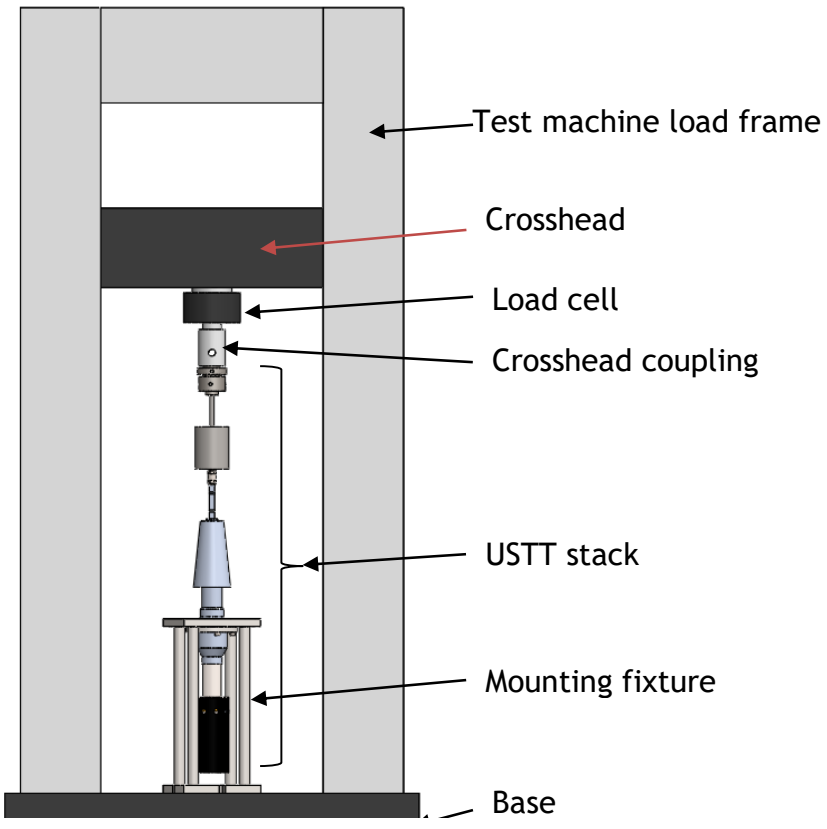

Figure 3.3 - Ultrasonic Tensile Test set-up

applies tension to a specimen at a pre-programmed crosshead speed and displacement.

An ultrasonic transducer (Sonic Systems L500) excites the base of the specimen, via tuned components called the booster and ultrasonic horn (Figure 3.4).

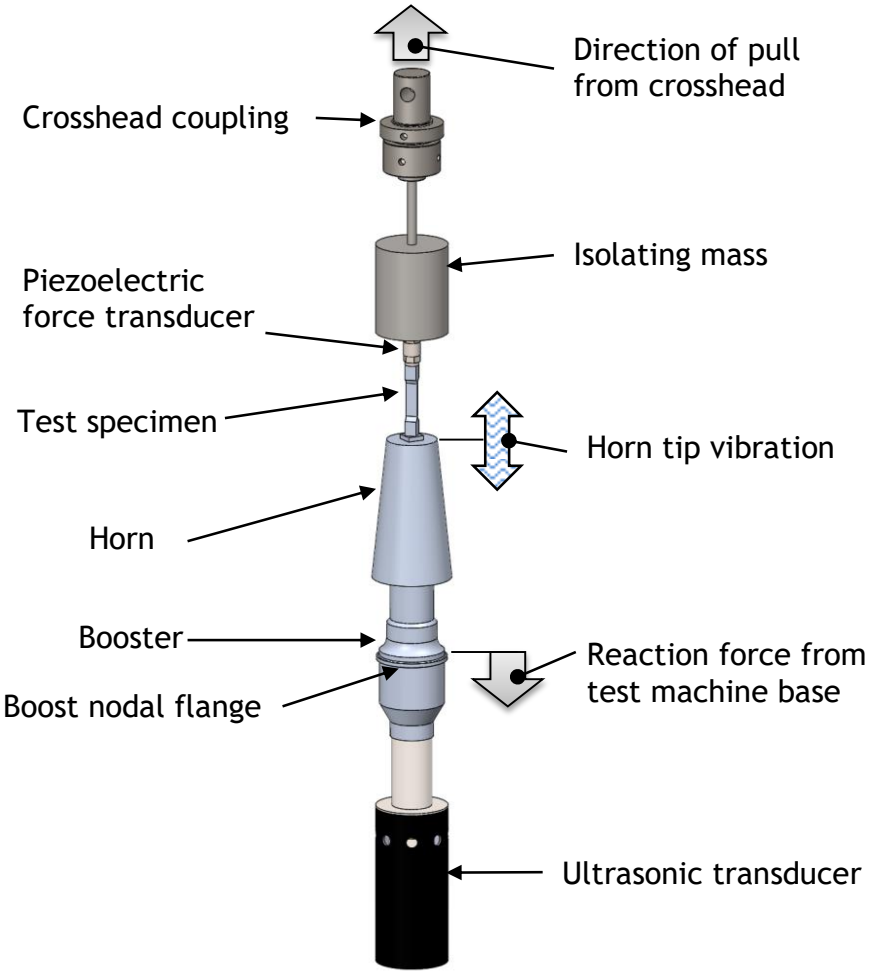

Figure 3.4 - Ultrasonic Tensile Test, ultrasonic stack

The transducer-booster-horn assembly excites axial ultrasonic vibration with an amplitude that can be varied from zero to a maximum amplitude of 10 µm, at a set frequency of 20 kHz, +/- 500 Hz. The ultrasonic generator which supplies the ultrasonic transducer with electrical power employs an electronic resonance tracking system to detect declining resonance (and therefore transfer of electrical to mechanical power). It can correct the frequency generated in a range of up to +/- 500 Hz to maintain resonance. The top of the specimen is connected to the crosshead via a piezoelectric force transducer and an isolating mass.

L500 ultrasonic transducer

The ultrasonic transducer used in this work, Figure 3.5, is a Langevin type transducer as described in the Introduction.

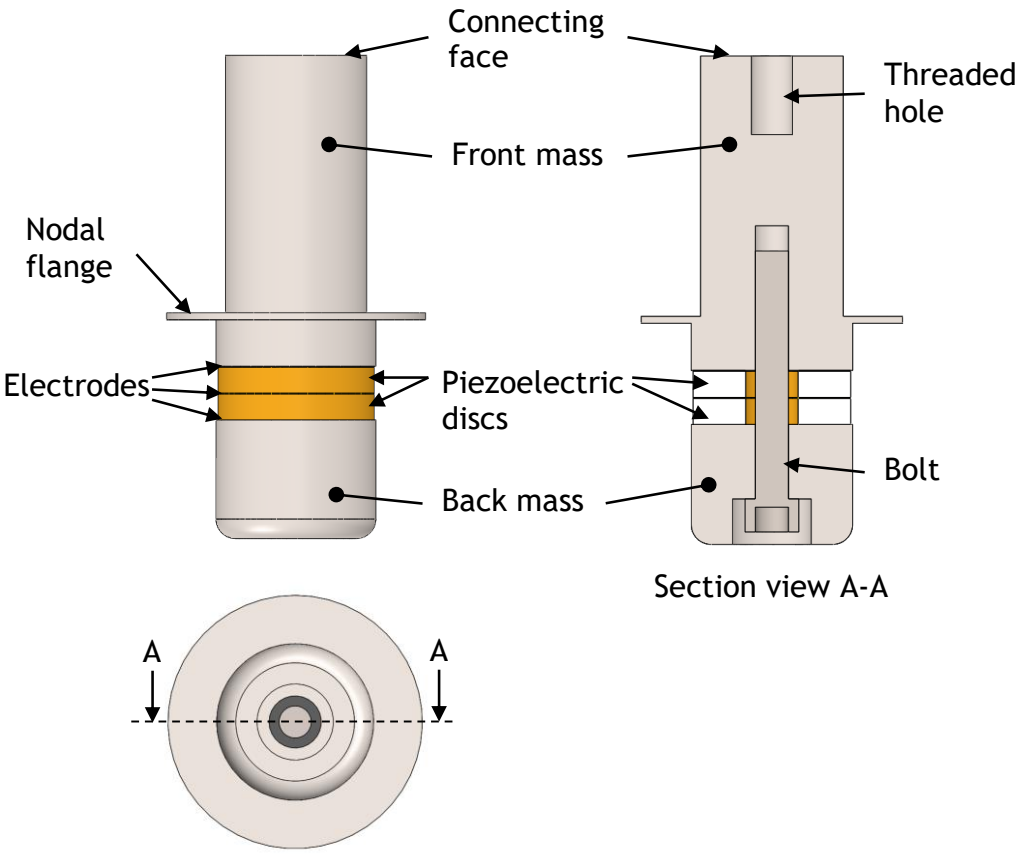

Figure 3.5 - L500 ultrasonic transducer

The piezoelectric elements (single crystal or ceramic) are often disc shaped. They are made to a thickness tuned to produce a resonant mode in their axial direction at the desired operating frequency of the transducer. They are surrounded on either side by tuned parts, commonly made of metal aluminium or titanium to benefit from these metals' property of low acoustic loss. On one side the front mass forms an integral horn, shaped to direct the vibration from the piezo discs to the area of application of the vibration, usually through tuned wave guides attached to the transducer's connecting face by a threaded stud.

On the opposite side to the discs is a short cylinder named the back mass, which serves as one side of the clamp, and also acts to reflect ultrasonic energy travelling in the opposite direction to the point of vibration application, back into the transducer. The length of the whole assembly is designed to coincide

with a halfwave length of the frequency of operation, so that a resonance condition is excited and optimal vibration output is achieved.

A bolt passes through the back mass and the piezoelectric elements, terminating in the front mass or horn. Tightening this bolt provides the compressive preload force required to prevent the piezoelectric elements from failing. To each side of the piezoelectric discs is placed a thin copper disc. These form the electrodes which permit connection of the piezoelectric discs to an electrical power supply designed to drive ultrasonic transducers. It is called the ultrasonic generator, and uses mains power to produce a sinusoidally oscillating electric potential at a set required frequency and variable amplitude.

Horn

The aluminium horn in Figure 3.4 was developed and tested for a previous study on acoustoplasticity in metal tensile testing [43]. It was designed such that its first longitudinal (L1) mode resonates at a frequency of 20 kHz, developing maximum displacement at its tip (‘Horn tip vibration’ in Figure 3.4) at the operating frequency of the ultrasonic transducer used in both that work, and this thesis. The horn is conical so that, when resonating in its L1 mode, it magnifies the displacement applied at the input end (connected to the booster) with a theoretical ratio of 2:1, developing twice the displacement at the horn tip. (In the course of the work undertaken for this thesis, the gain was found to be a little less, closer to 1.8:1.)

Booster

The booster (Figure 3.4) is a commercial item modified for use in the USTT, which is clamped into the mounting fixture (Figure 3.3). This fixture, in turn, connects to the base of the load frame, completing the load path from the crosshead through the USTT apparatus to the load frame base. Similar to the horn, the booster has been made such that the resonance frequency of its first longitudinal mode is 20 kHz. In this mode, the extreme ends of the booster are anti-nodes and displacement is at a maximum, with the amplitude ratio from the input end to the output being 1:1. The L1 mode has a displacement nodal plane at the booster’s mid-point (‘Nodal flange’ in Figure 3.4). A flange around the

booster's circumference is located here, to facilitate mounting into the mounting fixture. As the displacement is theoretically zero at the nodal plane, connecting to the booster at this location prevents vibration transmission to the mounting fixture and on to the wider test machine structure. If they are excited, the dynamic response of the mounting fixture and the test machine, may come to influence the loading on the specimen, so it is important to isolate the vibrating parts of the USTT stack. In addition, it is possible that vibration transmitted as far as the crosshead could interfere with the force measurement, though this is perhaps unlikely given that the long transmission path through the heavy structure of the load frame will damp the ultrasonic vibration. The horn, booster and ultrasonic transducer are all connected by threaded steel studs.

The experimental set-up (excluding the isolating mass) largely follows many of those reported in the literature [9], [13], [15], [30] so that the influences and veracity of experimental results of this configuration can be explored and shall be relevant to future testing of the APE.

3.2.2 Specimen description

The specimen was based on the ISO 6892-1 specification [74] for a tensile test specimen, except with the ends adapted to attach directly to the ultrasonic horn and the force transducer via screw threads (Figure 3.6).

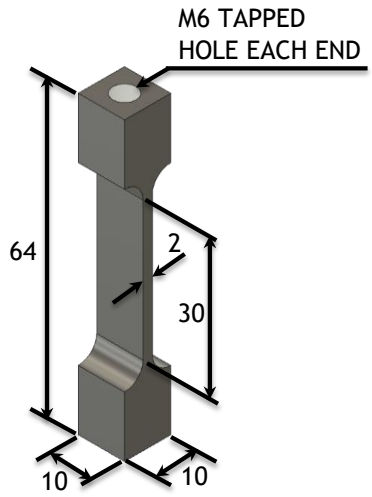

Figure 3.6 - Specimen geometry

During testing care was taken to ensure the threaded connections were appropriately tight, based on prior experience. Slack joints manifested as

substantial audible noise in the form of loud screeching, and, upon dismantling, evidence of grinding and heating was found on the interface surfaces.

The geometry has rectangular cross-section of the centre portion, providing a flat surface for optical photogrammetry measurement. Specimens (Figure 3.7) were made from two materials.

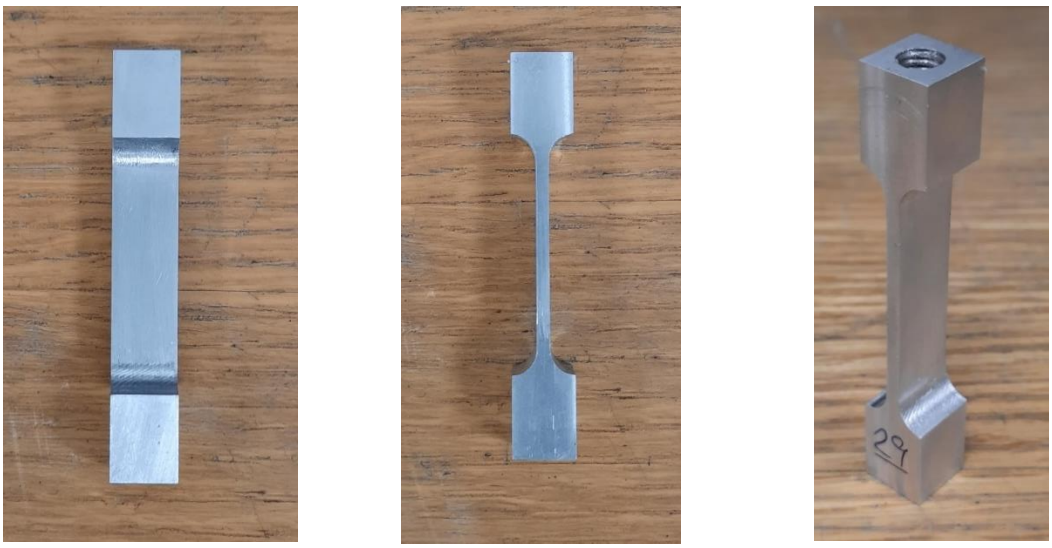

Figure 3.7 – USTT specimen

The first, a soft, commercially pure aluminium of the 1000 series was used in testing plastic deformation with ultrasonic excitation. It was selected for its heritage in providing clear observations of acoustoplasticity, previously discussed in Section 2.1.1. Specimens were also made of a second material, an aluminium alloy (Al 5083) and used for investigating apparatus dynamics limited to elastic deformation. The low yield strength of the pure aluminium made inadvertent and unintended deformation of those specimens likely during the course of the dynamics tests. Instead, the much stronger aluminium alloy was used for this work, as the material properties relevant to elastic dynamic loading in a USTT, elastic modulus and density, were very similar between the two metals. This is discussed further in the chapter on experimental modal analysis of the USTT, Chapter 5.

3.2.3 Dynamics of USTT

The combination of a slow, quasi-static extension with an elastic oscillation at kilohertz frequencies produces an elastic-plastic loading which is unique among

mechanical tests. Take as an example an ultrasonic tensile test where the crosshead connected to the top of the specimen moves upwards at a speed of 5 mm/min, and the tip of the ultrasonic horn vibrates the bottom of the specimen at 20 kHz with an amplitude of up to 10 μm. In the period of one cycle the advance of the crosshead is extremely small.

The crosshead displacement, Δ_{CH}, is in general the crosshead velocity v_{CH} multiplied by the time t, equation (3.5):

$$\Delta_{CH} = v_{CH} \cdot t \tag{3.5}$$

In one cycle the crosshead advance is the crosshead speed multiplied by the oscillation period, T, equation (3.6) below. At 20 kHz one cycle has a period of 50 μs, and the crosshead speed is assumed constant at 5 mm/min.

$$\Delta_{CH} = v_{CH} \cdot T = \frac{5}{60} * 50 \times 10^{-6} = 4.17\ nm \tag{3.6}$$

The crosshead displacement in once cycle is found to be 4.17 nm. From equation (3.2), for a specimen with a parallel length of 30 mm, the plastic strain imposed by a crosshead displacement is found by equation (3.7):

$$\varepsilon_p = \frac{\epsilon}{L_0} = \frac{4.17 \times 10^{-9}}{0.03} = 0.139 \times 10^{-6} \tag{3.7}$$

This value of crosshead displacement requires a plastic deformation of 0.139 microstrain by the end of each cycle, regardless of when and how the strain is fulfilled over the duration of the cycle.

It is desirable to estimate the strain-rate of the plastic deformation, for use in evaluating potential experimental techniques. A method is presented here in which a simplified model of the extension of the specimen is used to estimate the duration of the elastic and plastic portions of the vibration cycle.

First, the extension of the specimen is defined as the difference between the crosshead advance, Δ_{CH}, and the oscillatory displacement of the horn tip, u_{HT}, equation (3.8):

$$\epsilon = \Delta_{CH} - u_{HT} \tag{3.8}$$

The definition of the horn tip displacement u_{HT} has an impact on the ease of solution. It was found convenient to define the oscillation cycle as beginning at the point just after the previous plastic deformation; that is, beginning with the elastic unloading and reloading of the specimen, with the plastic deformation occurring at the very end of the cycle. This is logical, as the irreversible nature of the plastic deformation means that, once the motion of the horn tip reverses direction, the plastic deformation ceases. The effect is to reset the cycle – the relaxation is elastic, and so the cycle begins again.

It is to capture this effect that the equation for horn tip displacement was arranged as follows, equation (3.9):

$$u_{HT} = U_0 - U_0 \cdot \cos(\omega t) \tag{3.9}$$

In equation (3.9), by using cosine the cycle begins at the extreme displacement position, corresponding to the beginning of a new elastic unloading-reloading sweep. This is multiplied by the displacement amplitude is U_0. Taking this away from a constant value equal to the displacement produces the effect that the displacement of the horn tip begins at zero and is positive throughout the cycle. This is shown in Figure 3.8 as the curve ‘horn tip position’, and it can be seen that equation (3.9) corresponds to a model of the horn tip in which it starts from its furthest distance from the crosshead, moves towards it and then retracts as it completes one cycle.

The crosshead displacement from equation(3.5) is also plotted in Figure 3.8 as ‘crosshead advance’. Note that the ordinate has been made valueless, and the curves are diagrammatic, as the extremely small advance of the crosshead in one cycle makes it impractical to plot it in real values.

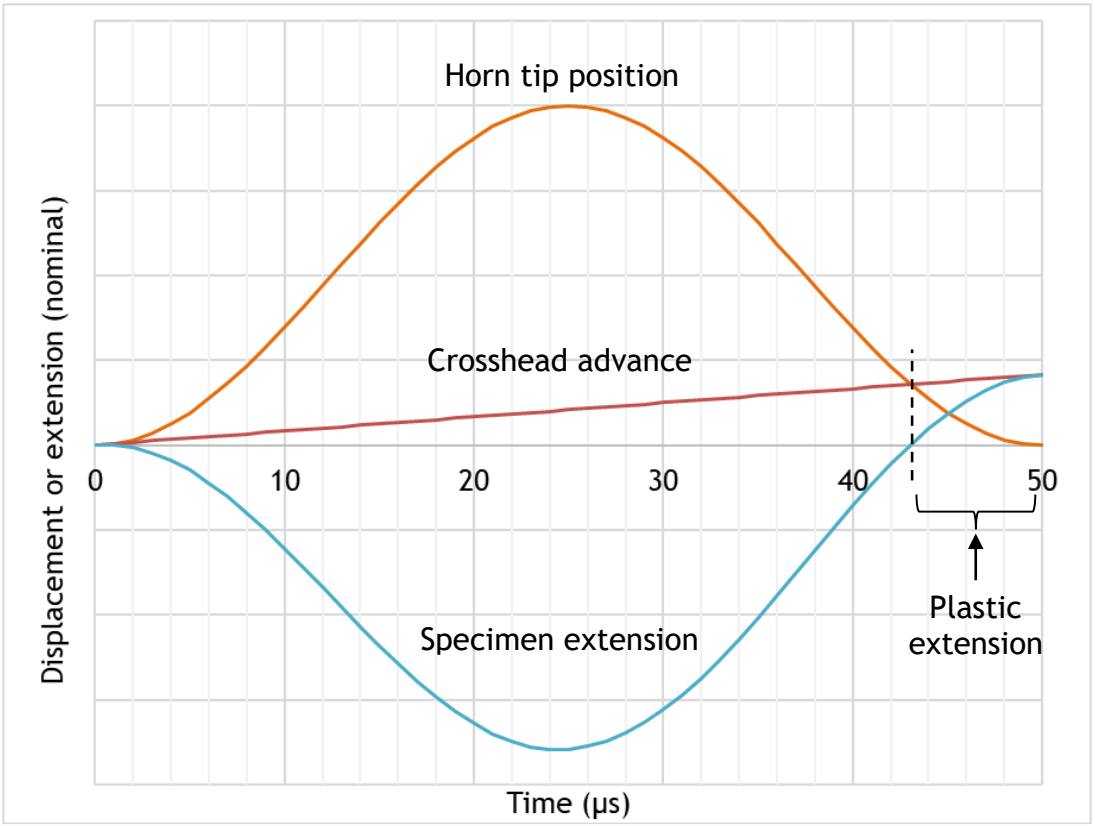

Figure 3.8 - Diagram of horn tip and crosshead motion and resulting extension

Substituting equations (3.5) and (3.9) into equation (3.8) results in an expression for the total extension, equation (3.10):

$$\epsilon = v_{CH} \cdot t - (U_0 - U_0 \cdot \cos(\omega t)) \tag{3.10}$$

This is plotted as curve 'Specimen extension' in Figure 3.8. As the cycle begins on the tail of plastic deformation from the previous cycle, the stress in the specimen begins at the elastic limit of the material. As the horn tip advances towards the crosshead faster than the latter can move, the extension is negative, and the tension in the specimen reduces. The motion of the horn tip acts to unload the specimen elastically, and then reload it elastically until such a point is reached when the distance between the horn tip and the crosshead is equal to the length of the specimen as it was at the start of the cycle. At this point the extension is zero. Because the crosshead has advanced during the cycle, this will be some time tp before the horn tip can complete its oscillation. At this time the stress in the specimen will have returned to the elastic limit, and further extension will cause plastic deformation. Finding the time t_p enables

a first order estimate of the strain rate to be calculated. At time t_p, $\epsilon = 0$, so that equation (3.10) becomes equation (3.11):

$$0 = v_{CH} \cdot t_p - \left(U_0 - U_0 \cdot \cos\left(\omega t_p\right)\right) \tag{3.11}$$

This equation cannot be solved analytically. The time t_p was found using the Goal Seek tool in Excel to calculate a value of time which brought the value of extension closest to zero to 3 decimal places. This method calculated $t_p$to be 0.242 μs. By assuming strain-rate to be linear over the duration of plastic deformation, a value for it was estimated using equation (3.12):

$$\dot{\varepsilon}_p = \frac{\varepsilon_p}{t_p} = \frac{0.139 \times 10^{-6}}{0.242 \times 10^{-6}} = 0.574\ s^{-1} \tag{3.12}$$

If it is assumed that plastic deformation does not occur during the elastic unloading/reloading stages, then it is estimated that it occurs in the last 0.242 μs, inducing a strain rate of around 0.6 s^{-1}. By contrast the elastic strain has an amplitude of around 300 microstrain and a strain rate of 38 s^{-1}.

Specimen parallel length	30 mm
Crosshead velocity	5 mm/min
Total extension	7 mm
Vibration frequency	20 kHz
Vibration displacement amplitude (uniform across horn tip surface)	0 to 10 μm
Elastic strain amplitude per cycle	300 microstrain
Crosshead displacement per cycle	4.17 nanometres
Plastic strain per cycle	0.139 microstrain

Table 3.1 - USTT key parameters

The amount of plastic strain and the time spent in plastic deformation in one cycle are dwarfed by the oscillatory elastic strain amplitude and duration. This is a loading case very different from all other mechanical tests, and it presents a

challenging set of circumstances for experimental mechanics techniques already established for other mechanical tests.

3.3 Review of experimental mechanics techniques

The first three problems of non-quasi-static loading and response inhomogeneity are shared with the field of high strain-rate and impact materials testing. A review of techniques used in this field [77] reveal some initially promising methods, showing that the high velocities and accelerations within ultrasonic tensile testing are not, in fact, excessive, compared to impact testing, where strain-rates can reach $10^8\ s^{-1}$.

To avoid the problem of inertia of the force measurement transducer altering or contributing to the response of the test structure, a non-contact method is desirable. Two different technologies – Finite Element Model Updating (FEMU) and the Virtual Fields Method (VFM) - have converged on the same basic technique, in which kinematic data is used to infer force. The strain fields are either inferred or calculated directly.

FEMU arose from the field of vibration measurement where the goal is to fully characterise a structure's dynamic response by creating an FE model and adjusting its mass and stiffness properties until its kinematic response matches that from experiment [78]. It has been used generally within the field of materials identification [79], and to characterise a high strain-rate load frame in order to correct for ringing in the specimen [80].

The alternative method is a form of photogrammetry, where a high-speed camera is used to capture images of a test as it progresses. Image registration software such as Digital Image Correlation (DIC) has developed to find displacement over the entirety of the field-of-view, permitting full-field strain mapping and calculation of the acceleration field. The latter is a significant advance. Researchers working on high-rate testing [81], [82] have combined the acceleration field across a deforming specimen with continuum mechanics principles to develop a method of calculating the stress anywhere within the specimen. This local stress field can be combined with the continuous strain field to perform identification, that is find the stress-strain relationship,

anywhere within the specimen. This has been developed to a high level with a method call the Virtual Fields Method (VFM) [83].

Applicability of VFM to the USTT

At first, the use of high-speed photogrammetry and VFM appears particularly attractive. However, this technique still requires a known force value on at least one of the boundaries of the acceleration field, as the technique only finds the change in stress over the field. An absolute force, required for material identification, requires a force measurement at one end of the specimen. In the two studies [81], [82] a piezoelectric force transducer was used. However, no attempt is made to account for the inertial effects within the force transducer itself. In the impact experiments, inertial effects would manifest as a ripple in the force measurement, as the transducer rings in an impulse response. As the studies report testing of polymers, it is possible the low mass and low elastic modulus (in other words, low impedance) in comparison to the force transducer means this ripple is insignificant.

In the testing methods mentioned so far, in the impact and high-strain rate testing, the loading is monotonic – that is, the imposed loading increases continuously throughout the test (although the actual loading on the specimen may vary, depending on the amplitude of ringing). The parameter of interest is the steady-state strain-rate response. The specimen is accelerated once to a steady strain rate, or in the case of impact tests, undergoes a single deformation event. It may be possible to claim that high frequency inertial effects within the transducer can be ignored if they are assumed to decay within a time which is short relative to the time span of the test. This assumption could not be applied to the ultrasonically excited material testing, where the oscillatory loading is continuous (for the duration of the excitation).

Previous ultrasonic excited materials characterisation with high-speed camera

Ultrasonic excitation has been used in combination with high-speed imaging and VFM, to reach a part of the strain-rate testing space which is too high for hydraulic test machines, but too low for Split Hopkinson Pressure Bars or other impact tests [84]. The specimen is mounted on the end of the ultrasonic horn. In

this fixed-free condition, the free end forms a perfectly defined boundary. There is no stress at the free end, which can be used as the single necessary boundary condition for finding the full stress field from the acceleration field.

This cannot be applied to the ultrasonic tensile test. The definition of acoustoplasticity is that an elastic vibration, with an amplitude which would not cause plasticity on its own, causes a drop in the flow stress of a quasi-static plastic deformation which is already occurring, maintained by a load source other than the vibration. There must be an external source of deformation such as the load frame, which implies a boundary force measurement by a measurement transducer will always be necessary.

The test in [84] happens all in one timescale. The plastic deformation within one cycle is a significant portion of the total cyclic strain. Identification of the elastic-plastic behaviour is carried out within one cycle. In contrast, the extremely short duration and small quantity of plastic deformation present in one cycle in an USST (Table 3.1) shows that performing a similar identification from one cycle is not practical. In the example in Table 3.1, the advance of the crosshead during one vibration cycle was 4.17 nm. This is minute, both in absolute terms and with respect to the amplitude of elastic displacement due to ultrasonic excitation, which was 10 μm. The DIC method cannot resolve displacements on the nanometer scale over a specimen tens of mm long, limiting these high-speed imaging techniques to measuring the elastic motion of the specimen. Even if this were not the case, the number of frames current high-speed cameras can capture is severely limited, commonly around 100 to 200 frames before requiring the images to be saved and the camera reset. To properly resolve the motion of a vibration at 20 kHz a frame rate of around 500,000 fps is necessary [84], [85]. At this frame rate such cameras will record around 200 μs. This is only adequate for capturing a few cycles. The high-speed camera-based technique will not cover an entire tensile test lasting a minute or more.

Whilst high-speed photogrammetry techniques still offer a useful alternative for determining the dynamic loading on the specimen, they cannot measure the plastic strain in the specimen either within one cycle, nor over the duration of

the USTT, and an additional method for assessing the full-field plastic deformation over the duration of the tensile test is required.

Application of the piezoelectric force transducer in the USTT

High-speed photogrammetry techniques can measure the dynamic loading without making contact with the specimen, over a small number of cycles. However, it is important to attempt to measure the combined quasi-static and oscillatory force, to calculate the true drop in flow stress $\Delta\sigma_{pk}$, preferably over a substantial portion of the period of ultrasonic excitation. For this purpose, the implementation of the piezoelectric force transducer in the USTT is still required, despite its shortcomings as a contact method. As already mentioned, whilst in previous studies [81], [82] the influence of ringing on force measurements could be treated as a transient problem, and corrected for accordingly. In the USTT the continuous application of ultrasonic excitation means the steady-state frequency response of the specimen and the force transducer must now be considered. Force transducers, as systems for converting a mechanical measurand into an electrical signal, have both a structural and electrical frequency response [86]. The force measurement will suffer from distortion when the force loading includes a high frequency oscillatory component, reducing its accuracy and potentially leading to erroneous conclusions being drawn about the nature of acoustoplasticity. This problem and ways to address it will be explored in Chapter 4.

Application of strain gauges in the USTT

The installation of strain gauges on the specimen offers a direct, local measurement, avoiding problems of impedance of joints and masses found in the remote measurement from force transducers. Disadvantages of being physically attached to the specimen are gauge de-bonding or fatigue failure in the wires and their soldered joints. This is a particular risk for ultrasonic excitations that create cyclic fatigue loading at high frequency. As a contact method with a physical sensor which deforms to produce a signal, the inertia of the gauge and its bonded joint will incur a frequency-dependent response, imposing an upper limit on the frequency the gauge can resolve accurately. The length of the gauge

also imposes a frequency limit. These issues are discussed further in Chapter 7, which studies the application of strain gauges to the ultrasonic tensile test.

Whilst photogrammetry techniques can struggle to resolve the small strains in the elastic portion of a stress-strain curve in a metal, strain gauges are ideally suited to this task. Strain gauges are however limited in the total strain they can measure – commonly up to around 5%. The plastic deformation during an USTT is around 20% and strain gauges are therefore limited to measuring the elastic motion of the specimen. Strain gauges will provide a continuous measurement of strain for as long as they are intact and connected to the data acquisition equipment. They would be capable of measuring strain for the duration of the USTT, fulfilling a role similar to the piezoelectric force transducer, if it were not for limits imposed by the fatigue life of the gauge and its wires, or the bond between gauge and specimen.

Given the limits on strain and fatigue life, strain gauges located on the test piece offer an opportunity to calibrate the dynamic response of a force transducer which is used simultaneously in a USTT with purely elastic, oscillatory, loading [87]. The force transducer, validated in this way, can then be used in a full plastic ultrasonic test. Such an experiment is demonstrated in Chapter 7.

3.4 Summary

It is evident that no one technique can provide a comprehensive picture of acoustoplasticity, let alone sufficient data for proper material characterisation and phenomenological modelling. Instead, all of these methods should be employed to gather sufficient data, and provide mutual confidence in the results.

In this work an investigation is conducted on the frequency response of the piezoelectric force transducer, the specimen and surrounding fixtures, estimating the fidelity of the force reading using a FE model adjusted with velocity measurements. This result is verified using strain gauges attached directly to the specimen. Further, the strain gauge-force transducer relationship

was used to generate a correction factor which was applied directly to the force measurement in ultrasonic tensile tests.

Finally, to address the issue of measuring the full-field plastic strain over the duration of a USTT, a system was developed which used a synchronised strobe to filter out the vibration motion, permitting a standard industrial camera to image the specimen at a comparably low frame rate, over the duration of the test.

4 Investigation of effects of oscillatory loading on the piezoelectric force transducer in a USTT

The piezoelectric force transducer remains a crucial part of a set-up capable of characterising an ultrasonically vibrating test piece, and hence identifying the stress-strain response indicative of acoustoplasticity. As a contact method where the sensor is physically embedded in the test structure, the device's measurement will be influenced by both the position of the sensor in the structure, and the sensor's electro-mechanical frequency response. The investigations within this chapter evaluate both of these influences.

4.1 Influence of sensor location within test structure on USTT

As has already been discussed, the loading along a USTT apparatus is not homogeneous. When excitation is applied a standing wave is set up within the structure from the ultrasonic transducer to the specimen and beyond. Standing waves have nodes where the displacement amplitude is zero and the strain and stress amplitudes are at a maximum. When employing a contact method to measure force, its location has a direct effect on the magnitude of the force measurement [16], [17]. Deliberately mounting the force sensor to a node, ensures that the force measured provides an upper limit of the stress within the specimen.

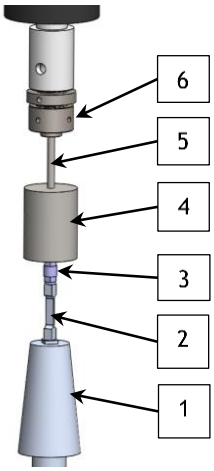

Figure 4.1 - Isolating mass in USTT stack

1. Horn
2. Specimen
3. Piezoelectric force transducer
4. Isolating mass
5. Isolating spring
6. Coupling into test machine load cell

To guarantee that the force transducer was mounted at a displacement node, a cylinder of stainless steel was introduced between it and the crosshead mounting (Figure 4.1 and Figure 4.2). The cylinder, herein called the isolating mass, had a mass much greater than the specimen (2 kg compared with 8 grams).

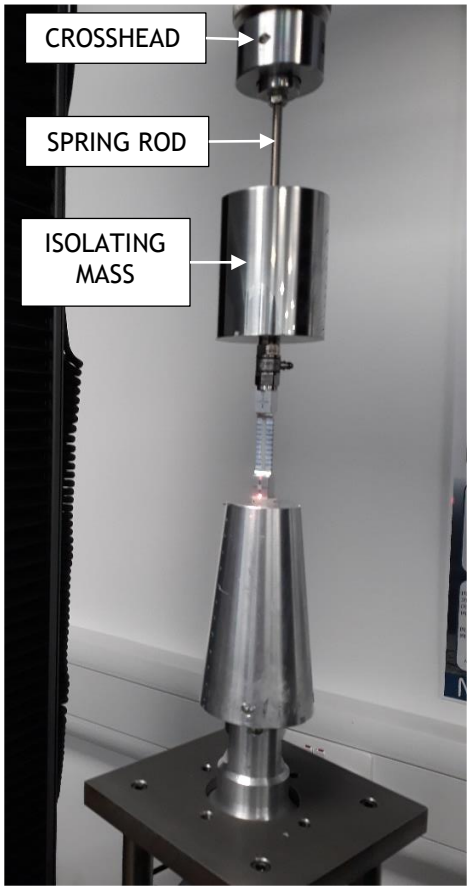

Figure 4.2 - Isolating mass within USTT stack

In their analysis of a mass-loaded bar, Kinsler and Frey [70] demonstrate that a block attached to the end of a vibrating bar will emulate a rigid boundary condition, providing the mass of the block is much greater than that of the bar.

They developed a relation between the mass of the terminal block and the location of stationary nodes within the vibrating bar, Figure 4.3.

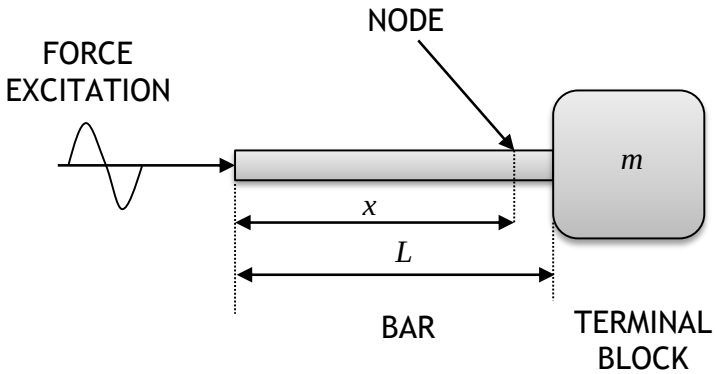

Figure 4.3 - Mass-loaded bar model

For a bar of length L attached to a terminal block of mass m, excited at frequency ω, equation (4.1) describes the location of the node in the bar as the vibration waveform approaches a half wavelength, and the node nears the terminal block:

$$\tan\big(k(L-x)\big) = \frac{\rho_L c}{\omega m} \tag{4.1}$$

Where k, ρ_L and c are, respectively, the stiffness of the bar, the density per unit length and speed of sound of the bar material. The variable x is the axial location of the node of the first longitudinal mode of vibration within the bar.

In equation (4.1), as the mass increases x tends to L, and the node moves towards the terminal block, until it is coincident. This suggests the highest mass possible should be used, however, there are practical limits on the mass which will be discussed shortly.

To identify an acceptable mass for the isolating mass for the USTT, equation (4.1) was rearranged to find x for a range of terminal block masses, Figure 4.4. The properties of the specimen were inserted for the bar dimensions and material properties.

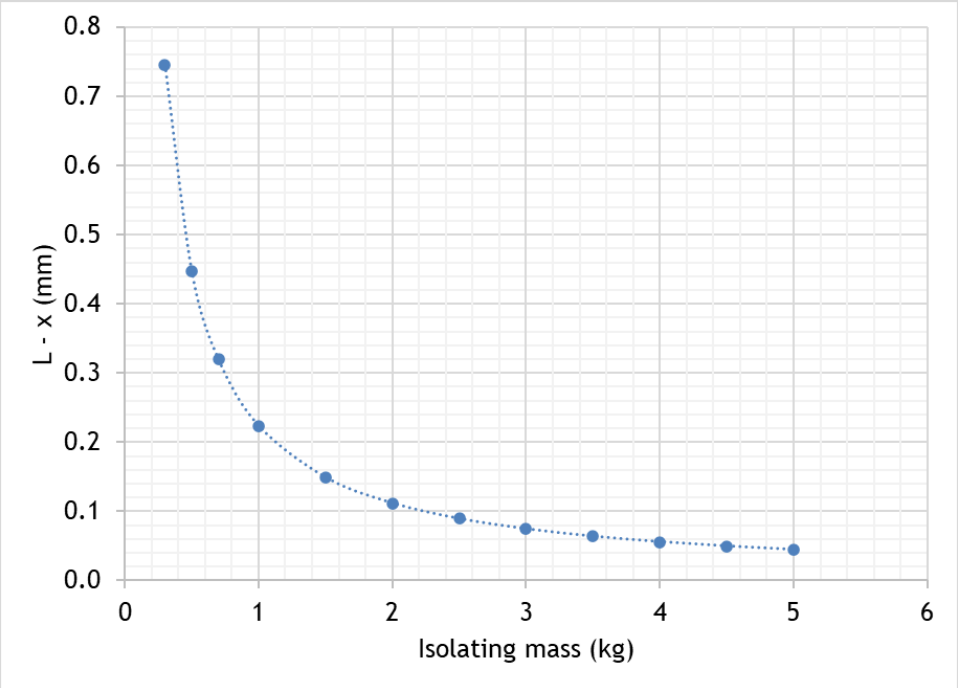

Figure 4.4 - Convergence of bar node on isolating mass

At a terminal block mass of 2 kg, the node is 0.11 mm from the end of the specimen. Above this mass, every additional kilogram moves the node at most 0.02 mm towards the block. Considering that 0.1 is already small compared to

the general dimensions of the specimen, 2 kg mass was selected as the best compromise between mass and convergence of the node on the specimen end.

In contrast to the arrangement outlined by Kinsler and Frey, in the ultrasonic tensile test the block must be further connected to the crosshead, so the load frame may continue to apply the quasi-static load. The isolating mass was connected to the crosshead by a long thin rod, arranged to act as a solid spring. To investigate and optimise the geometry of the rod, the proposed arrangement was modelled as a lumped-parameter system, the rod and the isolating mass components idealised respectively as a spring and point mass with one single degree-of-freedom (S-DOF), Figure 4.5.

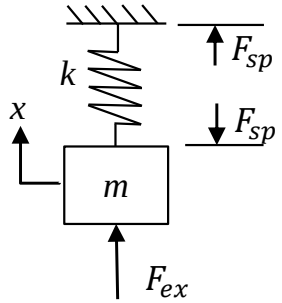

Figure 4.5 - S-DOF lumped-parameter model of isolating mass

The S-DOF system in Figure 4.5 is excited by a steady-state harmonic force with amplitude F_{ex} and frequency ω, resisted by the inertia of mass m and the spring force F_{sp}, and resulting in displacement amplitude X. The dimensionless amplitude is given by equation (4.2) [88]:

$$\frac{Xk}{F_{ex}} = \frac{1}{\sqrt{\left[1-\left(\frac{\omega}{\omega_n}\right)^2\right]^2 + \left[2\zeta\left(\frac{\omega}{\omega_n}\right)^2\right]^2}} \tag{4.2}$$

Where k is the spring stiffness and the natural frequency of the system is defined by equation (4.3):

$$\omega_n = \sqrt{\frac{k}{m}} \tag{4.3}$$

The term ζ is the damping ratio, which can be neglected if the system damping is light. As the spring rod was made of steel, a material in which damping is low, in the initial design study damping was ignored.

Let $X_{ex} = \frac{F_{ex}}{k}$, the displacement of m caused by the excitation force in the absence of resonance effects; then a parameter called the magnification factor, β, is defined as in equation (4.4) [89]:

$$\beta = \frac{X}{X_{ex}} = \frac{1}{\sqrt{\left[1 - \left(\frac{\omega}{\omega_n}\right)^2\right]^2}} \tag{4.4}$$

Taking only the positive part of the square root, the non-dimensional magnification factor varies with the frequency ratio $\frac{\omega}{\omega_n}$ as in Figure 4.6:

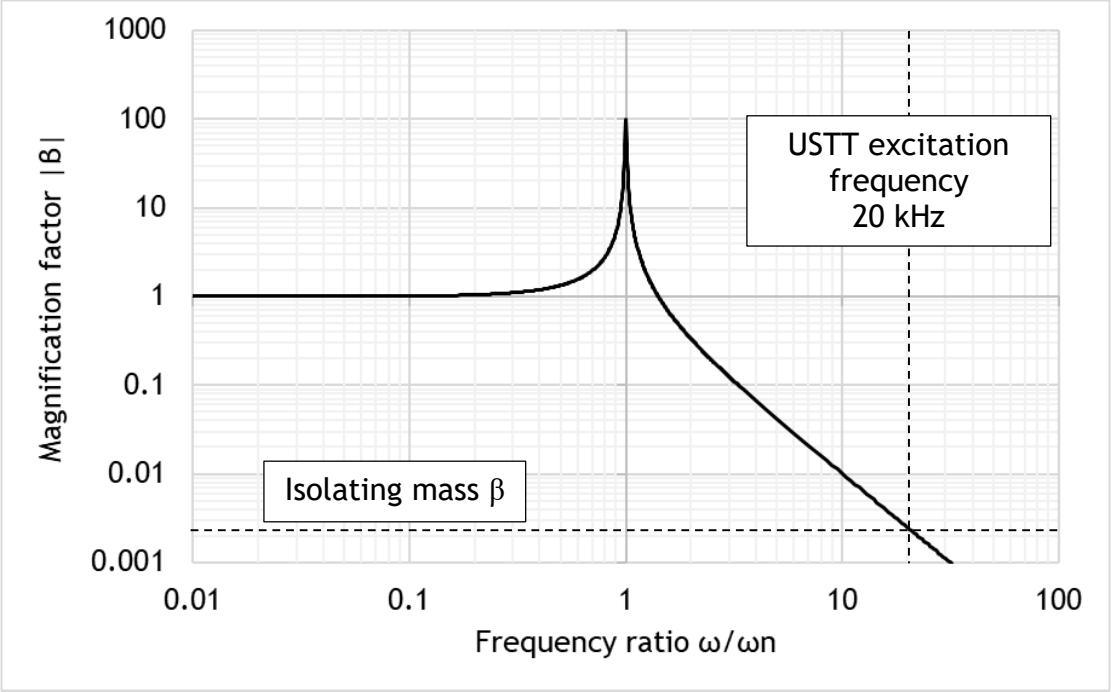

Figure 4.6 - Magnification factor

As the excitation frequency increases beyond the natural frequency of the S-DOF system, the response amplitude attenuates. This is a result of the excitation

force being increasingly diverted to accelerate the mass m, causing a reduction in the force available to compress spring k and a corresponding loss of displacement amplitude [88].

From equation (4.2) and Figure 4.6, the system natural frequency (equation (4.3)) must be minimised to achieve the highest attenuation of the oscillatory vibration amplitude. The stiffness k of the spring rod with diameter D and length L was found from equation (4.5):

$$k = \frac{\pi D^2 E}{4L} \tag{4.5}$$

Where E is the elastic modulus of the rod material, which was mild steel. With the mass of the isolating mass already determined, and the diameter of the spring rod set by the minimum strength required to support the USTT quasi-static load, the problem then reduced to finding the optimal rod length.

Equations (4.3) and (4.5) suggest minimising the natural frequency by maximising the rod length. However, the practicalities of construction and the physical limits of the USTT impose limits on the length of the system. In addition, the potential for lateral vibration is minimised by keeping the rod length a short as possible, whilst still achieving the goal of high attenuation of the vibration amplitude. A rod length of 60 mm was selected, with a predicted natural frequency of 1087 Hz, and, from equation (4.4), a magnification factor of 0.0025. This value is plotted on Figure 4.6, and indicates a high level of attenuation – any vibration reaching the isolating mass will be attenuated by a factor of 0.0025.

The models and equations developed here are suitable for design purposes. The efficacy of the isolating mass in creating a rigid boundary upon which to mount the PFT must be verified by experimental measurement. The real response of the isolating mass was assessed by measuring its vibration amplitude relative to the rest of the USTT structure, and this is treated in Chapter 5, Section 5.3.1.

A summary of the isolating mass system dimensions are presented in Table 4.1.

Isolating mass	
Material	stainless steel
Diameter	60 mm
Length	80 mm
Mass	2 kg
Spring rod	
Material	mild steel
Diameter	6 mm
Length	60 mm

Table 4.1 - Summary of isolating mass parameters

Whilst achieving the principal goal of imposing a rigid boundary on the test-machine mounted side of the force transducer, there are additional benefits to incorporating an isolating mass. Reflecting all the wave energy back into the vibrating test stack removes concerns about vibration energy leaking into the load frame – distorting the standing wave which is assumed to occur in the assembly between the ultrasonic transducer and the force transducer. Dynamically, it de-couples the tensile test stack from the load frame, preventing any response potentially excited in the load frame from influencing the vibration of the stack and the force measurement. This, in turn, limits the bounds of the structure which must be accounted for in a dynamic analysis. While non-infinite impedance can be realised within FE simulation, a rigid mounting is far easier to represent accurately as an encastré boundary condition. This is discussed further in Chapter 6 within the context of an FE model of the USTT.

4.2 Influence of frequency response of piezoelectric force transducer on the USTT

In general, when using any transducer to measure an oscillatory measurand, the dynamic response characteristics of the transducer and its signal conditioning, recording and display devices must be considered [86], [87], [90]. It is known that the structural response of a piezoelectric force transducer (PFT) to a steady-state vibration significantly influences the device's sensitivity. Sensitivity is a characteristic of all measurement instrumentation, defined as the ratio of the indicated value (the value read from the device) over the measurand (the

parameter intended to be measured). In the case of the force transducer, the measurand is the amplitude of the force applied to the ends of the transducer, while the indicated value is the amplitude of the transducer's electrical output [86], [87], illustrated in Figure 4.7.

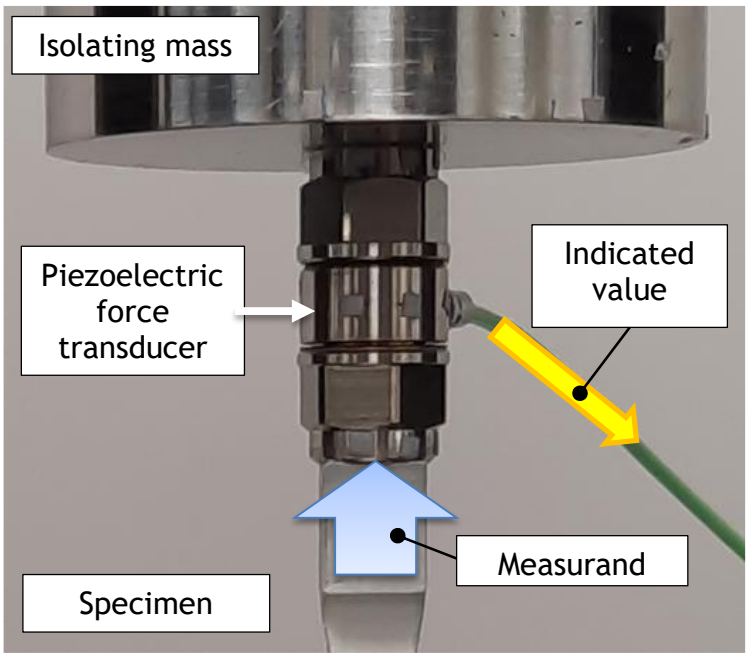

Figure 4.7 - force transducer measurand and indicated value

This electro-mechanical relationship is frequency dependant and is called the frequency response of a device. The frequency response can be severely non-linear, with the potential to either amplify or attenuate the measurand, depending on the proximity of the forcing frequency to the resonances and anti-resonances of the device embedded in the test structure [86], [91].

The upper limit of the bandwidth (-3 dB) of the charge amplifier used in these experiments (Kistler Charge Meter Type 5015) is 200 kHz, well in excess of that required to measure the 20 kHz excitation frequency with negligible error. The recording device (Picoscope 4424) has a bandwidth of 20 MHz, again, well in excess of that required to avoid amplitude error and aliasing. The frequency response of the electronic signal acquisition and recording system will therefore not be considered further.

4.3 Analysis of inertial effects by lumped-parameter model

To examine the characteristic frequency response of a force transducer and the effects of different mountings within a test structure the structure of the PFT has commonly been approximated by a lumped-parameter model [86], [90], [91].

In [91] two main types of PFT mounting arrangement were identified. In the first type, the desired measurement is the excitation force applied to a test structure. The PFT is located between the exciter structure and the test structure and the excitation force is applied through it. This is the classic arrangement for vibration testing with excitation applied by shaker via a long thin rod and a PFT.

In the second type, the desired measurement is the force between an excited test structure and its connection to a base mounting, which in [91] is termed the 'foundation'. This is the mounting type which applies to the USTT. An equivalent lumped-parameter model for the ultrasonic tensile test set-up used in this work is presented in Figure 4.8. In the models developed in [91] damping was neglected. This assumption was adopted, as the majority of the material used in PFT construction are metals, which in general have low damping factors.

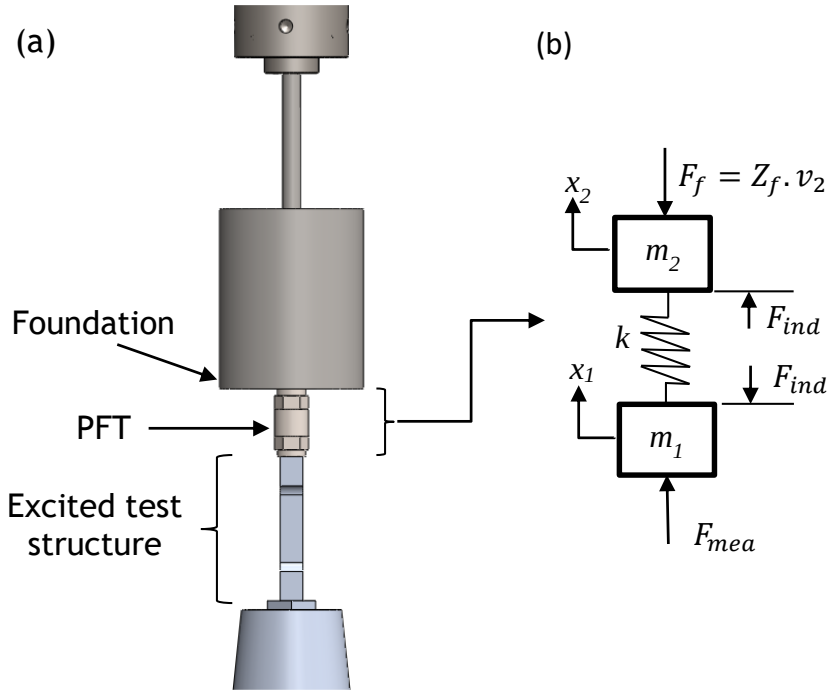

Figure 4.8 – Lumped-parameter model of piezoelectric force transducer

The construction and operation of a piezoelectric force transducer is key to understanding their frequency response. The sensing element is commonly a stack of ring-shaped piezoelectric crystals in the centre, which are encased and sandwiched between two end caps (m_1 and m_2 in Figure 4.8) [18]. The end caps are much larger and heavier than the piezo rings. When a force is applied across the end caps the rings are squeezed, and the piezo rings develop a charge in proportion to the resulting strain. As the relatively small mass of the rings can be neglected, they are represented by a spring k.

Under a static force, the measurand force F_{mea} and the indicated force F_{ind} are equal. An oscillatory measurand force, however, must accelerate the first end mass m_1 in order to affect the spring k. The movement of the second mass m_2 will also affect the compression of the piezo rings. This will depend on the reaction force F_f supplied by the foundation, which is the product of the foundation impedance Z_f and the velocity v_2 of mass m_2.

From this model it becomes clear that the vibration impedance of both the structure of the force transducer, and the foundation it is mounted on, affect the sensitivity frequency response F_{ind} / F_{mea}. The reaction force foundation impedance, Z_f, must include the stiffness of the threaded connection between the transducer end cap and, in the case of the ultrasonic tensile test, the isolating mass.

To explore frequency response analytically, initially the assumption was made that the foundation and the threaded connections were perfectly rigid (that is, the foundation impedance was infinite) and the system reduces to a single degree-of-freedom (DOF) comprising m_1 and k. The relationship F_{ind} / F_{mea}, known as *force transmissibility*, β_t, has been shown to reduce to equation (4.6) below if damping can be neglected [89], a reasonable assumption for the metal and ceramic components of the PFT.

$$\beta_t = \frac{F_{ind}}{F_{mea}} = \frac{1}{1 - \left(\frac{\omega}{\omega_n}\right)^2} \tag{4.6}$$

Where $\frac{\omega}{\omega_n}$ is the frequency ratio of the excitation frequency over the system natural frequency. Force transmissibility as defined by equation (4.6) is identical to the magnification factor defined by equation (4.4) and, when plotted in Figure 4.9 below, produces an identical curve to Figure 4.6. It is presented here in any case for clarity and to aid discussion.

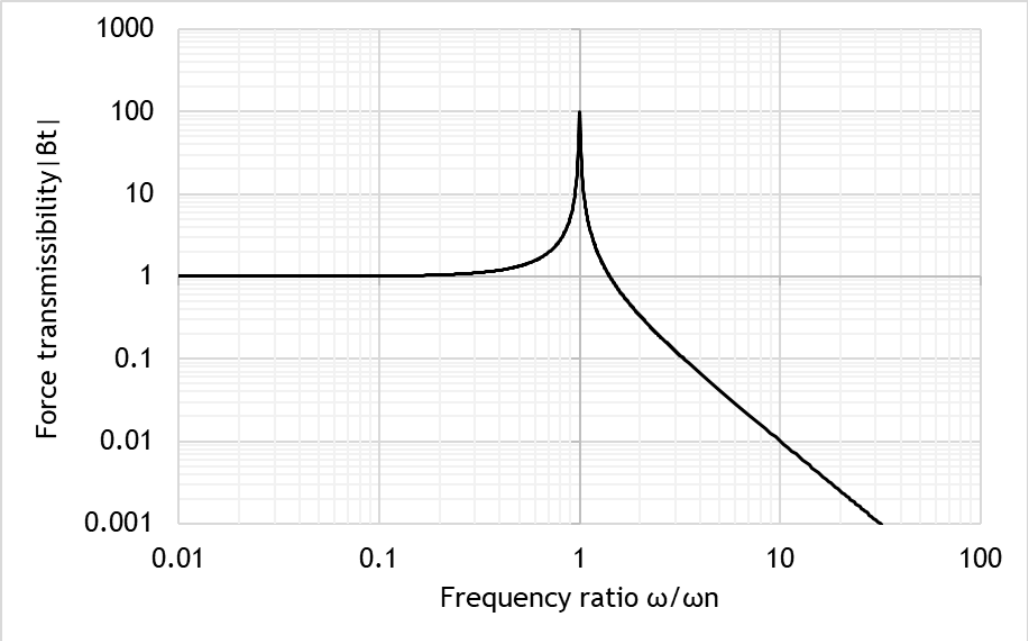

Figure 4.9 - Force transmissibility within force transducer structure

In Figure 4.9, as the forcing frequency of a steady state vibration approaches the natural frequency of the S-DOF system, the measurand force is *amplified* by the structural response. Beyond the natural frequency, the measurand is eventually *attenuated*.

In identical fashion to the phenomenon behind the functioning of the isolating mass, at frequencies much higher than the natural frequency, a portion of the measurand force is required to accelerate the mass m_1, reducing the force available to compress the piezo rings to generate the indicated force signal. This is the cause of the attenuation; where the force transmissibility is greater than 1, the force signal is amplified, due to the resonance of the PFT adding to the measurand to compress the piezo rings.

Notice that equation (4.6) enables a correction factor to be estimated, if the mounted resonance frequency is known.

4.4 Experimental assessment of PFT frequency response

4.4.1 Existing frequency response characterisation methods

In electrical circuit testing the frequency response is commonly found by recording the output signal from an oscillatory excitation input. Due to the electro-mechanical nature of force transducers, this approach cannot be applied to the transducer *in-situ*, even though it is known that the action of mounting a force transducer in a test structure will alter its sensitivity under dynamic loading. If, for example, the ultrasonic transducer were used to excite the USTT over a range of frequencies, the electrical signal emitted by the PFT would contain the structural response of all the components within the USTT, including the PFT itself. In this case, the influence of non-linear sensitivity in the PFT will be indistinguishable from the resonance behaviour of the rest of the structure with no way to definitively isolate individual contributions.

In the literature, several different experimental techniques have emerged to address this, but in general they follow the same approach, which is to characterise the dynamic response of the PFT in isolation to generate a model of its individual behaviour. This model can then be combined into a model of the whole test structure to predict the mounted response and impact on sensitivity. Two variants of this methodology were reviewed, the first based on the lumped-parameter model discussed previously, the second using FE modelling.

Characterisation efforts have previously focused on isolating the frequency dependent sensitivity of the force transducer by testing on very simple experimental set-ups from which it is easy to determine the force input spectrum. To examine the frequency dependence of sensitivity to steady-state vibration it is common practice to mount the force transducer on an electrodynamic shaker, and attach a load-mass atop the device [86], [90]. The shaker is excited over a frequency range within which the shaker supplies a constant acceleration. Any deviation from linear sensitivity must be due to the

frequency response of the force transducer. Pulse and step forces have also been used, to characterise the transient response of PFTs, for example [92].

These methods standardise the characterisation process, and allow comparison between devices. However, the deliberately simple apparatus employed, and the way the transducer is mounted, clearly differ from the ultrasonic tensile test, where both ends of the transducer are fixed rigidly to the test structure. Therefore, mounted resonance frequency values from shaker tests cannot be used directly. Applying a process of identification to the empirical sensitivity curve can yield the lumped model parameters of mass, stiffness and damping. These in turn can be used in the analytical lumped-parameter models described previously to estimate the mounted response of the force transducer within the test fixture [86].

In attempts to replicate similar tests for the PFT used in the USTT, it was found that the shaker method described above could not accommodate the very high frequency range required to examine the frequency range of interest, up to 70 kHz to include the nominal mounted resonance of the PFT. Shakers have their own non-linear response to excitation. The upper end of the usable range of a shaker is limited by its resonance frequency when the armature is loaded, typically 2 to 3 kHz for transducers of a similar mass to the one used here [86].

Here, a method was developed based around constructing an FE model of the force transducer alone which could be calibrated using the resonance frequency of the device's first longitudinal (L1) mode when in the free-free boundary condition (that is, unconstrained), before incorporating it into an FE model of the whole test structure [18]. In a fashion similar to finding the transmitted force F_{ind} in the lumped-parameter model, a prediction of the indicated value of force could then be found by interrogating the FE model at the midplane of the FE force transducer, the location of the piezo-crystal.

For the device used in these experiments (Kistler 9311B) the manufacturer provides a value for the free-free L1 mode of 70 kHz. As this was offered as a nominal value for the transducer product type, a simple experiment was performed to check the response of the PFT used in this work.

In the first longitudinal mode of a cylinder in the free-free condition, the greatest movement occurs at the ends. A nodal plane lies midway between them, at the centre of the cylinder [ref Graff]. As the PFT cable connects at the mid-plane, an approximation to the free-free condition can be achieved by suspending the PFT by its cable [86]. By applying a short force impulse to one end of the transducer the L1 mode is excited, and the natural frequency can be obtained from the transient response observed.

4.4.2 Natural frequency of the piezoelectric force transducer in free-free boundary conditions

The piezoelectric force transducer was suspended by its cable and tapped at one end with a plain metal bar. To deliver excitation energy to frequencies in the tens of kilohertz range the impulse must be as short as possible, which is achieved by applying the impulse with an impact tool made of a stiff material [78]. In this study the bar was made of steel. Applying the impulse at one end preferentially excited the desired L1 mode. The electrical output from the PFT was directed to an oscilloscope which converted the time domain signal to the frequency domain using a Fast Fourier Transform (FFT) tool, (Figure 4.10).

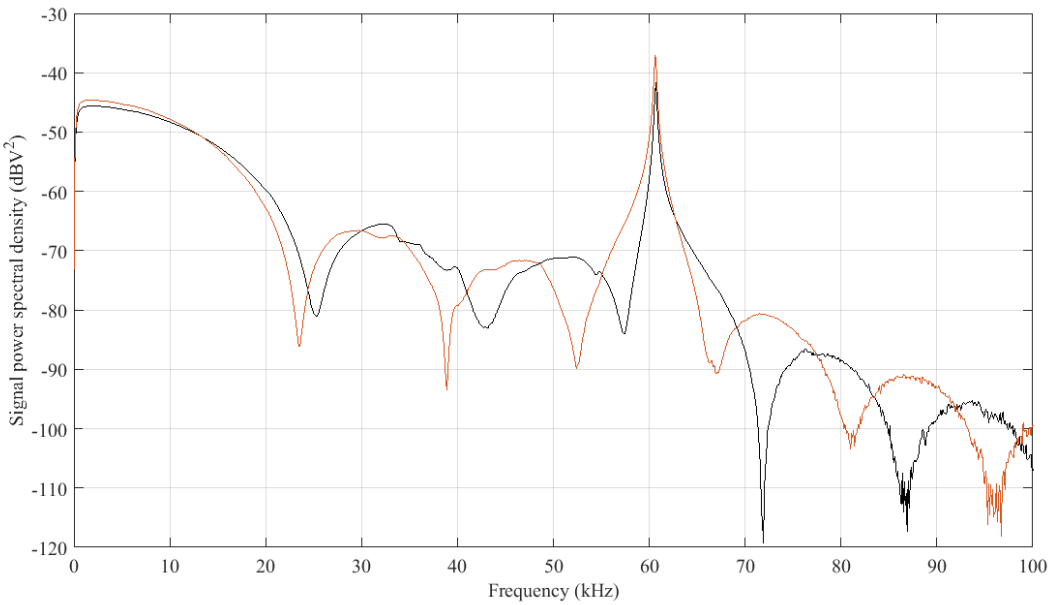

Figure 4.10 - Impulse test of force transducer in free-free condition

The test was repeated a number of times and, despite shifts in the rest of the curve, a large peak was observed consistently at 60.7 kHz. It is expected that

this corresponds to the L1 mode of the broadly cylindrical transducer structure, which is the mode which most affects the piezo rings within the PFT. The experimentally measured L1 resonance frequency is 13% lower than the value stated by the manufacturer. The general downward trend as frequency increases indicates that the impulse technique struggled to supply energy to the higher frequencies. In addition, it is thought the sharp dips in the curve are the consequence of the dynamic response of the bar used to apply the impulse. In general, in vibration characterisation experiments which use impulse excitation the impulse is delivered with a device called an impact hammer. Impact hammers are designed to have a characteristic response which is linear in the frequency range of interest, to avoid distorting the response measurement. However, the normal frequency limit of impact hammers currently available lies in the 10 – 20 kHz range, and therefore there is no advantage in their use in this experiment.

Despite these flaws, the influence of the characteristics of the impact tool has not obscured the L1 mode natural frequency, which is all that is required in the present study to characterise the PFT FE model.

4.4.3 FE approximation of the piezoelectric force transducer

The approach recommended by the manufacturer (Kistler) was followed, in which a solid shape with no internal structure is adjusted until its modal properties match those measured experimentally [18].

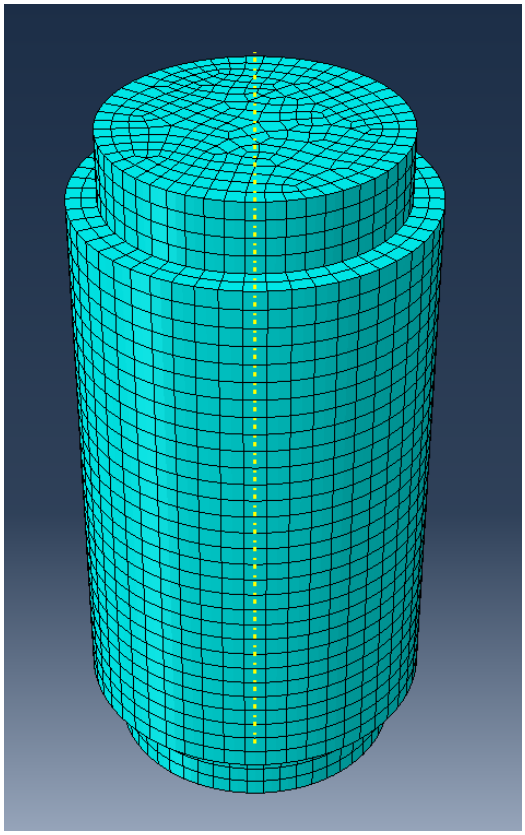

Figure 4.11 – FE mesh of proxy piezoelectric force transducer

An FE model was developed in which the transducer was represented by a solid body of similar, simplified outer geometry. This body was provided with a material model with homogeneous and isotropic properties. First the density of the material was adjusted until the total mass matched the real value of 28 grams. Next, the mode shapes and frequencies of the model were evaluated using an eigen procedure in FE software, which is described more fully in Chapter 6. Then the elastic modulus of the material was varied until the frequency of the first longitudinal mode matched that of the real transducer, determined in the impulse experiment. The resulting FE model parameters are presented in Table 4.2.

PFT FE-model specifications	
Radius	12.5 mm 15.0 mm
Length	30 mm
Stainless steel density	5622 kg/m^3
Poisson's ratio	0.29
Tuned modulus	68 GPa
Final natural frequency	60085 kHz

Table 4.2 - Final parameters of force transducer FE model

This model was subsequently incorporated into the FE analysis of the whole USTT assembly, which is described in Chapter 6. It will be seen that this tuned FE model contributed to accuracy of the USTT vibration response prediction, enabling estimation of the indicated force from FEA.

4.5 Analytical estimation of mounted resonant frequency and amplification factor

Two models were developed to estimate analytically the resonant frequency of the mounted transducer. The first was based on the lumped-parameter model developed earlier, and the second approximating the PFT as a homogenous solid rod.

From the literature on the mounted and free response of accelerometers, it is known that the relationship between free natural frequency and mounted resonance frequency of the lumped-parameter model in Figure 4.8 is defined approximately by equation (4.7) [93]:

$$\omega_{mr} = \frac{1}{\sqrt{2}}\omega_n \tag{4.7}$$

Where ω_{mr} is the mounted resonant frequency and ω_n the resonant frequency of the first longitudinal mode of the instrument freely suspended (with no connection at each end). As the latter is 60.7 kHz from the impulse experiment, the estimated mounted resonance frequency is then 42.9 kHz (3sf). Earlier, equation (4.6) was used to predict the frequency response effect on the amplitude of the force transmitted through the PFT end-mass, depending on the proximity of the excitation frequency to the natural frequency. Using the estimated mounted resonance and the excitation frequency of 20 kHz used in this study, equation (4.6) predicts the measurand will be amplified by a factor of 1.28 (3sf).

4.5.1 Approximation as a rod in free-free and fixed-free conditions

The lumped-parameter models of Figure 4.8 approximate the distribution of mass as point masses at each DOF. The structure of the PFT is distributed, if not continuous and homogeneous. To complement the lumped-parameter model, a continuous solid rod model was developed using standard equations for longitudinal vibration in a solid rod. Changing the boundary conditions on the rod from free-free to fixed at one end, Figure 4.12, demonstrates in principle the consequence of connecting a structure like the PFT to a much more rigid body such as the isolating mass.

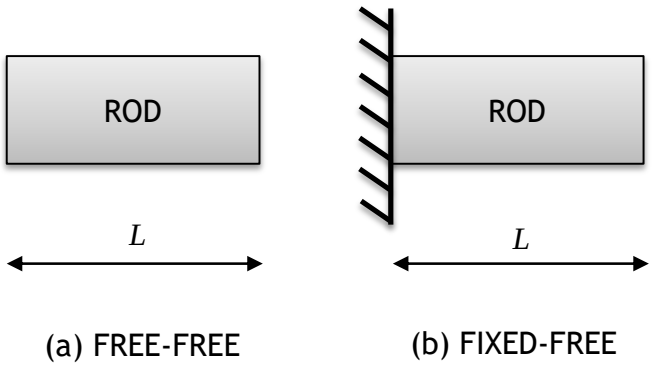

Figure 4.12 - Rod in the free-free and fixed-free boundary conditions

As the piezo rings are located at the centre of the PFT, the equations for the first longitudinal mode (L1 mode) of a sold prismatic rod were used, as they have a stress node at the rod's midplane.

Equation (4.8) defines the natural frequency of the L1 mode, ω_{L1}, of a prismatic rod of length L in the free-free condition is [94]:

$$\omega_{L1} = \frac{\pi . c}{L} \tag{4.8}$$

Where c is the speed of sound in the rod material. The corresponding equation for the same rod with a fixed boundary at one end is then equation (4.9):

$$\omega_{L1} = \frac{\pi . c}{2L} \tag{4.9}$$

Comparing equations (4.8) and (4.9) it is seen that when a rod's boundary conditions are changed from free-free to fixed-free the natural frequency of the rod's L1 mode will reduce by half. Once again, using the measured free-free resonance frequency of 60.7 kHz, the mounted resonance frequency estimated by this model is 30.25 kHz. The force transmissibility, equation (4.6), (or indeed the magnification factor, equation (4.4)) for an excitation frequency of 20 kHz on a system with this resonance frequency is found to be an amplification of 1.77 (3sf). The results are summarised in Table 4.3.

Prediction method	Mounted resonance (kHz)	Magnification factor (or force transmissibility) for PFT
Lumped model	42.9	1.28
Homogeneous rod	30.25	1.77

Table 4.3 - Magnification factors estimated by analytical models

These models are limited by their simplicity. The PFT is neither a solid homogeneous mass, nor is all the mass concentrated at each end with the centre portion only contributing stiffness. The difference between the two values suggest they are not suitable as an accurate correction factor for experimental data. However, they are robust first-order approximations which can be used to perform a sense-check on the magnification factor found from the FE model developed later in this thesis.

4.6 Implications of PFT frequency response on APE investigations

The ability of the transducer's structure to amplify or attenuate the measurand, demonstrated above through analytical model and experiment, has profound implications for the force measurements made in the body of research on acoustoplasticity. The effect applies equally to piezoelectric force transducers and strain-gauge based load cells. The effect does not necessarily make such devices unusable at the ultrasonic frequencies demanded by USTT, if the effect can be accounted for and the force data corrected [90], [91].

It is worth noting that load cells, which are used in the great majority of APE research, are a good example of the attenuating effect the device structure can have on the measurand. By virtue of their design, they are much more compliant than piezoelectric devices, with the result that their resonant frequency is much lower, often of the order of hundreds of hertz. The force transmissibility curve in Figure 4.9 shows that when such devices are used in ultrasonic tests the operating frequency will be far higher than the resonant frequency of the transducer, and the periodic part of the signal will be heavily attenuated, producing the mean value reading seen in the majority of papers on acoustoplasticity. This explains why most researchers could not resolve the oscillatory force, only reporting the mean.

4.7 Summary

This chapter studied the influence of the structural frequency response of the PFT and its location within the USTT on the accuracy of the force measurement made with it.

To ensure the PFT was mounted at a nodal point, and therefore measured the maximum force amplitude, an isolating mass was developed. This assembly provided a virtually rigid boundary on which to mount the PFT, and decoupled the PFT from the structural response of the test machine.

The influence of the structure of the piezoelectric force transducer on the device's frequency response was discussed and modelled as a lumped-parameter system. The property 'magnification factor' was introduced and plotted against frequency, revealing that the mass and stiffness characteristics of the PFT could lead to non-linear sensitivity, distorting the indicated force value by amplifying or attenuating the measurand. Proximity of the excitation frequency to the characteristic natural frequency of the S-DOF system determined whether the measurand was amplified or attenuated.

A critical conclusion is that, if not accounted for, using an unmodified indicated force measurement could lead to erroneous conclusions about flow stress reduction.

An impulse method was used to characterise the frequency response of the PFT experimentally, focusing on determining the natural frequency of the L1 mode of the transducer in the free-free condition. This result was used to tune an FE model of the PFT, developed for later incorporation into an FE model of the USTT, to provide a numerical simulation of the difference between the force measurand and the force indicated value.

To explore the effect of connecting the PFT to another structure on the resonance frequency of its L1 mode, an analytical model based on a solid rod was developed. It was found that the natural frequency of the L1 mode in the fixed-free boundary condition is half that of a rod in the free-free BC. The same analysis with the lumped-parameter models determined that the fixed-free

natural frequency is $\frac{1}{\sqrt{2}}$ of the free-free natural frequency. Estimates of the magnification factor were found for the lumped-parameter model and solid rod model. The salient point is that the natural frequency of the L1 mode, the mode shape most able to distort the PFT sensitivity, is significantly affected when it is connected to a wider test structure.

Finally, the implications of the influence of frequency response and the potential for distortion of the force measurand to produce misleading results and erroneous conclusions about flow stress reduction, was discussed with respect to studies in the literature.

5 Force investigation with EMA-calibrated FEA

5.1 Introduction

The very specific nature of the ultrasonic tensile test, incorporating an oscillatory loading at an ultrasonic frequency with a quasi-static load, limits the experimental mechanics techniques which can be used to characterise material response, and restricts these techniques to evaluating only one loading regime. Despite its shortcomings, it was found in Chapter 3 that the piezoelectric force transducer (PFT) remains the key transducer for measuring the loading on the specimen in an ultrasonic tensile test.

However, it was established in Chapter 4 on the frequency response of the PFT that its accuracy is seriously affected by the consequences of its own structural *impedance* in response to a high-frequency oscillatory load. The literature [91] suggested the impedance of the structures of the specimen, force sensor and fixtures, and the impedance of the interfaces between them, play a crucial role in *amplifying* or *attenuating* the *amplitude* of the oscillatory force signal, with the indicated value suffering either a positive or negative error over the measurand. The quasi-static force signal remains unaltered. The model and experimental studies support this view, at least within the scope of the structure of the force transducer modelled and tested.

In that study the focus was on the PFT, specifically looking at the response of the transducer, with limited information arising about the sensor's mounted response. There remains the task of verifying the force transducer measurement within the context of the ultrasonic tensile test, evaluating the effect of mounting the force transducer within the test fixtures. Beyond the purpose of verification of the PFT, developing another route to measuring the load on the specimen which is independent of the single-point, contact method of the PFT brings the benefit of a second direct measurement, useful in its own right.

The review of experimental mechanics techniques in Chapter 3 revealed that kinematic measurements (made using an ultra-high-speed camera or a laser doppler vibrometer (LDV)) could provide an evaluation of force, when combined with numerical methods.

In the literature on acoustoplasticity, no attempt has been made to characterise experimentally the structural response of the specimen within the ultrasonic-tensile test apparatus. There is an opportunity to examine this in detail in the context of the set-up developed here.

This chapter will investigate the use of a method which uses experimental vibration measurement to calibrate a numerical structural model, for measuring the dynamic steady-state oscillatory loading on the specimen-force transducer-fixture structure during the USTT. The aims are to provide an assessment of the fidelity of the piezoelectric force transducer, as well as address the need to characterise the stress throughout the specimen itself. The LDV method offers the additional benefits of providing a measurement of the impedance of the structure, throughout the tensile test stack, and enables characterisation of the fundamental response of the apparatus.

5.2 Investigation of USTT structure by Experimental Modal Analysis

In this experiment, experimental modal analysis (EMA) was used to determine the frequency and waveform of the first longitudinal (L1) mode occurring in the USTT stack (the mode excited by the 20 kHz operating frequency). An FE model of this assembly was developed and used in a numerical modal analysis, producing a simulated counterpart to the experimental L1 mode shape. By comparing the numerical and experimental waveforms the FE model was adjusted.

5.2.1 Fundamental modes of vibration and EMA

It is known that the dynamic response of a structure to an external force is determined by that structure's fundamental modal characteristics. All structures exhibit intrinsic preferred responses – called modes of vibration – which are a fundamental characteristic of the structure, independent of the level or kind of excitation. The vibration response of a real structure to an excitation can be viewed as the linear sum of each of the fundamental modes, each mode contributing in proportion to the extent to which it is excited at the forcing frequency. Experimental modal analysis (EMA) is a procedure in which measurements of the excitation force on a structure and the resulting vibration

response are used to identify that structure's mode shapes and their associated modal frequency and damping values [78].

In general, the vibration dynamics of a structure can be assessed in two ways: first, by measuring only the kinematic response levels, and second by simultaneously recording the excitation force and response. The former is known as *operational testing*; while useful, gathering the excitation input and response output enables *modal testing*. This method further identifies the underlying structural dynamic characteristics, and in particular, provides an estimate of modal damping, a parameter which is important to the accuracy of the prediction of the steady-state response in FE simulation. This is an approach commonly taken in ultrasonic device development, where EMA in combination with FEA is used to assess the vibration response, identify the real modal characteristics and validate the corresponding numerical simulation, thereby confirming real and predicted device performance. In this study, this methodology was adapted to the purposes of investigating the USTT test apparatus and generating an accurate FE model.

5.2.2 Experimental Modal Analysis

If the intrinsic characteristic structure is viewed as a system which is subject to inputs and produce outputs, then

RESPONSE = [SYSTEM] x EXCITATION

EMA uses the property that the modal frequencies, modal damping and mode shapes can be identified from the structure's experimentally measured system transfer function. By assuming a linear relationship between the input and output, then the formal definition of the structure's transfer function in the frequency domain is the ratio of the Laplace transforms of the output over the input, equation (5.1).

$$H(\omega) = \frac{\mathcal{L}(output)}{\mathcal{L}(input)} \tag{5.1}$$

5.2.3 Vibration measurement and FRFs

A variety of instruments are available for measuring vibration levels, converting the kinematic parameters of displacement, velocity and acceleration into a voltage signal. The accelerometer (measuring acceleration) is the most common device in use, while in ultrasonics the laser doppler vibrometer (velocity) dominates due to its ability to resolve the minute displacements involved. Excitation force is measured most often, by piezoelectric force transducer.

Examining the ratio of the input and output signals in the frequency domain reveals the system response over a frequency range, (5.2):

$$FRF(\omega) = \frac{FT(output)}{FT(input)} \tag{5.2}$$

The ratio of the three kinematic parameters over the excitation force in the frequency domain results in three frequency response functions (FRFs), Table 5.1:

FRF name	Parameter ratio	Laplace ratio
Compliance (receptance)	$\frac{Displacement}{Force}$	$\frac{\mathcal{L}(X)}{\mathcal{L}(F)}$
Mobility	$\frac{Velocity}{Force}$	$\frac{\mathcal{L}(V)}{\mathcal{L}(F)}$
Accelerance	$\frac{Acceleration}{Force}$	$\frac{\mathcal{L}(A)}{\mathcal{L}(F)}$

Table 5.1 - Available FRF definitions

As the laser doppler is used in ultrasonic vibration testing and LDVs measure velocity, mobility is the FRF used in characterising ultrasonically excited structures.

An FRF is a complex quantity, expressing the magnitude gain and phase difference between the excitation and the response signals. The FRF can be plotted as a pair of graphs of magnitude and phase (Bode diagram), or real and imaginary parts. Figure 5.1 shows a typical magnitude curve for a mobility FRF measurement.

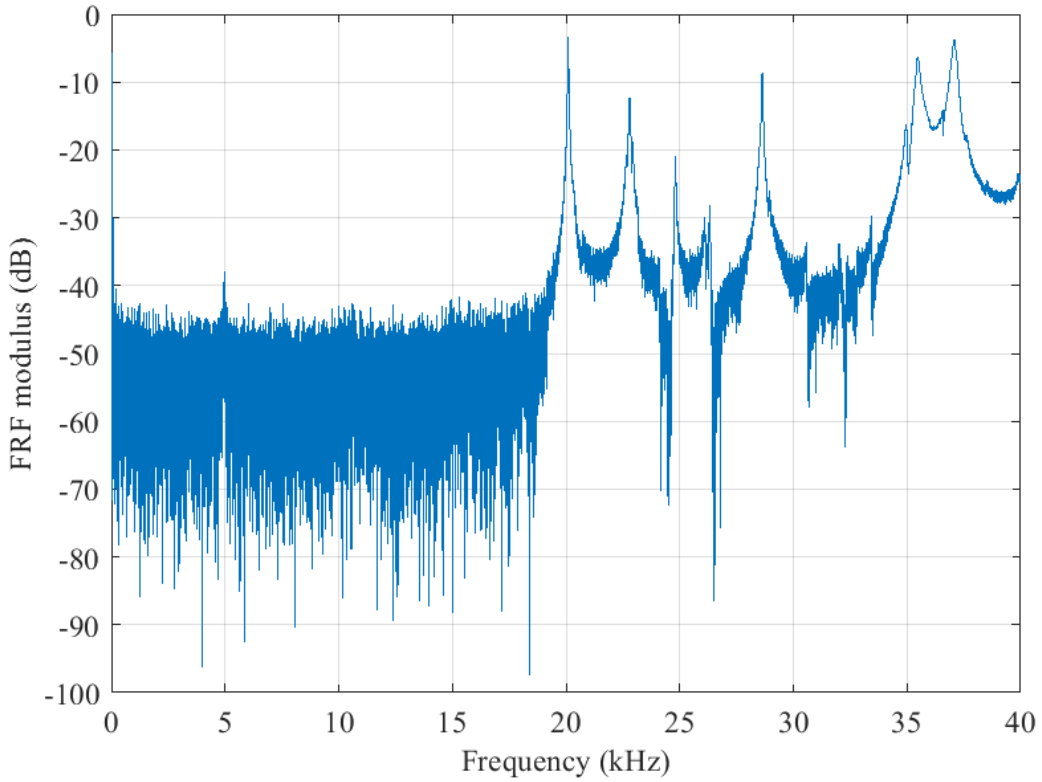

Figure 5.1 – Typical mobility FRF

The effect of the natural frequencies of the system on this particular measurement point are evident in the peaks in the curve, which indicate resonance.

5.2.4 Point and transfer FRFs - FRFs on a continuous structure

The nature of the vibration instrument devices means that measurements are collected at discrete points on the structure. Excitation is also applied, and measured, at discrete points. Different combinations of excitation and response points exist. The method used in this study uses single-point excitation, where the excitation remains stationary, and the device recording the response roves across the structure. Where the force and response measurement points coincide, the measurement is called a *driving point FRF*; otherwise, it is a *transfer FRF*.

Continuous structures can be represented in lumped-parameter approximation as a series of interconnected masses, springs and damping elements. Each mass is one single degree-of-freedom S-DOF, and the continuous structure becomes an

assembly of N degrees-of-freedom, or an N-DOF system. Assuming the system is linear, the general equation of motion for this N-DOF system is, equation (5.3):

$$[M]\{\ddot{X}\} + [M]\{\dot{X}\} + [M]\{X\} = \{F\} \tag{5.3}$$

Pursuing the analytical derivation of the FRF results in the following equation for the frequency response of each DOF in the N-DOF system, equation (5.4):

$$H_{ij}(\omega) = \sum_{r=1}^{N} \frac{\Phi_{ir}\Phi_{jr}/m_r}{{\omega_r}^2 - \omega^2 + 2i\zeta_r\omega_r\omega} \tag{5.4}$$

Where $H_{ij}(\omega)$ is the complex frequency response of the whole structure; ω is the frequency variable; ω_r, ζ_r and m_r are natural frequency, damping ratio and modal mass for the r^{th} mode. Lastly, Φ_{ir} and Φ_{jr} are the modal participation factors for the i^{th} and j^{th} DOFs.

In EMA, the experimental equivalent of $H_{ij}(\omega)$ is the FRF captured at each measurement point on the structure, where each point becomes one DOF in the N-DOF lumped-parameter model. The analytical expression (5.4) can be used to identify the modal parameters for each DOF by a process of fitting to each peak within the DOF's experimental FRF. The frequency of the peak reveals the natural frequency; damping can be found from the full-width half-maximum method [78]; and finally the height of the peak determines the value of the mode shape at point i, Φ_i. Once the mode shape contributions for a particular modal frequency are extracted from each DOF, when plotted they form the mode shape.

5.2.5 Excitation

In forced response testing, the vibration energy required to elicit a response from the test structure can be introduced using a number of methods or devices, the most common examples being the electro-dynamic shaker and the impulse hammer. The former converts an electrical signal into mechanical force via an electromagnet, much like a speaker. The electrical excitation signal can take a variety of forms, including sinusoidal, transient, periodic and random noise. Each combination has benefits for particular test types and structures, with

implications for how the data is processed into the FRFs required for modal analysis.

Following the precedent set in ultrasonic device characterisation, the ultrasonic transducer itself was used as the exciter [95], acting in a similar manner to the shaker by converting electrical energy to mechanical. This approach immediately restricts the test to the ‘single-point excitation’ type.

Modal testing typically uses sinusoidal or random excitation, and while both will produce an equivalent FRF, the former incurs a time penalty when ensuring each frequency sampled has reached steady-state and the previous excitation frequency has decayed sufficiently. By exciting all the modes at once random noise excitation shortens the test time substantially. This is useful when many data points must be acquired all over a structure.

In this test the signal generator integrated within the signal analyser (Quattro, Data Physics Corp.) provided a random noise signal of up to 1 V, over the frequency range 0 to 40 kHz to comfortably enclose the longitudinal resonance expected at 20 kHz. The excitation signal was passed through a power amplifier (QSC Professional Amplifier, RMX 4050a) set to a gain of 22 dB, to obtain an adequate signal to noise ratio from the LDV response signal.

5.2.6 Boundary conditions – test structure support

How the test structure is supported influences the structural response behaviour, and choice of mounting method and location can have a profound effect on the correct identification of modes. There are two classes of support. In the free condition, theoretically, the structure is free in all DOFs, and in reality, is very lightly mounted or suspended. In the grounded condition, the structure is connected at one or more points to the wider environment. As the USTT stack operates within the structure of the test machine, it is the mounted (grounded) response that is of interest, and so vibration characterisation was carried out with the USTT stack in-situ. It is connected to the test machine in two places, at the booster at the bottom and by the isolating mass at the top.

As already discussed in Chapter 4, perfectly rigid mounting is easy to implement in numerical simulation. However, real structures never achieve infinite impedance (zero mobility), and the impedance of the test structure will have some influence. If it can be shown that the mobility of the isolating mass is insignificant compared to that of the rest of the USTT stack, it can be considered effectively perfectly rigid mounting, and modelled as such in the simulation.

At the bottom mounting, a mounting flange on the booster is located at what is a nodal plane within the booster, at the operating frequency of 20 kHz. Virtually no transmission of motion is expected from the nodal flange to the mounting structure.

5.2.7 Measurements, data acquisition and FRFs

A number of methods and instruments can be used to measure the vibration response of a structure, both contact and non-contact. Contact devices such as the accelerometer and piezoelectric force transducer must be physically connected to the structure to operate, introducing extra mass loading and stiffness which, at the high accelerations achieved at ultrasonic frequencies, can introduce a significant error into the measurement. Non-contact instruments include the laser interferometer, the laser Doppler vibrometer and the ultra-high speed camera. In general, the LDV has proven especially convenient for the measurement of FRFs on ultrasonic devices. It also produces reliable results at the very small displacements (and strains) encountered over the length of the specimen and force transducer used in the USTT.

Response (output) measurement

In the present work a laser Doppler vibrometer (Polytec, 3D CLV) capable of measuring in three-dimensions (3D) was used to measure the surface velocity of the USTT stack, including components from the bottom of the horn to the top of the isolating mass. The 3D-LDV uses three lasers to convert the velocity of the surface (both in-plane and orthogonal to the plane of observation) into an electrical voltage signal. Measurements were taken at discrete points in a line parallel to the central axis of the stack, Figure 5.2.

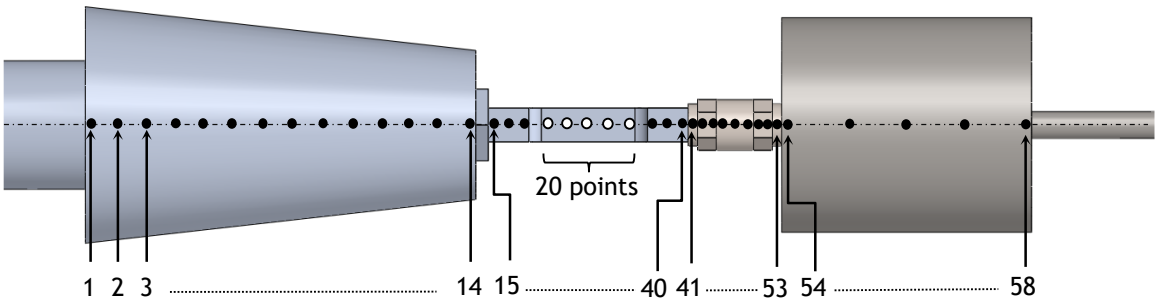

Figure 5.2 - FRF measurement points on USTT stack

Ordinarily, for complete characterisation of a cylindrical structure, lines are taken at each quadrant. As the test machine restricted access to the sides and rear of the USTT stack only one line at the front was acquired, with the assumption that this would be sufficient to characterise the longitudinal mode (the mode of interest), where the motion is dominated by motion in the axial direction.

The spatial density of measurement points was arrived at experimentally, increasing from the minimum number required to resolve the mode shape expected at 20 kHz, to that which ensured a clearly defined trend over the whole structure.

Force (input) measurement

A unique circumstance arises when using self-excitation to characterise ultrasonic transducers and connected apparatus. In this arrangement there is no point between the excitation source and the test structure in which to insert a force measurement device. Dividing the ultrasonic transducer to do so would destroy its structural resonance, rendering the test pointless. However, the driving force is usually a requirement for calculating a true FRF [78].

A valid FRF may still be calculated using the excitation signal from the signal generator as the ‘input’ to the Spectrum analyser. This is shown in the connection layout in the apparatus diagram, Figure 5.3. The force produced by the ultrasonic transducer is proportional to the amplitude of the electrical potential applied to its piezoceramic rings, and so too the signal from the signal

generator. In this case, the excitation signal may be used in place of the driving force measurement, as the 'input' for the FRF calculation, and this is common practice across ultrasonic device characterisation [95]–[97].

Further to this, in this study FRF data was obtained over the USTT stack from the base of the horn to the top of the isolating mass, excluding the booster and ultrasonic transducer. No driving point FRF measurement was made. To assess the effect of neglecting the point FRF on the recorded waveform, a transmissibility frequency response measurement was carried out, which is discussed in section 5.4.

5.2.8 Data acquisition and processing for FRFs and modal identification

In this work, data acquisition of the signals from the LDV and subsequent conversion to frequency response functions was performed by a PC-based spectrum analyser (Quattro, SignalCalc ACE, by Data Physics Corp.).

A spectrum analyser is one of a class of instruments used to determine the frequency response between two electrical signals. Although in the past fully analogue analysers were made, digital signal processing now dominates. The spectrum analyser used in the present work sampled the time-based analogue signals from the LDV using analogue-to-digital converter (ADC), at a rate sufficient to capture the highest frequency in the analyser's range of operation. Aliasing, a possible consequence of digitisation, was prevented by filters which remove frequencies above this range.

While transformation of time domain signals to the frequency domain is ordinarily carried out using the Digital Fourier Transform (DFT), the use of random noise excitation and resulting random response necessitate a preliminary step using statistical signal processing techniques. The equivalent of the FRF ratio of Fourier transforms in (5.2) can be found by first calculating the cross-correlation and auto-correlation of the input and output signals, before transforming them into the frequency domain using the DFT. The FRF is then the ratio of the resulting cross- and auto-power spectral densities. The number of spectral lines was selected to be 51200, over the frequency range 0 – 40 kHz, resulting in a resolution of 0.781 Hz (3sf). To eliminate frequency leakage errors

originating from applying the Fourier transform to finite samples of a signal, a Hanning window was applied to the time domain signals before processing.

FRFs were computed for each of the three orthogonal vectors of velocity from the LDV, for every measurement point. The resulting array of FRFs was then exported to modal analysis software (ME'Scope VES, Vibrant Technology Inc.) to carry out the curve fitting described in section 5.2.4, identifying the natural frequency, damping and mode shapes. These parameters were then used to calibrate the FE model, a process which is described in the following section.

5.2.9 Experimental apparatus and procedure

The apparatus for performing EMA on the USTT was arranged as shown in Figure 5.3. When installing the specimen, the crosshead position was adjusted to achieve a tensile preload of 100 N which was held throughout the FRF acquisition.

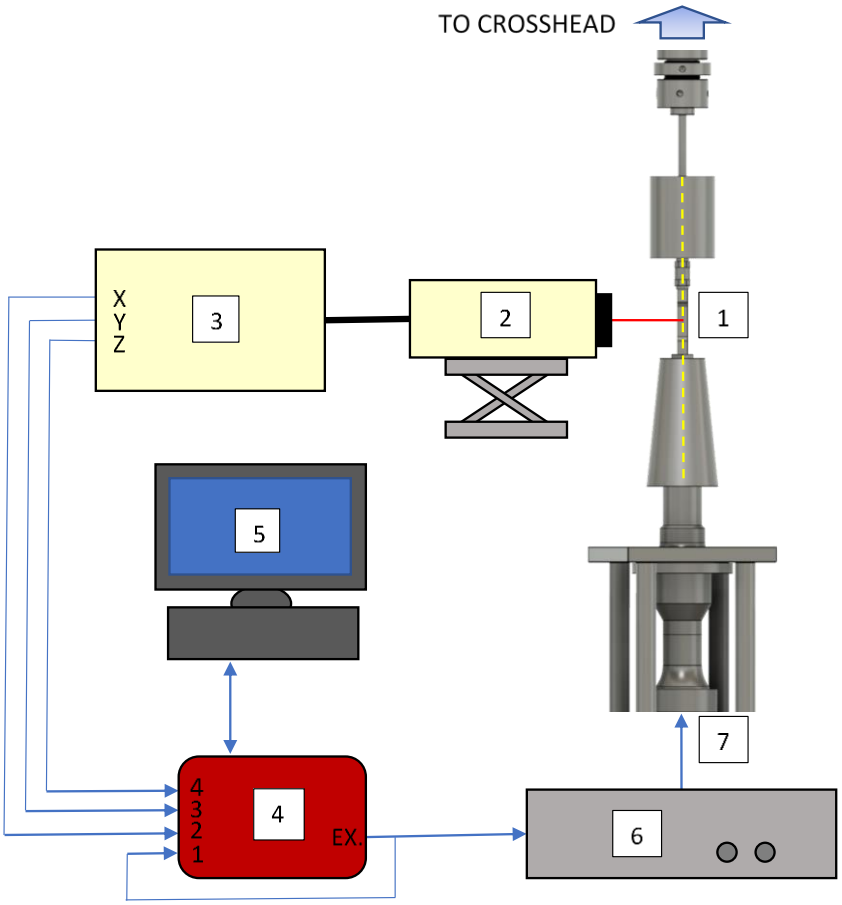

1. Laser beams aimed at measurement points along axis of stack
2. 3D-LDV (Polytec CLV-3D
3. LDV control unit (Polytec CLV-3000)
4. Spectrum Analyser (Data Physics Quattro)
5. Computer with software for DAQ and signal processing (Data Physics SignalCalc ACE)
6. Audio frequency power amplifier (QSC Professional Amplifier, RMX 4050a)
7. Ultrasonic transducer (Sonic Systems L500)

Figure 5.3 - EMA apparatus

Once the LDV laser head was aligned with the first measurement point (Figure 5.4), the signal analyser initiated the excitation and completed FRF acquisition, storing the data on a computer. The LDV laser head was moved to the next measurement point and the FRF acquisition process repeated, until FRFs were recorded for each point in Figure 5.2. The group of FRF records were exported to the modal analysis software to identify the natural frequencies, damping and mode shapes.

Figure 5.4 - LDV laser point on ultrasonic tensile test stack

5.3 Natural frequency and mode shape of L1 mode

Once the FRFs were imported into the modal analysis software, the peak corresponding to the resonance closest to the operating frequency of 20 kHz was identified. Using the modal curve-fitting tools on this peak, the resonant frequency, modal damping and mode shape vector were extracted. The procedure was repeated three times, recording three sets of EMA data and resulting modal parameters, Table 5.2.

EMA test no.	Natural frequency (Hz)	Damping factor (%)
1	20094	0.080253
2	20128	0.046330
3	20127	0.047152
Mean value	20116	0.057912
Std. dev.	15.8	0.015801

Table 5.2 - EMA extracted parameters of L1 mode

For each natural frequency, the mode shapes were exported, each eigenvector saved as a table of normalised displacement values for each measurement point. The values were plotted against the axial position of each DOF, Figure 5.5, up

the centreline of the USTT stack, from the base of the horn to the top of the PFT. The data points relating to each stack component have been separated by vertical dashed blue lines.

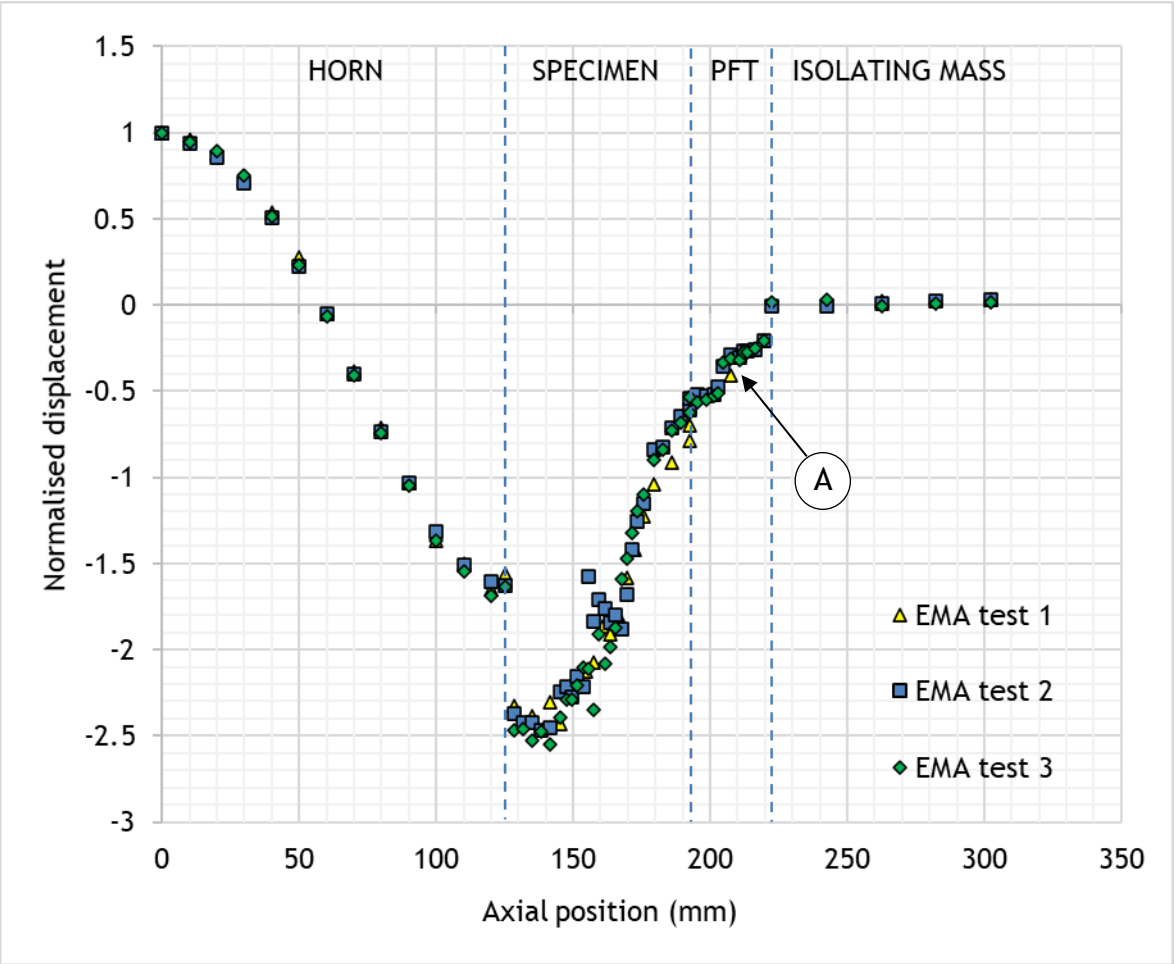

Figure 5.5 - L1 mode shapes from EMA

Over the horn there is little spread in the data points, and the smooth curve agrees with the classical waveform of displacement gain expected of a conical horn [65]. This provides a level of confidence in the experimental data.

The data becomes noisier over the specimen and the PFT, though the general trend is still clearly visible. A large jump is observed between the horn tip and the specimen.

The PFT displays a similar step, marked ‘A’ in Figure 5.5. The position was identified as the joint between the casing of the piezoelectric heart of the device and the fixing used to connect it to other components. These parts

correspond to the spring and end-mass in the model of the PFT developed in Chapter 4, section 4.3, supporting the use of this approach.

Finally, displacement of the isolating mass was observed to virtually zero, the slight differences between EMA tests being indistinguishable from noise.

It will be shown in subsequent sections how this waveform of the longitudinal vibration was used to calibrate an FE model, as part of the effort to verify the force transducer reading.

5.3.1 Assessment of the isolating mass

In Figure 5.5 the vibration response over the length of the cylinder of the isolating mass is negligible in comparison to the rest of the structure, confirming it performed as intended, presenting a high impedance boundary which reflected the vibration back into the stack. This supports the argument that it may be represented in the numerical model as a virtually rigid boundary condition.

5.3.2 Velocity profile

It is interesting to compare the mode shape extracted from the EMA to the profile of velocity recorded in an earlier experiment, before the introduction of the isolating mass, Figure 5.6. Here, the absolute values of velocity from the 3D-LDV's X, Y and Z direction outputs were plotted directly against axial position in a manner identical to the spatial sweep in the EMA. Because no reference signal was used, phase information is absent. It does, however, confirm the peak velocities reached at a nominal horn tip displacement of 10 μm are approximately 1.2 $m.s^{-1}$.

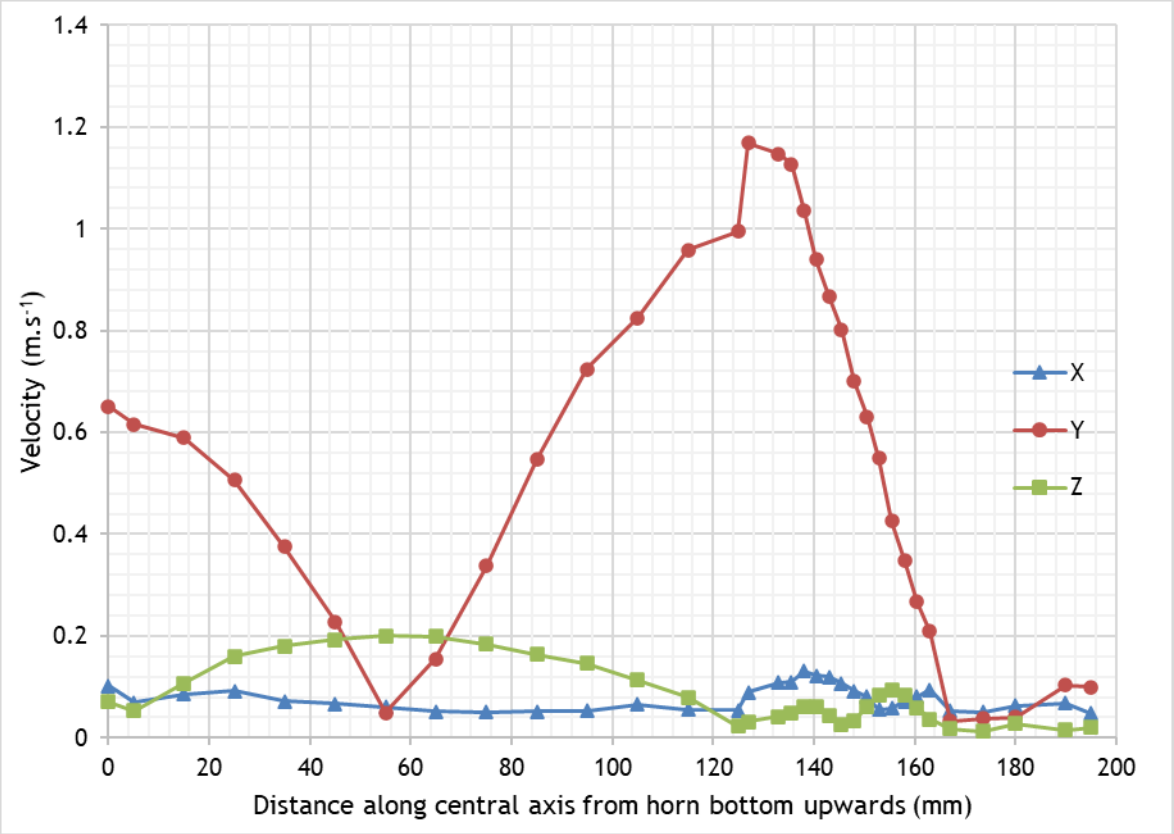

Figure 5.6 - Velocity profile without phase information

5.4 Mobility-transmissibility comparison

To address the concern that the lack of FRF data over the ultrasonic transducer, including a driving point FRF, could negatively affect the waveform extracted by the EMA process, a transmissibility measurement was made to compare to the mobility FRF curve.

In contrast to the frequency response functions defined in Table 5.1, the modal response of a structure can also be characterised using two kinematic measurements, one as the roving measurement and the other as a stationary reference signal. The frequency response is then the ratio in the frequency-domain of the roving response over the stationary reference; this ratio is known as a *transmissibility* frequency response [78].

In this study, a second 1D-LDV (Polytec OFV303) measured a stationary reference velocity, which was the axial velocity of the base of the ultrasonic horn. The 1D-LDV measures the normal component of surface velocity. As it could not be positioned to point directly at the horn's base, the 1D-LDV was placed

horizontally, co-planar with the base. Then, the laser beam was redirected towards the base of the horn via a mirror angled at 45°, such that the beam reached the horn perpendicular to the base. The 3D-LDV continued in its role as the roving instrument, recording the response velocity as it moved up the USTT stack axis in an identical manner to the EMA experiment, Figure 5.7. The transmissibility ratio was then the velocity response over the velocity reference, equation (5.5):

$$T(\omega) = \frac{\mathcal{L}(v_{resp})}{\mathcal{L}(v_{ref})} \tag{5.5}$$

Where $v_{ref}(\omega)$ is the reference velocity, $v_{resp}(\omega)$ the response velocity and $T(\omega)$ the transmissibility frequency response.

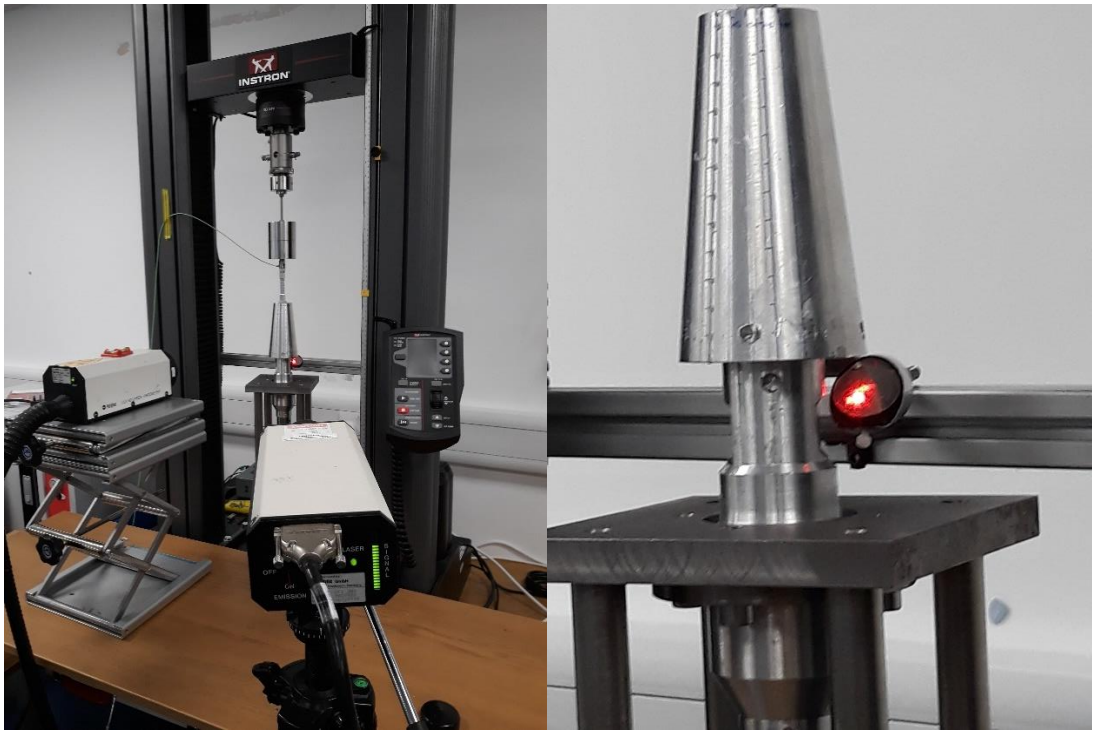

Figure 5.7 - (a) Transmissibility with two LDVs; (b) Mirror redirecting 1D LDV laser beam to horn bottom

The excitation, signal acquisition and processing to calculate the frequency response curves remained identical to those used in the EMA.

5.4.1 Results

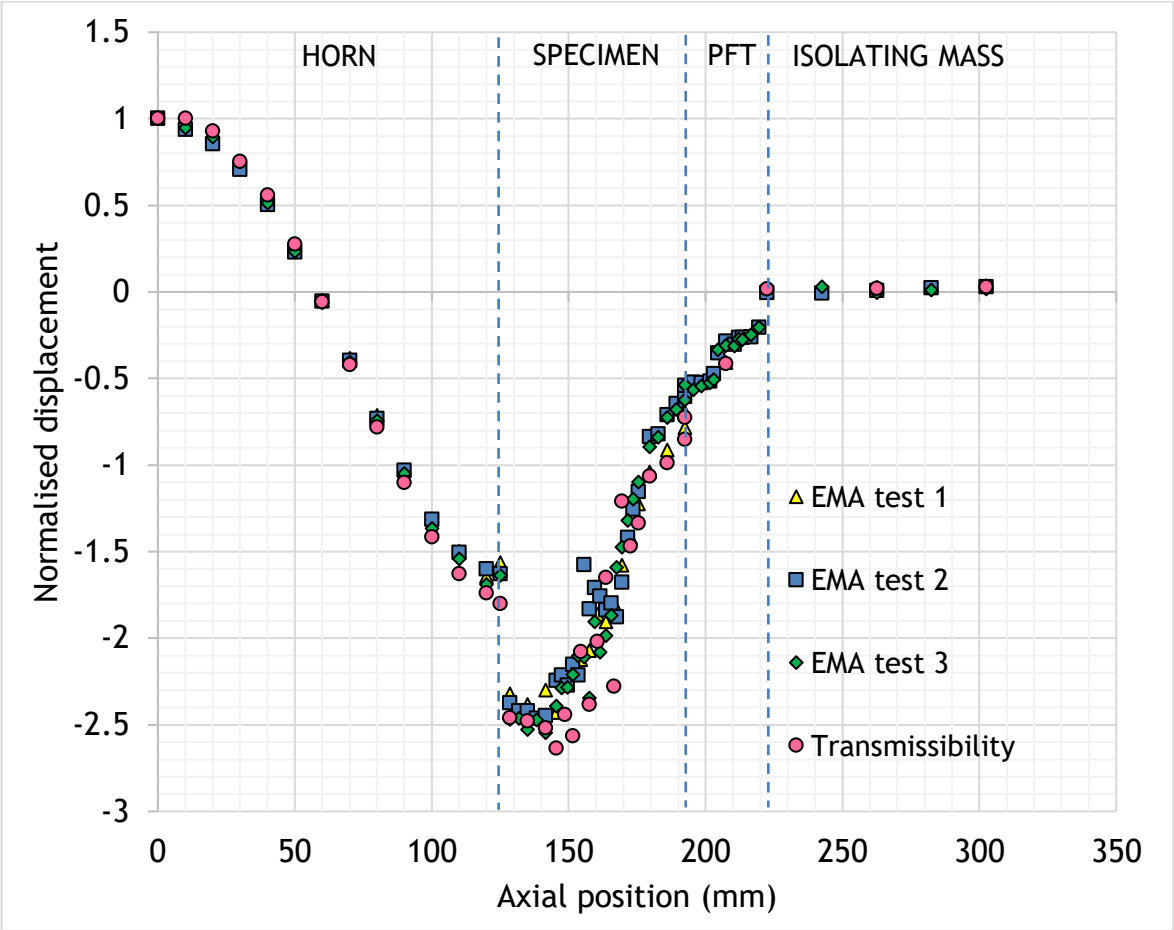

Figure 5.8 - Normalised ODS from mobility and transmissibility measurements

In Figure 5.8, the transmissibility normalised-displacement data have been overlaid on the EMA waveforms. The two measurement methods match well over the horn, force transducer and isolating mass. Along the specimen the transmissibility data points appear to contain greater error, though they follow the same trend as the mobility results.

The match between mobility and transmissibility data is sufficient to suggest that the lack of a true driving-point mobility measurement has not prevented the mobility FRFs from capturing the correct waveform.

5.5 Summary

EMA was employed to characterise the longitudinal vibration of the ultrasonic tensile test stack, from the base of the horn to the top of the PFT. Vibration measurements were limited to a line of measurement points following the axis

of the stack. Importantly, the EMA successfully identified the first longitudinal mode, estimating an average natural frequency of 20116 Hz, and modal damping factor of approximately 0.06%. The mode shapes, crucial for calibrating the FE model, were recorded.

In the course of FRF measurement the mobility of the isolating mass was assessed and found to be negligible compared to the rest of the test structure. This suggests it is functioning as intended, acting as a boundary with very high impedance which reflected the ultrasonic vibration, relaying only the quasi-static force to the crosshead. It may be assumed the PFT-isolating mass interface can be represented as a rigid boundary in FE simulation.

A transmissibility measurement of the L1 waveform confirmed the mobility measurement produced an undistorted FRF, despite the lack of a true driving point measurement.

6 Numerical modelling of USTT apparatus

Numerical modelling of the ultrasonic tensile test apparatus was performed in the software Abaqus CAE (Dassault Systèmes). Abaqus is a general-purpose commercial FEA program that provides a variety of solution procedures which can be chosen to suit the analysis task, as well as modules for importing model geometry and post-processing solution results. It has been used successfully to model ultrasonic devices, most often using eigen-analysis to calculate natural frequencies and mode shapes before finding the steady-state response with a frequency domain direct-solution procedure [95], [97]. The implicit direct-integration procedure in Abaqus has been applied to the time-domain solution of plastic deformation of a metal with ultrasonic vibration superimposed [43].

In general, finite element analysis is a numerical method for solving the partial differential equations (PDE) which arise in the analysis of continuous physical fields such as structural or fluid volumes, or thermal or electrical fields. The continuum domain is discretised into smaller volumes, or elements, within which a linear approximation to the field is valid. The linear polynomial equations are then assembled to form the FE approximation to the whole field, as a system of simultaneous equations, which is solved using matrix methods on a computer. FE discretisation is most often applied to the spatial domain. The method is extended to the time domain, to solve dynamic problems, either by directly incrementing through time (direct integration procedures) or by assuming harmonic excitation and solving in the frequency domain (for example, modal analysis using eigenvalue extraction, or steady-state analysis by direct inversion of the harmonic system equations).

Initially, a computer-aided drawing (CAD) package was used to model the geometry of the USTT apparatus, which was limited to the ultrasonic transducer, booster, horn, specimen and force transducer, Figure 6.1. The CAD model was imported into the FE package, where material properties, boundary conditions, and interaction between the assembled parts were defined. First, an eigen-analysis solved for the natural frequencies and mode shapes.

In an iterative approach, the model was adjusted such that the simulated mode shape of the first longitudinal mode (L1) of the structure converged on the L1 waveform found by EMA in section 5.3.

Then, the calibrated model was used in a steady-state dynamics procedure to predict the amplitude of the forces, strains and stresses within the structure when in resonance at the nominal operating frequency of 20 kHz.

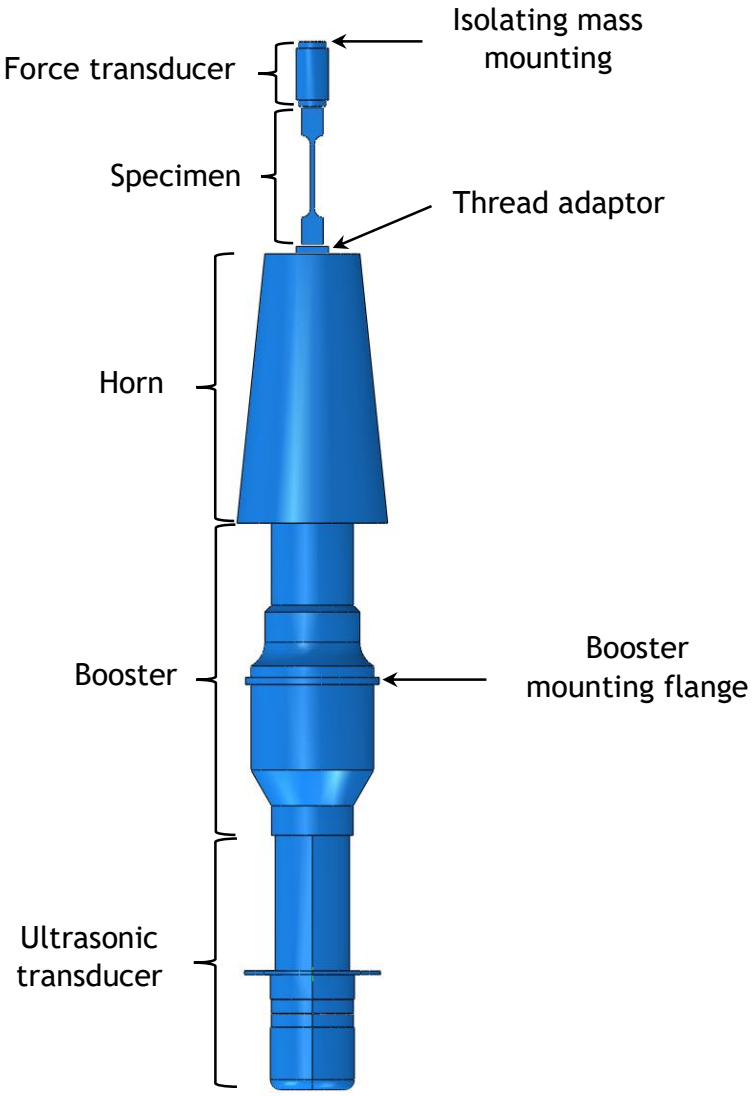

Figure 6.1 - FEA model geometry

6.1.1 Material properties

The material properties required by a dynamic analysis are the density (to provide the general mass) and the parameters which specify the mechanical constitutive relationship. All components in the assembly modelled were metal, with the exception of the piezoelectric rings in the ultrasonic transducer, which were made of a piezoceramic.

In this study, only the dynamic loading of the USTT was simulated, matching the experimental modal analysis. Deformation therefore remained within the elastic limit, with strains proving less than 0.04%. This permits the use of the Abaqus linear-elastic material model. The metal parts were assumed isotropic and homogeneous, and were fully defined by their density, Young's modulus and Poisson's ratio.

To use the voltage supplied to the ultrasonic transducer as a boundary condition, the piezoelectric material further required the electrical and electromechanical parameters of permittivity and piezometric properties. The elastic properties require tensor definition, due to their orthotropic nature. The ultrasonic transducer, and the piezoelectric material in particular, was modelled based on the procedure followed in [95], and was adapted for use in the present study from previous work by [98], [99].

6.1.2 Boundary conditions

In FEA, boundary conditions (BCs) can be imposed on surfaces, edges or nodes of a model, to represent physical constraints on a structure, such as mounting points. Different kinds of constraint are represented by limiting the nodal degrees of freedom – for example, in a rigidly fixed mounting all DOFs of the nodes within the BC are set to zero.

In the eigen-analysis, to calculate the natural frequencies and mode shapes correctly, good approximations to structural constraints are required. As already discussed, the impedance of supports can have a significant effect on the response of the test structure. In this study the extent of the structure modelled

was limited to the assembly from the ultrasonic transducer to the piezoelectric force transducer. The structural boundaries of this assembly were the upper and lower mounting points, at the booster nodal flange and the force transducer respectively, Figure 6.1. As the isolating mass was proven to be virtually immobile in the EMA, the end of the force transducer connected to the isolating mass was given an encastré BC (where displacement and rotation are set to zero). At the lower mounting, the booster was clamped into the test machine framework by the booster's nodal flange in Figure 6.1. The flange is located at the booster's nodal plane, where the displacement of the booster's first longitudinal mode is theoretically zero, preventing vibration transmission and isolating the lower mounting from the wider test machine. In the FE model, this allowed the mounting to be represented using an encastré BC on the booster flange surface.

In Abaqus, BCs can also be used to impose variables such as the electric potential across piezoelectric elements. Whilst more commonly the Load module in Abaqus is used to specify a force excitation, in this steady-state analysis, the excitation from the ultrasonic generator was simulated by defining a voltage BC across the piezoceramic rings. The amplitude of this BC is assumed to vary harmonically at the frequency specified in the steady-state step.

6.1.3 Interaction at assembly interfaces

In an FE model assembly, each part is discretised as a separate domain, with its own mesh. The FE code does not recognise any connection or interaction between domains simply because part surfaces are adjacent. Parts next to each other can pass through one-another or move away unless they are constrained or some interaction properties are specified. Connections like threaded and bonded joints, surface contact of parts or sliding of surfaces with friction must be approximated with an appropriate model.

For this purpose, Abaqus provides the interaction and constraints modules. Interactions between all parts can be set at a global level with the General contact tool, or each surface pair individually specified. Here, each set of mating parts were jointed using the 'tie' condition from the constraints module,

which imposes the condition that the displacements of nodes in each mating surface are equal (both surfaces are fully tied together).

This is a simplification of real joint behaviour that proved acceptable for the majority of the USTT assembly, with an exception at the joint between the horn and the specimen, which will be discussed shortly.

6.1.4 Discretisation of domains – mesh design

Once the geometry of parts, their materials and their interaction with an assembly have been defined, the next step is to discretise each domain. As mentioned previously, in the FE method the continuous domains of parts are sub-divided into smaller sub-domains called elements. Adjacent elements are connected at the corners and sides through vertices called nodes to form a grid known as the mesh. Several types of standard element have been developed and incorporated within FE codes, with different shapes and properties for different analysis types. Their selection depends on the model geometry, the material properties and behaviour specified, and the type of analysis to be performed. The choice of element and the number of elements used (the mesh density) has a significant impact on solution accuracy and processing time.

For the full 3D analysis of the solid parts in the USTT, the most relevant elements available in Abaqus CAE are the hexahedral, or brick, element (C3DR20), or brick, and the tetrahedral, or pyramidal, element (C3D15). Where model geometry is simple enough to permit their use, hexahedral elements are the most efficient, providing the same level of accuracy for the lowest mesh density. This element shape was used to mesh the majority of components in the assembly, the exception being the booster, where surfaces with double-curvature required the use of tetrahedral elements. The Abaqus mesh-quality tool was used to check for excessive element distortion or aspect ratio.

To calculate the displacements within them, elements use an interpolation function, which in Abaqus can be either linear or quadratic. Elements that use the quadratic interpolation function have extra nodes at the mid-points of their edges, which incurs a computational cost. However, they are less prone to certain errors than linear elements, and consequently reduce the mesh density

required. Quadratic elements are recommended for general structural analyses, which includes the modal and steady-state dynamic analysis carried out in this work [100].

For piezoelectric materials, Abaqus provides a version of the hexahedral element, extended to incorporate the piezo-mechanical properties and accept electric potential as a boundary condition.

Mesh density

The coarseness of the mesh in an FE model can have a significant effect on the predicted modal frequencies; ordinarily, a mesh convergence study is therefore performed to check the model converges on the parameter of interest, which in this case is natural frequency. In Abaqus, the mesh density is controlled by a parameter called the seed size, specifying the element spacing along geometry edges, and from which the automatic meshing algorithm can extend the volume mesh. Often, parts are given identical or similar seed sizes. However, in the USTT assembly, the difference in parts' size and aspect ratio presents a challenge. The ultrasonic transducer, booster and horn are much larger and thicker than the specimen and force transducer. Three different approaches were taken.

A mesh convergence study was performed on the FE model of the PFT, the development of which was described in Section 4.4.3. To check the desired resonant frequency of the stand-alone model of the PFT had been achieved, eigenvalue analyses were run for a range of mesh seed sizes, Figure 6.2.

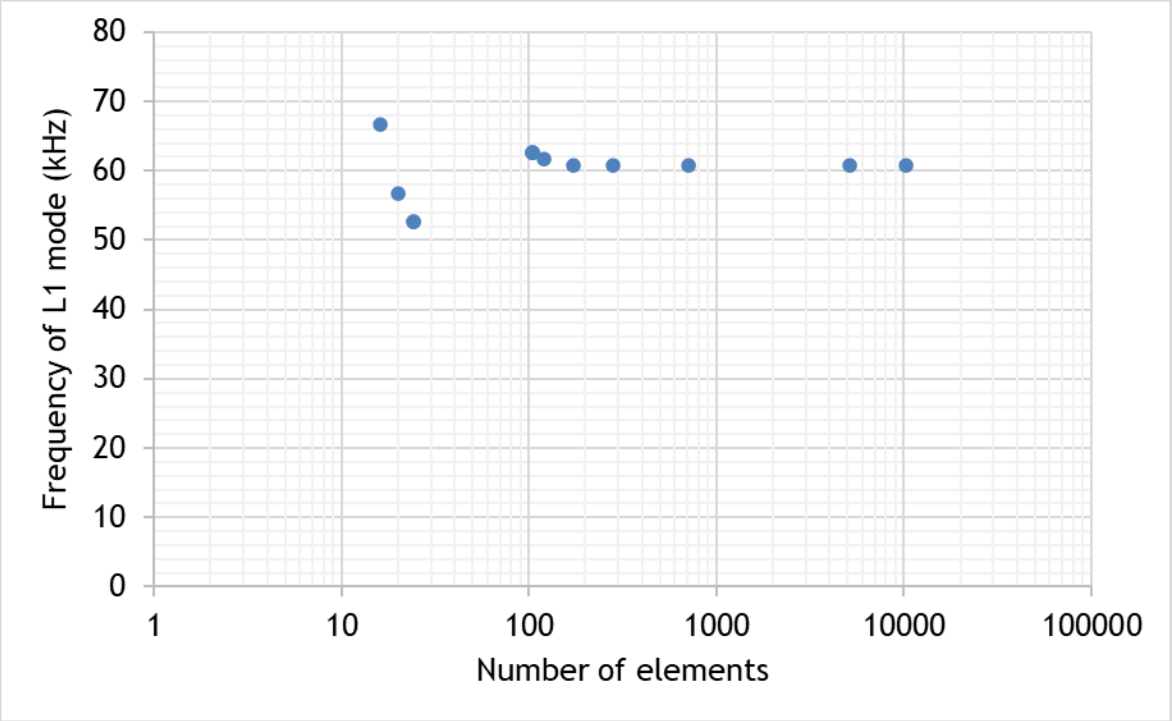

Figure 6.2 - Mesh sensitivity of proxy PFT

The modal frequency of the first longitudinal (L1) mode of the model PFT remains stable provided the mesh contains more than 150 elements. The mesh density was maintained at a value which exceeded this limit.

As the mesh in the ultrasonic transducer had already been determined during its development for previous research, mesh convergence studies were carried out for the horn and booster separately, following the method described for the PFT FE model.

The thin cross-section of the specimen's parallel length required a much finer mesh than would otherwise be needed to accurately solve the longitudinal vibration of a part of the specimen's length. C3D20R elements perform adequately in bending with a minimum of two elements through the thickness [100]. In the specimen, a seed size was chosen which created a minimum of two elements through the thickness of the specimen gauge length, Figure 6.3.

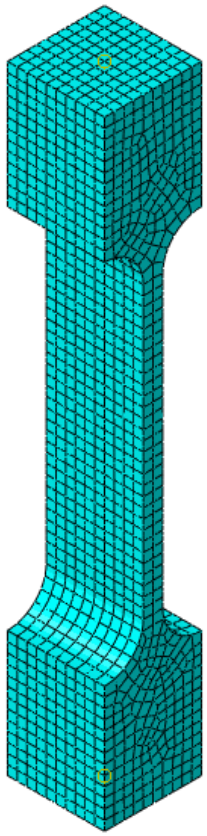

Figure 6.3 - Specimen mesh detail

The final mesh is presented in Figure 6.4.

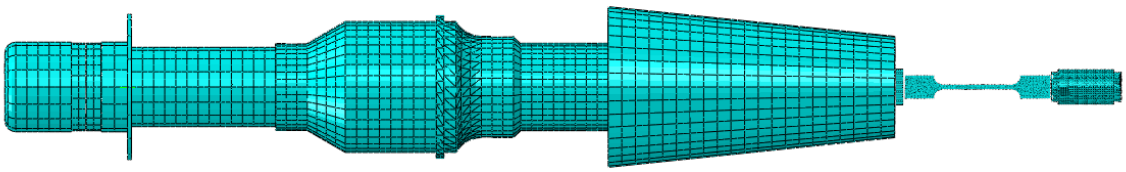

Figure 6.4 - FE mesh model of USTT

6.1.5 Analysis steps

Abaqus provides a suite of analysis procedures to solve a variety of problems, for example, structure, thermal, or electrical, any of which can be static or dynamic. Different analysis types can be performed on the same model, in a sequence. The analysis of a problem is divided into 'steps' to form an analysis history. To manage this process, Abaqus provides the Step module. Each step permits a new analysis procedure to be defined, and the assignment of new

boundary conditions, loads and solution output requests. Subsequent steps operate on the solution from the preceding analysis.

There are two classes of procedure – General, and Linear Perturbation. In a General procedure, the solution is found incrementally, in real or pseudo time, and may be used to solve both linear and non-linear problems. Non-linearities include non-linear materials or geometry, boundary conditions or interactions between bodies. The linear perturbation procedure assumes a linear relationship between the excitation or load and the response, and is calculated at a system state called the Base State. The solution of a General procedure may be used as the Base State for a linear perturbation analysis.

Whilst General procedures can be used to solve a dynamic problem, when the solution can be assumed harmonic analysis can be carried out with linear perturbation procedures in the frequency domain, simplifying the system of equations, and greatly reducing solution time [100].

To assess the FE model against the EMA modal results, the Abaqus eigenvalue extraction procedure (Frequency step) was employed to calculate the natural frequencies and corresponding mode shapes over a frequency range from 5 to 25 kHz. It was preceded only by the initialisation step, where BCs were applied to create the Base State. In using this linear-perturbation procedure, the assumption was made that the modal response of the USTT was linear, the same assumption being made when employing EMA to find the modes experimentally.

6.2 Experimental calibration of FE model

The Abaqus Frequency step results consist of a list of eigenvalues, and for each of these a corresponding eigenvector, recorded as normalised displacement for each node in the mesh. This can be displayed as a colour map or a plot of the deformed mesh. Using the deformed mesh display the L1 mode was identified, Figure 6.5.

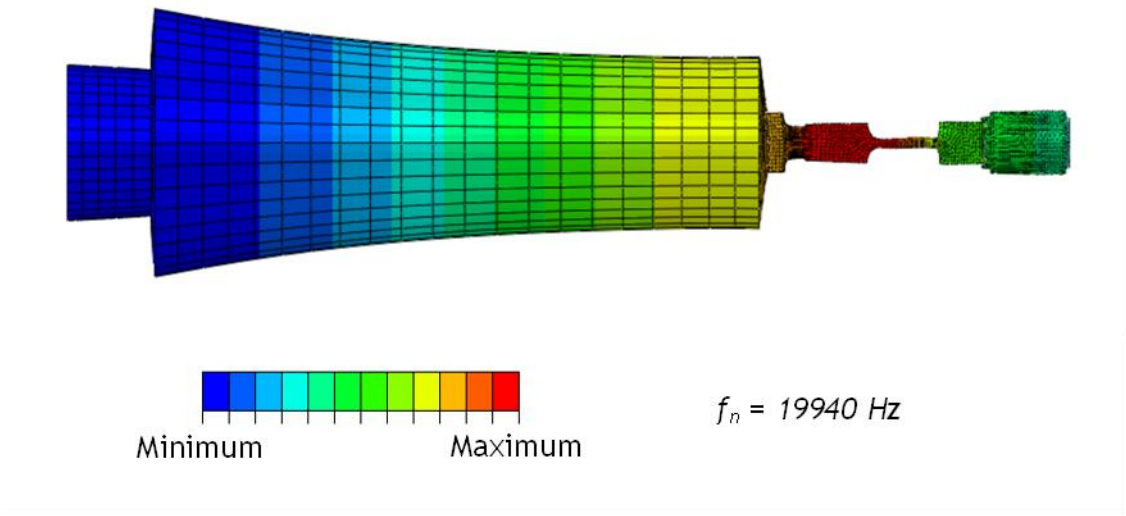

Figure 6.5 - colour map of axial displacement on deformed mesh, L1 mode

The natural frequency was calculated to be 19,940 Hz. This is 0.87% lower than the experimental value of 20,116 Hz.

The neighbouring modes, at 18,284 Hz and 21,067 Hz, are respectively a lateral bending mode (a) and a torsional mode (b) in Figure 6.6.

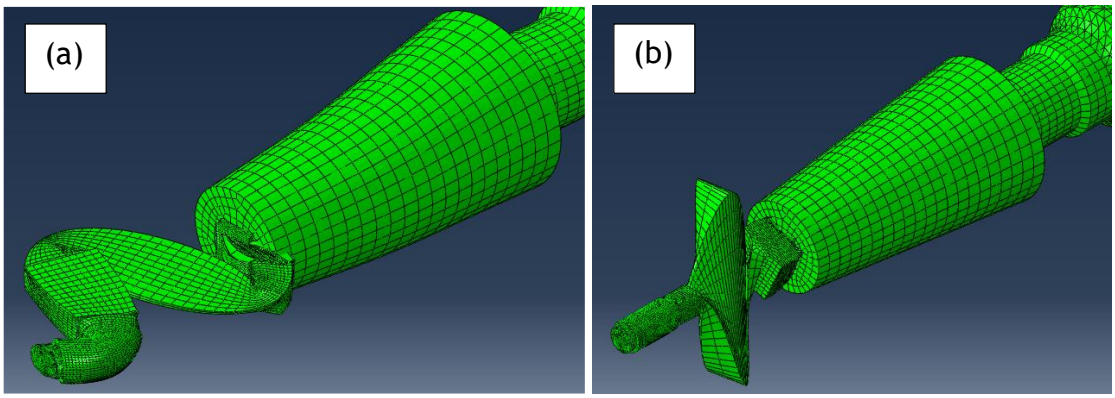

Figure 6.6 - Mode shapes neighbouring the L1 mode

To compare the simulated and experimental data, the predicted L1 mode shape was mapped in a manner which recreated the EMA procedure. Once the first longitudinal mode was identified from the eigenvector output (Figure 6.5), the normalised displacement of the surface of each component was extracted. Using the Abaqus Paths tool, line segments were defined on the surface of each part corresponding to the line of EMA measurements in Figure 5.4. Axial displacement was exported from each element the line segments intersected. The results have been collated with the experimental results for comparison, Figure 6.7.

Replicating the LDV surface measurements in simulation by extracting displacement on the surface of the USTT components was found to be crucial, as the latter can differ significantly from data taken from the true centreline of the assembly.

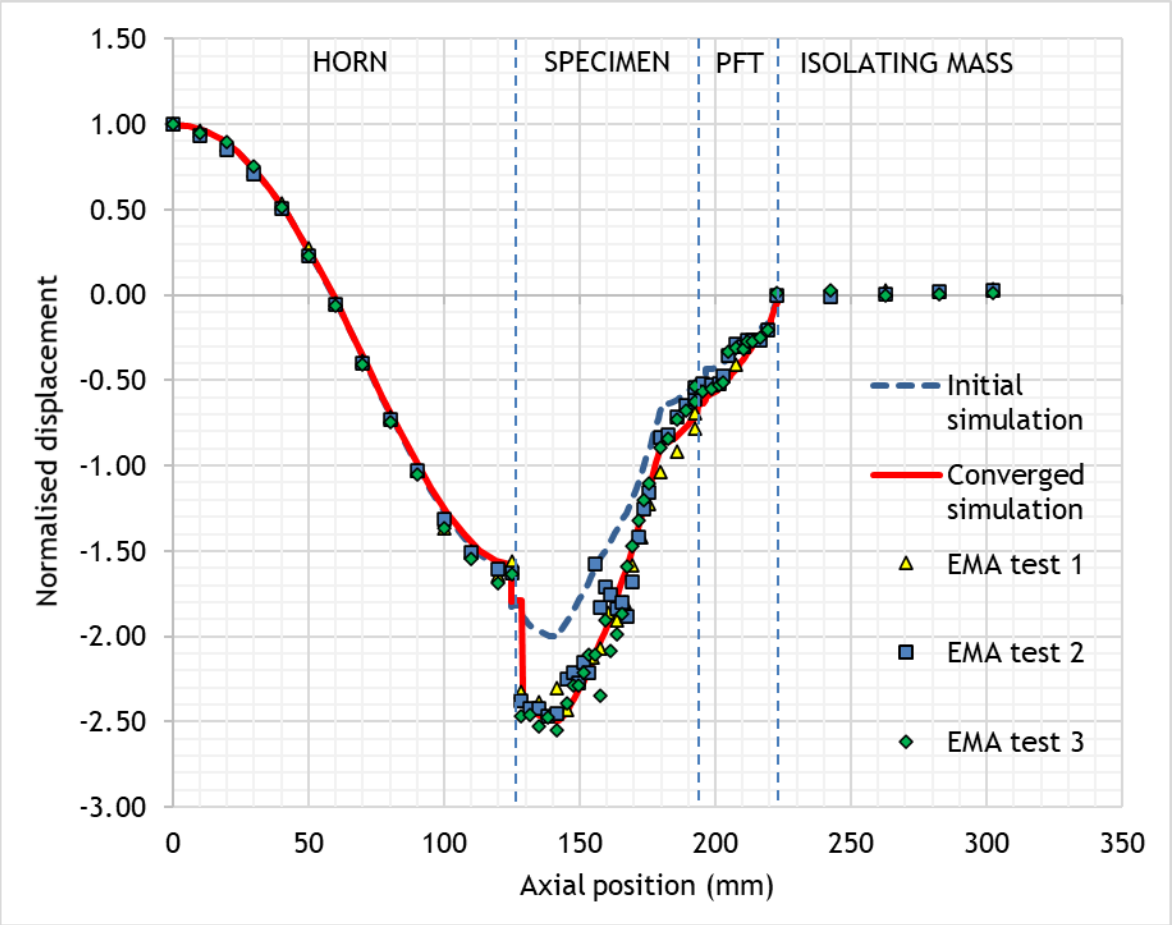

Figure 6.7 - Simulated and experimental L1 mode shape

In Figure 6.7, normalised displacement was plotted against the distance up the axis of the USTT stack, from the base of the horn to the top of the PFT. Beneath the experimental data, two simulated mode forms are presented: the dashed blue line titled 'Initial simulation' plots the result of the first model iteration, where all joints were connected with a perfect 'tie' constraint. The continuous red curve titled 'Converged simulation' plots the final iteration of model adaption, which will be described now.

6.2.1 Approximation of joint compliance

While the initial FE model iteration succeeds in capturing the dynamic motion of the horn, it fails to replicate the sharp step in amplitude at the interface between the horn and the specimen. The discrepancy appears to be continued from the joint along the rest of the specimen and PFT, the jump moving the course of the experimental data on the specimen downwards. The curve of the experimental data otherwise appears to have a similar trend to the specimen in the simulation.

In the real structure this interface is a threaded joint, where the components are held together with an M6 stud. Such connections are known to be far less stiff than the adjacent material of the components, and have a significant impact on the dynamic behaviour of a structure [101], [102]. There is evidence that, at frequencies under 13 MHz, the impedance of an interface can be well approximated by a simple Hookien spring model [103]. The impedance can be represented by introducing a thin layer with a modulus which is tuned to correctly match experimental data.

In the FE model (Figure 6.8), additional compliance at each joint was created by inserting a thin 0.5 mm pad between the components in each joint-pair. In meshing, care was taken to ensure each pad contained two elements through its thickness [101]. The elastic moduli of the pad was altered iteratively until the simulated mode shape converged on the experimental waveforms (the red curve “Converged Simulation” in Figure 6.7). The simulated and experimental waveforms now show good agreement, both in the magnitude of the step in displacement at the horn-specimen interface, and more generally over the length of the specimen and force transducer.

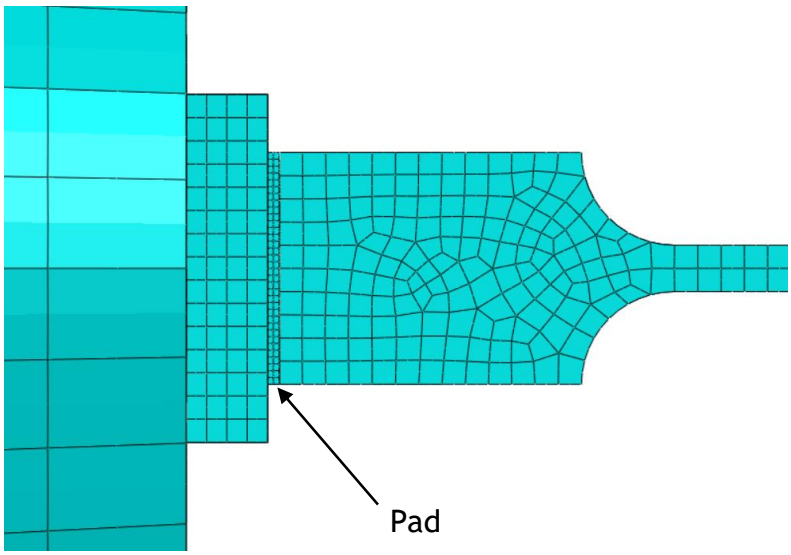

Figure 6.8 - Compliant pad between horn and specimen

The adjusted model also benefitted from the introduction of the tuned FE force transducer model developed in section 4.4.3. The reasonable agreement in gradient between simulation and experiment over the force transducer portion of the waveforms suggests that the FE model has succeeded in capturing, in gross, an average of the transducer device's mechanical impedance. This lends support to the method of modelling piezoelectric force measurement devices as a simplified FE model tuned with impulse data.

It was proposed in section 5.3 that the step observed within the waveform over the PFT is due to the discrete nature of the real force transducer's internal structure. Representing the PFT as a solid, homogenous body enabled simple and effective modelling, however it precluded any ability to capture deformation dynamics due to discontinuous internal structure. Currently, it is sufficient, that the overall impedance is captured by the FE model. However, the detail observed in the experimental mode shape suggests an avenue for improvement in future investigations, should the desired fidelity of the model warrant it.

In total, these improvements produce a simulated mode shape which clearly captures the phenomena dominating the dynamic motion, closely matching the majority of the experimental mode shape data from the three EMA tests.

6.3 Simulation of absolute force measurement from piezoelectric force transducer

In section 6.2, experimentally derived mode shapes were used to adjust the FE model such that it reproduced the correct eigenvalues and modes. In an eigenvalue analysis, the displacements and other variables are normalised and only make sense relative to one another; the absolute value of variables such as strain, stress and force are meaningless. To find absolute values of force and strain required for comparison with the experimental measurements from the force transducer and strain gauge, it was necessary to calculate the steady-state response.

6.3.1 Steady-state dynamic analysis

The Abaqus Steady-State Dynamics – Direct (SSD-D) procedure was added as an additional step following the Frequency step. Similar to the eigenvalue extraction, this is a linear perturbation which operates in the frequency domain, calculating the amplitude and phase response of kinematic and kinetic variables at discrete values of frequency over the range of interest. This frequency 'sweep' can be used to find the frequency response of a model. To carry out this new type of analysis, additional properties and settings are required.

6.3.2 Analysis definition for steady-state analysis

To define the SSD-D frequency sweep, Abaqus requires upper and lower frequencies bounding the range of interest, followed by the manner in which the calculation points are distributed over the frequency range. To extract the variable amplitudes over the L1 resonance at 19940, a sweep was created enclosing the interval 19,840 to 20,040 Hz (the L1 modal frequency +/- 100 Hz). Abaqus offers the option to divide the frequency range into intermediate intervals using system eigenfrequencies, should they be available. Enabling this option ensured variables were calculated at the L1 resonance found in the previous Frequency step.

Similar to the Frequency step, the Field Output requested included the displacement and nodal forces at each node, and strain and stress across the mesh.

6.3.3 Material definition for steady-state analysis

Obtaining quantitively accurate results in a steady-state analysis of forced vibration, especially at or near resonance, requires some level of damping within the structural model. If damping is absent the response at a natural frequency will be unbounded [100]. In the FE method, damping can be incorporated in a number of ways, including as a modal damping factor for each mode or within the material definition as structural (global) damping. In this study, the latter was implemented using the Abaqus Rayleigh damping model, where damping $[C]$ is composed of two parts, α_R and β_R, respectively proportional to the mass and stiffness matrices, $[M]$ and $[K]$ [100], equation (6.1):

$$[C] = \alpha_R[M] + \beta_R[K] \tag{6.1}$$

Rayleigh damping is related to the damping ratio, ζ_i, at the i-th natural frequency by equation (6.2) [88]:

$$2\zeta_i\omega_i = \alpha_R + \beta_R{\omega_i}^2 \tag{6.2}$$

At the high frequencies of ultrasonic vibration, the stiffness-dependant component, $\beta_R{\omega_i}^2$, dominates, and the mass-dependent component, α_R, can be neglected. The coefficient of the remaining stiffness-dependant part, β_R, can then be calculated from the damping ratio found experimentally in the EMA, section 5.3, for the operational frequency used in the steady-state analysis. The coefficient β_R calculated for the modal damping for the first longitudinal mode found by EMA is given in Table 6.1.

Frequency of L1 mode, from EMA	20127.5 Hz
Damping ratio for L1 mode, from EMA	0.0472 %
β_R	7.46453E-09

Table 6.1 - Rayleigh damping coefficient calculation

The adjusted force transducer FE model retained the material properties developed in section 4.2.

6.3.4 Boundary condition definition for steady-state analysis

An electric potential BC on the positive side of the piezoceramic disc was defined as a sinusoid with amplitude of 1 V, and a frequency corresponding to the frequency sweep intervals. The negative side of the disc received a constant BC of 0 V. After calculation of the response at this voltage, the amplitude was adjusted iteratively to achieve the desired displacement at the tip of the horn, to correspond to the experimental displacement intervals. This can be viewed as the simulation equivalent of increasing the power (voltage) on the ultrasonic generator to obtain the desired displacement output.

6.3.5 Variables at resonance of simulated L1 mode

By plotting a variable such as horn tip displacement over the frequency sweep, the resonance curve can be observed. All variables such as stress or force exhibit the same peak at the model's L1 resonant frequency of 19,940 Hz, Figure 6.9.

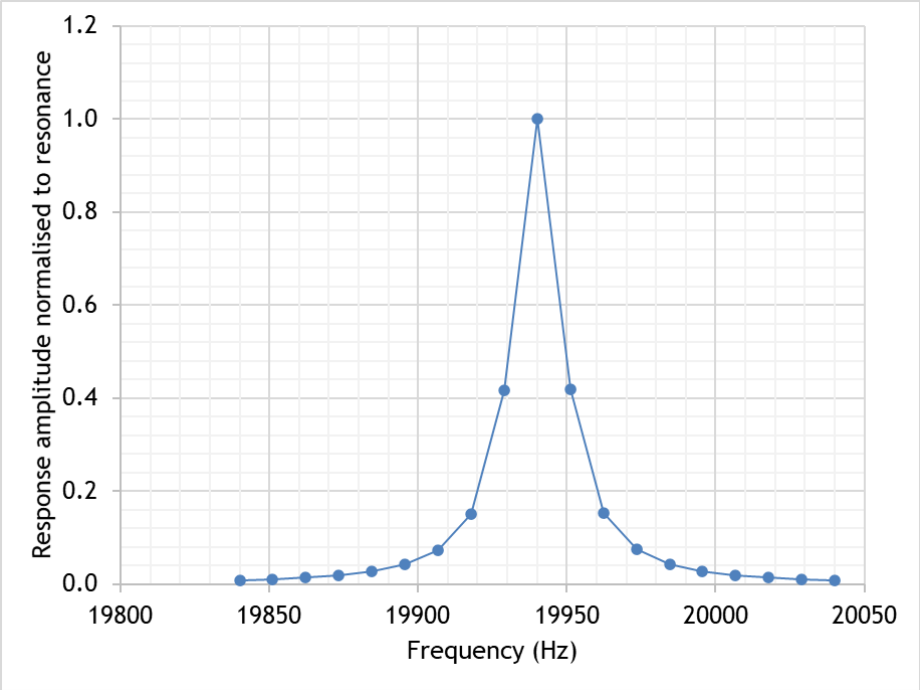

Figure 6.9 - Resonant peak in simulated frequency sweep

In the results that follow, only the variables from the resonant model run were plotted. As the ultrasonic generator was enabled to track the resonance of the ultrasonic transducer and coupled structures, results were extracted at the L1 resonance in the simulation.

6.3.6 Extracting axial force from FE model

For comparison with experimental force transducer data, a simulated equivalent to the instrument's indicated value was developed. As described in Chapter 4, the transduction element of the piezoelectric force transducer consists of a pair of piezo-crystal rings located at the centre of the transducer. To mimic this in the simulation, internal force was calculated at the mid-plane of the force transducer FE model. In Abaqus this is performed by the *Free Body Cut* tool, Figure 6.10, which sums the nodal forces on a specified cutting plane.

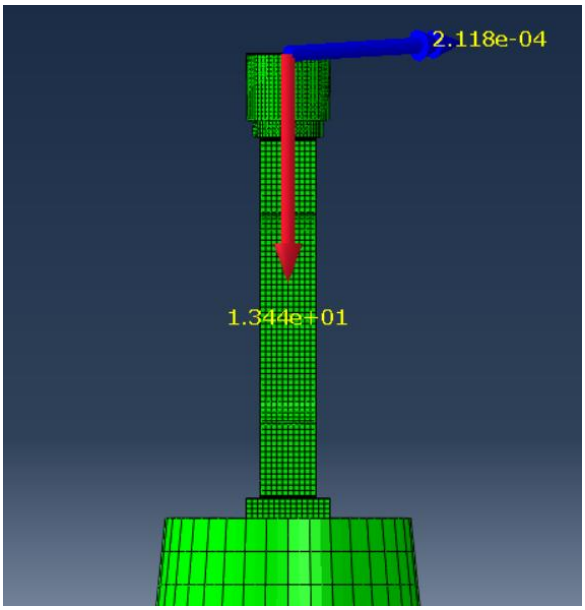

Figure 6.10 - Free Body Cut tool

When the horn tip displacement amplitude was 10 µm at 20 kHz, the force measured at the force transducer was approximately 1600 N. For the same frequency and displacement, in the FE model without the implementation of EMA-tuned joint compliance, the force at the mid-plane of the FE force transducer model was 590 N. Once the FE model was adjusted to replicate the experimental velocity ODS, this force changed to 1525 N.

6.3.7 Comparison of real and simulated force measurement

To explore this further, the force from the piezoelectric force transducer was recorded at increasing values of nominal displacement as indicated by the ultrasonic generator, ranging from 0 to 7 µm. The displacement amplitude of the horn's tip was measured by 3D-LDV.

The test was replicated in the simulation by controlling the voltage amplitude on the electric potential boundary condition, increasing the resulting displacement amplitude to mirror the experiment. The simulated force measurement was calculated using the Free Body Cut tool to find the internal force on the mid-plane of the FE force transducer, at each voltage amplitude. The simulated and experimental data are presented in Figure 6.11.

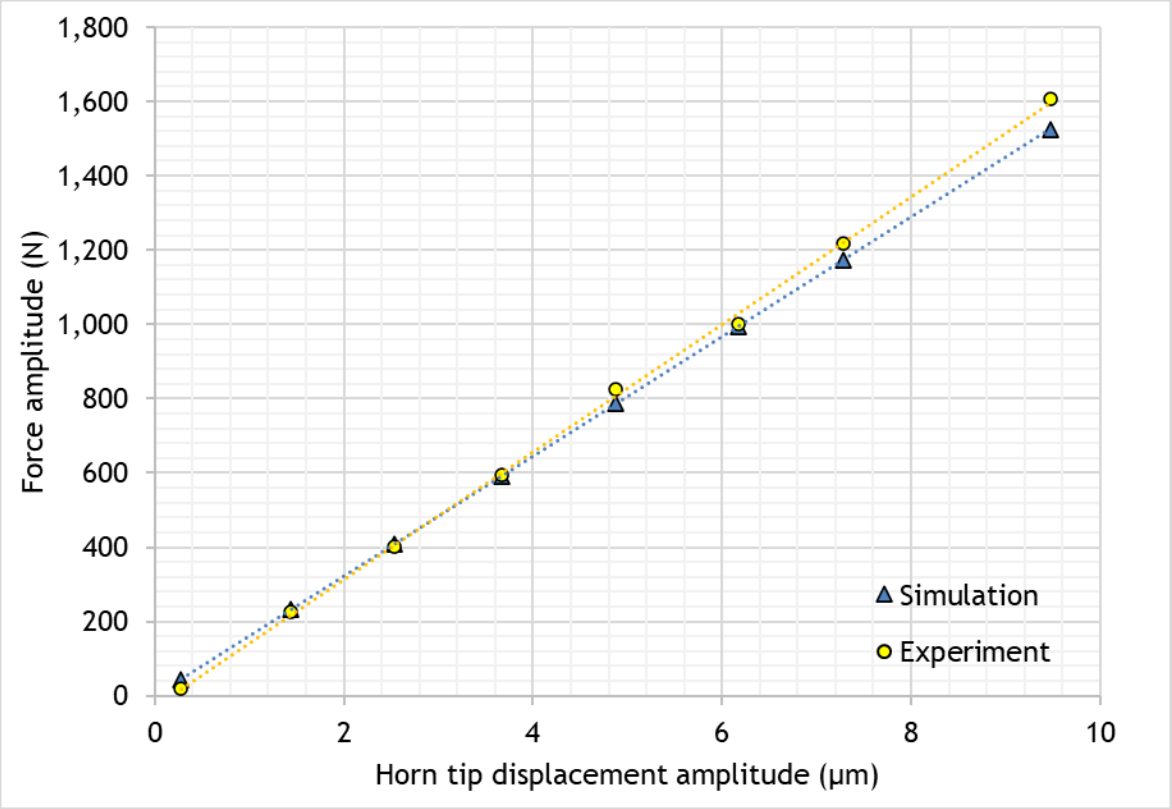

Figure 6.11 – Real and simulated force measurement against displacement

Figure 6.11 shows that the force-displacement relationship is linear. The simulated data exhibits a lower gradient by 5.8%. A difference in gradient suggests a systematic difference, for example due to small modelling errors, or that some non-linearity in the real structure has not been accounted for. This discrepancy indicates that the impedance of the horn-specimen joint varies with displacement amplitude (and so was not addressed by the EMA calibration). Yet this is a large improvement over the initial prediction of force, which was out by a factor of 2.6 at the 10 μm displacement amplitude. The good agreement between the experimental and simulated results supports the view that the EMA-FEA calibration method was successful.

6.3.8 Simulated magnification factor for force transducer structure

The FE model was used to find a simulated value for the force transducer's magnification factor, using the definition for the effect of the structure on the sensitivity of the PFT developed in Chapter 4. For the simulation this was interpreted as the ratio of the indicated force (at the mid-plane of the PFT FE model) over the measurand force (at the specimen-force transducer interface). This was compared to the previously estimated bounds from the lumped-parameter model and the rod approximation in Chapter 4, Table 6.2.

Prediction method	Magnification factor for force transducer mid-plane/force at input face
FE model	1.91
Lumped model	1.28
Homogeneous rod	1.77

Table 6.2 - Magnification factors from calculation and experiment

According to the numerical simulation, the analytical methods underestimate the amplification. It predicts that the frequency response of the PFT alone amplifies the measurand by almost a factor of two, at the L1 modal resonance frequency of the USTT. This represents a severe distortion of the measurement. The difference between the numerical and analytic approximations may be attributed to the inclusion of the mass and stiffness of the specimen attached to one end of the PFT, an extra impedance which must alter the response of the PFT.

A more accurate measurement of the amplification of force between the gauge section of the specimen and the force transducer was desired, and this will be addressed in the next chapter, where the relationship was verified experimentally by measuring the strain directly on the specimen.

6.3.9 Specimen stress profile

Going beyond the established quasi-static assumption of a tensile test that the force transducer reading is a valid measure of the constant force throughout the specimen, the 3D nature of the calibrated FE model can be used to predict the

stress distribution throughout the test structure. Figure 6.12 shows a full-field colour map of the normal stress in the direction of the specimen axis.

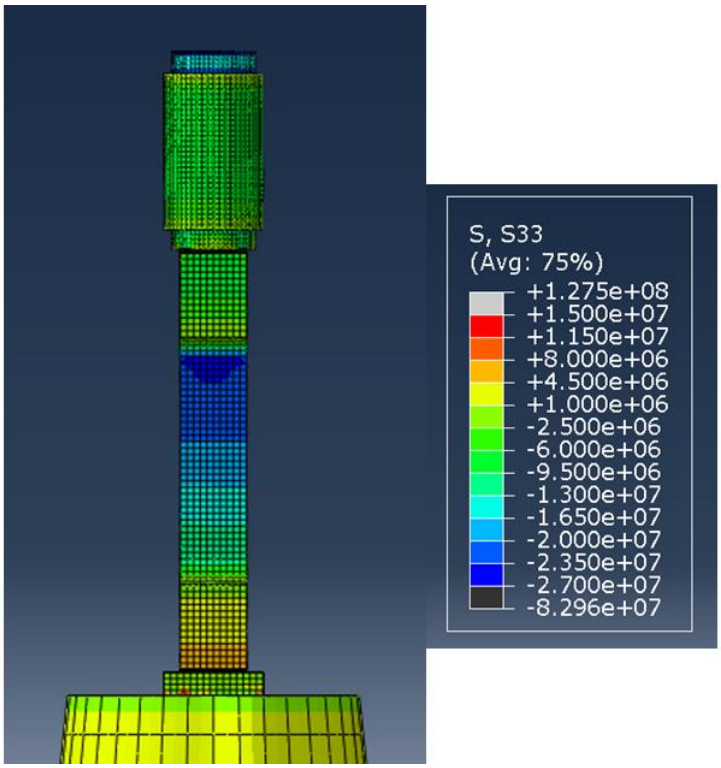

Figure 6.12 - Map of normal stress in specimen

For a better quantitative assessment the axial normal stress along the length of the specimen axis is shown in Figure 6.13. Two profiles are presented, from simulations with horn tip displacement amplitudes of 4.9 and 9.5 μm.

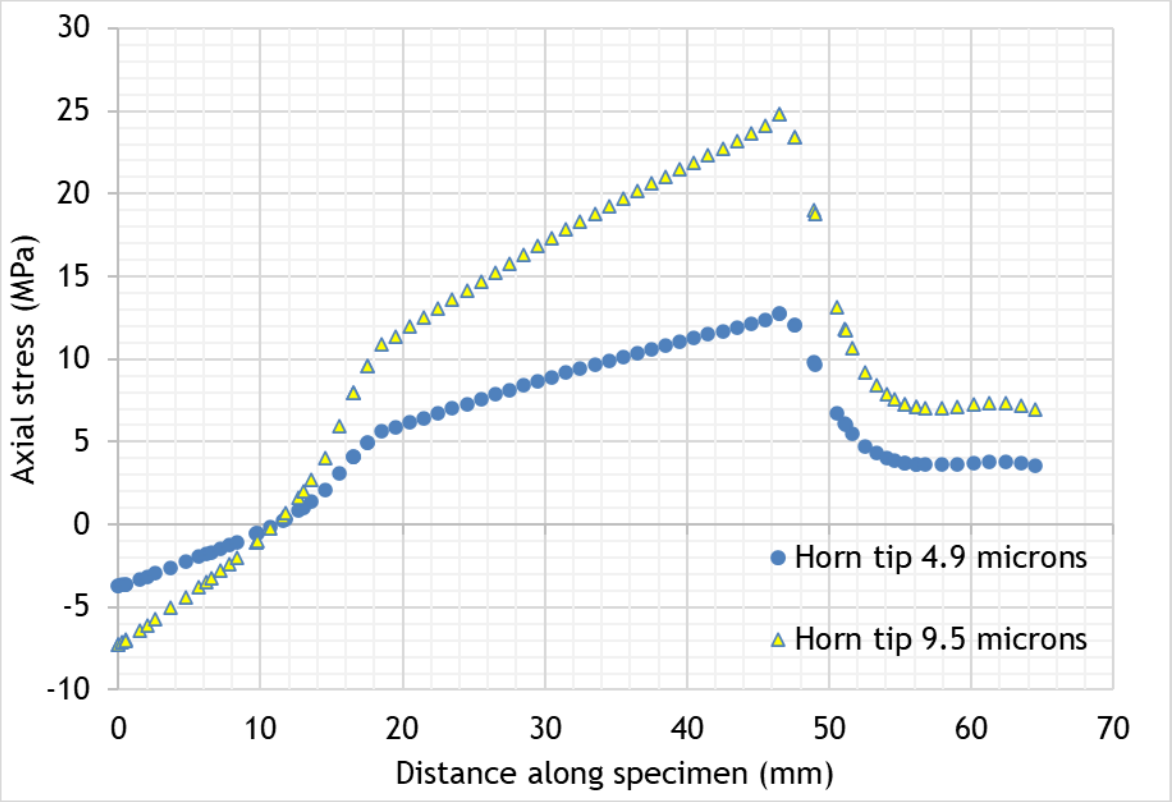

Figure 6.13 - Specimen axial stress profile

In contrast to the majority of the literature on APE, a prediction of the full-field distribution of dynamic stress throughout the specimen in an ultrasonic tensile test can now be examined. For a horn tip displacement amplitude of 9.5 µm, the stress amplitude along the gauge length varies from 11 MPa at the end adjacent to the horn, to 25 MPa in the root of the fillet at the end connected to the force transducer. The stress more than doubles from one end of the specimen to the other. This confirms the cautions of researchers who warned that the stress amplitude could not be assumed to be constant through the specimen [16], [17].

In the context of affirming the presence of the APE, when examining the stress data in an ultrasonic tensile the amplitude value of 25 MPa would be compared to the apparent drop observed in the mean flow stress. If it is less than this drop, it can be claimed that a genuine acoustoplastic effect has occurred.

6.4 Summary

Complimentary to the experimental characterisation of the vibration waveform in the preceding chapter, in this chapter a numerical model was constructed to predict the modal response of the USTT structure. By comparing the predicted

mode shape of the L1 mode to the EMA results, the FE model was calibrated, and was then used to investigate the difference in force between the specimen and the PFT.

The predicted L1 mode had a frequency of 19,940 Hz, against the experimental 20,116 Hz, a 0.87% difference. The predicted L1 mode shape did not replicate the EMA mode shape waveform until extra compliance was added to the joint between the horn and the specimen. This modification was successful in converging the simulated curve on the experimental waveform.

In a second experiment, the force measurement from the PFT was recorded for a range of vibration amplitudes. The test was simulated using the calibrated FE model, reproducing the linear relationship with a 5.8% difference in gradient. This supports the approach of using a calibrated FE model to investigate the effect of resonance on USTT apparatus, and predict the effect of ultrasonic excitation on the accuracy of the force measurement.

The FE model of the PFT embedded within the USTT test fixture finds a magnification factor of 1.91. This is significantly higher than the analytical models developed in Chapter 4 which could not fully account for PFT mounting in the wider test structure.

Over the length of the PFT, the simulated waveform agreed with the average gradient of the measured data, if not in the local variation. Differences were attributed to mismatch between the discontinuous internal structure of the real PFT, which can be observed in the jumps in the experimental waveform, and the homogeneous representation of the FE model.

The distribution of normal stress in the axial direction of the specimen was examined, as a colour plot and also plotted against axial location. This confirmed the inhomogeneous nature of the normal stress within the test piece. Consequences include the need to consider this effect when interpreting stress measurements; and that plastic deformation may be biased in proportion to the amplitude of the stress profile along the length of the gauge section.

7 Strain gauge verification of forces and mechanical gain factor

In the previous chapters, the investigations focused on the difference found between the PFT's indicated value and the measurand, which for the USTT is at the PFT-specimen interface. However, the force at this location is not ultimately the parameter of interest in the tensile test, which is the loading exerted upon the gauge section of the specimen. This will differ significantly from the PFT measurand. As discussed in the literature review, the dynamic force amplitude varies with the standing wave established in specimens by ultrasonic excitation [17]. In Chapter 6 the FE model was used to predict the level of variation of the oscillatory stress amplitude in the USTT test piece, Figure 6.13. It showed that the stress within the gauge length doubles from the end adjacent to the horn tip, to a peak at the end next to the PFT, demonstrating the large variation in dynamic load.

Strain gauges offer a method for measuring the dynamic stress directly on the gauge section, for a given ultrasonic excitation level. They work successfully in highly dynamic applications which require an extremely fast response, when used with an appropriate high-bandwidth amplifier [104], [105]. Strain gauges can measure elastic or plastic strain of up to around 5% [105]. However, in the ultrasonic tensile tests of soft aluminium specimens in this work, strains reach upwards of 23%, preventing their use in continuously monitoring specimen loading in the USTT. Any strain gauge method must therefore focus on characterisation of the elastic oscillatory deformation of the specimen.

In fatigue testing, test pieces very similar in shape to the dog-bone specimens used in this study are subjected to a cyclic load. Load cells are commonly used to measure the force in fatigue tests from which stress is calculated. The oscillatory load induces the same amplitude distortion error due to the frequency response of the test piece and force sensor structure, as described in Chapter 4. If any static preload is applied the load cell reports it correctly, as only the dynamic component of the loading is affected by the inertia of the transducer structure and fixtures.

However, the loading conditions in a fatigue test differ significantly to those in an ultrasonic tensile test. In high cycle fatigue testing, specimen loading is kept within the material's elastic limit, and the focus is on the number of cycles to failure by fracture. This is in contrast to the steady extension and plastic deformation of the specimen in a USTT. In addition, the frequencies used in fatigue testing are generally tens to hundreds of Hz, not the tens of thousands of Hz encountered in USTT. Yet the strategy evolved for coping with the effects of frequency response of specimen, force sensor and fixtures can be applied to the USTT.

The essential concept, set out in an ISO standard specifically for correction of load cell results in fatigue testing, is to use a 'replica' test piece of identical geometry to that intended for use, which has strain gauges applied to the point of maximum strain [87]. To compare the dynamic loading on the gauge length to the measurement from the PFT, the force on the test piece at the location of the strain gauge is calculated from the strain measurement. As the specimen is not loaded beyond the elastic limit of the test material a linear elastic constitutive relationship can be assumed to hold between the axial strain, ε_{SG}, measured on the surface of the specimen and the axial normal stress, σ_{SG} , over the specimen cross-section coincident with the strain gauge centroid, equation (7.1):

$$\sigma_{SG} = E \cdot \varepsilon_{SG} \tag{7.1}$$

Where E is Young's modulus of the replica test piece material. If the cross-sectional area of the test piece is A_{XS} then the internal axial force at the strain gauge location is equation (7.2):

$$F_{SG} = \sigma_{SG} \cdot A_{XS} = E \cdot A_{XS} \cdot \varepsilon_{SG} \tag{7.2}$$

Equation (7.2) applies irrespective of whether the strain measurement is static or dynamic. Shortly, it will be shown how F_{SG} can be used to calculated an empirical correction factor to convert from the oscillatory component of the PFT indicated value to the dynamic load on the gauge section at the location of the strain gauge. However, as described previously, the loading on a specimen in an USTT is composed of an ultrasonic vibration superimposed on the quasi-static

continuous load from the motion of the crosshead. As the difference between the PFT indicated force and the actual loading on the specimen is due to dynamic effects, any correction must be applied solely to the oscillatory component of the force measurement. The PFT force measurement F_{ind} is decomposed into its oscillatory and quasi-static components, respectively F_{PFT_osc} and F_{PFT_sta}, as shown in equation (7.3):

$$F_{ind} = F_{PFT\_osc} + F_{PFT\_sta} \tag{7.3}$$

Likewise, the force calculated from the strain gauge measurement, F_{SG}, must be resolved into oscillatory and quasi-static components, F_{SG_osc} and F_{SG_sta}, as in equation (7.4):

$$F_{SG} = F_{SG\_osc} + F_{SG\_sta} \tag{7.4}$$

An empirical correction factor κ can now be defined to convert from the oscillatory component of the PFT indicated value, F_{PFT_osc}, to the dynamic load on the gauge section, F_{SG_osc}, equation (7.5):

$$F_{SG\_osc} = \kappa \cdot F_{PFT\_osc} \tag{7.5}$$

In this study it was assumed that the superposition of the oscillatory and quasi-static components is linear, and that to find the total loading F_{axial} on the test piece during a USTT the correction factor κ can be applied to the oscillatory part of the force signal F_{PFT_osc}, before being linearly recombined with the quasi-static part, F_{PFT_sta}, equation (7.6):

$$F_{axial} = \kappa \cdot F_{PFT\_osc} + F_{PFT\_sta} \tag{7.6}$$

Where F_{axial} is restricted to the location of the strain gauges used to find κ. By definition, the quasi-static forces are equal: $F_{PFT\_sta} = F_{SG\_sta}$.

An assumption implicit in this method of correcting force data from a full USTT is that the correction factor developed from elastic oscillatory testing is applicable to oscillatory cycles of stress within which plastic deformation occurs. This author is currently unaware of evidence to support this view nor deny it.

Instead, it shall be argued that the correction factor κ originates in the structural impedance of the specimen, the PFT and the interface between them. Structural impedance itself depends on the properties of mass density and elastic modulus in a continuous medium such as the specimen, or component mass and stiffness in assemblies such as the PFT.

Within the specimen gauge section where the plastic deformation occurs, the effect of changes to geometric and material properties are considered. The geometry of the specimen contributes to the stiffness component of its structural impedance. It is possible some change in κ will be incurred by the extension of the gauge section during a USTT. This aspect has not been investigated, and would require further testing or simulation to evaluate the effect of changing the gauge section length. With regard to material properties, the properties governing plastic flow change continuously. However, considering that the mass density and elastic modulus of a material do not change regardless of plastic deformation [26], it may be argued that the structural impedance of the specimen material remains the same during plastic deformation in a USTT. It is possible this could be checked by measuring the speed of sound during plastic deformation.

During plastic deformation of the specimen, the properties of the PFT are unaltered and there will be no change in the component of κ contributed by it. The same is true of the interface joint, and the flared ends of the specimen where no plastic deformation occurs. Compared to the slender gauge section of the specimen, these parts together contribute the great majority of the inertia and stiffness (ie impedance) affecting the force signal reaching the PFT. It is therefore argued that κ will remain substantially unaffected by plastic deformation of the specimen.

During this study the test piece was not loaded beyond the elastic limit of the specimen material. In a set-up otherwise identical to a full USTT, the role of the crosshead was limited to applying a small preload on the specimen, and was stationary throughout the test. By applying the ultrasonic excitation to the specimen the empirical correction factor κ between the USTT test piece and the PFT indicated value was found. Then, during a full USTT where the specimen

was plastically deformed, the amplitude of the dynamic oscillatory part of the signal was multiplied by the correction factor and summed with the quasi-static part to reproduce the actual force on the specimen.

Some research has been carried out to move beyond the purely empirical correction set out in the standard, by developing transfer-function models of the replica specimen, load cell, fixtures and load frame [106], [107].

Strain gauges were employed in this study to:

- measure the dynamic (elastic) strain amplitude for a range of ultrasonic excitation levels;
- develop an empirical correction factor spanning from the gauge section to the piezoelectric force transducer; and
- provide an experimental strain measurement to compare with the FE model prediction of strain.

7.1 Method

Strain gauges are based on the principle that the electrical resistance of a metal wire is directly proportional to its cross-sectional area. Because of the law of conservation of volume, stretching the wire results in a proportional reduction in cross-sectional area, and a similar increase in resistance. Commonly, the wire in modern gauges is a serpentine track of metal, which is embedded within a plastic backing, Figure 7.1.

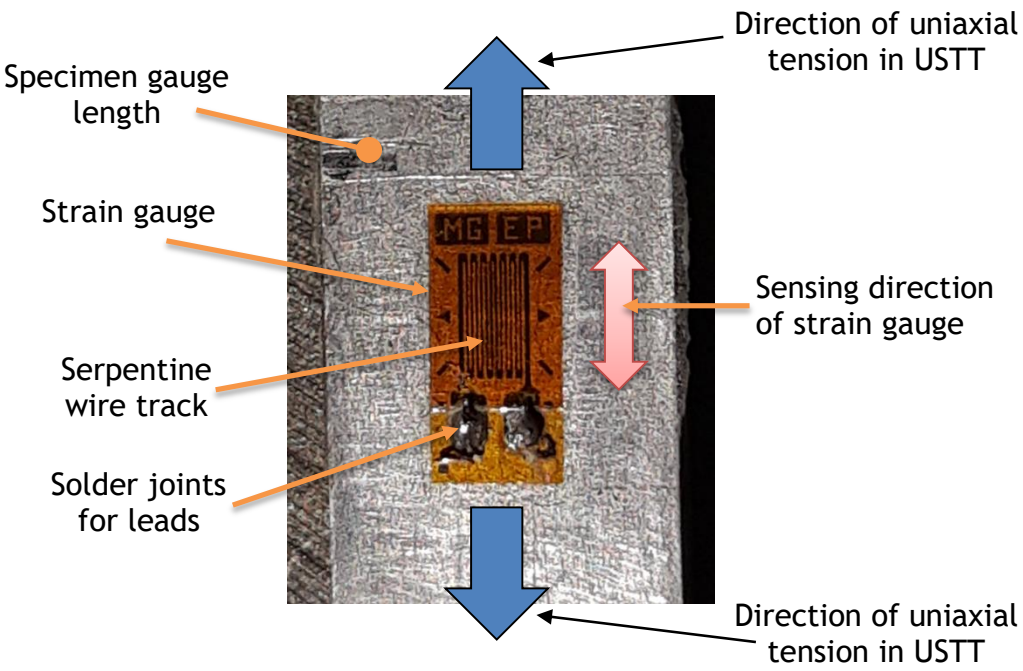

Figure 7.1 - Strain gauge sensing direction

To measure the strain of a part, the backing is bonded to the part's surface. When the part changes shape, the metal track stretches with the part's surface, and the change in resistance is measured by a voltmeter in conjunction with a bridge circuit.

The same ultrasonic tensile test apparatus described in Chapter 3 was used in this experiment. A replica test piece was constructed with geometry identical to the specimen intended for the ultrasonic tensile test (section 3.2.2), but from aluminium 5083-O, an alloy of higher strength than the soft aluminium commonly used in APE measurements. This was to avoid inadvertently exceeding the very low yield strength of the 1050-O aluminium specimen when collecting elastic oscillatory measurements. Though differing in strength, the tensile elastic modulus of aluminium alloys 5083 and 1050 are similar, respectively 70.3 GPa and 69.0 GPa [108], so the correction factor found using the stronger alloy can still be applied to results from the soft material with an error of under 3%.

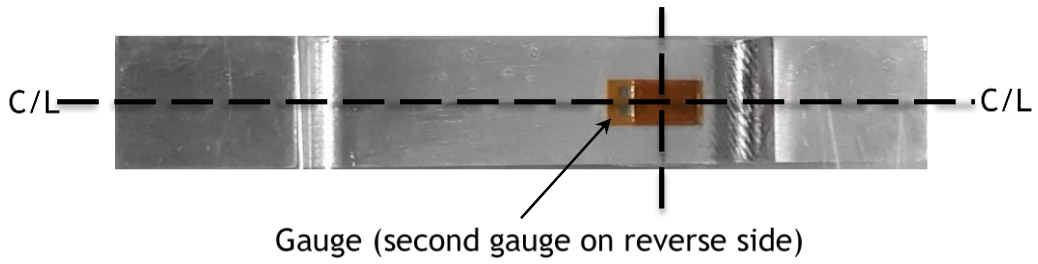

Figure 7.2 - Strain gauge location on specimen

Two uniaxial strain gauges (Vishay Micro Measurements EA-13-120LZ-120) were applied to the specimen, one on each face of the parallel section (Figure 7.2). The gauges had a gauge length of 3 mm and a gauge factor of 2.085 +/- 0.5%. The gauge factor, GF, of a strain gauge is the constant of linear sensitivity which the gauge manufacturer characterises and supplies with each batch of gauges. It is defined as the change in resistance R per strain [105], equation (7.7):

$$GF = \frac{dR/R}{\varepsilon_{SG}} \tag{7.7}$$

Where ε_{SG} is the strain in the sensing direction of the gauge, which is the direction of the long straight sections of the serpentine wire track (Figure 7.1).

Both gauges were oriented to measure the specimen's axial strain along the specimen surface centreline (Figure 7.2). Previous testing and simulation indicated that the strain in the parallel section would be highest adjacent to the force transducer. The gauges were therefore situated as close as possible to this end of the specimen.

The gauges were bonded to the specimen with cyanoacrylate adhesive, following manufacturer's instructions [109]. Lead wires were soldered to the gauge pads [110], ensuring the solder blobs remained as small as possible to minimise fatigue loading.

The two gauges attached to the test specimen – the 'active' gauges – were connected to form a Wheatstone bridge in ½ bridge configuration. By connecting them in diagonally opposite positions, R1 and R4 in Figure 7.3, any surface strain

in the specimen from bending was eliminated, while the axial strain was summed.

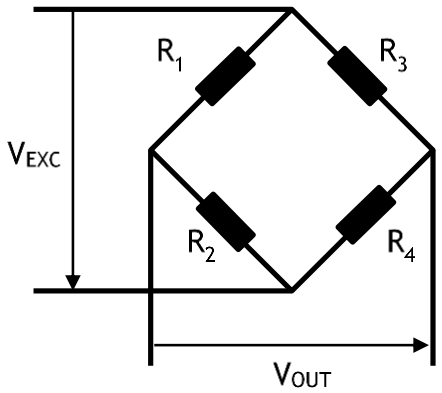

Figure 7.3 - Wheatstone bridge circuit schematic

The two ‘passive’ gauges at positions R2 and R3 in Figure 7.3 were attached to a second specimen in a manner identical to the test specimen. This specimen, however, remained unloaded throughout the test, instead providing compensation for any fluctuations in room temperature (Figure 7.4 and Figure 7.5). Solid materials change volume with temperature. A consequence of the physical effect of thermal expansion is that if the temperature of the test piece rises or lowers, it will expand or contract. A strain gauge applied to the test piece cannot discriminate between strain from thermal expansion and elastic strain. Fluctuations in room temperature which alter the test piece temperature will introduce an error into the strain measurement. This error was mitigated by attaching the two passive gauges R2 and R3 to a second identical specimen which remained unloaded throughout the test. The compensation specimen was held in close proximity to the specimen mounted in the test machine to ensure both test pieces experienced the same room temperature, and therefore matched in thermal expansion. Without loading, any strain detected by the passive gauges on the unloaded specimen was assumed to be due solely to thermal expansion which, through connection of the passive gauges in the R2 and R3 positions in the bridge, cancelled out the thermal error from the active gauges on the test piece proper.

An amplifier recorded the voltage difference across the bridge, amplified by a set gain of 1000, with the waveform recorded on an oscilloscope (Tektronix MDO 3014), Figure 7.4.

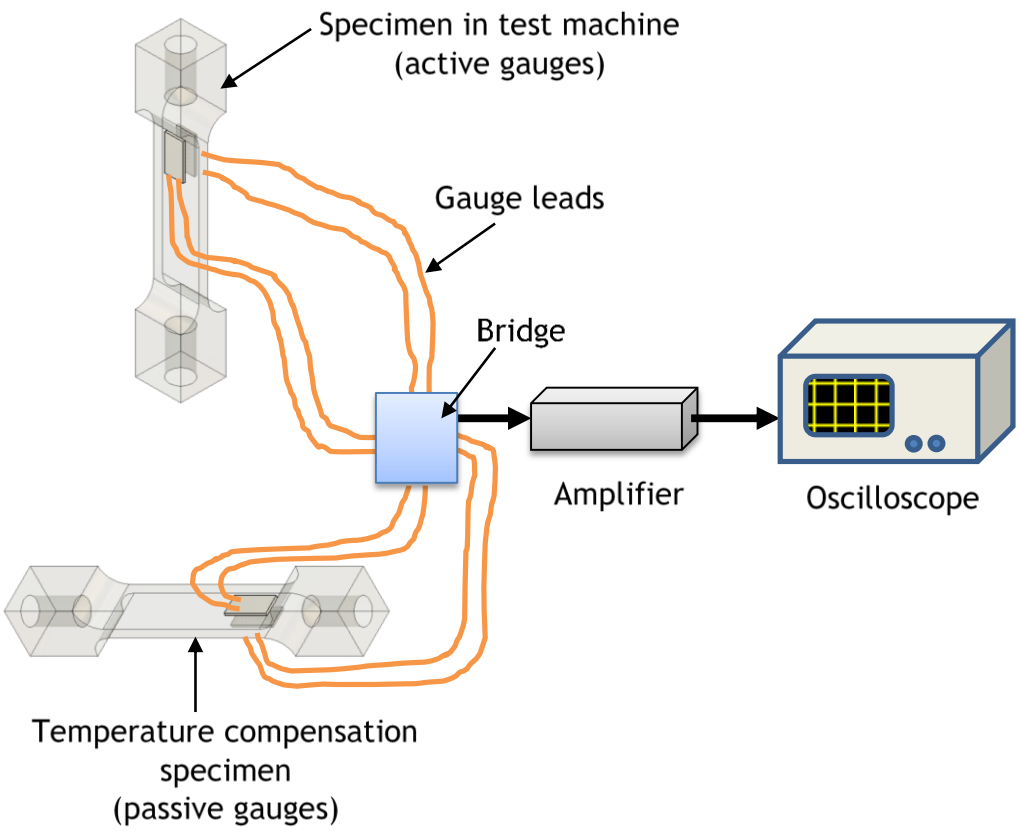

Figure 7.4 - Strain gauge recording apparatus

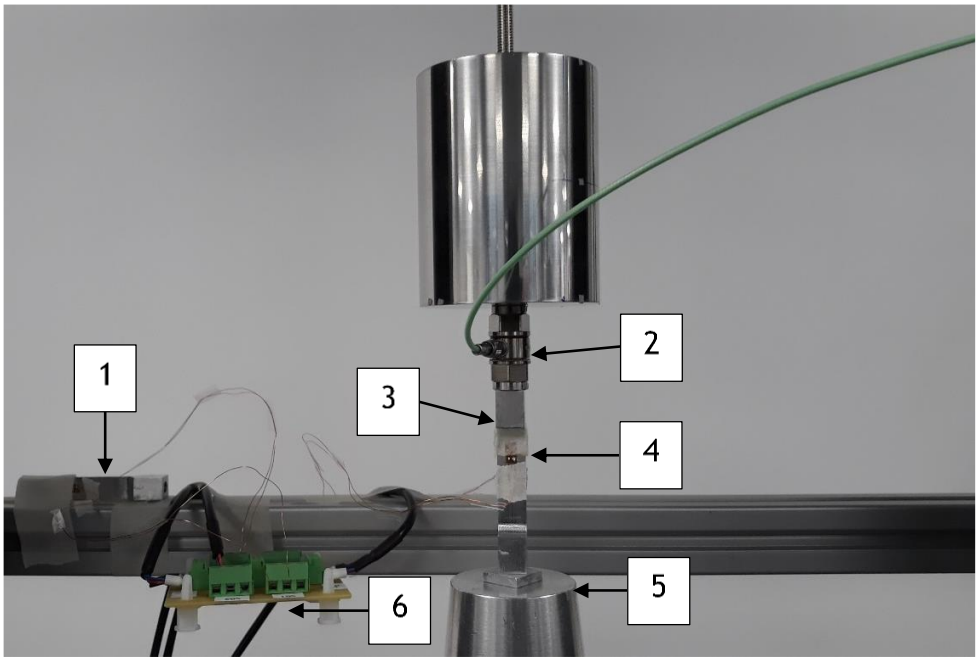

1. Temperature compensation gauge
2. Piezoelectric force transducer
3. Replica test specimen
4. Strain gauge (front)
5. Horn tip
6. Junction board

Figure 7.5 - Replica specimen and temperature compensation specimen installed on USTT

The measured voltage difference V_{AB} was related to the strain ε_{SG} measured by each gauge using the following relationship, equation (7.8) [105].

$$\varepsilon_{SG} = \frac{2}{GF} \cdot \frac{V_{AB}}{V_{EX}} \cdot \frac{1}{GAIN} \tag{7.8}$$

Where GF is the gauge factor, V_{EX} is the bridge excitation voltage and $GAIN$ is the gain the amplifier applies to V_{AB}. Note that this relationship is particular to the ½ bridge configuration.

Ultrasonic excitation was applied as it would be in the USTT, via the ultrasonic transducer and ultrasonic generator (Sonic Systems L500). The ultrasonic generator was used to apply varying levels of excitation, to elicit a response from the strain gauges and PFT over a range of vibration amplitudes. In a manner identical to the set-up in Chapter 5, a 3D-LDV was aligned to the horn tip and observed the real amplitude displacement achieved. The output from the

PFT was conditioned by a charge amplifier (Kistler Charge Meter Type 5015) and observed and recorded simultaneously with the strain signal and the three 3D-LDV signals.

7.1.1 Frequency response

Given the importance of measuring the true value of strain to this work, it was essential that the instrumentation and data acquisition systems caused no significant attenuation or distortion in the static-oscillatory signal; in electrical theory terms, a bandwidth of zero (DC) to 20 kHz or more [111].

To be certain of achieving the required gain and bandwidth a custom amplifier was constructed. Amplification was carried out in three stages, and the frequency response of each stage was checked and modified. Inside the amplifier, the voltage difference across the bridge was measured by an Instrument Amplifier (AD623) with gain set to 10. The signal was passed through two further op-amps, each with a gain of 10, resulting in a total gain of 1000. By splitting the gain across each of these three components the predicted -3 dB cut-off frequency of the whole amplifier system was approximately 50 kHz.

To quantify the amplifier's cut-off frequency, and also evaluate the gain attenuation at 20 kHz, a frequency response test was carried out. A signal generator (Agilent 33500B Waveform Generator) was used to apply an excitation sine wave to the bridge, simulating the active strain gauge input.

To avoid introducing error from the frequency response of the DAQ device, an oscilloscope capable of measuring radio frequency signals in the MHz (Tektronix MDO 3014) was used to measure the voltage amplitudes of both the excitation input signal and the response output from the amplifier. The amplifier's frequency response curve was created by finding the amplitude ratio δ (response amplitude divided by excitation amplitude) whilst varying the excitation frequency from 1 kHz to 60 kHz (Figure 7.6).

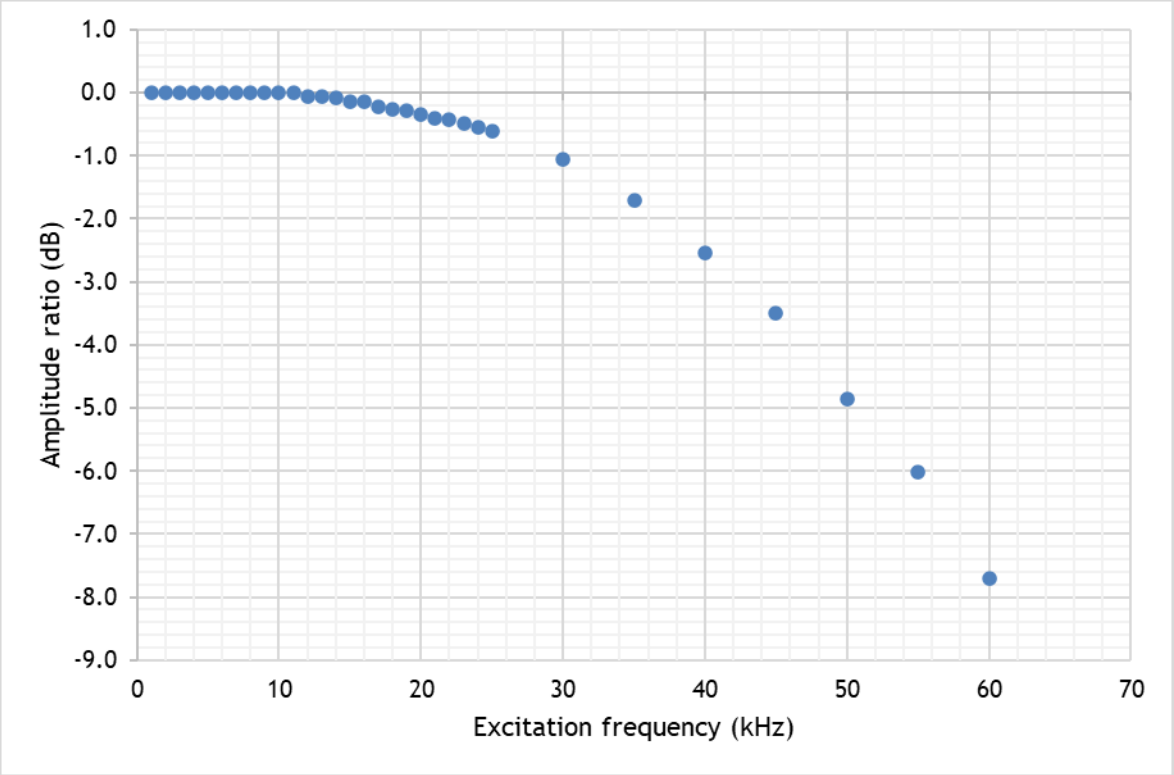

Figure 7.6 - Strain gauge amplifier roll-off curve - frequency response curve

The first noticeable change in the amplitude ratio occurs at 12 kHz, when the error is 0.006%. At the desired USTT frequency of 20 kHz, the amplitude ratio is 0.961 or -0.345 dB, an attenuation error of 4%. To compensate for this error the strain measurement data were multiplied by the inverse of the amplitude ratio δ, increasing the strain amplitude to the correct value. For calculating the strain from 20 kHz ultrasonic excitation, equation (7.8) was multiplied by $\frac{1}{\delta}$ to become equation (7.9):

$$\varepsilon_{SG} = \frac{2}{GF} \cdot \frac{V_{AB}}{V_{EX}} \cdot \frac{1}{GAIN} \cdot \frac{1}{\delta} \tag{7.9}$$

Electrical amplifiers and their roll-off curves are often characterised by the frequencies at which the gain drops by -1 and -3 dB [111]. These cut-off frequencies are tabulated below along with the 20 kHz frequency data (Table 7.1).

Cut-off gain (dB)	Cut-off frequency (kHz)	Amplitude ratio	Gain error
-0.35	20	0.961	4%
-1.00	30	0.891	11%
-3.00	43	0.708	29%

Table 7.1 - Strain gauge amplifier cut-off frequencies

As already mentioned in Chapter 5, when recording signals at ultrasonic frequencies care must be taken to avoid distortion of the signal by aliasing. The digital acquisition of a continuous signal involves sampling the signal at intervals of time. If the sample rate is low enough aliasing will result, where a signal of lower frequency is extracted from the real signal. To avoid this, a sampling rate greater than twice the highest frequency of interest (the Nyquist frequency) is required [112], though this presupposes a level of signal reconstruction post-test, and a rate over six times the frequency of interest is recommended. The amplifier and force transducer output were recorded using an oscilloscope with radio frequency capability (Tektronix MDO 3014). A sampling rate of 10^7 samples per second was used to resolve the strain signal in sufficient detail, whilst also exceeding the Nyquist frequency requirement.

Likewise, an LDV vibration velocity measurement was recorded using a PC-based oscilloscope (Picoscope 4424) with a bandwidth of 20 MHz, and a sampling rate set to 10^7 samples per second for the same reasons described above.

7.1.2 Frequency response of strain gauges

In general, gauges with short gauge lengths are more appropriate for dynamic testing where strain gradients and strain rates are high [105]. Shorter gauge lengths can reach higher frequencies, as their length is a smaller proportion of the wavelength in the test structure [112]. At 3 mm long, the gauge length of the gauges used in this experiment is just 1% of the wavelength of sound in aluminium, indicating their suitability for this test. A more systematic and detailed review of dynamic effects on strain gauges can be found in a study by Ueda and Umeda [104], who tested the overall frequency response of three standard gauge lengths. They identified sources of error related to geometry

(gauge length and width) and strain rate, and rise-time of the test structure, which comprised a gauge bonded to a test piece. Importantly, for the experiment discussed here, they found that the gauge factor – a measure of the sensitivity of a gauge – for a gauge length of 3 mm remained unchanged up to 100 kHz. Up to a frequency of 290 kHz, change in the gauge factor did not exceed 5%.

7.1.3 Thermal drift check

With the replica specimen mounted statically in the machine, a test was conducted to check the drift in the strain measurement resulting from the amplifier warming up. The amplifier output was recorded at intervals of approximately 15 minutes, Figure 7.7.

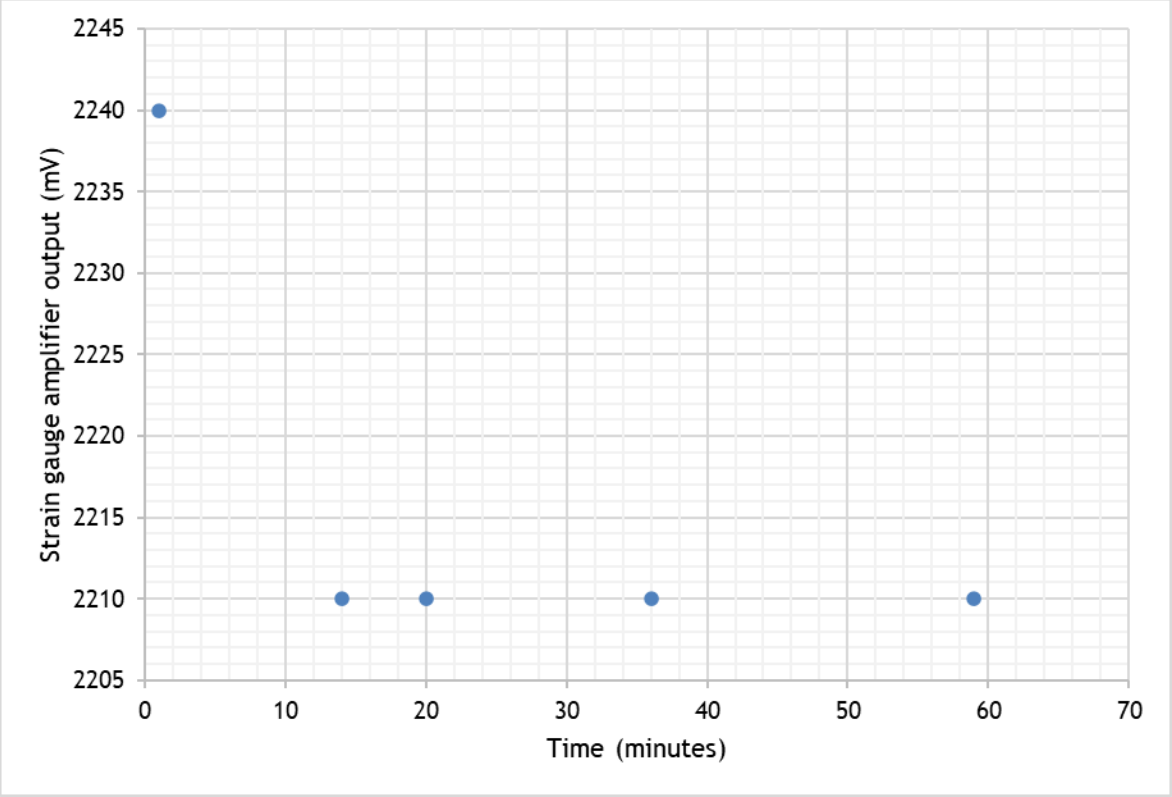

Figure 7.7 - Warm-up response of strain gauge amplifier

No appreciable difference could be discerned after 15 minutes. In subsequent experiments the amplifier was switched on 30 minutes before testing began to warm up.

7.1.4 Cross-sectional area of specimen gauge-length

In the calculations which follow of stress from the measured strain, the real cross-sectional area was used. For the rectangular section of the specimen gauge length, the cross-section area A_{XS} was calculated from equation (7.10):

$$A_{XS} = w \cdot d \tag{7.10}$$

Where w and d are respectively the width and thickness of the gauge length. Measurements of w and t were made using a digital micrometer on the specimen used as the loaded test piece in this study. They are presented in Table 7.2 with their respective average values and standard deviations. The uncertainty in the linear dimensions was taken to be three standard deviations, to define an uncertainty interval with a confidence level of 99%.

Measurement number	Width w (mm)	Thickness d (mm)
1	10.045	2.107
2	10.043	2.109
3	10.041	2.105
4	10.040	2.108
5	10.041	2.105
6	10.040	2.106
Average	10.042	2.107
Standard deviation	0.002	0.002
Uncertainty	0.006	0.005
Relative uncertainty	0.059%	0.233%

Table 7.2 – Measured dimensions of specimen gauge length

Table 7.3 presents the resulting cross-sectional area from equation (7.10) and the area uncertainty, which was found from the sum of the relative uncertainties of the linear dimensions.

Area A_{XS}	21.154 mm^2 (3 d.p.)
Relative uncertainty	0.291%
Area uncertainty	±0.062 mm^2 (3 d.p.)

Table 7.3 - Specimen cross-sectional area

7.2 Static benchmarking

A preliminary test under static load was carried out to check the strain gauges against the two commercial force sensors which had been calibrated by the manufacturer. Both the piezoelectric force transducer and load cell are expected to be accurate under a static load. From equation (7.2) the strain measurement was converted to a force using the measured cross-sectional area of the specimen (21.15 mm^2 ± 0.06 mm^2) and the elastic modulus for aluminium alloy 5083 of 70.3 GPa [108]. By measuring static force from the three measurement methods simultaneously the strain gauge system was benchmarked against the other two, providing a sense check and confidence in the strain measurement, Figure 7.8. Note that this was not used to calibrate the strain gauge system, as the gauges will produce an accurate reading if installed correctly.

Results

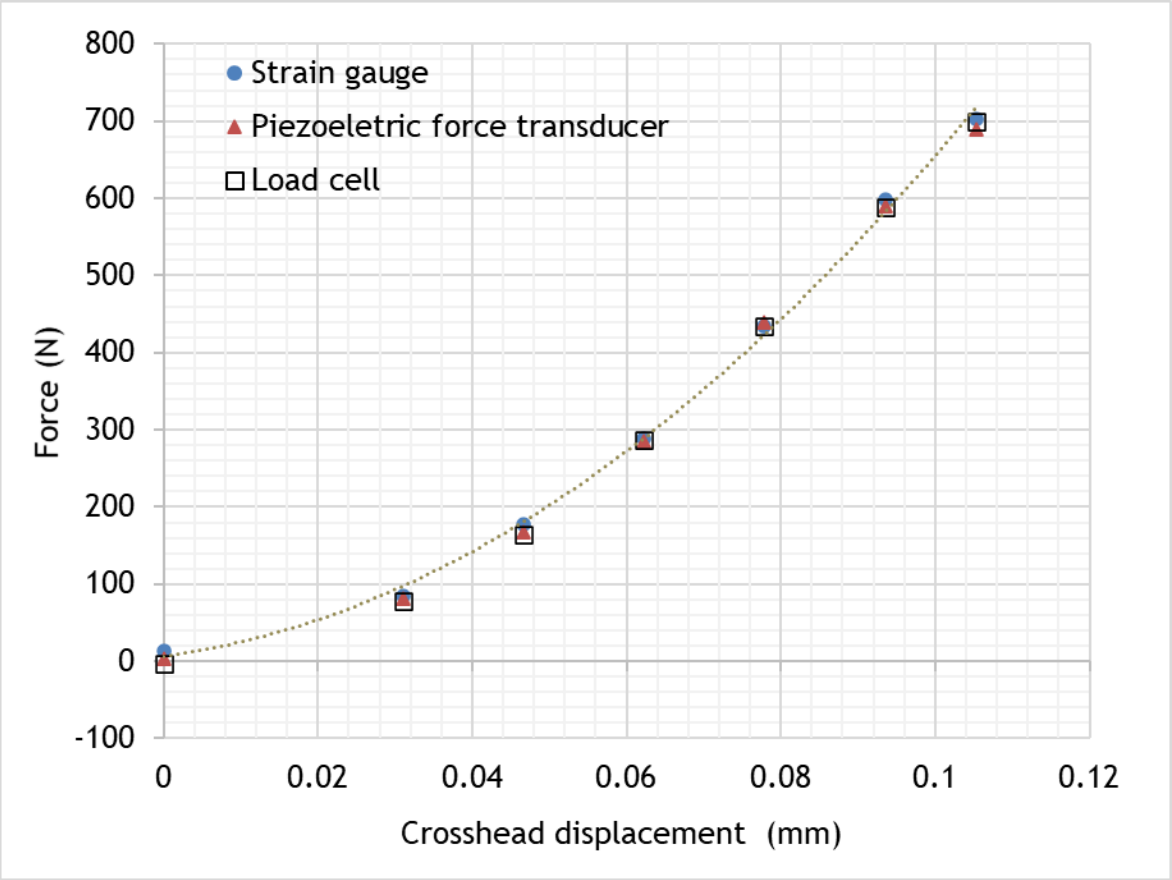

Figure 7.8 - Strain gauge static benchmark

The force-displacement data are plotted in Figure 7.8.

There is little difference between the force measured by the three instruments, particularly in the linear portion above 0.5 mm displacement. From this it may be concluded that the strain gauges and amplifier produce a force reading with an accuracy comparable to that of the other two commercial instruments. This is for the static case – any deviation between the instruments found in the dynamic test will then be attributable to inertial effects.

7.3 Dynamic test

The gauges used cannot exceed strains over 5%, preventing this system from being used to monitor the stress in the specimen in the full ultrasonic tensile test, where plastic deformation of up to 20% occurs. Instead, the quasi-static loading was limited to a static preload of 500 N (equivalent to 25 MPa in the specimen gauge section), to ensure the specimen remained elastic in tension once the oscillatory loading was superimposed.

The excitation displacement amplitude was increased to 1 μm pk-pk and after a short settling time the signals from the strain gauge amplifier, the force transducer charge amplifier and the LDV were recorded. This was repeated for displacement amplitudes up 8 μm pk-pk in 1 μm intervals. At 8 μm pk-pk the solder on the rear strain gauge broke, so the data from the final test was discarded.

7.3.1 FE model of dynamic strain gauge test

Using the FE model of the USTT created in Chapter 6, this dynamic test was simulated, to predict the force at the location of the strain gauges on the specimen as well as in the force transducer model.

The simulation of force measurement by the PFT using the Abaqus Free-Body Cut tool was described in Section 6.3.6. This method was repeated using the same FE model to extract the force on the cross-section of the specimen gauge section, at the location of the mid-point of the strain gauge, Figure 7.9.

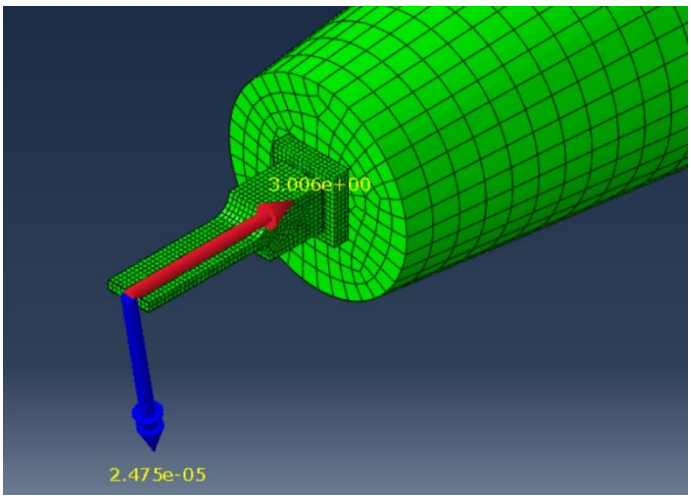

Figure 7.9 - Extracting simulated force at strain gauge location

In addition, the surface strain at the location of the strain gauge centroid was recorded.

The amplitude of the voltage boundary condition described in Section 6.1.2 was varied to match the horn tip displacement amplitude increments in the experiment (0.3 µm to 9.5 µm in approximately 1.3 µm intervals). Force at the PFT model and the stain gauge cross-section, and strain at the strain gauge centroid, were extracted for each displacement interval.

Results

The results of the experimental strain measurement and the simulated strain are presented in Figure 7.10. A significant high frequency noise component was present in the strain measurement signal, superimposed on the 20 kHz component of interest. To prevent it from distorting the evaluation of the peak-to-peak amplitude of the 20 kHz signal component, the noise was removed by smoothing the measurement data using moving average with a window of ten data points. The standard deviation over the window range was calculated for each moving average value, and averaged for that data set. This was repeated for each strain amplitude in Figure 7.10. The highest standard deviation found was 9.63 µ-strain, indicated by the error bars in Figure 7.10.

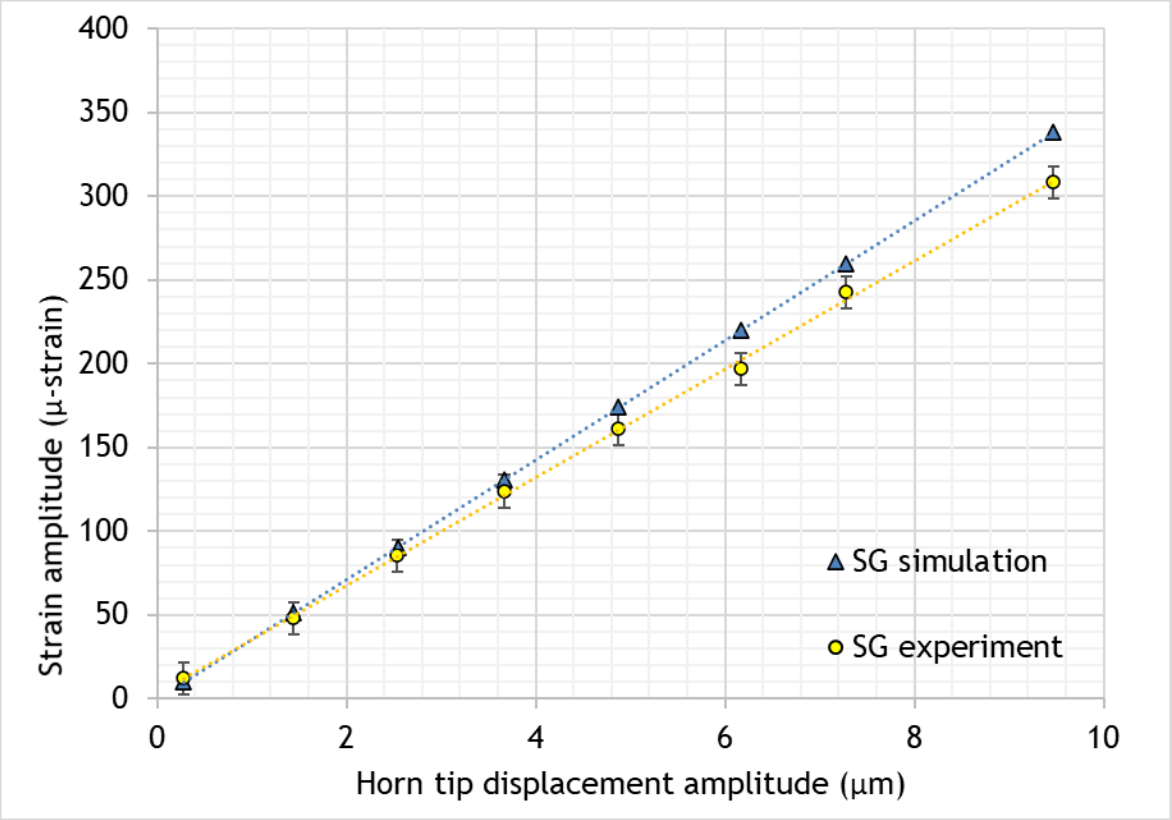

Figure 7.10 - Experimental and simulated strain measurement

In both experiment and simulation, the strain amplitude increases linearly with displacement amplitude. This is as expected – from any reference on waves in solids, the strain is directly proportional to the amplitude of the excitation [65]. There is, however, a difference in gradient; the gradient of the simulated curve is 10.0% greater that the experimental curve. Either the FE model method is overestimating the strain or the error lies with the dynamic strain measurement.

The difference in gradient suggests the error is systematic. Considering first experimental measurement error, which is proportional to the independent variable, the gradient difference could be due to such problems as gauge misalignment (where a component of the true axial strain is measured), or error in the signal conditioning parameters such as excitation voltage, gain or gauge factor. However, the agreement between the strain gauge and the force transducers in the static test suggests this is not the case. The distortion introduced by the frequency response of the amplifier has been accounted for. The sources of dynamic error that remain are the dynamic response of the gauge and the adhesive bonding it to the test piece [104], but as already discussed above, for the gauge used here this is negligible at the USTT frequency.

Aspects of the FE model which could produce a proportional error include material variables, geometry and the method of calculating strain at the location of the strain gauge. The values for elastic modulus, Poisson's ratio and density, all vital parameters in a dynamic simulation, were taken from the specification for aluminium 5083-O. Real values for the material used in this study can be obtained by performing a tensile test on samples from the aluminium billet used to make the test pieces. However, materials are made to strict standards and very little difference is expected.

Modelling the specimen based on measurements made on the test pieces after manufacture eliminated significant difference between the CAD geometry and the real specimens. Small differences which remain could contribute to the difference observed.

The model may not have fully captured the physics determining the dynamic motion of the USTT. For example, it is possible the joint impedance of the horn/specimen interface varies with the amplitude of the ultrasonic excitation, influencing the strain in the specimen.

Lastly, the magnitude of the strain reported by the FE model could be affected by the way strain was calculated from the elements in the vicinity of the strain gauge. The method by which strain was exported from the location of the strain gauge was eliminated as a source of error by a small investigation comparing the strain from the node at the centroid of the strain gauge, with the average of the strain from all the nodes in the area covered by the strain gauge. The difference found was negligible.

Further work is required to establish the sensitivity of the FE result to each of these parameters to identify those factors which require attention.

The experimental strain data in Figure 7.10 was used to calculate the force acting on the specimen cross-section at the location of the strain gauges. Force was calculated from the measured strain using equation (7.2) and the measured cross-sectional area of the specimen gauge length, Table 7.3. This is the desired measurand, not achievable with a force transducer, where the force is extracted at the location of the force transducer end. The force measured by the PFT,

simultaneously, is also shown in Figure 7.11, along with the simulated counterparts to both the strain gauge and PFT measurements.

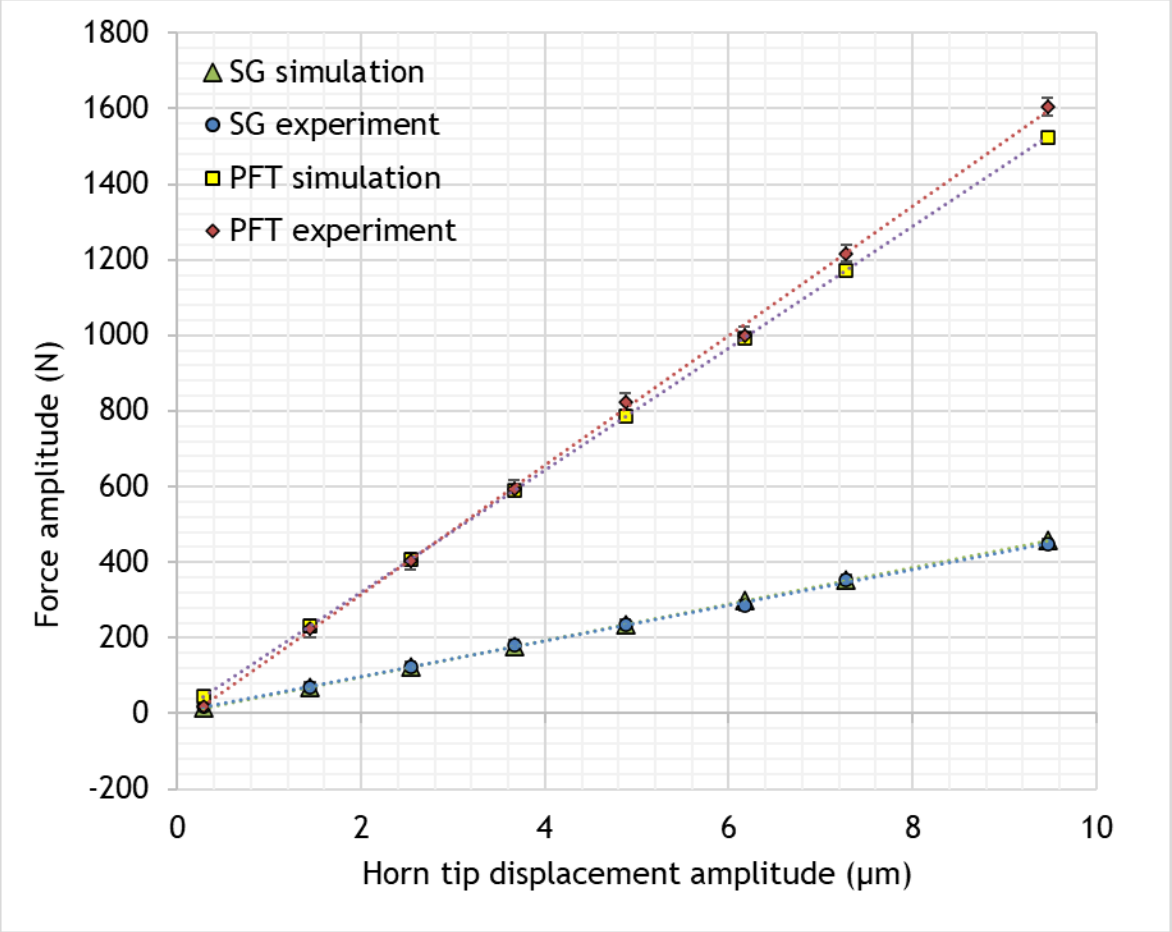

Figure 7.11 - Force from strain gauge and PFT, experimental and simulated

The real and simulated force-displacement data from the PFT, which have already been discussed in Section 6.3.7, show reasonable agreement with a difference in gradient of 5.8%.

The data for force calculated from the strain measurement, and the force extracted from the FE model at the strain gauge location, show a linear relationship with displacement amplitude, and are in very good agreement. This appears incongruous with the difference observed between the experimental and simulated strain values. However, the simulated force was not calculated from the simulated strain, but was extracted using the Abaqus Free Body Cut tool described in Section 6.3.6. It is thought that although the strain prediction is not in agreement with the measured strain, the FE model still predicts with accuracy the overall internal loading (stress) within the specimen. The FE method is formulated on the assumption of equilibrium between internal stress

and the imposed loading (in the case of the USTT simulation, the dynamic loading from vibration). FE software calculates the strain required to achieve equilibrium with the imposed loading, and so the stress predicted is correct even if the strain calculated differs from that measured in experiment.

It was observed from Figure 7.11 that the force measured by the PFT was much larger than the force derived from the strain gauge data. These variables have already been defined previously as F_{PFT_osc}, the oscillatory component of the indicated force, and F_{SG_osc}, the measurand of interest in this study. The amplitude distortion between them was examined by calculating the amplitude ratio, equation (7.11):

$$\alpha = \frac{F_{PFT\_osc}}{F_{SG\_osc}} \tag{7.11}$$

This is similar to finding the frequency response as the ratio of output amplitude over input, discussed earlier. It is also similar to the magnification factor found from the lumped-parameter models of the PFT in Chapter 4.

The calculation was repeated for the same forces in the FE model, with the results presented in Figure 7.12.

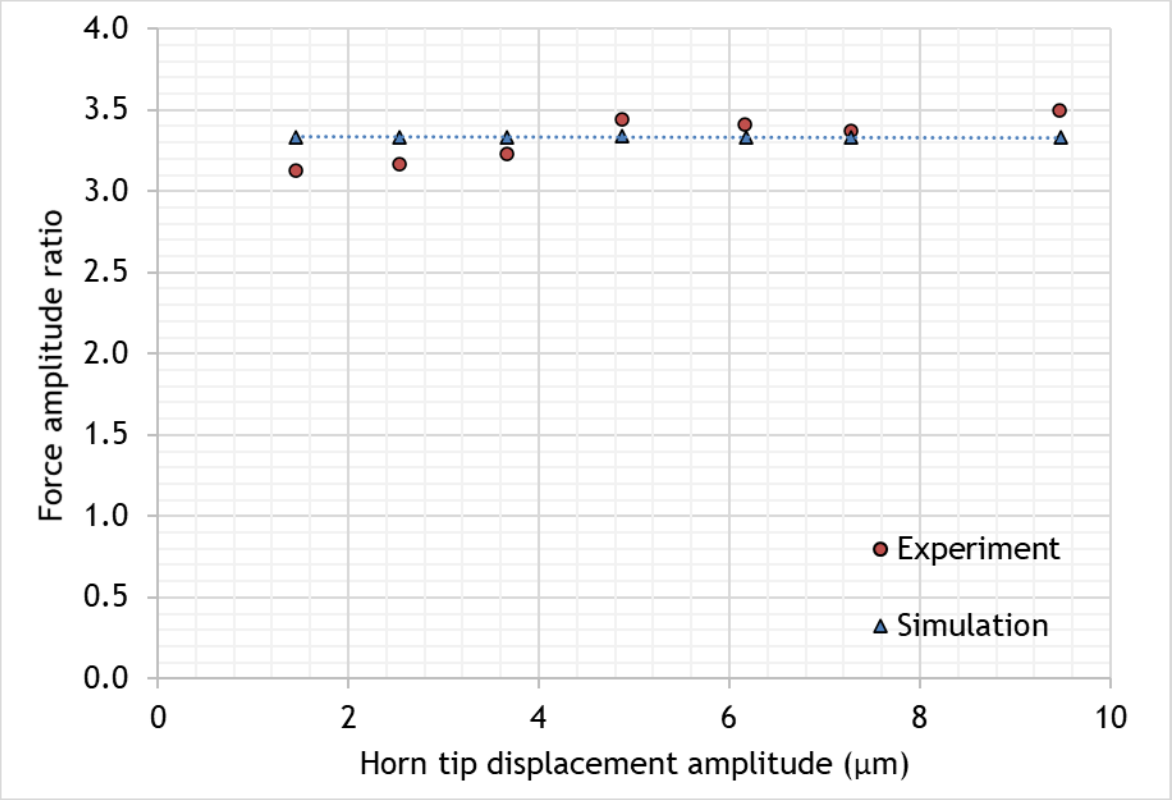

Figure 7.12 – Amplitude ratio - experiment against simulation

In the experiment the force amplitude ratio ranged from 3.13 to 3.50 (3sf), with a mean value of 3.32 and standard deviation of 0.15. The experimental amplitude ratio was very sensitive to variation in the data derived from the strain gauges and force transducer, resulting in the substantial scatter observed in the data points. The first data point in Figure 7.12 was removed, as the low signal-to-noise ratio at the lowest amplitude produced a small amplitude ratio inconsistent with the rest of the data. The FE model predicted a constant value of 3.33 for all horn displacement amplitudes.

Despite the variation in the measured amplitude ratio, the general trend agrees broadly with the simulated data points, and the mean value matches the simulation very closely. Currently, the FE model appears to provide the most reliable basis for estimating a correction factor.

The correction factor κ was defined at the start of this chapter in equation (7.5) as the coefficient required to convert the PFT indicated force value to the force on the gauge section, $F_{axial} = \kappa \cdot F_{PFT\_osc} + F_{PFT\_sta}$. This is simply the inverse of the amplitude ratio α defined by equation (7.11), as shown in equation (7.12):

$$\kappa = \frac{F_{axial}}{F_{ind}} = \alpha^{-1} = \frac{1}{3.33} = 0.300\ (3sf) \tag{7.12}$$

This study also demonstrates that a strain gauge system can be used in a USTT, despite the very high accelerations endured by the strain gauge and electrical connections. Though strain gauges are commonly used in mechanical testing, even at very high strain rates such as in Split Hopkinson Pressure Bar testing [77], APE has not previously been investigated using strain gauges applied directly to the specimen. They have been applied to other parts of the stack such as the horn [16].

7.4 Application of amplitude correction factor to ultrasonic tensile test

Ultrasonic tensile testing was carried out on specimens made from a commercially pure aluminium (1050-O). This form of aluminium, albeit in slightly different grades, has been used in studies of APE. Several of these investigations have found evidence of acoustoplasticity which could not be explained by other effects such as stress superposition or friction reduction, e.g. [10], [14], [15].

A preliminary test was conducted in which the excitation was applied in short bursts, to identify the minimum displacement amplitude needed to induce acoustoplasticity. The peak-to-peak displacement amplitude was increased in steps of approximately 2 μm, from 2 μm to 13.5 μm (pk-pk). The input displacement was recorded throughout the test using a 3D-LDV to measure the velocity of the base of the specimen at its junction with the horn, in a manner identical to that described in the EMA experiment, Chapter 5.

True strain was calculated from the recorded crosshead displacement over the parallel length of the specimen (30 mm) using equations (3.2) and (3.3). True stress was found from the force measurement, the measured cross-sectional area and the true strain, using equations (3.1) and (3.4). The stress data were then corrected using by multiplying by the correction factor $\kappa = 0.3$, calculated in equation (7.12).

To examine the quasi-static part of the stress, the mean value of the oscillatory ultrasonic frequency component of the force signal was found by applying a

moving average smoothing function as an operation performed in post-processing calculations (MATLAB).

From the 3D-LDV velocity data the displacement of the base of the specimen was derived.

Results

Figure 7.13 shows true stress plotted against true strain for the stepped displacement amplitude test. There are three curves: the true stress found from the force measurement (blue line); the true stress multiplied by correction factor κ (orange line); and the mean true stress (yellow line).

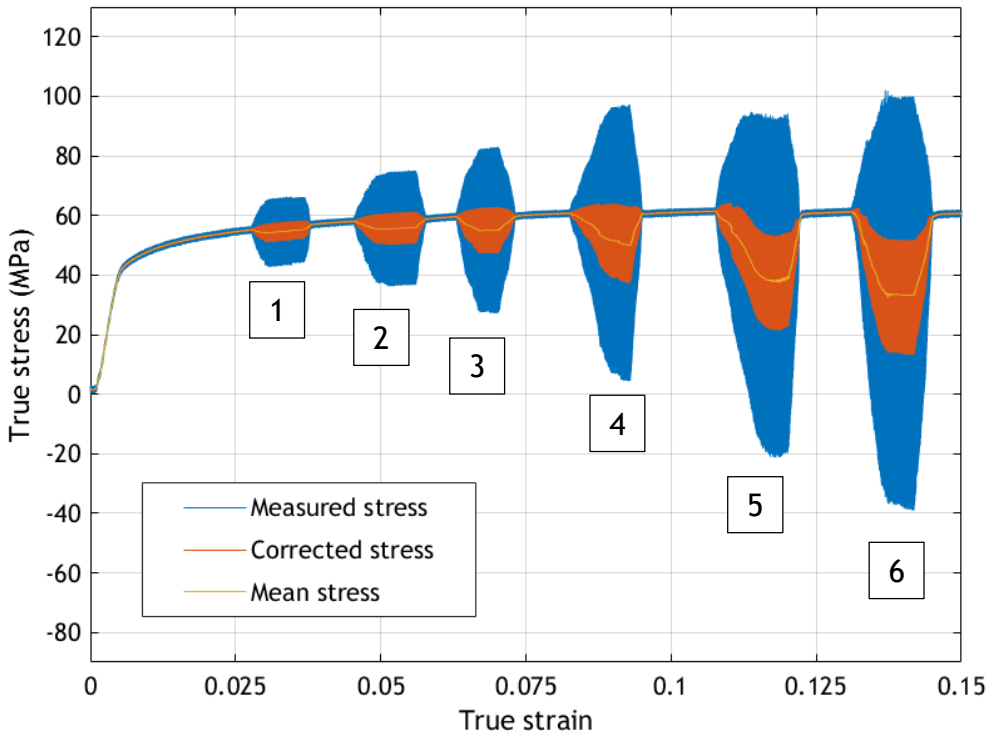

Figure 7.13 - USTT with stepped displacement amplitude

In Figure 7.13 there are six bursts of ultrasonic excitation numbered 1 to 6, each representing an increase in excitation displacement amplitude. At the 5th burst (displacement amplitude of 12.3 µm, achieving oscillatory stress amplitude of ~17 MPa) the corrected true stress dips below the trajectory of the flow stress expected, considering the path of the curve immediately preceding it. The difference is approximately 8 MPa. The same observation is made in the 6th burst

(displacement amplitude of 13.4 µm, achieving oscillatory stress amplitude of ~18 MPa), showing a decrease of 10 MPa.

A second test was then conducted on a specimen of the same material, with the displacement amplitude held constant at 14.0 µm, to exceed the values which prompted the APE in the preliminary test. The same procedure was used to calculate true stress from the force data, the corrected true stress, and the mean of the true stress, shown in Figure 7.14.

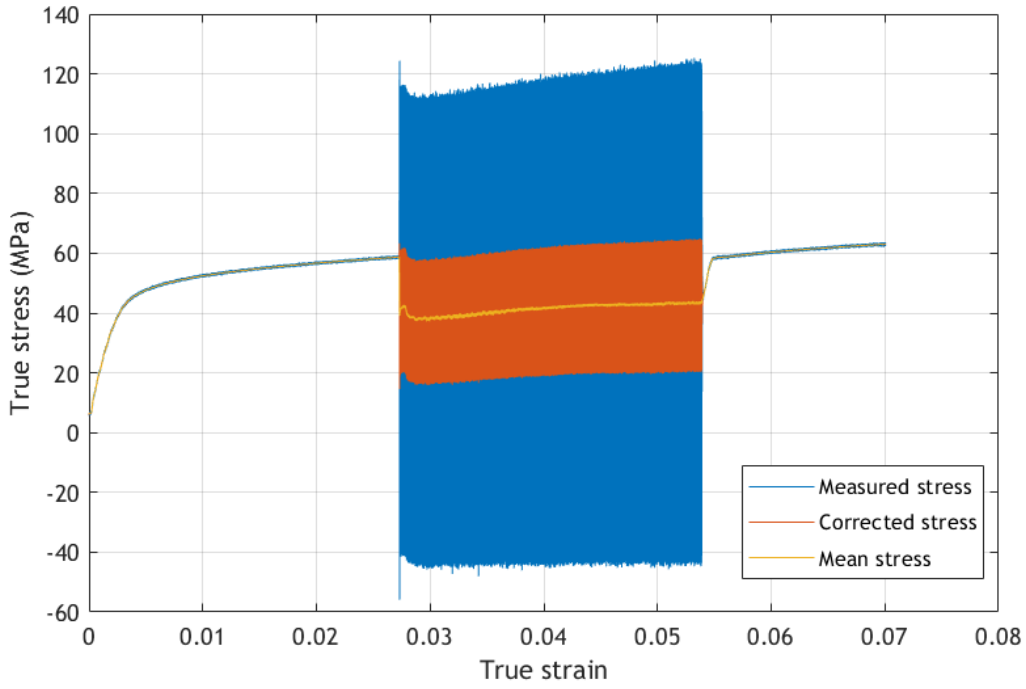

Figure 7.14 - USTT with constant displacement amplitude

It was found that the 14.0 µm displacement achieved an oscillatory stress amplitude of approximately 23 MPa over the duration of the US burst. The flow stress drop observed in Figure 7.13 was not replicated in this test. The peaks of the corrected oscillatory stress continue from the yield stress level achieved immediately before ultrasonic excitation began, and continues on a path similar to that expected without vibration. Repeating the test did not alter this observation. Therefore, in this case, the APE was not observed. It remains to be proved if higher amplitudes over a sustained period will elicit acoustoplasticity.

Many materials exhibit significant strain-rate dependence. The pure aluminium tested in this thesis is no exception, with similar grades of commercially pure

aluminium displaying positive strain-rate dependence in test from 10^{-4} to 10^{2} strain.s^{-1} [113]. A positive dependence on strain rate implies that flow stress will increase as strain-rate rises. If the superimposition of ultrasonic significantly increased the strain-rate on the specimen, it is expected the peaks of the oscillatory component of the stress measured would exceed the trajectory of normal yield strength. Such a phenomenon has been observed previously [72].

It is useful to compare the mean stress from the PFT force data to the stress calculated from the force measured by the test machine load cell, Figure 7.15. It was found that the results diverged, ending with a difference of around 3 MPa, or 5% of the maximum stress. Either one of the force sensors had accumulated a static drift.

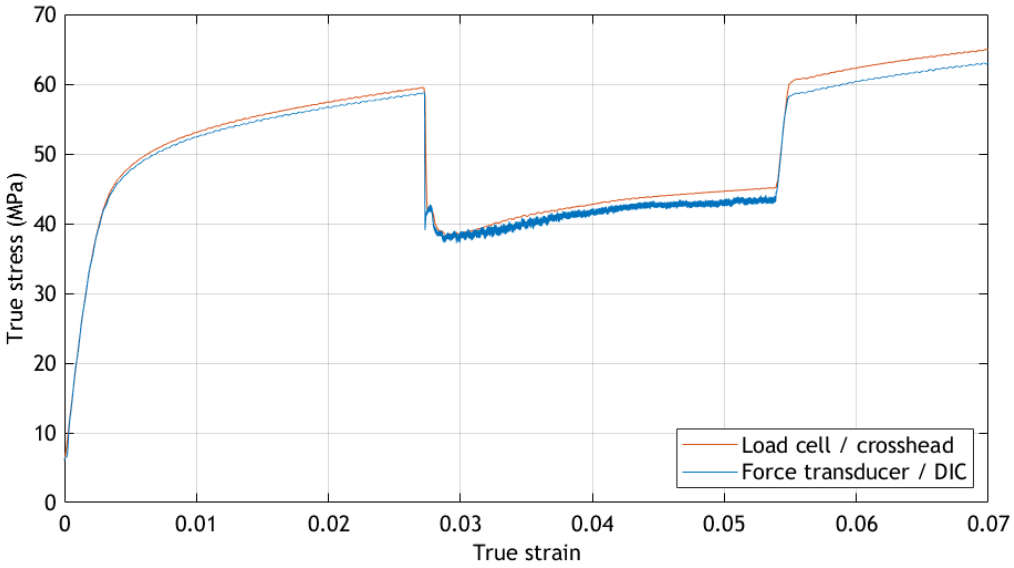

Figure 7.15 - USTT with constant displacement, PFT against load cell measurements

It is interesting to note that the measurement by the load cell matches the mean of the oscillatory signal. This is consistent with the theory that the effect of the characteristic frequency response of the load cell is to average out the oscillatory component of the force signal.

7.5 Summary

In this chapter, a method was developed in which strain gauges measured the strain on the gauge length of a specimen, and by calculating force from the strain measurement a comparison with the PFT force measurement was made.

A strain gauge signal amplifier which could measure the very high frequency strain signal from a USTT was developed. It was subsequently tested to characterise the amplitude distortion caused by its frequency response, calculating a correction factor to remove the distortion in post-test processing of the strain data. Thermal drift was also investigated.

Strain gauges were applied to a replica test piece made with identical geometry from an aluminium alloy similar to the soft aluminium which was to be the main focus of ultrasonic tensile testing.

Before proceeding to testing with ultrasonic excitation, the specimen was loaded statically at difference levels of force. The force calculated from the strain measurement was compared to the PFT and the test machine load cell, confirming the correct operation of the strain gauge system.

A test was performed in which the replica specimen was excited with ultrasonic excitation as it would be in the USTT. The strain from the strain gauges and force from the PFT were recorded at increasing displacement amplitudes. When the strain measurement was converted to force, this data revealed a large difference between the amplitude of force on the specimen gauge length (the desired measurand) and that measured by the PFT (the indicated value). The amplitude ratio was found to be 3.32 on average.

The FE model developed in the previous chapters was used to simulate the strain gauge experiment, producing results which were compared to the experimental strain, force and amplification ratio. While the strain measurement and simulation differed in gradient by up to 10%, the strain gauge-PFT amplitude ratio from the FE model agreed well with the average experimental value.

The amplitude ratio of 3.33 from the FE model was used to find a correction factor for use in a full USTT with plastic deformation. In a USTT on a soft aluminium, where the displacement amplitude was increased in steps, a decrease in the flow stress was observed at displacement amplitudes above 12.3 μm. A USTT was then performed on the same material with the displacement amplitude held constant at 14 μm over a longer period, achieving an oscillatory stress amplitude of 23 MPa. In this case, APE was not observed.

Further work is required to explore the effect of specimen plastic deformation on the correction factor κ, verifying its applicability to the combined elastic-plastic strain experienced by the specimen in an USTT.

8 Full-field measurement of plastic strain in ultrasonic tensile test

As discussed in Chapter 3, the inhomogeneous loading imposed on the test piece in a USTT means that the plastic deformation cannot be assumed to be equally distributed throughout the specimen gauge length, as is normally the case in quasi-static testing. To discover the material behaviour under such loading the local strain must be measured. In this chapter the use of imaged-based full-field strain measurement by Digital Image Correlation (DIC) was explored as a technique to examine the plastic deformation over the whole gauge length of a specimen in an USTT.

Video extensometry measures the strain between two distinct points in the images. A method called Digital Image Correlation (DIC) goes further by calculating the strain across the whole of the specimen face. Such a full-field measurement could reveal real-time changes in strain evolution during ultrasonic excitation, along the specimen's entire length. By building on previous work, [85], DIC was used to derive the evolving strain field during an ultrasonic tensile test. To capture images of a quality sufficient for accurate DIC, a system was developed which captured images of very short exposure at intervals triggered at the same point in the oscillation cycle. The specimens were again a soft, commercially pure grade of aluminium.

8.1 DIC for vibrating specimens

Digital Image Correlation is an image matching algorithm specialised in tracking the deformation of structures [114]. It measures displacement by tracking the movement of a pattern on the object's surface from successive images. An image is composed of pixels, each one a separate record of the grey level. In DIC an image is chosen as a reference image (commonly the first image in the sequence) which is sub-divided into a grid of pixel subsets – illustrated in Figure 8.1 as the red box in the first image. By matching the grey levels in each subset, the DIC correlation algorithm then locates each subset in subsequent images (the red box in the second image in Figure 8.1), tracking their motion. A displacement vector field is then constructed by tracking the movement of each subset in pixels (the red arrow in Figure 8.1).

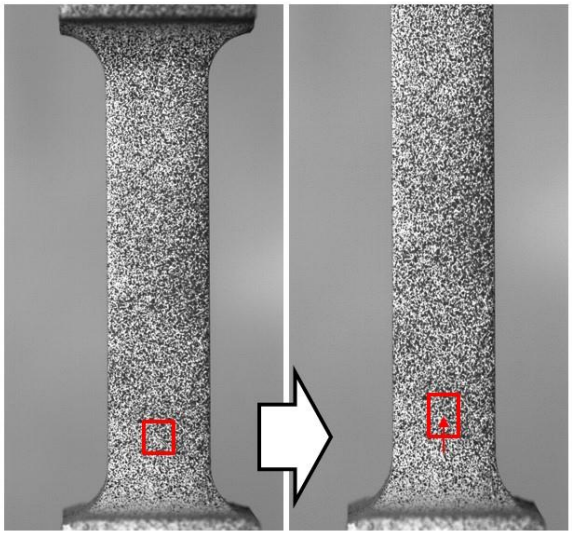

For the correlation to work the subsets must be individually unique, a condition which is easily met by spraying paint over the surface in a speckle pattern. Good contrast is also required, so a specimen for DIC must be coated first in white paint before a speckle pattern is created with black paint.

Figure 8.1 – pixel subset tracking in DIC

In this thesis, DIC was employed to evaluate plastic deformation over the quasi-static timescale. As DIC measures any motion of the speckles on the test object by detecting changes in pixel grey level, there is no way to discriminate between displacements from the quasi-static plastic deformation and the fast, elastic oscillatory motion. It is possible that the vibration motion, though not fully resolved, could introduce an error into the measurement of plastic strain on the quasi-static timescale. A strobe system was developed to eliminate this source of error.

The specimen, test machine and ultrasonic excitation apparatus described in Section 3.2 was used, with the addition of an imaging system and the strobe which will be described in detail shortly.

8.2 Apparatus

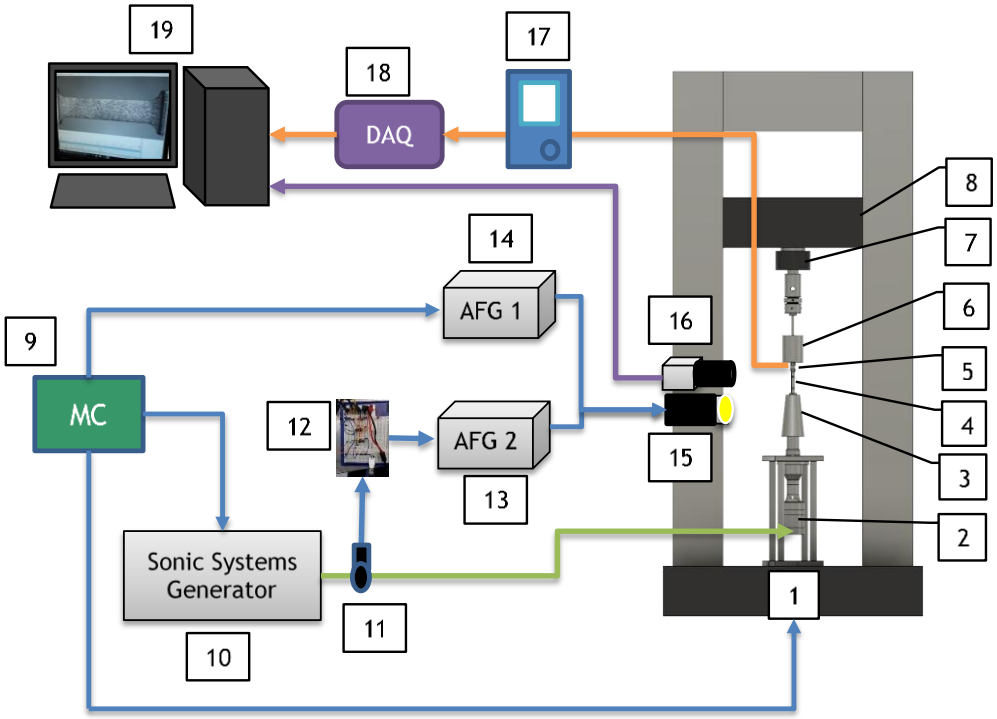

1. Test machine (Instron)
2. Ultrasonic transducer (Sonic Systems L500; resonant at 20 kHz)
3. Horn (amplifying displacement amplitude x2 at 20 kHz)
4. Test piece specimen
5. Piezoelectric force transducer (Kistler 9311B)
6. Isolating mass
7. Test machine load cell
8. Crosshead
9. Microcontroller (Arduino Mega)
10. Ultrasonic generator (Sonic Systems L500)
11. Current clamp
12. Signal conditioning unit
13. Arbitrary Function Generator (AFG) no.2 – vibration synchronous
14. AFG no.1 – fixed output
15. High-speed LED flash
16. Camera (PixeLink)
17. Charge amplifier (Kistler)
18. PC oscilloscope (Picoscope) for data acquisition (DAQ)
19. Desktop computer

Figure 8.2 - USTT DIC imaging system

The test apparatus can be divided into four independent systems: the tensile test (1, 4, 6, 7, 8); the superposition of ultrasonic vibration (2, 3, 10); the imaging system for DIC strain measurement (11 – 16, 19); and the piezoelectric force transducer and DAQ for dynamic force measurement (5, 10, 15). The first three systems were coordinated by the test-event sequence controller (9). The whole test machine was surrounded by a blackout curtain (not shown) to form a hide to keep out ambient light, ensuring the strobe was the only source of light.

Test specimen and Ultrasonic Tensile Test apparatus

To achieve the goal of examining the effect of ultrasonic vibration on the plastic deformation the 1050-O aluminium dog-bone specimen was used (as described in Section 3.2.2). For the DIC apparatus the specimen's key feature is its broad, flat surface which presents an adequate area of speckles for the DIC software from which to calculate strain accurately.

The ultrasonic tensile test was set up as described in Chapter 3, with a test machine providing the quasi-static loading and an ultrasonic transducer (Sonic Systems L500) introducing the 20 kHz ultrasonic excitation. As in previous tests (Table 3.1), the crosshead speed was set to 5 mm/minute, stopping at a total crosshead displacement of 7 mm.

The blackout hide precluded the use of an LDV to monitor the amplitude displacement directly throughout the test. Therefore, the excitation level was adjusted to achieve the same force amplitude measured by the PFT which caused the reduction in flow stress observed in the 6th excitation burst in Figure 7.13.

Estimation of error from specimen vibration

The error for this set-up, which stems from both the vibration displacement and velocity, was estimated as follows.

Displacement error

The vibration displacement amplitude was 10 μm, or 20 μm peak-to-peak. The error introduced by this motion depends on the spatial resolution of the imaging system. For a camera with a field-of-view (FOV) of width W and height H in m, and a sensor w_{px} wide by h_{px} high in pixels, the spatial resolution SR_{cam} in the width direction is equation (8.1):

$$SR_{cam}(W) = \frac{W}{w_{px}} \tag{8.1}$$

Similarly, the spatial resolution in the height direction is equation (8.2):

$$SR_{cam}(H) = \frac{H}{h_{px}} \tag{8.2}$$

To achieve the best spatial resolution the camera was aligned such that the greatest sensor dimension covered the longest dimension of the specimen. Thus, the spatial resolution in the direction of the vibration depends on the sensor width, w_{px}.

The FOV is a result of the distance between the lens and the object being imaged. There is a minimum limit to this distance, below which the lens cannot focus, and this defines the minimum FOV. The best spatial resolution is obtained by filling the FOV with the specimen, achieved by bringing the camera as close to the specimen as possible. Therefore, the minimum FOV represents the best achievable spatial resolution. The minimum FOV for this lens is 35 mm. This was the FOV value used in the estimation of system resolution. From equation (8.1) the best resolution over the length of the specimen was:

$$SR_{cam} = \frac{0.035}{2048} = 17.19\ \mu m/pixel\ (2dp) \tag{8.3}$$

In addition to the spatial resolution of the camera, DIC software can resolve pixel displacement to sub-pixel accuracy. The DIC software used, VIC-2D by Correlated Solutions, can resolve to 0.02 pixels [115].

For a DIC pixel resolution of SR_{DIC} the spatial resolution of the whole system was estimated as in equation (8.4):

$$SR = SR_{cam} \times SR_{DIC} = 17.19 \times 0.02 = 0.344\ \mu m\ (3sf) \quad (8.4)$$

This is the best theoretical resolution. In practice, noise from the camera sensor, distortion of the image and other noise sources reduces the resolution. This is known as the noise floor. The true value can only be determined once the camera system has been assembled and tested, however it is commonly found to be around 0.1 pixels [116]. This value, divided by a factor-of-safety of 2 as in equation (8.5), was used for the purpose of scoping out the system specifications.

$$SR = SR_{cam} \times SR_{DIC} = 17.19 \times \frac{0.1}{2} = 0.860\ \mu m\ (3sf) \quad (8.5)$$

This is smaller than the vibration displacement amplitude of 10 μm – and the total movement is the peak-to-peak amplitude of 20 μm – making the error introduced by it significant.

One method of removing the vibration displacement from the DIC measurement is to capture the images at the same point in the vibration cycle. This is known as strobing, a technique that has been used for centuries to study oscillating bodies [20]. This effectively acts as an optical filter by removing the oscillatory part, permitting only the quasi-static displacement to be seen in the images.

Velocity error

Another error could be introduced by the velocity of the vibration motion, which can reach 1.26 $m.s^{-1}$ peak. If the camera exposure is longer than the time it takes for a moving particle to traverse one pixel on the sensor then the particle will appear over two or more pixels. Images of objects moving this fast will appear blurred or smeared.

This effect is simply avoided by using an exposure smaller than the pixel traversing time [114]. Further, to avoid adding to the total measurement error,

the average pixel displacement γ during one exposure must be smaller than the noise floor of the system. The pixel displacement γ is found from equation (8.6):

$$\gamma = M_t \cdot v \cdot t_e \tag{8.6}$$

Where M_t is the image magnification (pixels/mm of object motion), v is the paticle velocity and t_e is the exposure time. Equation (8.6) was rearranged to find the maximum exposure time required to limit the motion-based error to a value below the noise floor, equation (8.7) below. In this calculation, the noise floor value of 0.1 pixels commonly reported for DIC imaging systems was again adopted from [116].

$$t_e = \frac{0.1}{\frac{1}{17.19 \times 10^{-6}} \cdot 1.26} = 1.36 \times 10^{-6}\ s \tag{8.7}$$

The exposure of an image can be controlled either by the shutter speed of the camera, or by limiting the time the specimen is lit up using a flash and blackout curtain. To achieve an exposure as short as 1.36 μs requires either an ultra-high-speed camera or an ultra-high-speed LED flash.

The solution selected to address both these error sources (displacement error and velocity blurring error) was to use a specially developed strobing high-speed flash triggered by a synchronising / triggering circuit.

8.3 Image acquisition

A speckle pattern was applied to the specimens by coating the specimen with a layer of white paint, followed by spraying black paint to form a pattern of random speckles (Figure 8.3).

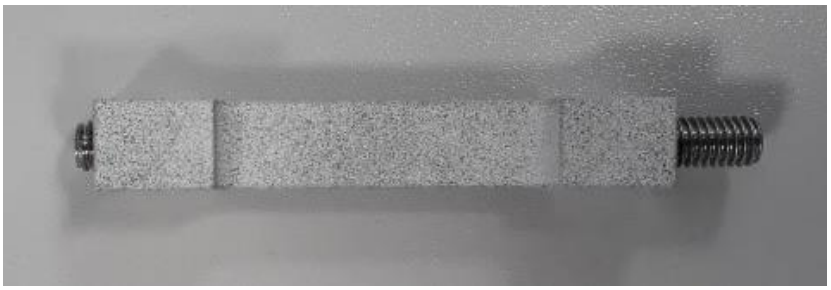

Figure 8.3 - Speckled specimen

An industrial USB camera (PixeLINK PL-D732MU-T Monochrome Imaging Camera with Trigger) was used to acquire the images, controlled via PC-based software which also stored the TIF images on the hard disc. The TIF file format was chosen as this format can be set to avoid the use of compression, which has been known to introduce error in the strain result [114]. A lens (Navitar MVL50M23) with a focal length of 50 mm was selected to optimise the Field of View (FOV) for the specimen parallel length of 30 mm, at the Minimum Focal Distance (MFD). This is the distance at which the image of the specimen fills as much of the sensor as possible whilst remaining in focus. The imaging specifications are summarised in Table 8.1. The displacement resolution was based on the noise floor typical for DIC [116].

Focal length	50	mm
Minimum focusing distance (MFD)	200	mm
Field of view @ MFD	35	mm
Sensor size - W	2048	px
Sensor size - H	1088	px
Pixel resolution	17.19	µm/px
Noise floor (typical)	0.1	px
Displacement resolution (typ)	1.72	µm
Noise floor (actual, found after test)	0.141	px

Table 8.1 – Estimated camera spatial resolution

The camera exposure and shutter interval were set to 10 ms and 250 ms (4 frames per second (fps)) respectively (Table 8.2).

Exposure	10 ms
Shutter interval	250 ms
Resulting frame rate	4 fps

Table 8.2 - Camera temporal resolution

Most flash units are not capable of delivering the short pulse required (approximately 1 μs). Most have a maximum strobing rate of around 5000 fps, and do not fit the required specification of light intensity, short pulse duration and high pulse rate. Willert et al [117] described the construction and evaluation of a high-intensity, short duration light source for imaging turbulent fluid flow. A key outcome was that LEDs can be driven with a voltage five to twenty times the normal rating without causing damage, as long as the duty cycle is kept very short. This approach was therefore adopted in this thesis, and a flash was developed using the Willert LED driving circuit (Figure 8.4).

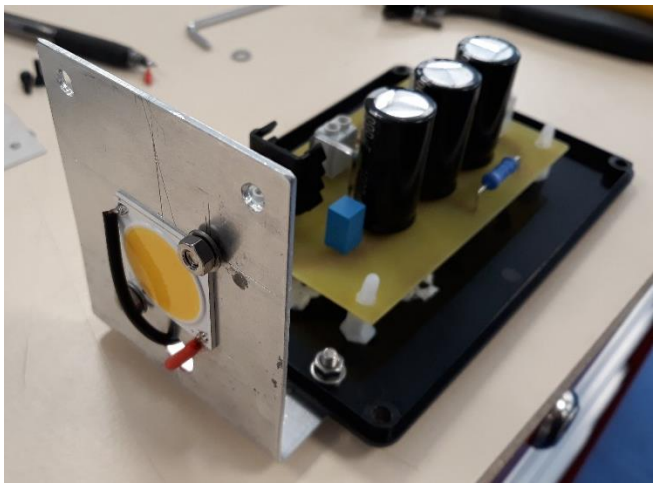

Figure 8.4 - High-speed LED flash; mounted COB LED with driving circuit behind

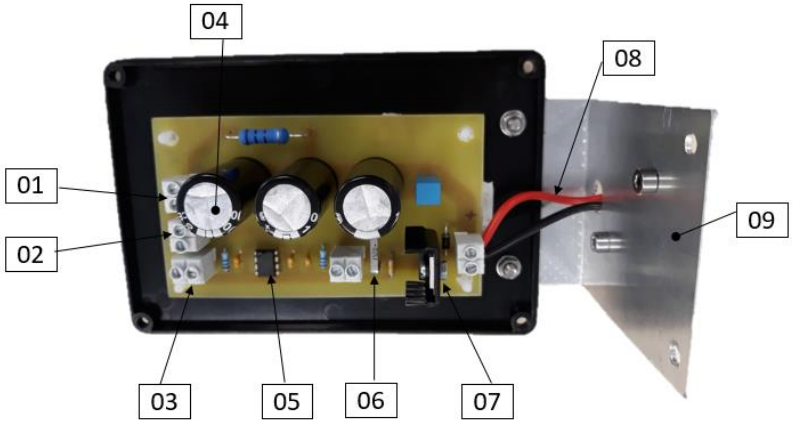

1. Capacitor power supply (+50 V)
2. FET power supply (+12 V)
3. Trigger signal in
4. Capacitor bank (70 V max)
5. FET driver
6. 0.02 Ω resistor for current measurement
7. FET
8. Cables to LED
9. LED mounting bracket

Figure 8.5 - Willert driving circuit for high-speed LED flash

The LED driving circuit (Figure 8.5) includes a bank of high voltage capacitors which were connected to the LED via a Field-Effect Transistor (FET). When the FET is turned on the capacitors discharge as quickly as the LED resistance allows, creating a very bright short burst of light.

Much brighter LEDs than those used in Willert *et al.* [117] are now available, combining higher light emitting efficiency with the introduction of chip-on-board (COB) LEDs, where many LEDs are fitted onto one unit. The LED used was the Cree CXB3070. At normal operating current of 2.8 A it is rated to produce 9413 lumens. The LED was mounted on the electronics enclosure with an aluminium bracket which also functioned as a heat sink.

The flash circuit operates on a trigger (+5 V Transistor-to-Transistor Logic (TTL) signal). One TTL pulse will prompt one flash; for continuous operation each

vibration cycle is required to trigger one flash. Figure 8.6 shows the oscilloscope traces observed during operation of the flash. Figure 8.7 is an enlarged version of the same, providing a clearer view of the trigger signal and the resulting current through the LED.

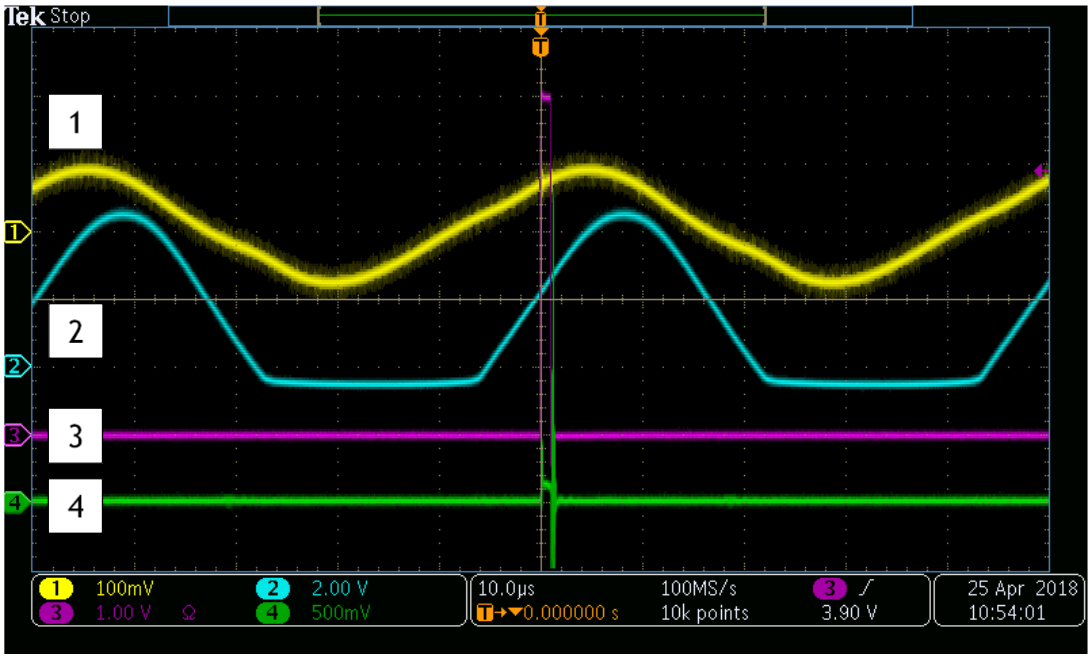

Figure 8.6 - Strobe triggering signals: 1. current clamp; 2. signal conditioning unit; 3. trigger; 4. LED current

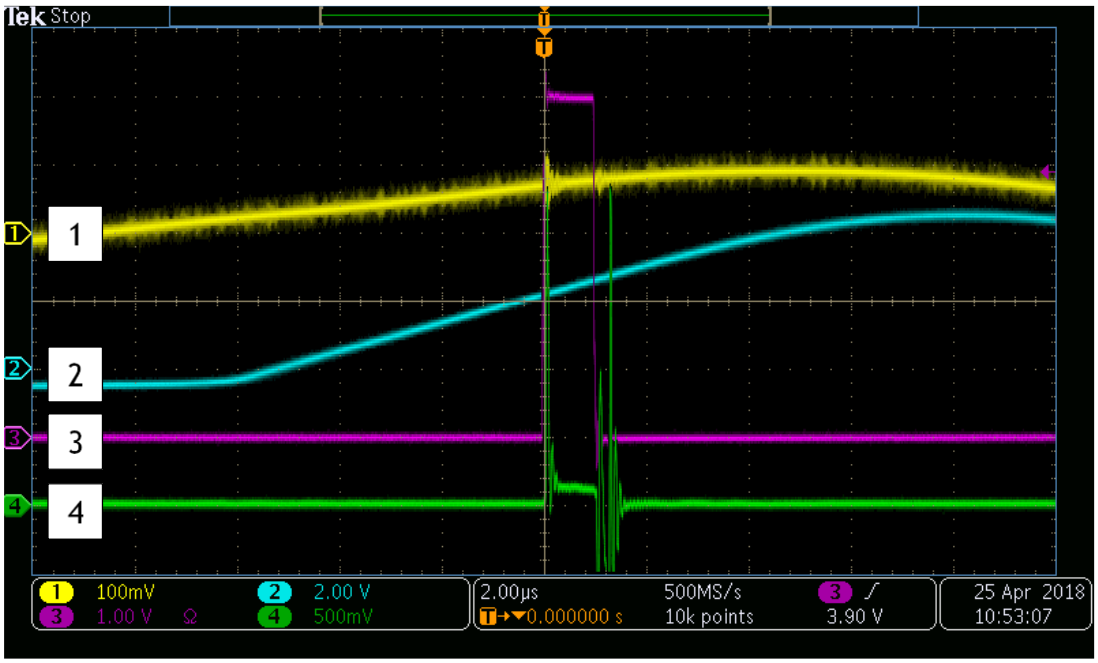

Figure 8.7 - Strobe triggering signals (enlarged): 1. current clamp; 2. signal conditioning unit; 3. trigger; 4. LED current

The flash pulses were synchronised with the vibration by continuously monitoring the current delivered to the ultrasonic transducer with a current clamp, signal 1 in Figure 8.6 and Figure 8.7. This signal was amplified and rectified (negative part removed) by a signal conditioning unit, signal 2, before being used to trigger an Arbitrary Function Generator (AFG). This device had been programmed to provide single square wave pulses, with the pulse-width determining the flash duration, signal 3, most clearly visible in Figure 8.7. This figure also shows signal 4 clearly, a measurement of the instantaneous current passing through the LED.

To maintain the light on the specimen during the periods when ultrasound was off, an additional AFG, also connected in such a way as to have the ability to trigger the flash, was programmed to run continuously at 20 kHz. This second AFG was triggered by a programmable microcontroller (Arduino Mega). The microcontroller scheduled all the events of the test, such as starting the tensile test machine, as well as switching between the internal-triggered AFG and the vibration synchronised AFG.

8.4 Tensile test programming and test event scheduling

A microcontroller (Arduino Mega 2560) was used to control some of the events comprising the USTT, those which had to occur in the correct order for a successful test, or for a set duration. This included starting the test machine; switching the ultrasonic generator on and off (to set the timing and duration of the US excitation with respect to the start of extension); and managing the handover of flash triggering from stand-in to vibration-synchronous.

The Instron test machine was pre-programmed to provide the tensile extension described above, which executed when triggered by closing a circuit on an eternal connection point. The USTT microcontroller was used to operate a relay, which completed this circuit, triggering the test machine, which then executed its pre-programmed test without further instruction or intervention.

In a similar manner, the ultrasonic generator includes an external connection which is normally open circuit; when closed, the excitation is turned on. Again, a relay, controlled by the microcontroller, was used to close and open this

circuit to respectively start and stop the excitation. The excitation sequence (Table 8.3) was programmed into the microcontroller code.

Time (s)	Event
0	Trip test machine
10	Start ultrasonic excitation
20	Stop ultrasonic excitation
30	Start ultrasonic excitation
40	Stop ultrasonic excitation
50	Start ultrasonic excitation
60	Stop ultrasonic excitation
100	Test machine stops crosshead and finishes program automatically

Table 8.3 - USTT event sequence

The following rationale applies to the sequence presented in Table 8.3. To ensure the ultrasonic excitation was applied within the plastic deformation stage, excitation was delayed 10 seconds after the test start. The vibration was applied for 10 seconds, long enough to establish a constant amplitude. To make most use of the rest of the deformation of the ductile 1050 material, this excitation was repeated in another two bursts, with 10 second intervals between.

8.5 Force measurement and acquisition

Force on the end of the specimen was measured by the test machine load cell and the piezoelectric force transducer. While the former recorded data in the Instron control system, the latter was recorded by a PC-based oscilloscope. During set-up, care was taken to ensure that both the load cell and piezoelectric force transducer were zeroed with the isolating mass, PFT and specimen connected, but with any load from the crosshead absent. All components were mounted except the connection between the specimen and the horn, which was left undone. In this way, both force sensors were checked and known to have the same zero measurement prior to the test. In completing the tensile test stack by connecting the specimen to the horn an axial load results which is reduced by adjusting the crosshead position. A small residual load remains, and

it is important that this is not removed by zeroing after connecting the specimen.

8.6 Results

The images acquired by the camera were processed using a commercial DIC software (Correlated Solutions VIC-2D) to extract displacement and strain maps as arrays of data, one for each image captured. The data arrays are typically plotted in a two-dimensional (2D) colour plot superimposed on the image of the specimen; an illustrative selection from the 399 images processed are presented here in Table 8.4 and Table 8.5.

In Table 8.4 the scaling was set to 'autoscale'; that is, strain scale set to the maximum and minimum for each image, providing a view of the local strain variations occurring at that moment in the test.

Table 8.4 - Full-field strain maps of USTT (auto-scaled)

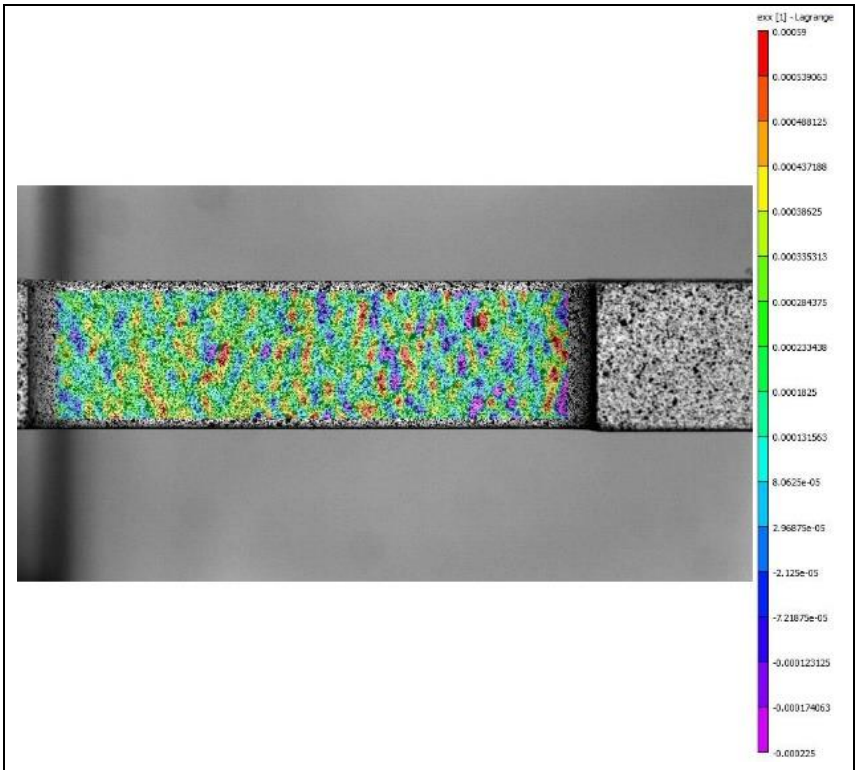

Image 015 (autoscale), t = 3.75 s

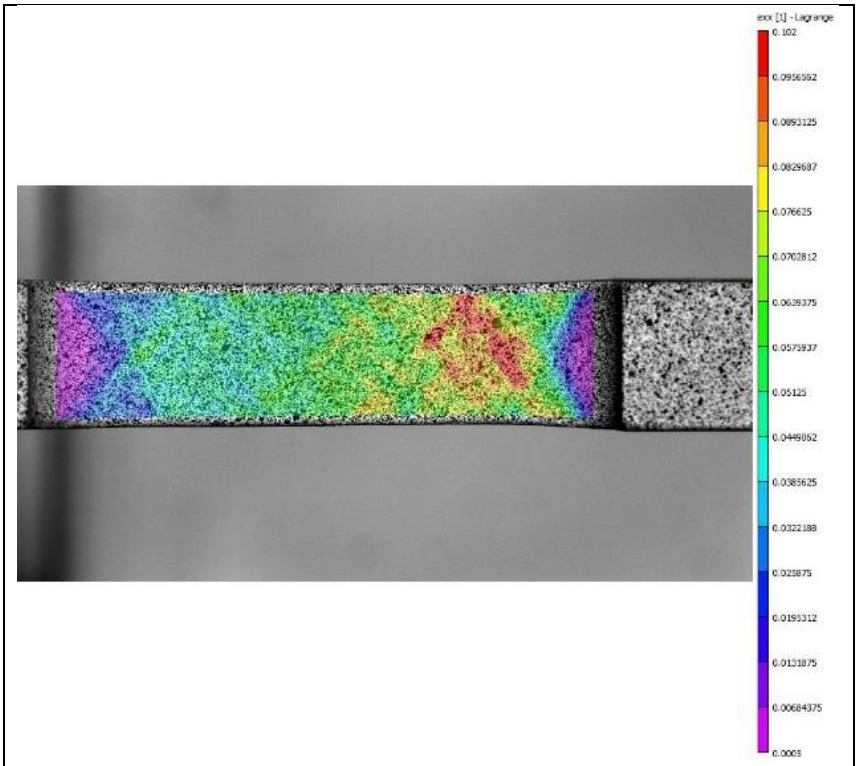

Image 100, t = 25 s

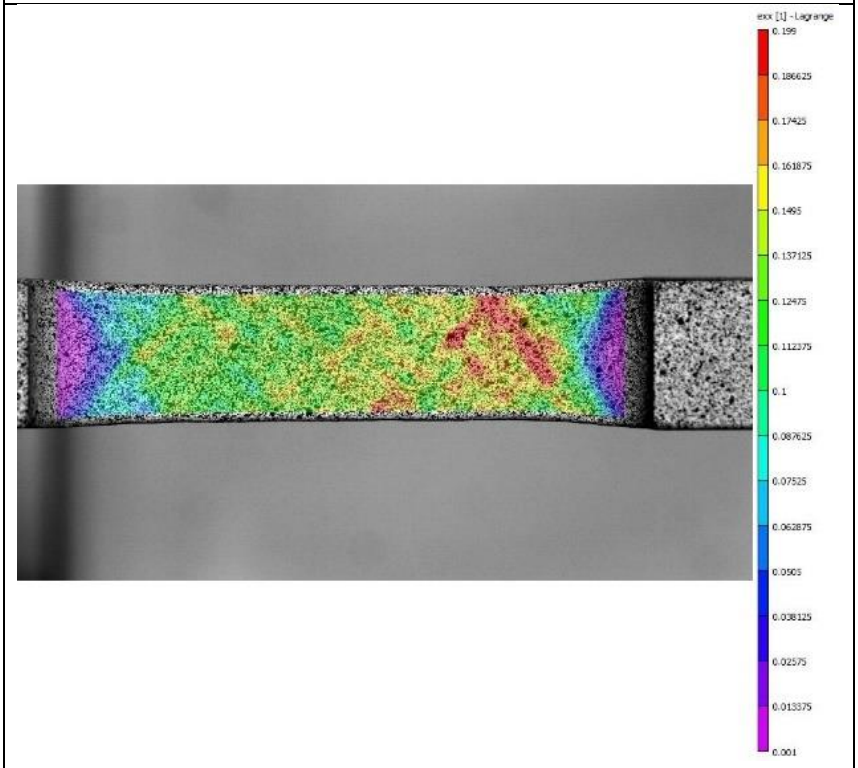

Image 200, t = 50 s

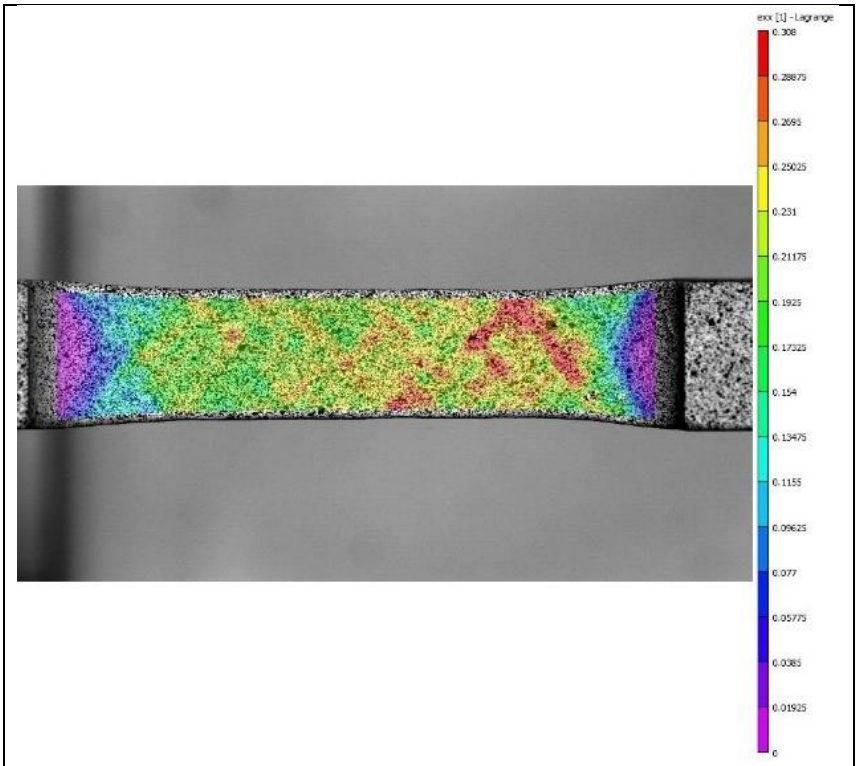

Image 300, t = 75 s

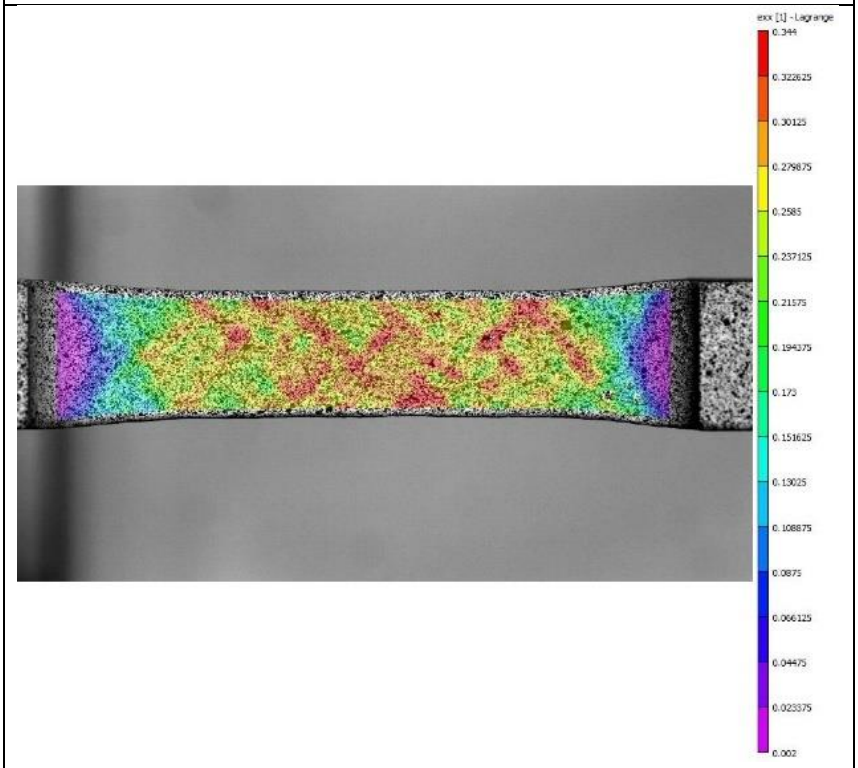

Image 398, t = 99.5 s

Table 8.5 shows the same full-field strain maps with the scale fixed to 0 – 0.35 strain, providing an overview of total strain changes throughout the test.

Table 8.5 - Full-field strain maps of USTT (fixed scale)

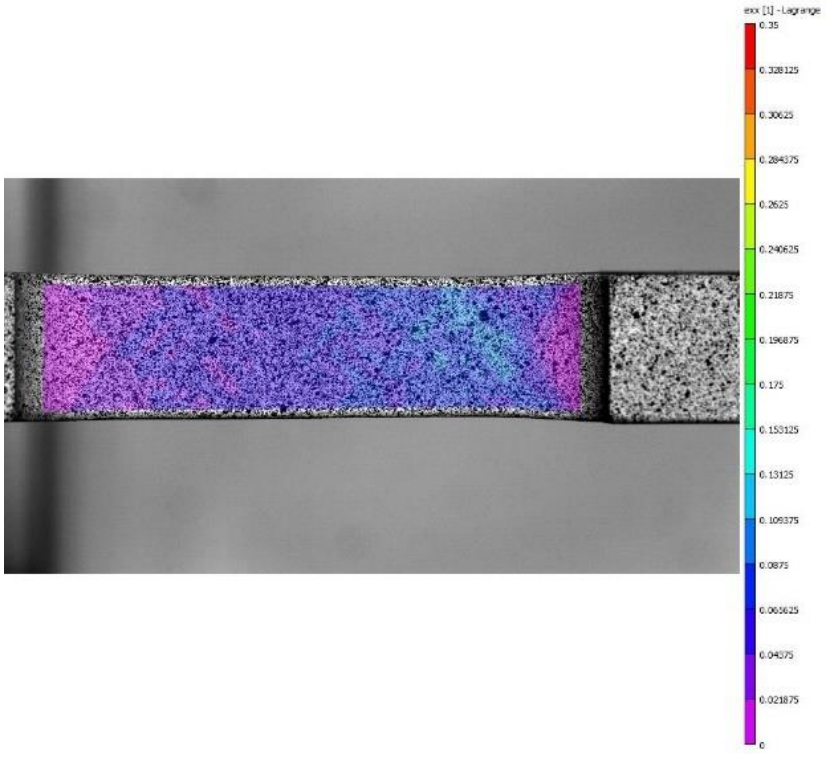

Image 100, t = 25 s

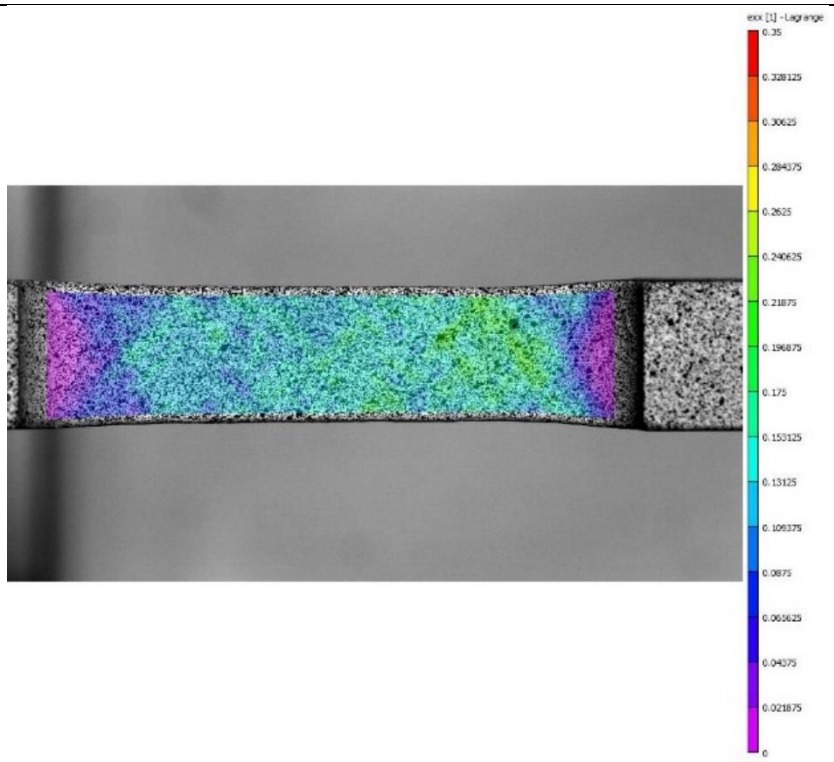

Image 200, t = 50 s

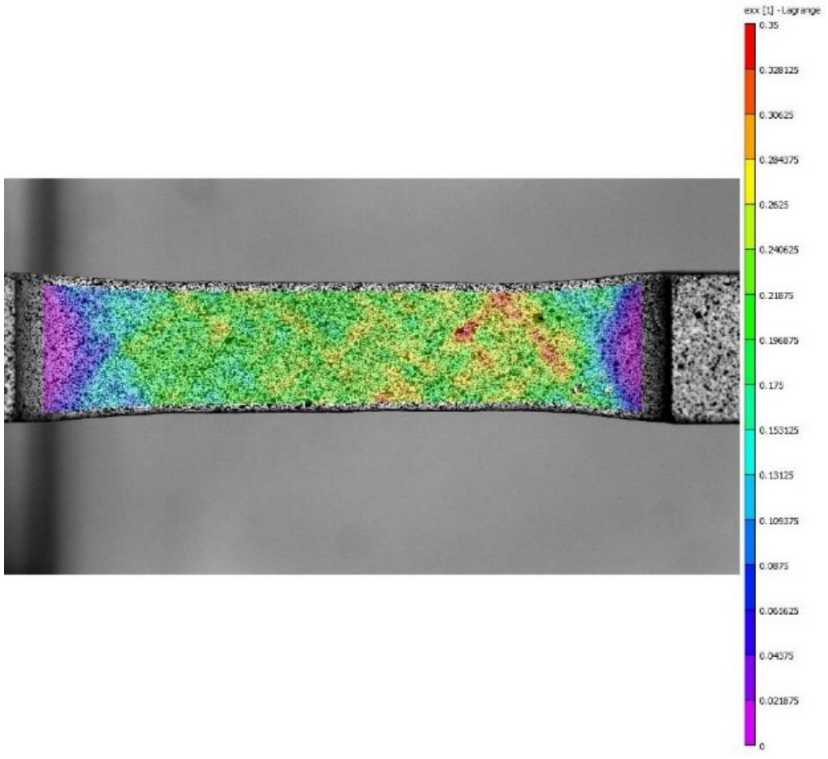

Image 300, t = 75 s

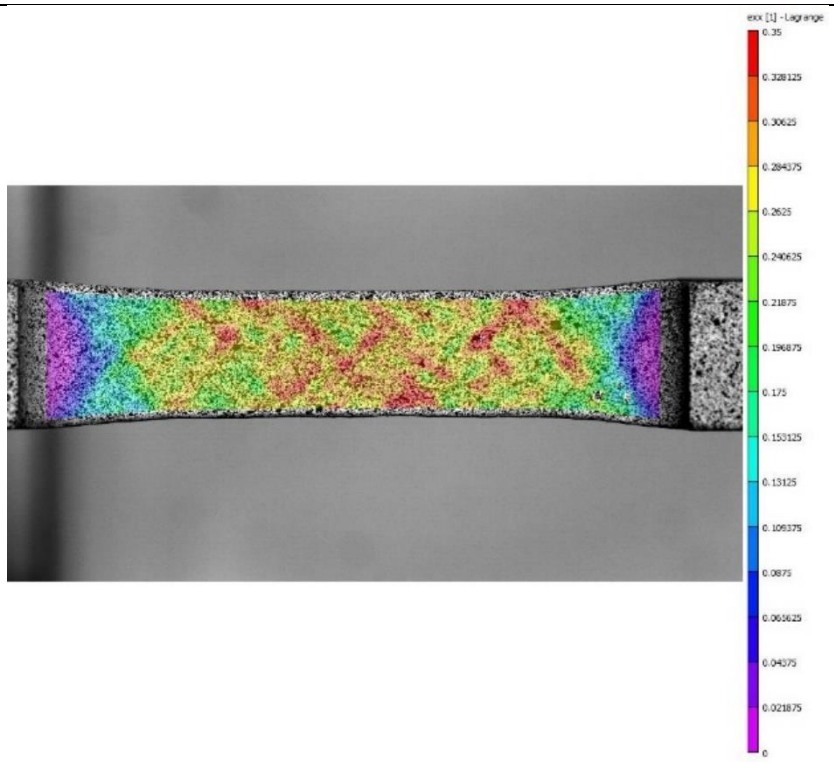

Image 398, t = 99.5 s

In Table 8.4 bands of strain can be discerned. They are of the order of 1 - 2 mm wide and make an angle of around 45° to the tensile stress axis. They are similar in appearance to Luders bands, a form of plastic instability common in steel [76]. They also resemble a shear band formation common in aluminium alloys undergoing the Portevin-Le Chatelier (PLC) effect, though these occur at the microscopic scale and there is no sign of the serrations in the stress-strain curve characteristics of the PLC effect [118]. The bands can be seen travelling along the specimen axis throughout the test; ultrasonic excitation does not appear to disrupt the process.

The 2D strain maps show great detail and following through the images reveals the complexity of the strain evolution during deformation. However, quantitative interpretation is made much easier if the strain data are graphed. The 2D data arrays were manipulated to plot single 1D arrays which correspond to viewing strain along a single line on the specimen axis at one instant in time (Figure 8.8, Figure 8.9), or strain at a single point over time (Figure 8.12).

Each of the DIC images results in a 2D array of strain from which was extracted a single profile of axial strain up the specimen centreline. As the images were taken in a defined sequence in time, the profiles can be plotted together to produce a surface of strain in time and axial position, Figure 8.8.

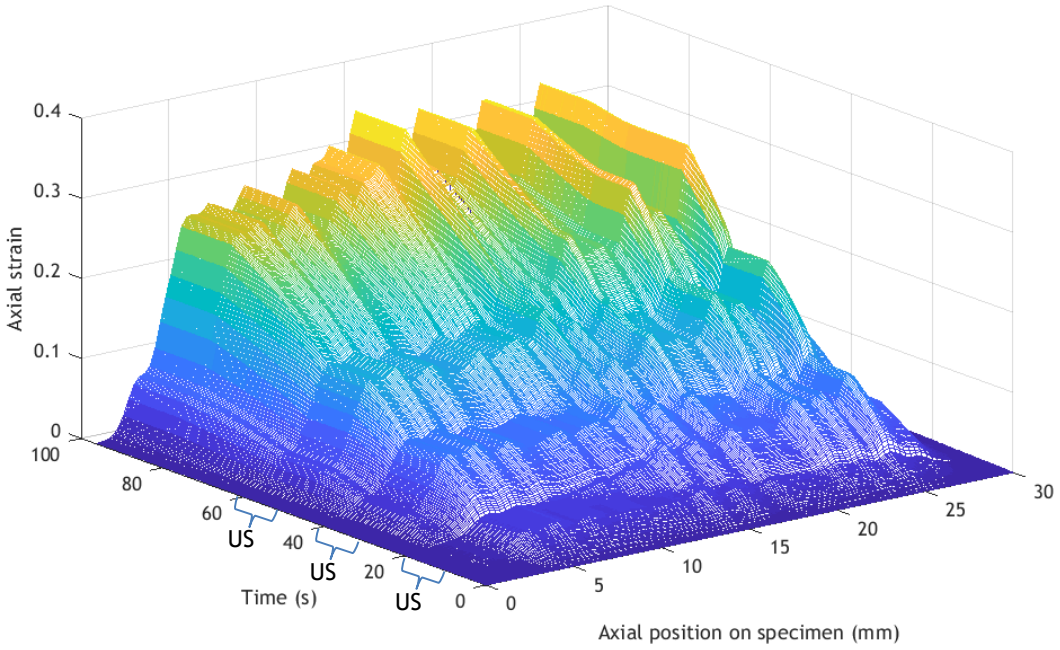

Figure 8.8 - Quasi-static axial strain, against position and time

Figure 8.8 illustrates the volume of data available from the DIC method, compared to extensometer where only the overall gauge length is monitored. Bursts of excitation are marked ‘US’ on the time axis. There is a wealth of local detail too, which in Figure 8.9 reveals that the plastic strain undergone by the specimen varies by as much as 20% in a ripple around the mean trend. This could have implications for post-mortem microscopy, which by its nature makes very localised examinations, blind to wider inhomogeneity in the deformation. Microscopy results are often assumed to be representative of the bulk of the material.

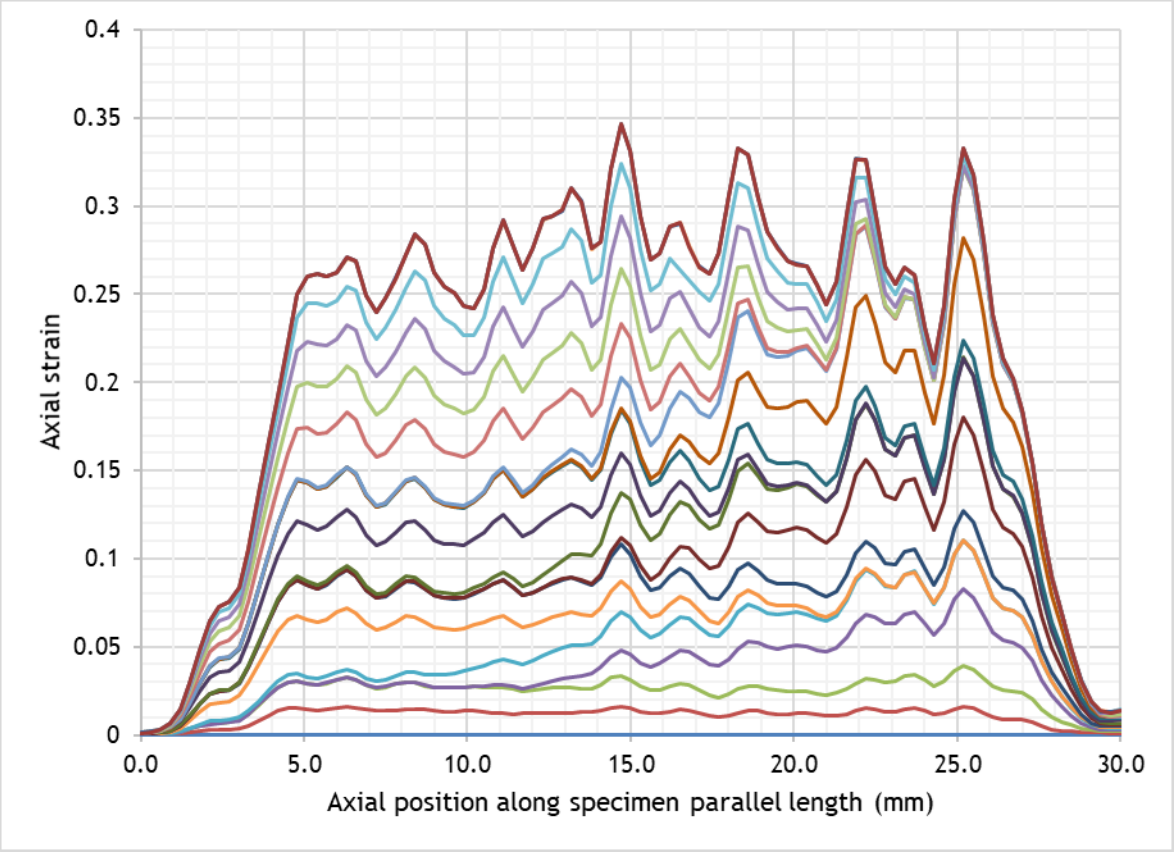

Figure 8.9 - Axial strain against axial position

In Figure 8.9, every 20th curve from the whole strain data set was plotted. To bring further clarity, the following plots were developed to focus on datasets associated with one ultrasonic excitation burst, or at selected axial locations on the specimen. The timing of the ultrasound bursts, as they manifest within the strain data, are given in Table 8.6.

Event	Time (s)
Start	0
1st burst - begin	9.25
1st burst - end	19.50
2nd burst - begin	29.25
2nd burst - end	39.50
3rd burst - begin	49.25
3rd burst - end	59.75

Table 8.6 - Ultrasonic excitation burst times evident in strain datasets

Data sets just before, during and after the first ultrasonic burst (US Burst 1) are presented in Figure 8.10. Further curves at time 1s, 5s, and 25s, were added in

dashed lines to add context, indicating the strain profile developing before any excitation, and a period after it stopped.

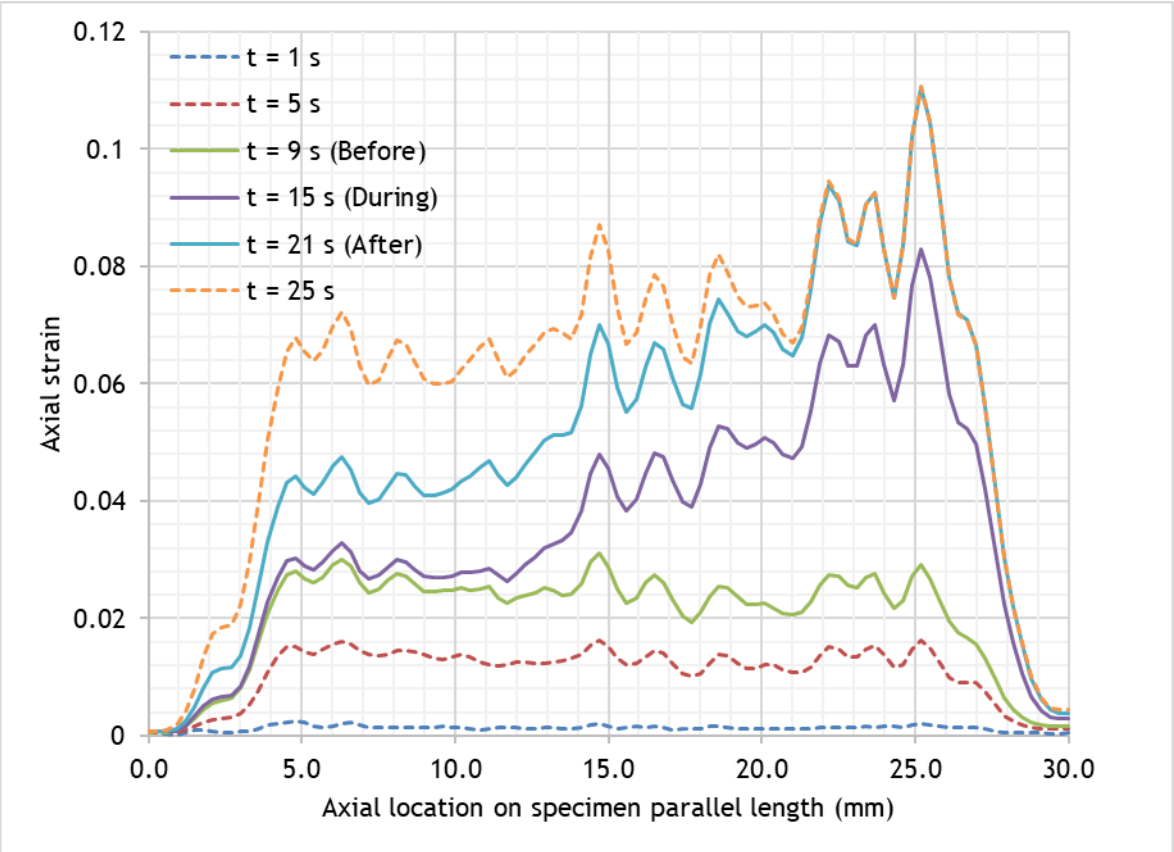

Figure 8.10 - Axial strain before, during and after US Burst 1

The first three curves before excitation begins are very similar. The strain is evenly distributed along the specimen axis (within a band of variability of ~0.005 strain) and only differing by increasing in mean value. Once excitation begins the profile changes greatly in the upper section of the specimen, from 15 mm to 30 mm. The local detail is similar, but superimposed on a gradient which lifts the end connected to the PFT and the isolating mass. Nearest this end, strain increases sharply to 0.076 strain, leaving the material between 0 and 15 mm to stagnate.

Between the profiles at t = 21 s and 25 s this effect appears to reverse when excitation stops at t = ~20 s. Again, local variation is preserved while the gradient of the underlying trend flattens out, as the plastic strain along the length of the gauge section recovers to its pre-excitation distribution. Plastic deformation occurs in the horn-end section, 0 to 15 mm, whilst strain from 15 to 30 mm pauses. It is thought that the plastic deformation gained at the end

connected to the PFT during the ultrasonic excitation came at the expense of deformation elsewhere. Once the inhomogeneous loading stops, the greater work-hardening incurred at the mounted end encourages deformation to momentarily relocate to the softer material at the horn end.

At each end of the specimen gauge section, the strain follows a steep gradient from the value which dominates the majority of the gauge section, down to zero. When examining the centreline in the colour maps of strain (Table 8.4) it is clear this is a consequence of the strain distribution near the filleted ends of the specimen.

To plot strain against time over the duration of the whole test, three locations along the centreline slice were selected as representative of the horn-end, the mid-plane and the mounted end of the specimen as shown in Figure 8.11. Strain data at the very ends, 0 and 30 mm, were avoided as the fillets at the specimen ends restrict the local strain in their vicinity. This is observed in the bow-shaped areas of purple at the ends of the strain maps in Table 8.4. Locations 5 and 25 mm were selected as being the least and greatest values, respectively, which still captured the trend of the strain, see the extreme ends of Figure 8.9).

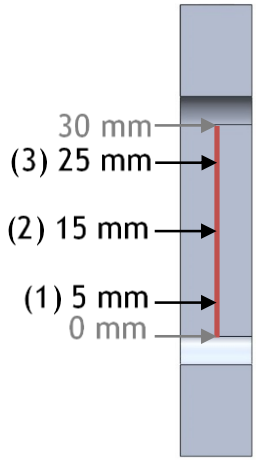

Figure 8.11 - Locations of strain/time data sets

The plots of strain over time at the three locations are presented in Figure 8.12.

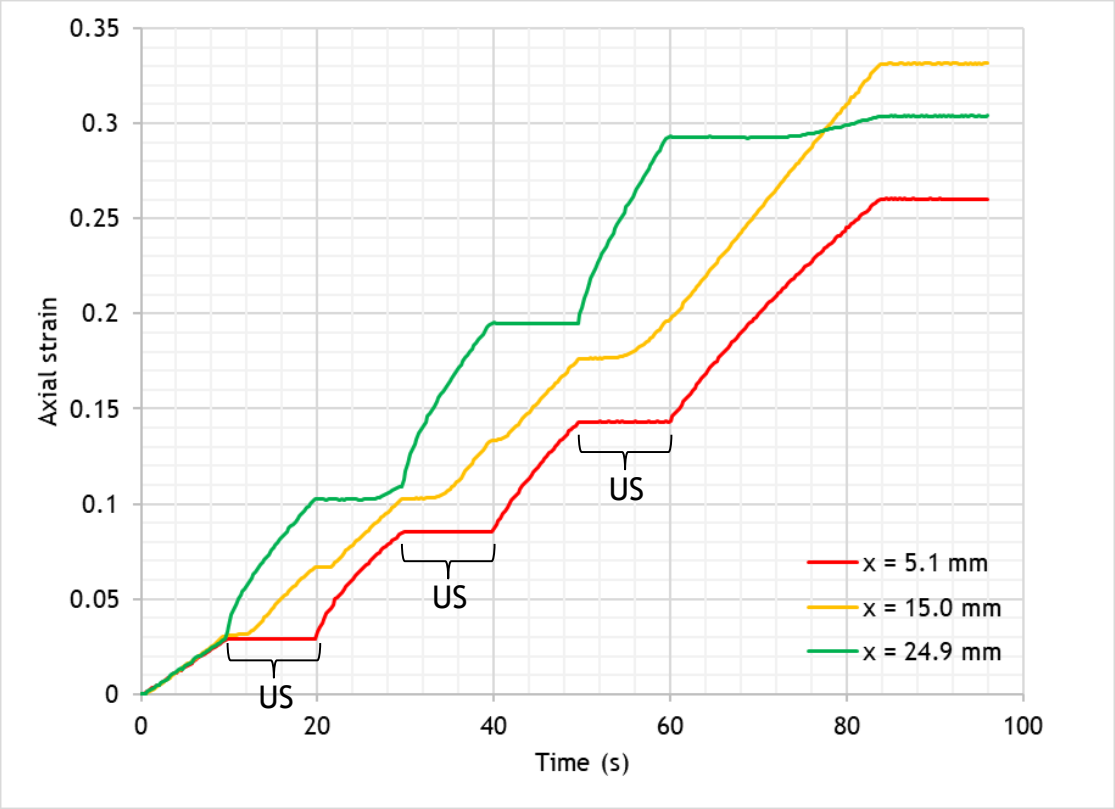

Figure 8.12 - Axial strain against time, at selected locations on specimen

Plotting strain against time accentuates the influence of ultrasonic excitation already identified in Figure 8.10. Busts of excitation are marked 'US' on the time axis. At first the three curves are identical, as strain is initially evenly spread over length. Then, as the first US burst begins at 9 s, the curve of strain at 24.9 mm (mounted end) accelerates, while in the curve of 5.1 mm (horn end) strain stops completely. Through the excitations, strain concentrates towards the mounted end. This repeats for each burst. Finally, after the last excitation burst, the strain evens out again over the length of the parallel section.

Ultrasonic excitation has very clearly affected the distribution of plastic deformation, concentrating it towards the mounted end where the stress amplitude is highest. The effect is transient - it occurs during excitation and recedes afterwards, the strain distribution returning to the even axial strain distribution it began with. This is likely the result of each part of the specimen trying to reach the same level of work-hardening as the rest - or rather, the unequal levels of work-hardening act to divert plastic deformation to those portions which can bear less load, ie those areas which have deformed less and gained less work-hardening. Notably, the ultrasonic excitation imposes this

general trend on the global strain, whilst seemingly leaving the local strain structure unaffected.

If provided with the camera frame rate, the DIC software can also calculate the strain-rate from each strain data point. As with the strain data arrays, 1D arrays were isolated and plotted, to present charts of strain-rate along the axis of the specimen (Figure 8.13), and strain-rate at selected locations over time (Figure 8.14).

In a similar effort to simplify the plots of strain-rate, strain-rate against axial position, Figure 8.13, were also generated at the same points in time (before, during and after US Burst 1); strain-rate against time over the duration of the test, Figure 8.14, was plotted at the same locations in Figure 8.11.

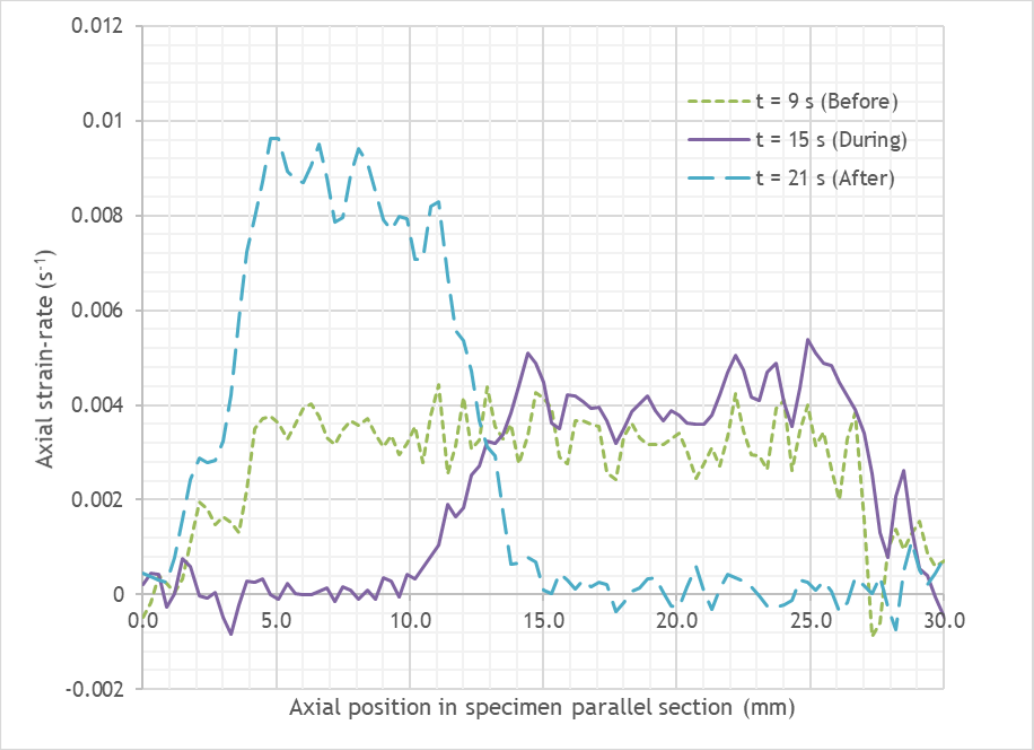

Figure 8.13 - Strain-rate against axial position, before, during & after US Burst 1

The plot of strain-rate just before, during and after the first US burst, Figure 8.13, only serves to reinforce the points made above. Before the first US burst, the rate of strain is evenly distributed along the specimen, similar to the strain distribution. During excitation the strain-rate does concentrate at the mounted end, where the oscillatory stress amplitude is highest. Unexpectedly, the majority of the profile is flat, ramping up from zero over a short distance

between 10 mm and 15 mm on the specimen parallel length. Somehow, after US burst 1 ends, the recovery of the even distribution of strain induces double the strain-rate in the portion of the material where deformation had lain dormant.

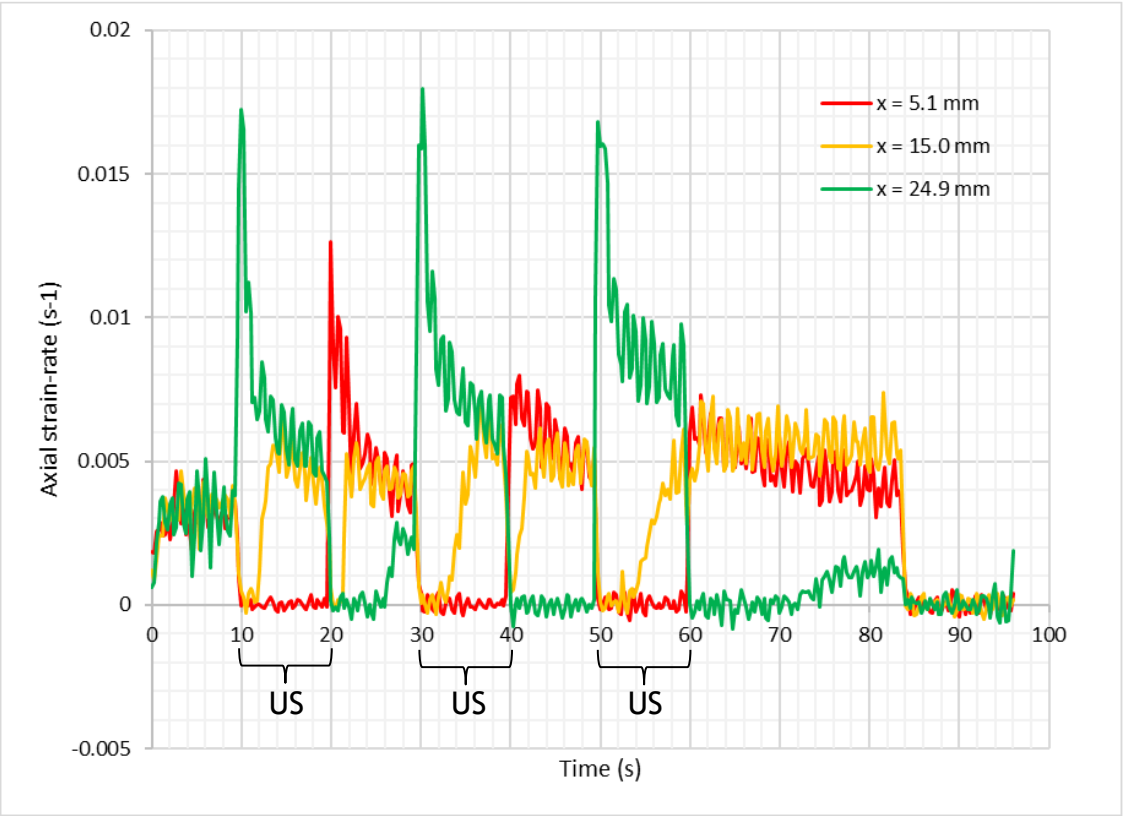

Figure 8.14 - Axial strain-rate against time, at selected locations on specimen

In Figure 8.14 absolute values of strain rate are 0.005 to 0.008 strain.s-1 for each end, but switching places when ultrasonic excitation is on or off. The order of magnitude of these strain-rates is still comparable to that of ordinary tensile test with the same crosshead speed. Excitation appears to do nothing unusual beyond shifting the focus of the plastic strain, increasing the strain-rate at the mounted end during excitation, then the rate compensates at the other end once the vibration stops. It is clear in this plot that, whichever end is not favoured by plastic deformation, the strain-rate drops to zero, highlighting how the plastic deformation moves entirely to either the mounted end or the horn end.

Unexcited tensile test

The test was repeated without any ultrasonic excitation, to compare with the excited specimen data. The axial strain over the length of the specimen is presented in Figure 8.15.

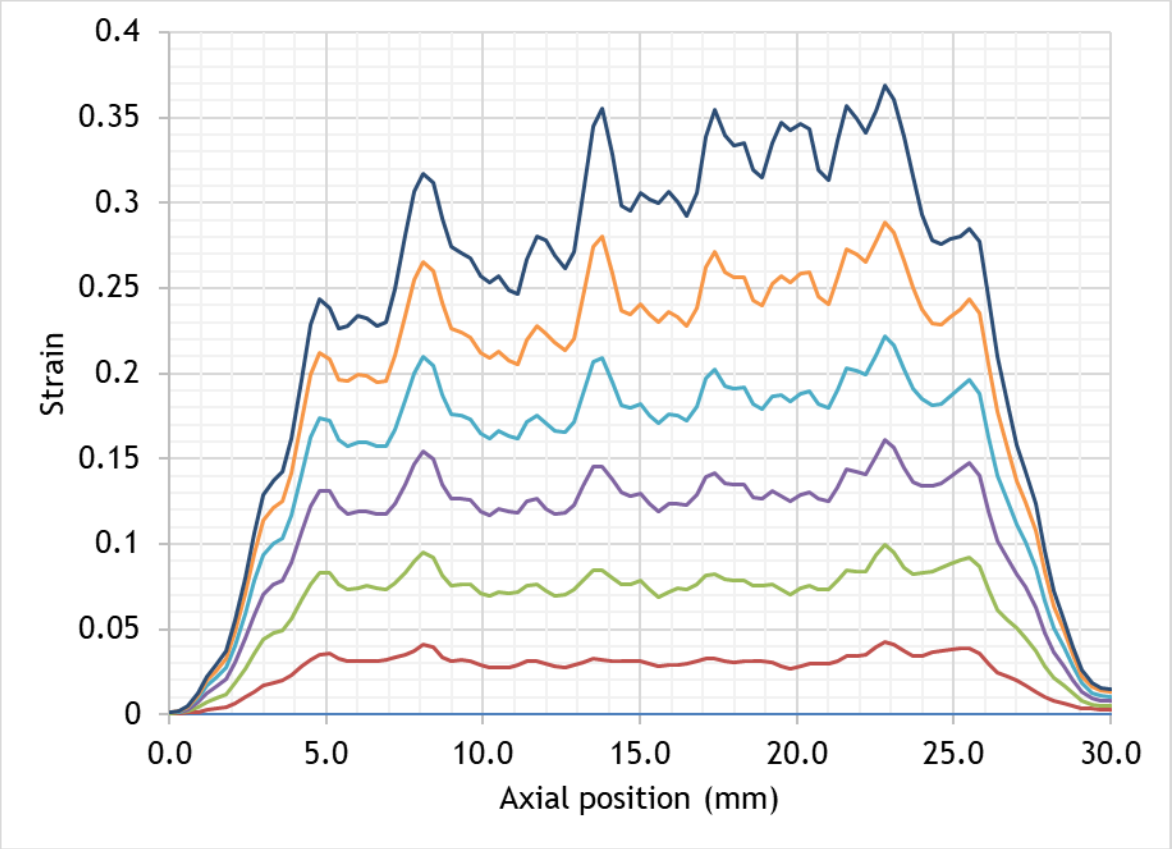

Figure 8.15 - Axial strain over gauge length, unexcited specimen

In Figure 8.15, the axial strain remains constant about a mean value over the length of the gauge section, for approximately half the duration of the test. As necking begins, deformation becomes biased towards the upper end of the specimen connected to the PFT.

Comparing to Figure 8.9 (with US excitation), at first there appears to be little difference, with the same distribution of strain found in each, and the same necking bias ending the test. However, the differences between with and without ultrasonic excitation become more obvious once strain is plotted over time, Figure 8.16.

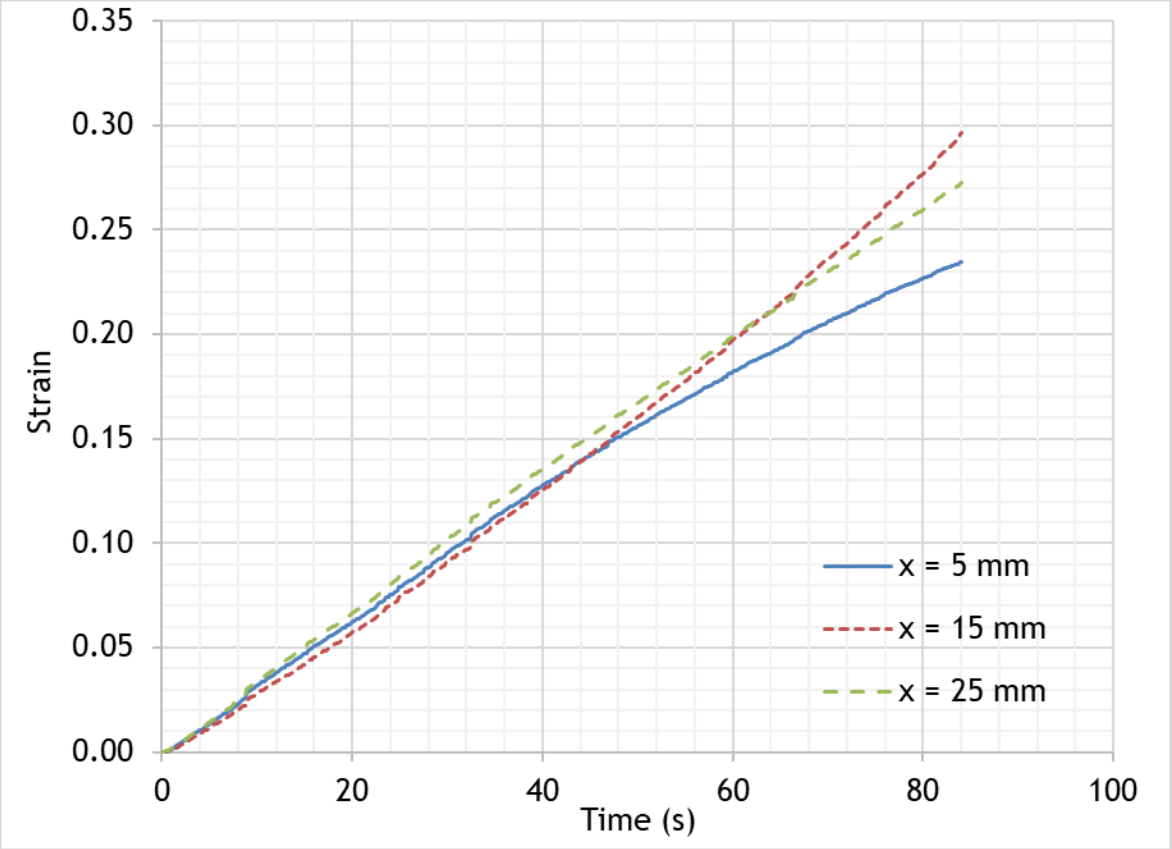

Figure 8.16 - Strain over time, unexcited specimen

At all three chosen sampling locations, the strain increases steadily in a smooth curve. Contrast this with the curves in Figure 8.12 for the US excited specimen. The sharp changes in strain rate which coincide with US excitation are not observed. In Figure 8.16 the strain rate at each location is not constant or equal to that at the other locations. The gradient is constant over the first half of the test, then, as necking begins, the strain rates diverge. Near the necking site the strain rate increases, and consequently the strain rate elsewhere reduces, as all the plastic deformation concentrates at the necking site. This is consistent with the behaviour expected in normal plastic deformation, distinct from the severe gradient changes observed when US excitation is applied.

The evolution of strain rate is further observed in the plots of strain rate over time presented in Figure 8.17. Despite the short excursions of 0.0005 to 0.001 strain.s^{-1} magnitude, the underlying trend is constant at approximately 0.003 strain.s^{-1} for the first half of the test period. Thereafter, the strain rates diverge as necking initiates and progresses, as already discussed. This can be contrasted to the strain rate in the excited specimen, Figure 8.14, where the strain rate switches between zero and 0.005 strain.s^{-1}.

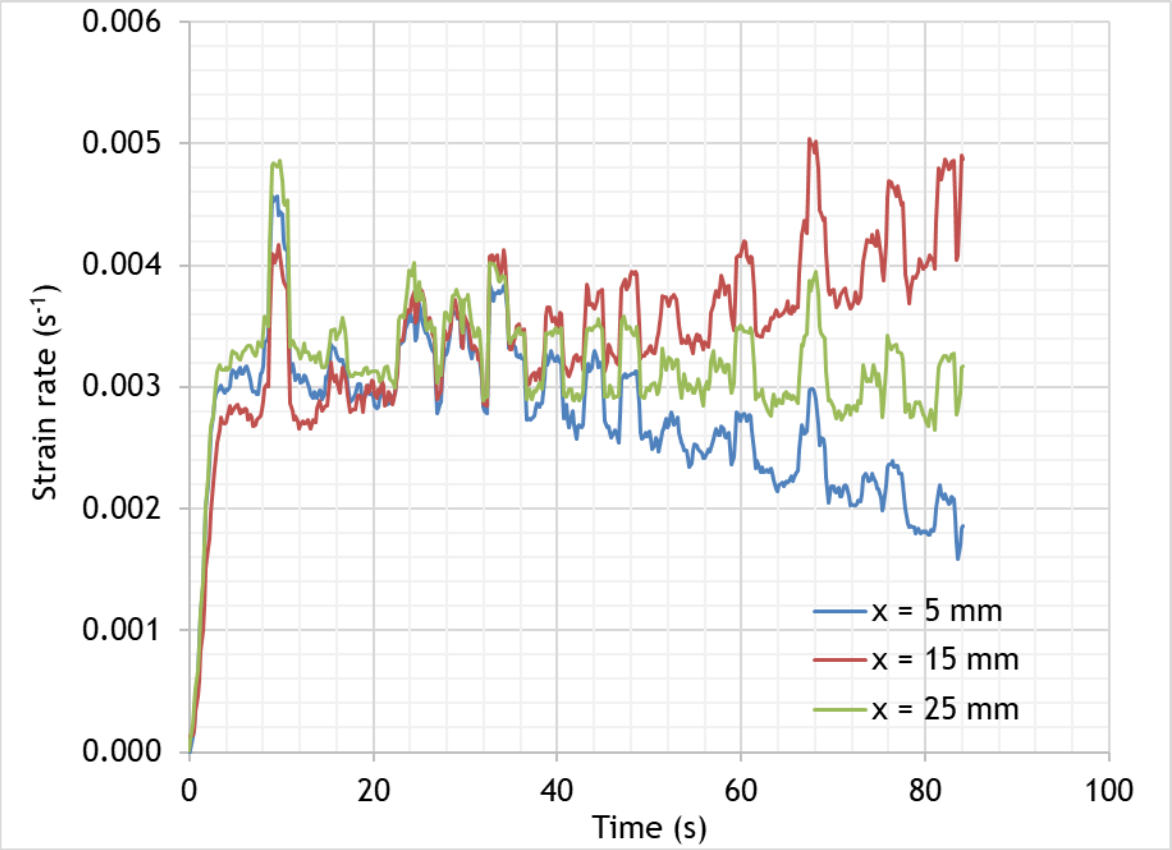

Figure 8.17 - Strain rate over time, unexcited specimen

The final comparison to be made is with the axial distribution of axial strain rate over the gauge length of the unexcited specimen, Figure 8.18. Here, the strain rate was taken at the same time intervals used in Figure 8.13. It was found to be constant around a mean value of 0.0028 strain.s^{-1} over the portion of the specimen gauge length between 5 mm and 25 mm. Below 5 mm and above 25 mm the strain rate reduces gradually. It is supposed this is due to the proximity of the fillets connecting the parallel length to the specimen ends. At no point in the test of the unexcited specimen did the strain rate decrease to zero over parts of the length, as it does in Figure 8.13 during the application of US excitation.

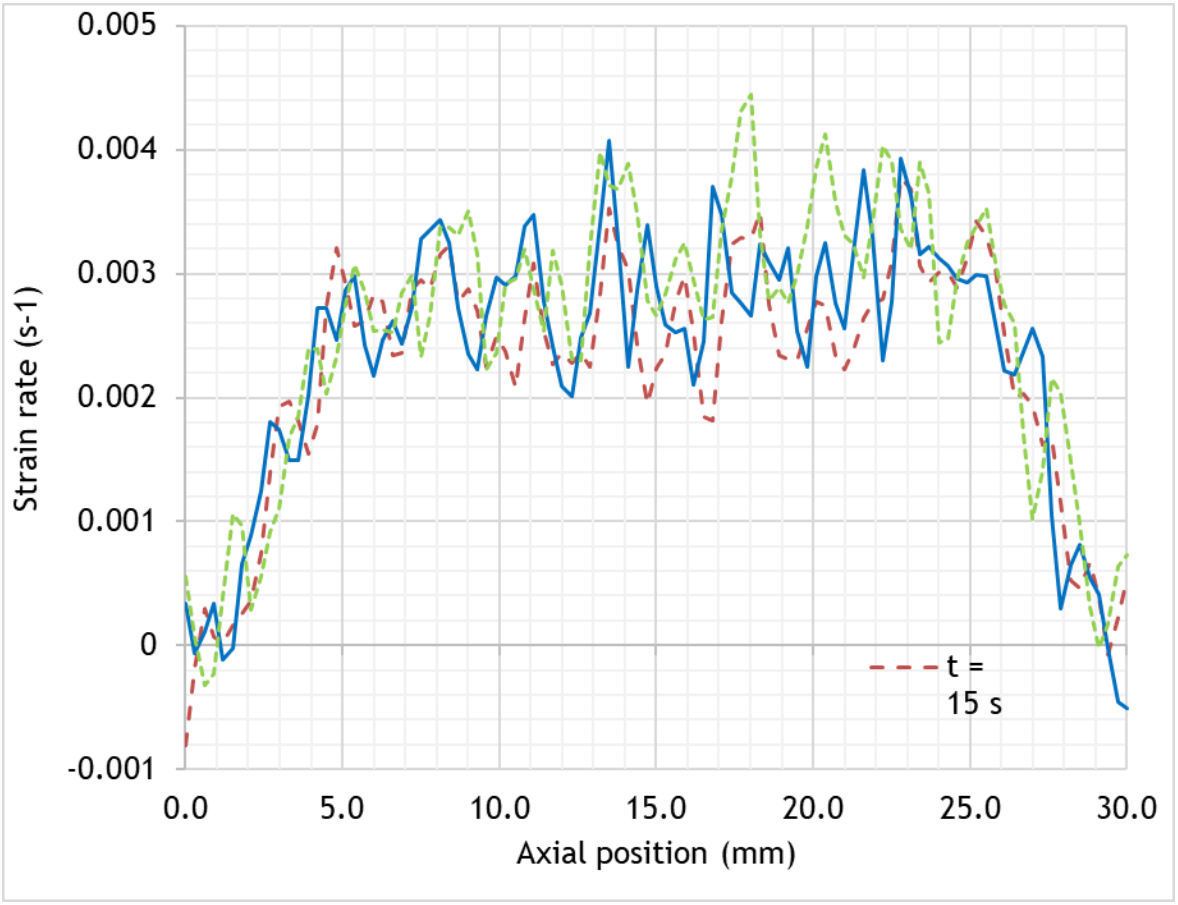

Figure 8.18 - Strain rate over gauge length, unexcited specimen

The contrast provided between the deformation activity of the excited and unexcited specimens is consistent with the theory that the plastic deformation responds to the bias of the stress amplitude towards the PFT caused by the vibration waveform having a node at the isolating mass connection.

Stress-strain graph

The DIC software offers a video extensometry function which calculates a global strain value over a virtual gauge length set within the software. This was combined with the PFT force measurement to plot a stress-strain curve for the specimen. Following the same method set out in Section 7.4, true stress was calculated from the force measurement from the PFT using equations (3.1) and (3.4), and multiplied by the correction factor $\kappa = 0.3$ to find the true stress at the end of the gauge length adjacent to the PFT (equation (7.5)). As in Chapter 7, smoothing provided a value for the mean true stress.

The true strain was calculated from the DIC video extensometer (VE) output (equations (3.2) and (3.3)). The true stress, corrected true stress and mean true stress against true strain are presented in Figure 8.19.

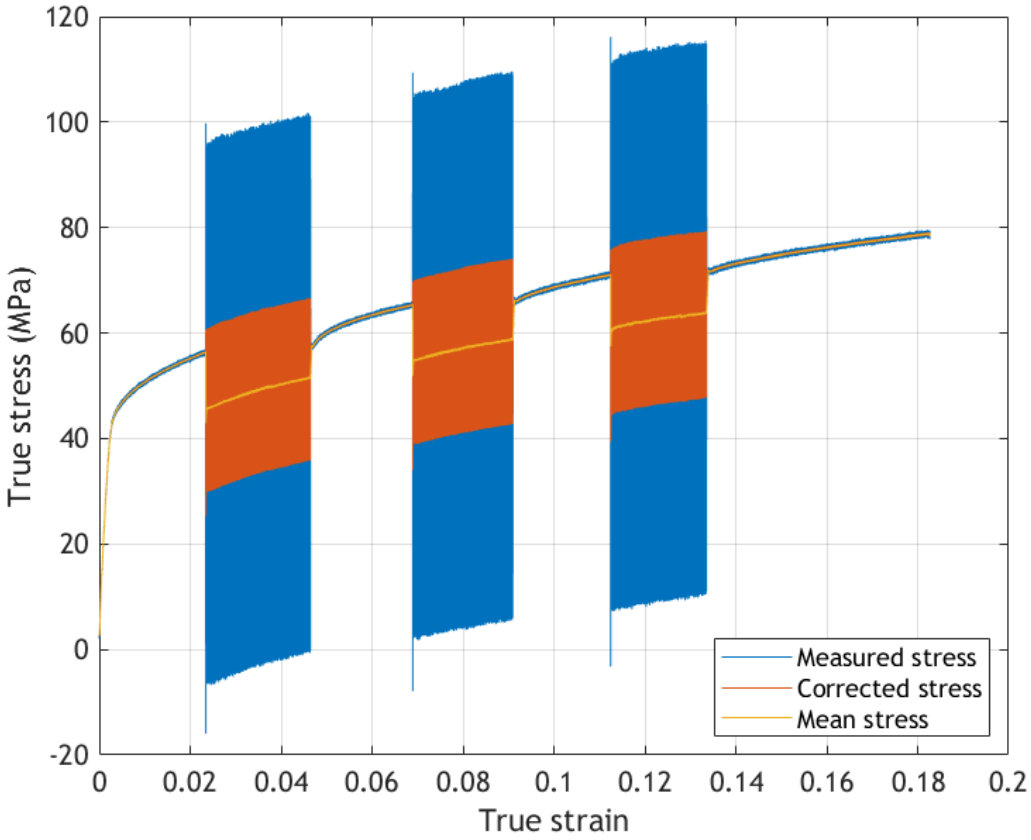

Figure 8.19 - True stress-true strain, USTT experiment with DIC

The three bursts of ultrasonic excitation are clear in the measured true stress (blue curve, 'Measured stress'). The first excitation burst has a constant stress amplitude of approximately 50 MPa ± 1 MPa, repeated in the second and third bursts. This is reduced by the correction factor to an amplitude of 15 MPa ± 1MPa (orange curve, 'Corrected stress'). This is greater than the fall in the mean true stress (yellow curve, 'Mean stress') which coincides with the start of the ultrasonic burst. The mean stress reduces by 10.5 MPa, 10.3 MPa and 10.2 MPa in the first, second and third bursts respectively. The axial stress predicted by correcting the measured stress is significantly higher than the trajectory of the yield stress curve immediately preceding each US burst. Although there are materials which display such behaviour, where increasing strain rate enhances the yield strength, this is not found in the literature pertaining to the aluminium 1050 material tested in this study. A more likely explanation for the mismatch is

a change in the vibration response of the USTT stack caused by dismantling and reassembly required to insert a new specimen. It is possible the amplification of force amplitude experienced by the PFT may have been altered by this process, and so the correction factor derived in Chapter 7 was inaccurate for this set-up.

As the correct true stress amplitude did not fall below the level of the normal yield stress curve APE was not observed in this test.

Despite the extension of 7 mm over a gauge length of 30 mm potentially resulting in a strain of 0.233, the total strain measured by the VE was 0.2005 strain, leading to a final true strain value of 0.183.

The true stress-true strain curve was also derived for the unexcited specimen from the PFT force measurement and the DIC virtual extensometer measurement. It is presented in Figure 8.20 alongside the mean true stress curve for the excited test.

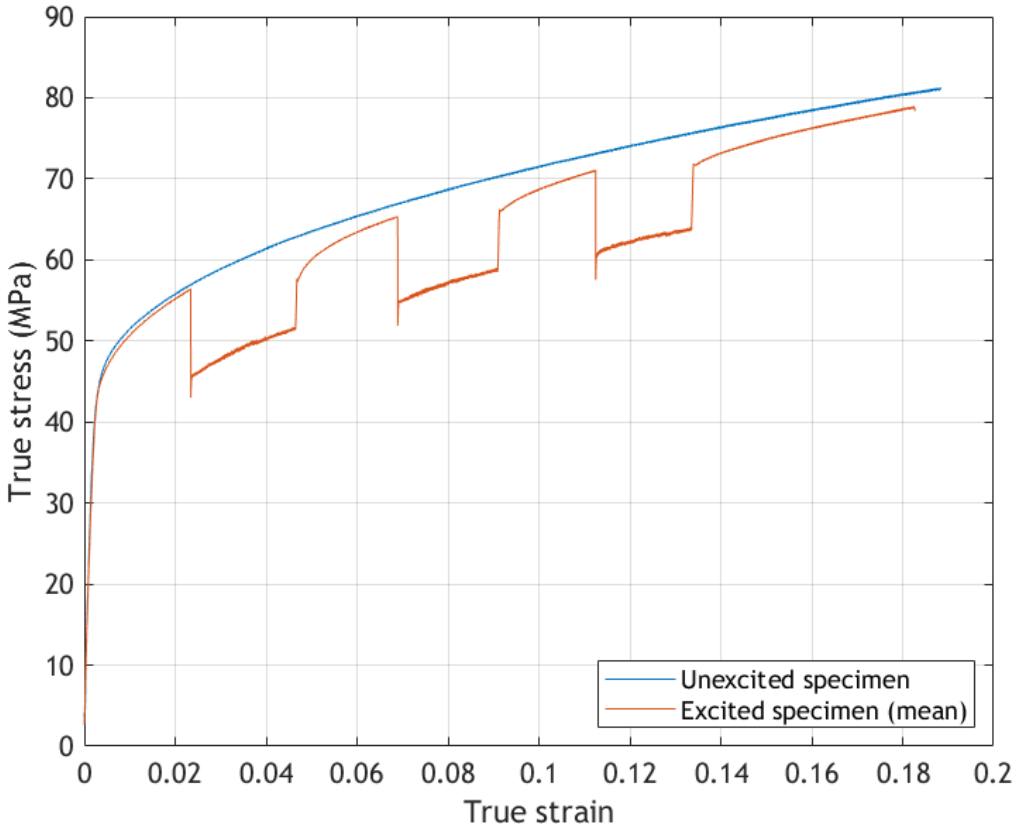

Figure 8.20 - True stress-true strain, unexcited test

The unexcited specimen curve protrudes beyond the end of the excited curve as the total strain measured by the VE was found to be 0.2073 (0.188 true strain), slightly higher than the same value for the excited specimen.

The stress-strain curve of the excited specimen (orange curve, ‘Excited specimen’) tracks the path of the stress-strain curve of the unexcited specimen (blue curve, ‘Unexcited specimen’) until the first burst of US excitation. During this burst the mean stress of the excited specimen decreases sharply by 10 MPa, then continues parallel to the unexcited specimen data. This is consistent with the hypothesis that the material yield strength remains unaltered by US excitation, and that the underlying flow stress curve is unaffected, only appearing to reduce when the oscillatory component of the force signal is removed.

At the end of the burst, once the ultrasonic excitation stops the flow stress in the excited specimen returns gradually to a trend following that of the unexcited specimen, though never recovering fully to the same level. This is repeated to a lesser degree in the next two excitation bursts.

To investigate this further, the force measurement from the test machine load cell for the excited specimen was plotted against the PFT force measurement of the same test, Figure 8.21.

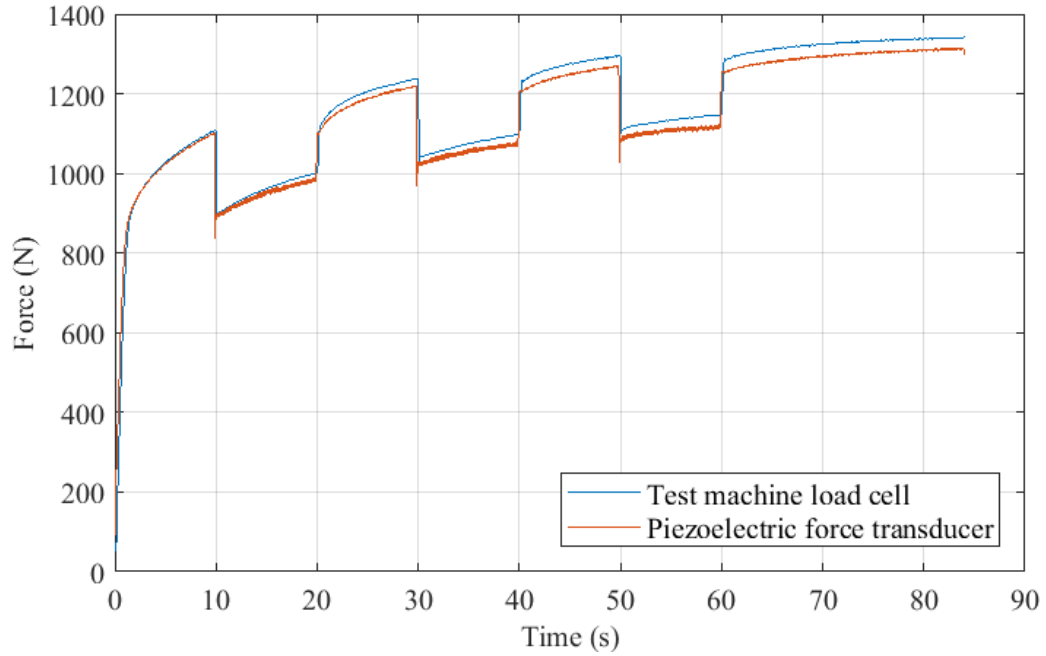

Figure 8.21 - Comparison of force from PFT and load cell, excited specimen

It was observed that the two curves are identical in most details, including the recovery at the end of each excitation burst, with the exception of the overall gradient of the PFT curve. This is approximately 5% lower than the load cell measurement, suggesting the PFT measurement acquired a 5% drift. This finding was also identified in the measurements discussed in Section 7.4. As this error is not observed during static loading of the PFT and the load cell, the drift is attributed to an effect of the US excitation on the PFT.

As the recovery of the flow stress after each burst is observed in both PFT and load cell measurements, it can be concluded that this is a real phenomenon in which the US excitation has affected the yield response of the test material.

Further analysis of the stress-strain data could yield a constitutive equation for the relationship between the corrected true stress and true strain.

8.7 Summary

The bias of the oscillatory stress amplitude towards the mounted end of the specimen directly affects the strain distribution and strain-rate for the duration of the US burst. This effect reverses once the excitation stops.

During excitation a strain rate of 0.004 strain.s^{-1} is reached at that part of the gauge section coincident with the vibration waveform node. Directly the excitation is stopped, plastic strain stops in this location, while the strain rate approximately doubles in the rest of the gauge length. This is in contrast to the average of 0.0036 strain.s^{-1} observed before the US bursts, and a similar figure found in the test of an identical specimen without US excitation.

The detailed mapping of strain will assist post-mortem microscopy, guiding sample location and providing real local plastic strain value to inform interpretation of microscopy results. Further work is required to develop a constitutive relationship from the corrected stress-strain data.

The US excitation generated an oscillatory stress with an amplitude of 50 MPa, and also caused a reduction of the mean flow stress of 10 MPa. When corrected, the measured true stress amplitude was 15 MPa. When recombined with the mean true stress the flow stress during US excitation still exceeded that expected from the path of the flow stress immediately preceding the burst. This was attributed to differences in the amplification error between the test performed in Chapter 5 and the test in this study.

It does not appear that the processes of deformation were affected during the period of ultrasonic excitation, but only their localisation. This is concurrent with the hypothesis that ultrasonic excitation simply acts to increase or decrease the stress load in a localised way, corresponding to the standing wave established by the vibration. It does not support the view that ultrasound can be applied to a specimen as a form of energy which can be passed into the specimen to effect an identical change in material properties, simultaneously throughout the extent of the test piece. A form of recovery behaviour was observed after each burst of excitation ceased, which may be attributable to the influence of US vibration on the dislocation network structure within the material, possibly suggesting the excitation may have disrupted the work-hardening processes normally present.

9 Conclusions and further work

9.1 Conclusions

This thesis presented methodologies for accurate measurement of stress and strain in the ultrasonic tensile test (USTT). The implications of inhomogeneous distribution of stress within an ultrasonically excited specimen were addressed by investigations focusing on the fidelity of the piezoelectric force transducer (PFT) when measuring a high frequency oscillatory force, and its relationship with the loading experienced by the specimen. The inhomogeneous plastic strain response was observed by adapting a standard optical full-field strain measurement technique for use on an ultrasonically excited test piece.

Several experimental mechanics techniques commonly used for material characterisation under static and dynamic loading were examined. Despite having inherent weaknesses with respect to measuring ultrasonic loading, the piezoelectric force transducer was found to retain a crucial role in determining the existence of a true reduction in flow stress, the key feature of acoustoplasticity.

To ensure the force was measured at the point of highest stress in the standing wave set up within the USTT stack, the PFT was connected to the crosshead via the isolating mass. By virtue of its inertia, the isolating mass (a cylinder of steel much bigger than the specimen or PFT) imposed the condition of a displacement node at the PFT-isolating mass connection. It was later shown during vibration measurements made over the length of the stack that the isolating mass performed as intended, exhibiting negligible vibration motion compared to the rest of the structure. As stress is a maximum at displacement nodes, the PFT therefore measured the highest stress over the specimen-PFT assembly.

Lumped-parameter modelling enabled an analysis of the frequency response of the PFT, and in particular, the influence of the PFT's structure on the measurement of an oscillatory force. It was shown that inertial effects could severely distort the input force, or measurand, before it reached the sensing part of the device which produced the electrical force measurement, or indicated value. The proximity of the frequency of the oscillatory measurand to

the resonant frequency of the PFT's first longitudinal mode determined whether the measurand was either amplified or attenuated.

The error introduced by this distortion into the measurement of oscillatory force propagates directly into the calculation of stress amplitude in the specimen, critical for determining the existence of the acoustoplasticity. If left unaccounted for, the error will undermine the conclusions and constitutive models built upon USTT stress-strain data. This has an impact on all of the previous work on the acoustoplastic volume effect. A simple impulse method was used to find the natural frequency of the first longitudinal mode of the PFT, used later in a finite element model of the whole USTT stack.

The dynamic response of the USTT stack was investigated using the Experimental Modal Analysis (EMA) technique. Whilst supplying the ultrasonic transducer with a random noise excitation signal, a Laser Doppler Vibrometer (LDV) was used to measure the velocity response of the ultrasonic horn, specimen, PFT and isolating mass. A signal analyser and specialist software were employed to extract the mode shape of the first longitudinal mode, the mode excited at the operational frequency of the USTT.

An FE model of the ultrasonic tensile test apparatus was constructed, including an FE representation of the piezoelectric force transducer. The latter was created as a homogenous solid, with material properties altered to make the FE model match the frequency response from the impulse experiment. This approach enabled the inclusion of the PFT, a device with a complex internal structure which would otherwise present great difficulties in modelling explicitly.

Following an eigenvalue analysis of the FE model, the mode shape of the first longitudinal mode predicted by the numerical model was compared with that found in the EMA, revealing the significant influence of joint impedance at the horn-specimen interface. The FE model was adapted to include extra compliance at this connection, which was adjusted until predicted and experimental mode shapes converged. The calibrated FE model was then used to predict the force experienced by the force transducer at its centre (the FE equivalent of the PFT indicated value) for increasing values of ultrasonic excitation amplitude.

Comparison with equivalent experimental force measurements showed good agreement, the prediction reproducing the observed linear relationship with a 5.8% difference in gradient. Of particular relevance to the accurate measurement of flow stress reduction, the FE model reported the simulated PFT indicated value to be greater than the measurand at the specimen-PFT interface by a factor of 1.91. This demonstrated that the structure of the PFT has a powerful amplifying effect on the amplitude of the oscillatory component of force on the PFT's connection with the specimen.

A methodology was developed using strain gauges to measure the amplitude of oscillatory strain directly on the gauge length surface of a replica specimen. By calculating force from the strain measurement, a comparison with the PFT force measurement was made. The displacement developed at the tip of the ultrasonic horn was varied from around 1.5 to 9.5 μm. The ratio of the amplitude of force measured by the PFT over the force amplitude calculated from the specimen strain measurement was found to range from 3.13 to 3.50, with a mean value of 3.32. The experiment was replicated with the FE model of the USTT developed previously, which predicted an amplitude ratio of 3.33, constant over all vibration displacement amplitudes. The simulated value was used to find a correction factor, applied to a full ultrasonic tensile test on a soft aluminium which exhibited acoustic softening in many previous studies. Once the correction factor was applied to the data, the peaks of the oscillatory stress reached the normal yield strength of the test material. Though the mean stress was reduced during the periods of excitation, no real reduction in flow stress was observed. This is consistent with the theory of stress superposition, and no effect on material properties is required to explain the results.

To observe the evolution of plastic deformation throughout the duration of the USTT, a standard optical method of measuring full-field strain was adapted for use on the ultrasonically excited specimen. A strobe system was synchronised with the specimen vibration in order to eliminate dynamic motion from images of the specimen deformation, captured using an ordinary USB industrial camera such as are commonly used in video extensometry. Digital Image Correlation (DIC) was used to process the images to find strain and strain rate across the whole face of the specimen gauge length. The data revealed that, in the

absence of ultrasonic excitation, plastic deformation was evenly distributed over the length of the specimen, with some local variation, as would be expected of a normal tensile test. In contrast, during the periods of excitation, plastic deformation became focused at the end of the specimen connected to the PFT, corresponding to the location of minimum displacement, and maximum stress, in the specimen. The strain rate increased significantly in this location, while elsewhere plastic strain stopped completely. This remains consistent with the theory of stress superposition. It does not support the view that ultrasonic energy can be delivered into a specimen to cause the same change in intrinsic material properties through its full extent, in a manner similar to the supply of energy through the application of heat.

It was shown that the full-field strain mapping available from DIC can provide useful insight into the influence of ultrasonic excitation on the transient distribution of strain and strain-rate. It may also prove useful in directing post-mortem microscopy.

By improving the accuracy of material characterisation carried out in ultrasonic mechanical testing, this work will have a beneficial impact on the design and optimisation of industrial ultrasonic metal forming processes.

9.2 Innovations

Work presented in this thesis which is thought novel within the particular field of acoustoplasticity:

- Deployment of isolating mass to guarantee boundary condition at force transducer, and retain vibration within USTT stack;
- EMA assessment of USTT stack inclusive of specimen and force measurement device;
- Within the field of APE, use of strain gauges on specimen to measure oscillatory loading directly;
- Generation of a correction factor for oscillatory stress amplitude from EMA-FEA method, or from strain gauge method, and application to USTT.

9.3 Further work

To aid further investigations into the nature of material behaviour under ultrasonic excitation, further improvements and development could include the following:

- Significant effort was required to adapt the FE model of the joint between the ultrasonic horn and the specimen, such that the simulated waveform matched that found by EMA. A much stiffer joint should be developed to investigate if this will reduce, or even eliminate this requirement.

- Conversely, the methodology of using non-contact observation of velocity or displacement could be trialled on compressive uniaxial testing, to investigate whether the compliance in the specimen-platen interface can be replicated within FEA. The objective would be to successfully predict the difference in oscillatory loading amplitude between the specimen and a force transducer on the other side of the platen, the arrangement commonly used in such tests.

- With regards the PFT, representing it as a homogeneous solid produced satisfactory results and presented the rest of the test structure with the correct impedance, confirmed by the overall match with EMA mode shape data. However, resolving the homogeneous PFT geometry into, at the least, two end caps and a compliant centre section, would enable the FE model to capture the detail observed in the EMA waveform over the real PFT. An FE model developed this way could be readily compared to the lumped-parameter models where the PFT is represented as two end masses connected by a spring.

- As an accurate and robust correction factor is the most useful contribution of this work so far, testing should continue to establish the cause of differences between the strain gauge and FE model predictions of force on the specimen, and the amplification of force between specimen and PFT. It is noted that improvements in technique could be

made with regards to the application of strain gauges which would improve the endurance of the system.

- The effect of specimen plastic deformation on the correction factor κ should be explored to verify its applicability to the combined elastic-plastic strain experienced by the specimen in an USTT.

- The ultimate goal of obtaining full-field stress and strain data is to identify the local stress-strain relationship at any location over the specimen gauge section. However, in the present work stress throughout the specimen can only be extrapolated from the absolute measurement of the force transducer via the FE prediction of the oscillatory stress amplitude distribution. (Alternatively, the strain gauge-based correction factor can be used if the location of identification is limited to the axial position of the strain gauges.) Further work is required to combine this information with the full-field plastic strain measurement to produce a local stress-strain curve.

- Having found no evidence of a true reduction in flow stress in aluminium 1050-O, it remains to test other aluminium alloys, and other materials which it has previously been claimed exhibit acoustoplasticity.

- Similarly, due to apparatus limitations it was only feasible to test at the single frequency of 20 kHz, up to a maximum specimen displacement of approximately 14 μm, and more importantly, achieving a maximum stress amplitude of 23 MPa. Frequency has previously been discounted as an influence on APE, however stress amplitude remains a good candidate for further exploration. The question of how APE varies with stress amplitude, and whether there is a critical threshold of stress amplitude above which APE will occur, remains unresolved.

- Depending on the outcome of this review, research effort on ultrasonically assisted metal forming may be better refocused onto the friction-reduction phenomena. The methods demonstrated here should be applied to the compressive test, so that the benefits of accurate force

measurement may be brought to bear on the friction reduction claimed for ultrasonic excitation.

10 List of References

[1] F. Blaha and B. Langenecker, “Dehnung von Zink-Kristallen unter Ultraschalleinwirkung,” *Naturwissenschaften*, vol. 42, no. 20, p. 556, 1955, doi: 10.1007/BF00623773.

[2] B. Langenecker, “Effects of Ultrasound on Deformation Characteristics of Metals,” *IEEE Trans. Sonics Ultrason.*, vol. 13, no. 1, pp. 1–8, 1966, doi: 10.1109/T-SU.1966.29367.

[3] K. W. Siu, A. H. W. Ngan, and I. P. Jones, “New insight on acoustoplasticity - Ultrasonic irradiation enhances subgrain formation during deformation,” *Int. J. Plast.*, vol. 27, no. 5, pp. 788–800, 2011, doi: 10.1016/j.ijplas.2010.09.007.

[4] R. K. Dutta, R. H. Petrov, M. J. M. Hermans, and I. M. Richardson, “Accommodation of Plastic Deformation by Ultrasound-Induced Grain Rotation,” *Metall. Mater. Trans. A Phys. Metall. Mater. Sci.*, vol. 46, no. 8, pp. 3414–3422, 2015, doi: 10.1007/s11661-015-2910-8.

[5] R. K. Dutta, R. H. Petrov, R. Delhez, M. J. M. Hermans, I. M. Richardson, and A. J. Böttger, “The effect of tensile deformation by in situ ultrasonic treatment on the microstructure of low-carbon steel,” *Acta Mater.*, vol. 61, no. 5, pp. 1592–1602, 2013, doi: 10.1016/j.actamat.2012.11.036.

[6] S. Bagherzadeh and K. Abrinia, “Effect of Ultrasonic Vibration on Compression Behavior and Microstructural Characteristics of Commercially Pure Aluminum,” *J. Mater. Eng. Perform.*, vol. 24, no. 11, pp. 4364–4376, 2015, doi: 10.1007/s11665-015-1730-8.

[7] A. Deshpande and K. Hsu, “Acoustic energy enabled dynamic recovery in aluminium and its effects on stress evolution and post-deformation microstructure,” *Mater. Sci. Eng. A*, vol. 711, pp. 62–68, Jan. 2018, doi: 10.1016/j.msea.2017.11.015.

[8] H. Zhou, H. Cui, and Q. H. Qin, “Influence of ultrasonic vibration on the

plasticity of metals during compression process," *J. Mater. Process. Technol.*, vol. 251, no. November 2016, pp. 146–159, 2018, doi: 10.1016/j.jmatprotec.2017.08.021.

[9] G. E. Nevill and F. R. Brotzen, "The effect of vibrations on the static yield strength of a low-carbon steel," *Am. Soc. Test. Mater.*, vol. 57, pp. 751–758, 1957.

[10] Z. Yao *et al.*, "Acoustic softening and residual hardening in aluminum: Modeling and experiments," *Int. J. Plast.*, vol. 39, pp. 75–87, 2012, doi: 10.1016/j.ijplas.2012.06.003.

[11] K. W. Siu, H. Liu, and A. H. W. Ngan, "A universal law for metallurgical effects on acoustoplasticity," *Materialia*, vol. 5, p. 100214, Mar. 2019, doi: 10.1016/j.mtla.2019.100214.

[12] H. Zhou, H. Cui, Q. H. Qin, H. Wang, and Y. Shen, "A comparative study of mechanical and microstructural characteristics of aluminium and titanium undergoing ultrasonic assisted compression testing," *Mater. Sci. Eng. A*, vol. 682, no. June 2016, pp. 376–388, 2017, doi: 10.1016/j.msea.2016.11.021.

[13] Z. Yao, G.-Y. Kim, L. Faidley, Q. Zou, D. Mei, and Z. Chen, "Effects of superimposed high-frequency vibration on deformation of aluminum in micro/meso-scale upsetting," *J. Mater. Process. Technol.*, vol. 212, no. 3, pp. 640–646, Mar. 2012, doi: 10.1016/j.jmatprotec.2011.10.017.

[14] J. Hu, T. Shimizu, and M. Yang, "Investigation on ultrasonic volume effects: Stress superposition, acoustic softening and dynamic impact," *Ultrason. Sonochem.*, vol. 48, no. April, pp. 240–248, 2018, doi: 10.1016/j.ultsonch.2018.05.039.

[15] Y. Daud, M. Lucas, and Z. Huang, "Modelling the effects of superimposed ultrasonic vibrations on tension and compression tests of aluminium," *J. Mater. Process. Technol.*, vol. 186, no. 1–3, pp. 179–190, 2007, doi: 10.1016/j.jmatprotec.2006.12.032.

[16] I. Kristoffy, “Metal Forming With Vibrated Tools,” *J. Eng. Ind.*, vol. 91, no. 4, pp. 1168–1174, 1969, doi: 10.1115/1.3591766.

[17] A. E. Eaves, A. W. Smith, W. J. Waterhouse, and D. H. Sansome, “Review of the application of ultra- sonic vibrations to deforming metals,” *Ultrasonics*, no. July 1974, pp. 162–170, 1975.

[18] Kistler Instruments Ltd, “Kistler Instruction Manual - Quartz Force Links 9301B - 9371B.” .

[19] A. P. Cracknell, *Ultrasonics*. Wykeham Publications (London) Ltd, 1980.

[20] J. W. r. B. R. Strutt, *The theory of sound*, 2nd ed. Dover, 1945.

[21] J. A. Gallego-Juárez and K. F. Graff, *Power Ultrasonics: Applications of High-Intensity Ultrasound*. 2014.

[22] M. Lucas, A. Gachagan, and A. Cardoni, “Research applications and opportunities in power ultrasonics,” *Proc. Inst. Mech. Eng. Part C J. Mech. Eng. Sci.*, vol. 223, no. 12, pp. 2949–2965, 2009, doi: 10.1243/09544062JMES1671.

[23] R. W. Wood and A. L. Loomis, “The physical and biological effects of high-frequency sound-waves of great intensity,” *London, Edinburgh, Dublin Philos. Mag. J. Sci.*, vol. 4, no. 22, pp. 417–436, Sep. 1927, doi: 10.1080/14786440908564348.

[24] S. Kalpakjian and S. R. Schmid, *Manufacturing processes for engineering materials*, 4th ed. Prentice Hall-Pearson Education, 2003.

[25] D. Hull and D. J. Bacon, *Introduction to Dislocations*, 5th ed. Butterworth-Heinemann, 2011.

[26] M. F. Ashby and D. R. H. Jones, *Engineering materials 1 : an introduction to properties, applications and design*, 2nd ed. Butterworth-Heinemann, 2003.

[27] G. I. Taylor, “The Mechanism of Plastic Deformation of Crystals. Part I. Theoretical,” *Proc. R. Soc. A Math. Phys. Eng. Sci.*, vol. 145, no. 855, pp. 362–387, Jul. 1934, doi: 10.1098/rspa.1934.0106.

[28] T. A. Read, “The Internal Friction of Single Metal Crystals,” *Phys. Rev.*, vol. 58, no. 4, pp. 371–380, Aug. 1940, doi: 10.1103/PhysRev.58.371.

[29] C. E. WINSPER and D. H. SANSOME, “A REVIEW OF THE APPLICATION OF OSCILLATORY ENERGY TO METALS DEFORMING PLASTICALLY,” in *Advances in Machine Tool Design and Research 1967*, Elsevier, 1968, pp. 1349–1360.

[30] B. Langenecker, “Work-softening of metal crystals by alternating the rate of glide strain,” *Acta Metall.*, vol. 9, no. 10, pp. 937–940, 1961, doi: 10.1016/0001-6160(61)90112-2.

[31] B. Langenecker, “Dislocation Damping in Macrosonic Fields,” *Phys. Rev.*, vol. 145, no. 2, pp. 487–491, May 1966, doi: 10.1103/PhysRev.145.487.

[32] F. Blaha and B. Langenecker, “Plastic behaviour of metals under ultrasonics,” *J. Phys. Metall.*, vol. 51, p. 636, 1960.

[33] S. Abdul Aziz and M. Lucas, “The Effect of Ultrasonic Excitation in Metal Forming Tests,” *Appl. Mech. Mater.*, vol. 24–25, pp. 311–316, 2010, doi: 10.4028/www.scientific.net/AMM.24-25.311.

[34] S. A. Aziz and M. Lucas, “Characterising the acoustoplastic effect in an ultrasonically assisted metal forming process,” *IOP Conf. Ser. Mater. Sci. Eng.*, vol. 42, no. 1, 2012, doi: 10.1088/1757-899X/42/1/012017.

[35] B. Langenecker and C. W. Fountain, “Neutron-acoustic irradiation of aluminium single crystals,” *Philos. Mag.*, vol. 11, no. 111, pp. 513–519, Mar. 1965, doi: 10.1080/14786436508224238.

[36] T. Ohgaku and N. Takeuchi, “The Blaha Effect of Alkali Halide Crystals,” *Phys. Status Solidi*, vol. 102, no. 1, pp. 293–299, 1987, doi: 10.1002/pssa.2211020130.

[37] O. Izumi, K. Oyama, and Y. Suzuki, “On the Superimposing of Ultrasonic Vibration during Compressive Deformation of Metals,” *Trans. Japan Inst. Met.*, vol. 7, no. 3, pp. 158–161, 1966, doi: 10.2320/matertrans1960.7.158.

[38] O. Izumi, K. Oyama, and Y. Suzuki, “Effects of Superimposed Ultrasonic Vibration on Compressive Deformation of Metals,” *Trans. Japan Inst. Met.*, vol. 7, no. 3, pp. 162–167, 1966, doi: 10.2320/matertrans1960.7.162.

[39] B. Langenecker, “Ultrasonic treatment of specimens in the electron microscope,” *Rev. Sci. Instrum.*, vol. 37, no. 1, pp. 103–106, 1966, doi: 10.1063/1.1719922.

[40] Z. Yao, G. Y. Kim, L. Faidley, Q. Zou, D. Mei, and Z. Chen, “Effects of superimposed high-frequency vibration on deformation of aluminum in micro/meso-scale upsetting,” *J. Mater. Process. Technol.*, vol. 212, no. 3, pp. 640–646, 2012, doi: 10.1016/j.jmatprotec.2011.10.017.

[41] J. Hu, T. Shimizu, T. Yoshino, T. Shiratori, and M. Yang, “Evolution of acoustic softening effect on ultrasonic-assisted micro/meso-compression behavior and microstructure,” *Ultrasonics*, vol. 107, p. 106107, Sep. 2020, doi: 10.1016/j.ultras.2020.106107.

[42] F. Ahmadi, M. Farzin, and M. Mandegari, “Effect of grain size on ultrasonic softening of pure aluminum,” *Ultrasonics*, vol. 63, pp. 111–117, 2015, doi: 10.1016/j.ultras.2015.06.015.

[43] Y. Daud, “Experimental and finite element investigation of ultrasonic metal forming applications,” University of Glasgow, 2006.

[44] R. Pohlman and E. Lehfeldt, “Influence of ultrasonic vibration on metallic friction,” *Ultrasonics*, vol. 4, no. 4, pp. 178–185, 1966, doi: 10.1016/0041-624X(66)90244-7.

[45] A. V. Kozlov and S. I. Selitser, “Peculiarities in the plastic deformation of crystals subjected to the acoustoplastic effect,” *Mater. Sci. Eng.*, vol. 102,

no. 2, pp. 143–149, 1988, doi: 10.1016/0025-5416(88)90568-X.

[46] A. V. Kozlov and S. I. Selitser, “Kinetics of the acoustoplastic effect,” *Mater. Sci. Eng. A*, vol. 131, no. 1, pp. 17–25, 1991, doi: 10.1016/0921-5093(91)90340-S.

[47] M. Tanibayashi, “A Theory of the Blaha Effect,” *Phys. Status Solidi*, vol. 128, no. 1, pp. 83–94, 1991, doi: 10.1002/pssa.2211280109.

[48] G. a. Malygin, “Acoustoplastic effect and the stress superimposition mechanism,” *Phys. Solid State*, vol. 42, no. 1, pp. 72–78, 2000, doi: 10.1134/1.1131170.

[49] A. Rusinko, “Analytical description of ultrasonic hardening and softening,” *Ultrasonics*, vol. 51, no. 6, pp. 709–714, 2011, doi: 10.1016/j.ultras.2011.02.003.

[50] A. Siddiq and T. El Sayed, “Acoustic softening in metals during ultrasonic assisted deformation via CP-FEM,” *Mater. Lett.*, vol. 65, no. 2, pp. 356–359, 2011, doi: 10.1016/j.matlet.2010.10.031.

[51] H. Sedaghat, W. Xu, and L. Zhang, “Ultrasonic vibration-assisted metal forming: Constitutive modelling of acoustoplasticity and applications,” *J. Mater. Process. Technol.*, vol. 265, pp. 122–129, Mar. 2019, doi: 10.1016/j.jmatprotec.2018.10.012.

[52] K. W. Siu and A. H. W. Ngan, “Oscillation-induced softening in copper and molybdenum from nano- to micro-length scales,” *Mater. Sci. Eng. A*, vol. 572, pp. 56–64, Jun. 2013, doi: 10.1016/j.msea.2013.02.037.

[53] D. François, A. Pineau, and A. Zaoui, *Mechanical Behaviour of Materials Vol 1*. Elsevier, 2012.

[54] E. Schmid, “Effects of energy radiation on the plastic deformation of metals,” *Materialprufung*, vol. 4, no. 8, pp. 274–283, 1962.

[55] Y. Daud, M. Lucas, and Z. Huang, “Superimposed ultrasonic oscillations in

compression tests of aluminium," *Ultrasonics*, vol. 44, no. SUPPL., pp. 511–515, 2006, doi: 10.1016/j.ultras.2006.05.116.

[56] T. Liu, J. Lin, Y. Guan, Z. Xie, L. Zhu, and J. Zhai, "Effects of ultrasonic vibration on the compression of pure titanium," *Ultrasonics*, 2018, doi: 10.1016/j.ultras.2018.04.006.

[57] M. Yang, L. Bai, Y. Li, and Q. Yuan, "Influences of Vibration Parameters on Formability of 1060 Aluminum Sheet Processed by Ultrasonic Vibration-Assisted Single Point Incremental Forming," *Adv. Mater. Sci. Eng.*, vol. 2019, pp. 1–12, Apr. 2019, doi: 10.1155/2019/8405438.

[58] Z. Xie, Y. Guan, J. Lin, J. Zhai, and L. Zhu, "Constitutive model of 6063 aluminum alloy under the ultrasonic vibration upsetting based on Johnson-Cook model," *Ultrasonics*, vol. 96, pp. 1–9, Jul. 2019, doi: 10.1016/j.ultras.2019.03.017.

[59] Z. Yao, G.-Y. Kim, L. Faidley, Q. Zou, D. Mei, and Z. Chen, "Micro Pin Extrusion of Metallic Materials Assisted by Ultrasonic Vibration," in *ASME 2010 International Manufacturing Science and Engineering Conference, Volume 1*, 2010, pp. 647–651, doi: 10.1115/MSEC2010-34159.

[60] Z. Yao, G.-Y. Kim, L. Faidley, Q. Zou, D. Mei, and Z. Chen, "Experimental Study of High-Frequency Vibration Assisted Micro/Mesoscale Forming of Metallic Materials," *J. Manuf. Sci. Eng.*, vol. 133, no. 6, p. 061009, 2011, doi: 10.1115/1.4004612.

[61] A. Prabhakar, G. C. Verma, H. Krishnasamy, P. M. Pandey, M. G. Lee, and S. Suwas, "Dislocation density based constitutive model for ultrasonic assisted deformation," *Mech. Res. Commun.*, vol. 85, pp. 76–80, 2017, doi: 10.1016/j.mechrescom.2017.08.003.

[62] A. Siddiq and T. El Sayed, "Ultrasonic-assisted manufacturing processes: Variational model and numerical simulations," *Ultrasonics*, vol. 52, no. 4, pp. 521–529, 2012, doi: 10.1016/j.ultras.2011.11.004.

[63] Q. Mao, J. M. Gibert, and G. Fadel, “Investigating Ultrasound-Induced Acoustic Softening of Aluminum 6061,” in *Volume 8: 26th Conference on Mechanical Vibration and Noise*, 2014, doi: 10.1115/DETC2014-34579.

[64] C. J. Wang, Y. Liu, B. Guo, D. B. Shan, and B. Zhang, “Acoustic softening and stress superposition in ultrasonic vibration assisted uniaxial tension of copper foil: Experiments and modeling,” *Mater. Des.*, vol. 112, pp. 246–253, 2016, doi: 10.1016/j.matdes.2016.09.042.

[65] K. F. Graff, *Wave motion in elastic solids*. 1991.

[66] M. A. Meyers, “The Dynamic Behavior of Materials: An Introduction,” *Jom*, vol. 62, no. 1. pp. 14–15, 2010, doi: 10.1007/s11837-010-0003-0.

[67] M. L. T. Cossio *et al.*, *Springer Handbook of Acoustics*. 2007.

[68] V. Fartashvand, A. Abdullah, and S. A. Sadough Vanini, “Investigation of Ti-6Al-4V alloy acoustic softening,” *Ultrason. Sonochem.*, vol. 38, pp. 744–749, Sep. 2017, doi: 10.1016/j.ultsonch.2016.07.007.

[69] L. Faidley, G.-Y. Kim, Z. Chen, D. Mei, Q. Zou, and Z. Yao, “Experimental Study of High-Frequency Vibration Assisted Micro/Mesoscale Forming of Metallic Materials,” *J. Manuf. Sci. Eng.*, vol. 133, no. 6, p. 061009, 2011, doi: 10.1115/1.4004612.

[70] L. E. Kinsler, A. R. Frey, A. B. Coppens, and J. V. Sanders, *Fundamentals of Acoustics 4th edition*. 2000.

[71] C. E. Winsper, G. R. Dawson, and D. H. Sansome, “An introduction to the mechanics of Oscillatory metalworking,” *Met. Mater.*, pp. 158–162, 1970.

[72] S. Abdul Aziz, “Characterising the effective material softening in ultrasonic forming of metals,” University of Glasgow, 2012.

[73] A. Deshpande, A. Tofangchi, and K. Hsu, “Microstructure evolution of Al6061 and copper during ultrasonic energy assisted compression,” *Mater. Charact.*, vol. 153, pp. 240–250, Jul. 2019, doi:

10.1016/j.matchar.2019.05.005.

[74] “BS EN ISO 6892-1:2016 Metallic materials — Tensile testing Part 1: Method of test at room temperature,” 2016.

[75] H. Czichos, T. Saito, and L. Smith, Eds., *Springer Handbook of Materials Measurement Methods*. Berlin, Heidelberg: Springer Berlin Heidelberg, 2006.

[76] F. A. McClintock and A. . Argon, *Mechanical Behaviour of Materials*. Addison-Wesley, 1966.

[77] J. E. Field, S. M. Walley, W. G. Proud, H. T. Goldrein, and C. R. Siviour, “Review of experimental techniques for high rate deformation and shock studies,” *Int. J. Impact Eng.*, vol. 30, no. 7, pp. 725–775, Aug. 2004, doi: 10.1016/j.ijimpeng.2004.03.005.

[78] D. J. Ewins, *Modal Testing: Theory, Practice and Application*. Wiley, Research Studies Press, 2000.

[79] É. Markiewicz, B. Langrand, and D. Notta-Cuvier, “A review of characterisation and parameters identification of materials constitutive and damage models: From normalised direct approach to most advanced inverse problem resolution,” *Int. J. Impact Eng.*, vol. 110, pp. 371–381, Dec. 2017, doi: 10.1016/j.ijimpeng.2017.01.028.

[80] G. Haugou, J. Fabis, B. Langrand, E. Deletombe, and E. Markiewicz, “Iterative Experimental / Numerical Procedure For Improvement Of Dynamic Experimental Facilities,” in *Structure Under Shock and Impact VII (SUSI2002)*, 2002, doi: 10.2495/SU020111.

[81] S. Aloui, R. Othman, A. Poitou, P. Guégan, and S. El-Borgi, “Non-parametric identification of the non-homogeneous stress in high strain-rate uni-axial experiments,” *Mech. Res. Commun.*, vol. 35, no. 6, pp. 392–397, Sep. 2008, doi: 10.1016/j.mechrescom.2008.04.005.

[82] R. Othman, S. Aloui, and A. Poitou, “Identification of non-homogeneous stress fields in dynamic experiments with a non-parametric method,” *Polym. Test.*, vol. 29, no. 5, pp. 616–623, Aug. 2010, doi: 10.1016/j.polymertesting.2010.03.013.

[83] P. Transactions, O. F. The, R. Society, M. P. Sciences, and F. Pierron, “Beyond Hopkinson ’ s bar,” no. September 2015, 2014, doi: 10.1098/rsta.2013.0195.

[84] R. Seghir and F. Pierron, “A Novel Image-based Ultrasonic Test to Map Material Mechanical Properties at High Strain-rates,” *Exp. Mech.*, vol. 58, no. 2, pp. 183–206, 2018, doi: 10.1007/s11340-017-0329-4.

[85] D. Wang, M. Lucas, and K. E. Tanner, “Characterising the Strain and Temperature Fields in a Surrogate Bone Material Subject to Power Ultrasonic Excitation,” *Strain*, p. n/a-n/a, Aug. 2013, doi: 10.1111/str.12047.

[86] R. Kumme, O. Mack, B. Bill, C. Gossweiler, and H. R. Haab, “Dynamic Properties and Investigations of Piezoelectric Force Measuring Device,” 2000.

[87] “ISO 4965-1:2012 Metallic materials — Dynamic force calibration for uniaxial fatigue testing Part 1:Testing Systems.”

[88] W. T. Thomson and M. D. Dahleh, *Theory of Vibration*, 5th ed. 1998.

[89] A. A. Shabana, *Theory of Vibration - An Introduction*, 3rd ed. Cham: Springer International Publishing, 2019.

[90] M. Kobusch, “Characterization of Force Transducers for Dynamic Measurements,” 2015.

[91] W. Braender, “High Frequency Response of Force Transducers,” *Bruel & Kjaer Technical Review*, pp. 15–22.

[92] Y. Fujii, “A method for calibrating force transducers against oscillation

force," *Meas. Sci. Technol.*, vol. 14, no. 8, pp. 1259–1264, Aug. 2003, doi: 10.1088/0957-0233/14/8/310.

[93] M. Serridge and T. R. Licht, *Bruel & Kjaer Piezoelectric Accelerometers and Vibration Preamplifiers Theory and Application Handbook*. 1987.

[94] A. Shabana, *Vibration of Discrete and Continuous Systems*. Cham: Springer International Publishing, 2019.

[95] H. Al-Budairi, "Design and analysis of ultrasonic horns operating in longitudinal and torsional vibration," 2012.

[96] A. Cardoni, "Characterising the dynamic response of ultrasonic cutting devices," University of Glasgow, 2003.

[97] R. S. Cleary, "Resonant ultrasonic bone penetrating needles," University of Glasgow, 2020.

[98] X. Li, M. Lucas, and P. Harkness, "Full and Half-Wavelength Ultrasonic Percussive Drills," *IEEE Trans. Ultrason. Ferroelectr. Freq. Control*, vol. 65, no. 11, pp. 2150–2159, Nov. 2018, doi: 10.1109/TUFFC.2018.2867535.

[99] X. Li, P. Harkness, K. Worrall, R. Timoney, and M. Lucas, "A Parametric Study for the Design of an Optimized Ultrasonic Percussive Planetary Drill Tool," *IEEE Trans. Ultrason. Ferroelectr. Freq. Control*, vol. 64, no. 3, pp. 577–589, Mar. 2017, doi: 10.1109/TUFFC.2016.2633319.

[100] Dassault Systems, "Abaqus 2018 Analysis User's Guide," 2018.

[101] D. M. Mulvihill, H. Brunskill, M. E. Kartal, R. S. Dwyer-Joyce, and D. Nowell, "A Comparison of Contact Stiffness Measurements Obtained by the Digital Image Correlation and Ultrasound Techniques," *Exp. Mech.*, vol. 53, no. 7, pp. 1245–1263, Sep. 2013, doi: 10.1007/s11340-013-9718-5.

[102] M. R. W. Brake, Ed., *The Mechanics of Jointed Structures*. Cham: Springer International Publishing, 2018.

[103] B. W. Drinkwater, R. S. Dwyer-Joyce, and P. Cawley, “A study of the interaction between ultrasound and a partially contacting solid—solid interface,” *Proc. R. Soc. London. Ser. A Math. Phys. Eng. Sci.*, vol. 452, no. 1955, pp. 2613–2628, Dec. 1996, doi: 10.1098/rspa.1996.0139.

[104] K. Ueda and A. Umeda, “Dynamic response of strain gages up to 300 kHz,” *Exp. Mech.*, vol. 38, no. 2, pp. 93–98, Jun. 1998, doi: 10.1007/BF02321650.

[105] W. N. Sharpe, Ed., *Springer Handbook of Experimental Solid Mechanics*. Boston, MA: Springer US, 2008.

[106] J. P. Hessling, “Dynamic calibration of uni-axial material testing machines,” *Mech. Syst. Signal Process.*, vol. 22, no. 2, pp. 451–466, Feb. 2008, doi: 10.1016/j.ymssp.2007.07.010.

[107] J. P. Hessling, “Models of dynamic measurement error variations of material testing machines,” *Mech. Syst. Signal Process.*, vol. 23, no. 8, pp. 2510–2518, Nov. 2009, doi: 10.1016/j.ymssp.2009.05.009.

[108] “Matweb.” http://www.matweb.com/ (accessed Jun. 15, 2020).

[109] Vishay Precision Group, “Instruction Bulletin B-152 Strain Gage Installations with M-Bond 450 Adhesive,” 2016. [Online]. Available: http://www.vishaypg.com/docs/11130/11130B130.pdf.

[110] Vishay Precision Group, “VPG Tech Note TT-609: Strain Gage Soldering Techniques,” 2015.

[111] E. C. Bell and R. W. Whitehead, *Basic Electrical Engineering & Instrumentation for Engineers*. 1977.

[112] B. A. Gregory, *An Introduction to Electrical Instrumentation and Measurement Systems*. London: Macmillan Education UK, 1981.

[113] H. Yamada, T. Kami, R. Mori, T. Kudo, and M. Okada, “Strain Rate Dependence of Material Strength in AA5xxx Series Aluminum Alloys and Evaluation of Their Constitutive Equation,” *Metals (Basel).*, vol. 8, no. 8,

p. 576, Jul. 2018, doi: 10.3390/met8080576.

[114] H. Schreier, J.-J. Orteu, and M. A. Sutton, *Image Correlation for Shape, Motion and Deformation Measurements*. Boston, MA: Springer US, 2009.

[115] “Correlated Solutions VIC-2D system specification.” https://www.correlatedsolutions.com/vic-2d/ (accessed Feb. 11, 2021).

[116] W. Le Page, “digitalimagecorrelation.org.” https://digitalimagecorrelation.org/ (accessed Jun. 20, 2021).

[117] C. Willert, B. Stasicki, J. Klinner, and S. Moessner, “Pulsed operation of high-power light emitting diodes for imaging flow velocimetry,” *Meas. Sci. Technol.*, vol. 21, no. 7, 2010, doi: 10.1088/0957-0233/21/7/075402.

[118] S. Tamimi, A. Andrade-Campos, and J. Pinho-da-Cruz, “Modelling the Portevin-Le Chatelier effects in aluminium alloys: a review,” *J. Mech. Behav. Mater.*, vol. 24, no. 3–4, pp. 67–78, Aug. 2015, doi: 10.1515/jmbm-2015-0008.